ENTRO
NILE BASIN INITIATIVE
INITIATIVE DU BASSIN DU NIL

Eastern Nile Technical Regional Office (ENTRO)

Eastern Nile Climate Assessment: Rainfall Analysis

7th NCCR Internship Batch

Theme II: Eastern Nile River Basin Future Rainfall Projections

(Final Report)

Prepared By:

- Mohammed Adil Hassan
- Esraa Merghani Osman
- Moses Hakim Caesar
- Sisaynew Getahun

February 13th 2024

Table of Content

Executive Summary

Water resources play a pivotal role in fostering socio-economic advancement and environmental equilibrium on a global scale. In regions like the Eastern Nile Basin (ENB), where rainfall patterns exhibit intricate and dynamic characteristics, a profound comprehension of trends and future projections is imperative for the sustainable management of water resources. This report delves into the analysis and projection of rainfall patterns within the ENB, employing advanced statistical and spatial analysis techniques to unravel crucial insights.

The analysis conducted unveils substantial variability in rainfall patterns across the ENB, attributable to the multifaceted influences of climate change and global atmospheric systems. By meticulously evaluating 8 CMIP6 climate models, we have gleaned key insights into rainfall trends and projections extending up to the year 2060. Notably, while certain models demonstrate commendable reliability in capturing seasonal patterns and distribution, others exhibit variances in performance across different sub-basins of the ENB. However, the ultimate result for future projections over the basin is that most models indicate an increasing rainfall trend up to 2060.

Among all the 8 models, GFDL-CM4, GFDL-ESM, Nor-ESM2-MM, BCC-CSM2, and MPI-ESM performed well when compared with observed data statistically, using metrics such as R2, cc, NSE, PBIAS, RMSE, and MAE, or symmetrically distributed while using box plots for all sub-basins of the ENB.

In this study, Spatial anomaly mapping and analysis offered valuable insights into the spatio-temporal dynamics and variability of rainfall within the Eastern Nile Basin, shedding light on significant variability and uncertainty across all models and scenarios. It becomes apparent that there is a notable level of uncertainty present across all models, alongside significant spatio-temporal variability within the ENB. However, certain models portray normal conditions, while others depict wet or dry conditions for the same period and scenario. This divergence underscores the complexity inherent in predicting future rainfall patterns and highlights the need for further investigation and refinement in modeling techniques to better understand and anticipate regional climate dynamics.

The evaluation underscores the importance of refining CMIP6 models to enhance accuracy and reliability, particularly through downscaling initiatives like CORDEX and dynamical bias correction techniques. Collaborative efforts between researchers and climate modellers are essential for advancing model development and improving uncertainty quantification.

Integrated assessment studies are recommended to address socio-economic implications of climate change and develop adaptive strategies within the ENB. Additionally, enhancing ground station networks can support accurate model evaluation and bias correction processes.

List of Figures

List of Tables

1.0 Introduction:

1.1 Background for the Assignment

The demand for freshwater across various sectors including water supply, energy production, food cultivation, and environmental preservation is steadily rising due to shifts in economic and social dynamics worldwide. Recognizing water as a fundamental element for socio-economic progress and environmental stability, it requires meticulous consideration throughout the planning, development, and execution of projects. However, rainfall serves as a pivotal component in the hydrological cycle, influencing the availability of freshwater resources across terrestrial ecosystems through its intricate processes and transformations. Understanding rainfall patterns, both historically and in future projections, is essential for informed decision-making in water resources development and management endeavours.

The Eastern Nile region demonstrates significant variability in rainfall patterns, which manifests both spatially and temporally. This variability is increasingly influenced by climate change, resulting in shifts in global atmospheric systems including seasonal changes and alterations in temporal and spatial distributions. Consequently, decisions regarding the planning and management of water resources must grapple with uncertainties exacerbated by both natural variability and climatic shifts.

Therefore, quantifying trends in rainfall across different temporal scales and projecting future trajectories becomes imperative for ensuring the sustainable management of water resources in the Eastern Nile region.

1.2 Objective

The primary objective of this assignment is to collect vital insights into rainfall trends and projections through the application of statistical and spatial analysis techniques within the Eastern Nile Basin. Furthermore, it seeks to establish meaningful comparisons and correlations between current observations and future forecasts obtained from the evaluations of rainfall trends and projections. This endeavour is geared towards informing decision-making processes and strengthening transboundary water cooperation efforts. However, the Eastern Nile Climate Assessment, with a central focus on rainfall analysis, outlines two key themes within the framework of this assignment:

Theme I: Eastern Nile River Basin Rainfall Trend Analysis

This theme focuses on conducting a comprehensive examination of rainfall anomalies and trends spanning the past 20-30 years within the Eastern Nile River basin. This involves correlating various datasets, including satellite datasets and ground-truth rainfall data whenever accessible. The tasks entail sourcing such data from diverse national and global repositories to facilitate thorough analysis.

Theme II: Eastern Nile River Basin Rainfall Projection

The quantification of rainfall projections is of paramount importance for the planning of future water resources development and the formulation of climate adaptation strategies. The primary task of this theme is to procure rainfall projections from multiple simulations conducted within the Coupled Model Inter-comparison Project Phase 6 (CMIP6) General Circulation Models (GCMs). Subsequently, rainfall projections are conducted for the Eastern Nile River basin, spanning up to 2060. This meticulous analysis and projection endeavour play a critical role in fostering informed decision-making and enhancing resilience in response to the evolving climate dynamics within the Eastern Nile Basin. This report will focus only on this theme.

2.0Literature Review

2.1 Historical Trends and Climate Projections in the ENB

The historical patterns of rainfall across the Eastern Nile Basin (ENB) have demonstrated significant variability and discernible trends over time, as noted in various studies (Conway et al. 2005; Awulachew et al. 2013). These studies underscore the importance of comprehending these historical trends to forecast potential alterations in rainfall patterns and their ramifications for water resources, agriculture, and socio-economic systems within the region. Moreover, Figure 1, sourced from the CHIRPSv2 dataset (Funk et al. 2015), provides an overview of the annual mean rainfall across the four sub-basins within the ENB. This visualization vividly portrays the fluctuation in rainfall patterns over time, highlighting a distinct increasing trend from 1981 to 2022. This trend signifies a significant elevation in the average rainfall within these sub-basins during the specified period, corroborating and bolstering the discourse presented in prior studies regarding the evolving precipitation dynamics in the ENB.

One of the primary challenges in forecasting the future lies in the inability to empirically measure or analyse phenomena that have yet to occur. To address this challenge, researchers develop models that serve as simplified representations, often as mathematical formulas or algorithms, utilizing known historical data and assumptions about future conditions to make logical predictions. General circulation models (GCMs)[1] are frequently employed to simulate complex atmospheric processes, mimicking the dynamic interplay of air, water, and solar energy in the atmosphere. While predominantly instrumental in forecasting long-term climate trends, GCM outputs also shed light on potential short-term weather variations.

Predictions of climate patterns through modern, high-definition climate models play an increasingly pivotal role in facilitating informed decision-making and devising tailored strategies for both adapting to and mitigating climate change. However, the substantial variability in climate coupled with limited data availability in the ENB has posed challenges for prior studies in identifying consistent, unified trends. East

[1] https://www.ipcc-data.org/guidelines/pages/gcm_guide.html

Africa, housing 75% of ENB countries, emerges as a region particularly susceptible

Figure 1: Historical trends using mean annual rainfall (mm/year) from CHIRPSv2 1 (1981 – 2022) for (a) Main Nile, (b) Tekeze-Atbara, (c) Blue Nile, and (d) Baro-Akobo-Sobat-White Nile sub-basins

to climate change and its associated extremes, with a majority of its population living in poverty. The Intergovernmental Panel on Climate Change (IPCC) has foreseen an escalation in the frequency and intensity of extreme weather events in the region due to climate change (IPCC 2014; Sutton and Tobin 2011). Climate models serve as indispensable tools for simulating past climate conditions (Otieno and Anyah 2013), analysing present-time variability (Mbigi et al. 2022), and projecting future extreme events (Ayugi et al. 2021), emphasizing the critical need to validate the efficacy of these models before employing them in impact studies or sector-specific applications within a particular region.

The World Climate Research Programme (WCRP), established in 1980 under the joint sponsorship of the International Science Council (ISC) and the World Meteorological Organization (WMO), coordinates research endeavours aimed at elucidating the multi-scale dynamic interactions between natural and social systems influencing climate (WCRP 2021a). The WCRP's Working Group on Coupled Modelling (WGCM) oversees the Coupled Model Inter-comparison Project (CMIP), instituted in 1995 to standardize the development and evaluation of climate models (WCRP 2021b). CMIP members synchronize their efforts with assessment reports issued by the IPCC[2], which was established in 1988 by the United Nations to furnish policymakers with regular scientific assessments regarding climate change. IPCC assessment reports are sequentially numbered, with the fifth assessment report (AR5) released in 2013. The CMIP6 models are slated for inclusion in AR6 (Hausfather 2019). Assessing the impact of climate change across diverse sectors within the basin has posed challenges due to discrepancies in previous studies employing GCMs (Addisu et al. 2015). These models, though extensively utilized, lack local precision, resulting in highly varied findings across research endeavours, e.g. (Conway and Hulme 1993; Strzepek, Yates, and El Quosy 1996; Conway 2000; Elshamy et al. 2009; Jury and Funk 2013).. Factors contributing to these disparities encompass the basin's rainfall variability, temporal and spatial data coverage limitations, and disparate statistical methodologies employed in each study (Samy et al. 2019). More disconcerting is the inconsistency among GCMs themselves, with projections for the same region yielding contradictory outcomes—some predicting heightened impacts, while others anticipate decreases in climate variables such as rainfall.

The most recent state-of-the-art climate model experiments are gradually becoming available as part of the Coupled Model Inter-comparison Project Phase 6 (CMIP6) ensemble. Since the late twentieth century, CMIP has orchestrated climate model experiments involving numerous international modelling teams worldwide, fostering a deeper understanding of past, present, and future climate change dynamics. The CMIP6 phase represents a substantial advancement over CMIP5, encompassing a broader array of modelling groups, future scenarios, and diverse experiments. Further reading available at (https://wcrp-cmip.org/). However, CMIP6 GCMs deviate from their predecessors, boasting higher spatial

[2] https://www.ipcc.ch/

resolutions, enhanced parameters of cloud microphysical processes, and additional earth system components such as biogeochemical cycles and ice sheets (Gidden et al. 2019). A notable distinction between CMIP5 and CMIP6 lies in their future scenarios. While CMIP5 projections are founded on 2100 radiative forcing values for four GHG concentration pathways (Alaminie et al. 2021), CMIP6 employs Shared Socioeconomic Pathways (SSPs) deemed more realistic for envisaging future scenarios (Almazroui et al. 2020). Furthermore, another update of CMIP6 is the development and support of the inter comparison model, focusing on biases, processes, and climate model feedbacks (Kawai et al. 2019).

2.2 Global Climate Models

The major challenge in climate change projections is the selection of an appropriate subset of GCMs. GCM simulations are associated with large uncertainties due to model resolution, mathematical formulation, initial assumptions, and calibration processes that restrict the use of all GCMs for reliable projections of climate at the regional or local scale (Su et al. 2013; Ahmadalipour et al. 2017). Mostly it is assumed that more up-to-date, higher-resolution, and more complex models will perform better and produce more robust projections than previous- generation models (O'Neill et al. 2016). Numerous CMIP phases have been instituted, with CMIP6 representing the latest iteration, offering significant improvements over its predecessors. A total of 53 CMIP6 models listed in (https://esgf-node.llnl.gov/projects/cmip6/), providing comprehensive details on institutions, model IDs, resolution, and other pertinent information. However, as gleaned from surveyed literature, Table 1 delineates the top 24 models utilized in East Africa and the ENB regions, alongside their respective institutions, model names, and resolution data.

Table 1: Top CMIP6 Models Utilized in East Africa and the Eastern Nile Basin

NO	Model Name	Institution	Country	Horizontal Resolution
1	ACCESS-ESM1-5	Commonwealth Scientific and Industrial Research Organization-The Bureau of Meteorology (CSIRO-BOM)	Australia	1.9°×1.2°
2	AWI-CM-1–1-MR	The Alfred Wegener Institute (AWI)	USA	0.94°×0.94°
3	BCC-CSM2-MR	BBC (British Broadcasting Corporation)	China	1.1°×1.1°
4	CAMS-CSM1-0	CAMS(Chinese Academy of Meteorological Sciences)	China	1.1°×1.1°
5	CanESM5	Canadian Centre for Climate Modeling and Analysis (CCCMA)	Canada	2.8°×2.8°

6	CMCC-CM2-HR4	Euro-Mediterranean Center on Climate Change (CMCC)	Italy	0.95°×1.25°
7	CNRM-CM6-1-HR	Centre National de Recherches Meteorologiques and Centre Europeen de Recherche et Formation Arancees en Calcul Scientifique (CNRM-CERFACS)	France	0.5°×0.5°
8	E3SM-1–0	Energy Exascale Earth System Mode E3SM-Project	USA	0.94°×1.25°
9	EC-Earth3	EC-Earth Consortium	Europe	0.7°×0.7°
10	GFDL-ESM4	The National Oceanic and Atmospheric Administration-Geophysical Fluid Dynamics Laboratory (NOAA-GFDL)	USA	1.3°×1°
11	GFDL-CM4	The National Oceanic and Atmospheric Administration-Geophysical Fluid Dynamics Laboratory (NOAA-GFDL)	USA	1.3°×1°
12	GISS-E2-2-G	NASA Goddard Institute for Space Studies (NASA- GISS)	USA	1.25°×1.25°
13	HadGEM3-GC31-MM	The Met Office Hadley Centre (MOHC)	UK	0.942°×1.25°
14	IITM-ESM	Indian Institute of Tropical Meteorology (IITM)	India	1.9°×1.9°
15	INM-CM5-0	Institute of Numerical Mathematics (INM)	Russia	2°×1.5°
16	IPSL-CM6A-LR	Institute Pierre-Simon Laplace (IPSL)	France	2.5°×1.3°
17	KACE-1–0-G	National Institute of Meteorological Sciences and Korea Meteorological Administration (NIMS-KMA)	South Korea	1.875°×1.25°
18	KIOST-ESM	Korea Institute of Ocean Science & Technology (KIOST)	Korea	1.88°×1.88°
19	MIROC6	Japan Agency for Marine-Earth Science and Technology (JAMSTEC)	Japan	1.4°×1.4°

20	MPI-ESM1-2-HR	Max-Planck-Institute for Meteorology	Germany	0.9°×0.9°
21	MRI-ESM2-0	Meteorological Research Institute (MRI)	Japan	1.125°×1.125°
22	NorESM2-MM	Norwegian Climate Center (NCC)	Norway	0.94°×1.25°
23	TaiESM1	Consortium for Climate Change Study (CcliCS)	Taiwan	1.25°×0.94°
24	UKESM1-0-LL	Met Office Hadley Centre (MOHC)	UK	1.9°×1.3°

2.3. GCM Scenarios

Future levels of greenhouse gas emissions are subject to change based on economic, technological, and political factors. Models are run with various scenarios to represent plausible possibilities for the future. Although future outcomes rarely align precisely with any single scenario, modelling provides valuable guidance for planning purposes. The CMIP climate change scenarios represent different levels of radiative forcing, indicating the ratio of energy absorbed by the Earth's atmosphere to that reflected back into space per square meter. These scenarios are measured against a reference value of 0.0 at the start of the industrial revolution in 1750 (NOAA 2021). The values include:

- 0.0: Radiative forcing reference value at the start of the industrial revolution in the year 1750
- 2.3: Radiative forcing in the year 2011
- 2.6: A target for radiative forcing in the year 2100 that is considered ideal, but improbable
- 4.5: A target for radiative forcing by 2100 that is considered practical
- 8.5: A probable level of radiative forcing by 2100 if no significant actions are taken to mitigate CO2 emissions

The CMIP uses five shared socioeconomic pathway (SSP119, SSP126, SSP245, SSP370, and SSP585) scenarios that can each incorporate different levels radiative forcing, which are described in greater details by (Hausfather 2018). These SSPs are based on five narratives describing alternative socio-economic developments, including sustainable development, regional rivalry, inequality, fossil-fuelled development, and middle-of-the-road development.

2.4. Projected Changes in Rainfall and its impacts in the EN basin

Projections regarding rainfall changes in the ENB suggest complex and varied scenarios, with models indicating potential alterations in precipitation patterns due to climate change. Some studies forecast an overall increase in precipitation, while others project a decrease (see section 2.1). Previous studies have revealed the

Nile's (where ENB is located) high sensitivity to climate shifts, underlining considerable uncertainty in climate projections (Butts et al. 2016). However, in line with the Nile Basin Initiatives' (NBI) Climate Adaptation Strategies[3] and NBI Flood and Drought Risk Mitigation[4], a consensus emerges in the expectation of heightened variability, including more intense and erratic rainfall events alongside longer dry spells. Moreover, In the ENB, climate change projections indicate heightened aridity, more frequent and severe flooding, and intense drought. These changes have led to famine, human displacement, loss of life, and significant ecosystem and biodiversity shifts in specific regions. Floods are widespread, notably in Sudan and South Sudan in the ENB, and often followed by droughts. Therefore, we are studying these projections in this report because they are crucial for better preparation and for planning future water resources development, as well as formulating climate adaptation strategies that promote informed decision-making and enhance resilience in response to the evolving climate dynamics within the Eastern Nile Basin.

3.0 Data and Methods

3.1. The Study Area:

The Nile is one of the longest rivers in the world, with an extensive drainage basin of 3.2 million km², accounting for nearly 10% of Africa's landmass. The river flows through eleven countries, including Burundi, DR Congo, Egypt, Ethiopia, Eritrea, Kenya, Rwanda, South Sudan, Sudan, Tanzania, and Uganda, meandering through a rich tapestry of landscapes and climatic zones. The Nile Basin nurtures a population of over 257 million people (projected to be 591 million people by 2025 according to (Merem et al. 2020)), representing approximately 54% of the total inhabitants across the Nile Basin riparian countries. The Nile Basin has a variety of ecosystems, including arid and semi-arid regions. The general topography of the Nile basin is characterized by mountain ranges such as Upper Kagera and Ethiopian Plateau, ridged topography, and steep slopes such as Upper Blue Nile and Upper Tekeze Atbara basins. These features not only contribute to flow but also contribute to erosion, land degradation, and downstream sediment transport (NBI 2016). Population distribution in the basin is shaped by various factors such as climate, rainfall, soil fertility, mineral resources, and social and economic infrastructure. However, the availability of water, whether from large bodies or rainfall, seems to have the most significant impact, outweighing other influences. This is why the riparian communities are heavily dependent on the water resources and rainfall for their livelihoods. For example, agriculture is the backbone of the Nile Basin, supporting tens of millions of people and accounting for over 75% of the basin's workforce and one-third of its gross domestic product (GDP) (Mohamed 2017).The Nile basin is divided into two broad sub-systems: The Eastern Nile sub-system (ENB) and the Equatorial Nile sub-system. The ENB is further divided into

[3] https://ikp.nilebasin.org/en/action-area/climate-change-adaptation
[4] https://ikp.nilebasin.org/en/action-area/flood-and-drought-risk-mitigation#

four sub-basins: the Baro-Akobo-Sobat-White Nile in the west, the Blue Nile, the Tekeze-Atbara on the east, and the Main Nile from Khartoum to the Nile delta, as shown in Figure 2. The ENB covers an area of 1.8 million km² spanning four countries: South Sudan, Ethiopia, Sudan, and Egypt (Figure 2). The main Nile is considered the largest sub-basin of the ENB, covering 44% of its total area, followed by Baro-Akobo-Sobat-White Nile covering 26% of its total area, then the Blue Nile with 17%, while the Tekeze-Atbara-Setit is the smallest sub-basin covering 13% of the area (Mostafa et al. 2016).

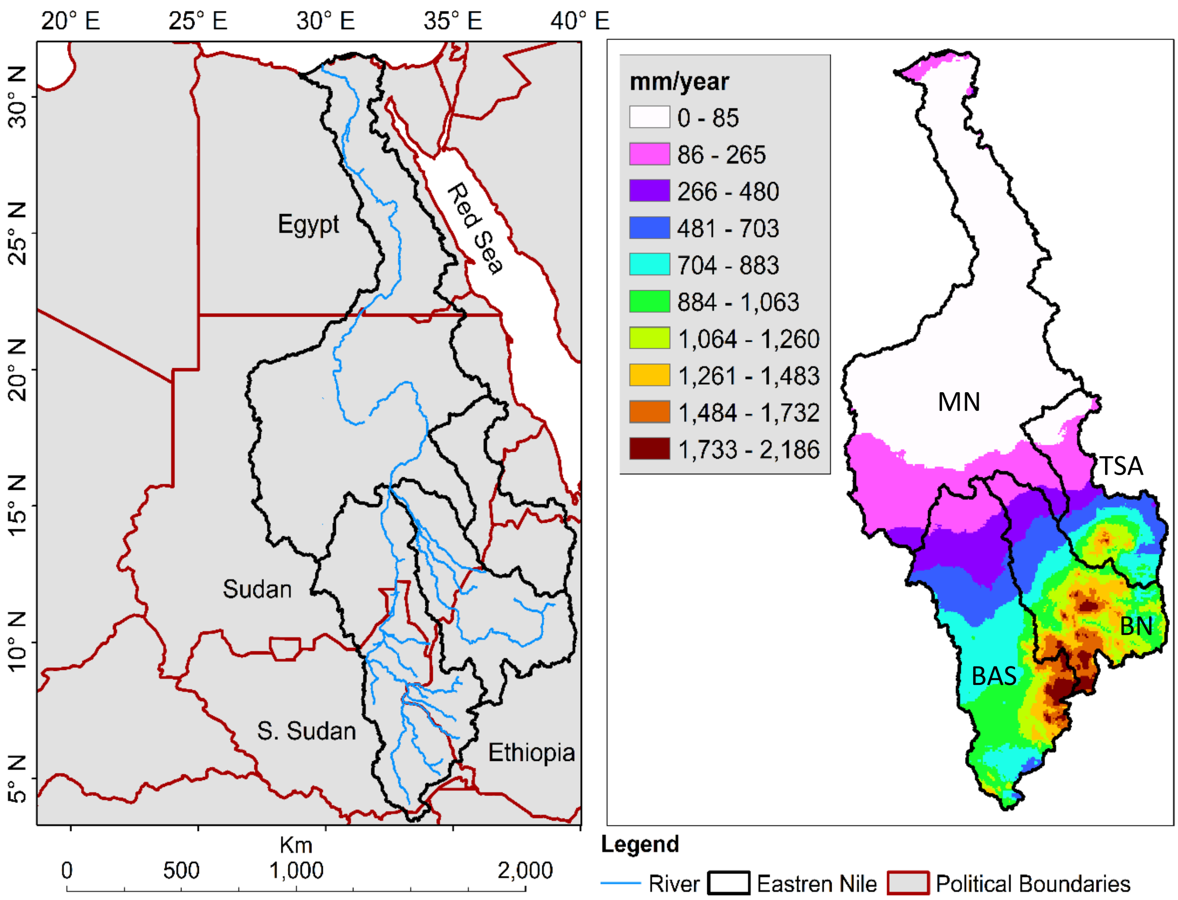

Figure 2: (Left) Eastern Nile Basin geographical extent, (Right) The mean annual rainfall for Eastern Nile Basin from 1981-2022 using CHIRPSv2 dataset . Note: The Figure created by the Authors using QGIS.

The Blue Nile originates from Lake Tana in the Highlands of Ethiopia, while the White Nile flows from the Highlands of Uganda through South Sudan and meets the Blue Nile in Sudan to form the Main Nile River that flows northward to the Mediterranean Sea through Egypt (Figure 2). The topography of the basin shows a big drop in elevation along the course of the rivers, from more than 3000 m.a.s.l. (meters above sea level) at the upper high lands to the sea level at Nile Delta in Egypt. The climate of the basin varies significantly; it encompasses five climate zones that vary from tropical, to subtropical, arid, semi-arid, and Mediterranean zones. The rainfall amount ranges from more than 2000 mm in the upper highlands up to 0 mm in some parts in Sudan and Egypt, as shown in (Figure 2). The basin accumulates runoffs of four sub-basins: Blue Nile (56%), Atbara (15%), White Nile-Albert (14%), and Sobat (15%), contributing more than 85% of the total annual flow of the Nile (Digna et al. 2018), estimated as 84 billion cubic metres (BCM) measured at the High Aswan Dam (HAD), making it the major sub-basin for the River Nile.

3.2. Observed Rainfall Data

The Eastern Nile Basin presents a challenging landscape for acquiring ground-based rainfall data, impeding effective water management and agricultural planning efforts(Gebremicael et al. 2022), thereby hindering effective decision-making and resource allocation in the region. To address this issue, we chose to utilize satellite-based datasets such as the Climate Hazards Center InfraRed Precipitation with Stations (CHIRPS) (Funk et al. 2015). CHIRPS has been selected to be considered as observed data for this analysis because of its wide application in similar contexts and fine spatial (0.05°) and temporal (daily) resolutions. It extends from 1981 to date, and is freely available dataset. The CHIRPS dataset shows good agreement with the ground observations in different climatic zones worldwide (Dinku et al. 2018), including excellent performance in the ENB region (Nashwan, Shahid, and Wang 2019; Basheer and Elagib 2019; Ayehu et al. 2018; Belete et al. 2020). This dataset developed by the Climate Hazards Group of the University of California It is a blended dataset that combines satellite measurements and in-situ rainfall measurements from the Global Telecommunication System (GTS). The CHIRPS dataset is a quasi-global rainfall dataset covering 50°S to 50°N (accessible at https://data.chc.ucsb.edu/products/CHIRPS-2.0/).

3.3. CIMP 6 Global Climate Models:

In this study, we carefully selected 8 GCMs included in the CMIP6 experiments, accessible through the Earth System Grid Federation portal (https://esgf.node.llnl.gov/search/cmip6/), based on two distinct categories. Initially, we chose 4 models, namely MIROC6, MPI-ESM, MRI-ESM2, and ACCESS-CM2, for their demonstrated ability to accurately replicate the general characteristics of precipitation variables, as validated by recent international studies (Ortega et al. 2021; Srivastava et al. 2020; Klutse et al. 2021; Wang et al. 2021). Subsequently, we placed greater emphasis on selecting an additional four CMIP6 GCM models to evaluate future climate trends and projections, particularly focusing on the eastern Nile basin region. These models, namely GFDL-ESM4, NorESM2-MM, BCC-CSM-2MR, and GFDL-CM4, were chosen for their superior performance and high-resolution in climate modelling. The ensemble members are categorized into four indices representing global attributes specific to each model: "r" for realization, "i" for initialization, "p" for physics, and "f" for forcing. The ensemble names "r1i1p1f1" and "r1i1p1f3" indicate that the ensemble members share the same initial and physical conditions but differ in forcings, with "f1" derived from atmospheric model inter-comparison project (AMIP) one-moment aerosol (OMA) simulations, and "f3" derived from E2.2 OMA simulations (ozone field update). Below is the intensive survey conducted for the second category of models selected for their best performance in the region.

1. GFDL-ESM4

The GFDL-ESM4, short for Geophysical Fluid Dynamics Laboratory-Earth System Model 4, is an American model developed by The Geophysical Fluid Dynamics Laboratory (GFDL) under the National Oceanic and Atmospheric Administration (NOAA). Released in 2018, this model operates at a spatial resolution of 1.3° longitude by 1° latitude (Held et al. 2019). It is part of the suite of GFDL global models within CMIP6, which includes e.g., GFDL-AM4, CM4, CM4CI92, ESM4, GRTCODE, OM4P5B, and GFDL-RFM-DISORT. The model has been evaluated extensively in the East Africa and ENB region. For instance, (Ngoma et al. 2021) assessed 15 different Global Climate Models (GCMs) of CMIP6 to simulate rainfall over Uganda from 1981 to 2014 using statistical metrics such as mean bias error, normalized root mean square error, and pattern correlation coefficient. Their results indicate that the GFDL-ESM4 model was the best among the other GCM models used in this study. Additionally, in a study by (Babaousmail et al. 2021) in North Africa, 15 CMIP6 models were evaluated for their accuracy in reproducing spatial and temporal rainfall variability from 1951 to 2014. Robust statistical metrics like ECDF, Taylor diagram (TD), and Taylor Skill Score (TSS) were employed. The findings revealed six models that excelled in statistical performance. Notably, the GFDL-ESM4 model stood out among the top performers, displaying minimal over/underestimation during both dry and wet months.

In a most recent study led by (Omay et al. 2023) aimed to identify the top 10 models excelling in replicating rainfall patterns across the IGAD region in Eastern Africa from 1981 to 2014, the GFDL-ESM4 model demonstrated superior performance compared to other models, particularly in the highlands of western Ethiopia, significant areas in South Sudan, southern Sudan, and extensive regions in Uganda, and ranked among the top 10 models for accurately representing rainfall patterns in the Arsi region of Ethiopia. Furthermore, GFDL-ESM4 model also emerged as the top-performing model in accurately simulating rainfall patterns in Ethiopia when evaluated among 37 CMIP6 against Ethiopia's Enhancing National Climate Services (ENATS) gridded rainfall dataset to simulate observed rainfall from 1981 to 2014 (Berhanu et al. 2023), using Taylor Skill Score (TSS) metrics for both mean monthly (June-September) and seasonal (February-May) rainfall.

2. NorESM2-MM:

The Norwegian Earth System Model version 2 (NorESM2), developed by the Norwegian Climate Center (NCC), is a coupled climate model that includes the atmosphere, ocean, sea ice, and land surface components. NorESM2-MM is a version of the model with a resolution of 0.94° × 1.25°. It is one of the models used in the CMIP6. The model is driven by CO2 concentration and has been evaluated for its ability to simulate the historical climate under the CMIP6 forcing (Seland et al. 2020).

Numerous studies for rainfall projection have been conducted in the East Africa and ENB to evaluate the performance of the NorESM2-MM model. In the evaluation conducted by (Omay et al. 2023), 23 CMIP6 historical simulations covering the IGAD regions of Eastern Africa were assessed using various qualitative and quantitative metrics. These metrics included total rainfall, annual cycle, continuous, categorical, and volumetric statistical measures, as well as scatter plots, Cumulative Distribution Function (CDF) analysis, and coloured code portraits. They were used to analyse the patterns of total rainfall against daily precipitation data from 1981 to 2014 sourced from CHIRPS as a reference dataset. The study's findings highlighted NorESM2-MM as one of the leading performers among the CMIP6 models for accurately simulating precipitation patterns, particularly in the IGAD East Africa regions, notably in South Sudan.

Furthermore, (Rettie et al. 2023) demonstrated that outputs from 16 CMIP6 GCMs, initially associated with coarse resolution, biases, and high uncertainty, can be effectively corrected and downscaled for regional impact modelling. The study utilized the biases correction constructed analogues with quantile mapping reordering (BCCAQ) statistical downscaling technique to generate climate change projections at a 10km spatial resolution under three emission scenarios (SSP2-4.5, SSP3-7.0, and SSP5-8.5), referencing the CHIRPS dataset for ground observation. The evaluation revealed that this downscaling approach notably mitigated model biases and produced higher resolution daily data compared to the original GCM outputs. Ultimately, the study's findings indicate that simulations from NorESM2-LM and NorESM2-MM models are effective for precipitation projections in East Africa. (Feyissa et al. 2023) researched climate model performance and future scenarios (SSPs) in Ethiopia's Omo River basin using 20 CMIP6 GCMs. Historical evaluations based on CHIRPS data ranked models. NorESM2-MM model effectively simulated basin historical precipitation, but highlighting challenges in projecting future fluctuations despite downscaling and bias correction. Finally, it also indicated in above mentioned (Berhanu et al. 2023), that the NorESM2-MM one of the top-performing models (i.e. GFDL-CM4, GFDL-ESM4, NorESM2-MM, CESM2, ENSEMB_4) and recommended for regional climate projections under SSPs in Ethiopia.

3. BCC-CSM-2MR

The Beijing Climate Center Climate System Model (BCC-CSM) is a climate model developed by the Beijing Climate Center (BCC), China. BCC-CSM2-MR, with spatial resolution of 1.1 degree, is one of the three models configured for CMIP6. It has been used to simulate the Earth’s climate and predict future climate change. The model has undergone significant improvements in many aspects, including the tropospheric air temperature and circulation at global and regional scale and climate variability at different timescales, the diurnal cycle of precipitation, inter-annual variations of SST in the equatorial Pacific, and the long-term trend of surface air temperature (Wu et al. 2019). Among the 12 different CMIP6 models, BCC-CSM-2MR exhibited excellent agreement with the observational datasets (GPCC) for precipitation over Ethiopia during the baseline period (Alaminie et al. 2021).

4. GFDL-CM4

It is a GFDL's latest multipurpose atmosphere-ocean coupled climate model (GFDL-CM4). It consists of GFDL's latest atmosphere and land models at about 100 km horizontal resolution (1 degree Lat x 1.25 degree Lon) (Held et al. 2019). The model results have been extensively evaluated against observations. The paper of (Adcroft et al. 2019) makes the case that CM4.0 ranks high among state-of-the-art coupled climate models by many measures of bias in the simulated climatology and in its ability to capture modes of climate variability such as the El Niño-Southern Oscillation and Madden-Julian Oscillation. The paper also discusses some potential weaknesses, including unrealistically large internal variability in the Southern Ocean and insufficient warming before 1990 in the simulation of the twentieth century. In our region, this model has gained extensive usage and consistently outperformed others in numerous studies, particularly in Ethiopia (Berhanu et al. 2023; Feyissa et al. 2023; Gebisa et al. 2023), a country contributing approximately 85% of the Nile's flow. Its widespread application underscores its reliability and effectiveness in this critical region.

However, detailed information about these models, including ensemble member, country of origin, scenarios, and atmospheric resolution, can be found in Table 2.

Table 2: Summary of the selected GCM CIMP6 models

No	Model's Name	Calendar Type	Country	Resolution	Ensemble	Scenarios
1	GFDL-ESM4	365 days	USA	1.3°×1°	r1i1p1f1	1.ssp119 2.ssp126 3.ssp245 4.ssp370 5.ssp585
2	GFDL-CM4	365 days	USA	1.3°×1°	r1i1p1f1	1.ssp245 2.ssp585
3	NorESM2-MM	365 days	Norway	0.94°×1.25°	r1i1p1f1	1.ssp126 2.ssp245 3.ssp370 4.ssp585
4	BCC-CSM2-MR	365 days	China	1.1°×1.1°	r1i1p1f1	1.ssp126 2.ssp245 3.ssp370

5	ACCESS-CM2	365 days	Australia	1.9*1.3	r1i1p1f1 r1i1p1f3	1.ssp370 2.ssp585
6	MPI-ESM	Standard (366 days)	Germany	0.9°×0.9°	r1i1p1f1	1.ssp119 2.ssp126 3.ssp245 4.ssp370 5.ssp585
7	MRI-ESM	Standard (366 days)	Japan	1.125°×1.125°	r1i1p1f1	1.ssp119 2.ssp126 3.ssp245 4.ssp370 5.ssp585
8	MIROC6	Standard (366 days)	Japan	1.4°×1.4°	r1i1p1f1	1.ssp119 2.ssp126 3.ssp245 4.ssp370 5.ssp585

3.4. Methodology

Rainfall variable data from the Shared Socioeconomic Pathways (SSP) scenarios (ssp119, ssp145, ssp245, ssp370, and ssp585) within the CMIP6 were acquired for the years 2020-2060, alongside historical data spanning 1990 to 2014, in NetCDF format. To streamline the analysis, global data were confined to the boundaries of the Eastern Nile Basin using the ENB shape file. Subsequently, the data were clipped by coordinates (~ 26° to 40° latitude and 2° to 32° longitude) in NetCDF format. The data underwent zonal statistic multiband analysis in QGIS to extract the mean daily rainfall for five subbasins: Tekezi Setit Atbara Subbasin (TSA), Baro Akobo Subbasin (BAS), Blue Nile (BN), Upper Main Nile (UMN), and Lower Main Nile (LMN). The extracted data were then exported to CSV format and organized into daily, monthly, and annual intervals for further analysis. To convert from kg.m2/s to mm/day, the data was multiplied by 86,400. Quality checks were performed by plotting the CSV data for each scenario and sub basin to ensure adherence to normal rainfall hydrograph patterns and to identify any irregular values. Given that most of the NetCDF files were in a 365-day format (i.e., not considering leap years), addressing data gaps, especially on the 29th of each leap year, involved averaging values from the 27th and 28th of February, as well as the 1st and 2nd of March (two days before and after the gap).

Ultimately, following data preparation, extensive statistical, comparative, and spatial analyses were undertaken for the CIMP6 models, using monthly average comparisons, boxplots, scatterplots, statistical metrics, annual trend, distributions, and spatial anomaly. The objective was to assess historical performance against observed data for each sub basin. This evaluation aimed to identify models that performed well historically, thus enabling the utilization of their projections to quantify future scenarios for each basin. Below is a brief explanation about the used methods:

- Monthly average analysis:

In this analysis, long-term monthly mean time series plots were employed to discern seasonal fluctuating patterns across various precipitation datasets from CMIP6 in comparison to the observed CHIRPS data. This comparative analysis facilitated the identification of the dataset that best captured the seasonal patterns observed in the data.

- BoxPlots:

A box plot, also known as a box-and-whisker plot, is a graphical representation of the distribution of a dataset. It provides a concise summary of the central tendency, dispersion, and skewness of the data, along with identifying potential outliers. Developed by John Tukey in 1970 (Tukey 1977), box plots have become a staple in exploratory data analysis due to their simplicity and effectiveness in conveying key statistical information. box plots serve as invaluable tools for exploring and summarizing the distributional characteristics of datasets, providing essential insights into central tendency, variability, and outliers. Their simplicity and effectiveness make them indispensable in data analysis and visualization across various fields. Below are the components of the box plot

Components of a Box Plot:

A typical box plot consists of several key components (McGill, Tukey, and Larsen 1978):

- Median (Q2): The line inside the box represents the median, or the 50th percentile, of the dataset. It divides the data into two equal halves.
- Quartiles (Q1 and Q3): The box represents the interquartile range (IQR), which spans from the first quartile (Q1) to the third quartile (Q3). Q1 and Q3 respectively represent the 25th and 75th percentiles of the data.
- Whiskers: The whiskers extend from the edges of the box to the minimum and maximum values within a specified range. The length of the whiskers may vary depending on the chosen criteria, such as 1.5 times the IQR or the actual minimum and maximum values.
- Outliers: Data points lying beyond the whiskers are considered outliers and are plotted individually.

Interpreting a Box Plot:

Box plots are invaluable tools for understanding the distributional characteristics of a dataset (Heumann and Shalabh 2016):

- Symmetry and Skewness: The symmetry of the box indicates the symmetry of the data distribution. A perfectly symmetrical distribution will have a median line positioned centrally within the box. Skewed distributions will have medians off-center.
- Spread and Variability: The length of the box (IQR) reflects the spread of the data. A longer box suggests greater variability, while a shorter box indicates more consistent data.

- Outliers: Outliers, if present, are visually apparent as individual data points beyond the whiskers. They provide insights into potential anomalies or errors in the dataset.

  Advantages of Box Plots:
- Simplicity: Box plots offer a straightforward and intuitive way to visualize key statistical properties of a dataset.
- Robustness: Box plots are resistant to the influence of extreme values and outliers, making them ideal for summarizing skewed or non-normal distributions.
- Comparative Analysis: Multiple box plots can be juxtaposed to compare the distributions of different datasets or groups, facilitating insightful comparisons.

- Scatter Plots

A scatter plot visually represents the relationship between two or more variables or datasets by plotting points on a two-dimensional plane. Each point corresponds to a pair of values for the variables being studied, with one variable typically plotted along the x-axis and the others along the y-axis. The position of each point on the plot indicates the values of the variables being compared.

Scatter plots are valuable for identifying patterns or correlations between variables and can reveal the strength and direction of these relationships. They are effective for detecting outliers, clusters, and other patterns in the data that may not be evident through summary statistics alone. Used extensively in statistics, data analysis, scientific research, and engineering, scatter plots provide an intuitive means to explore and communicate relationships between variables.

- Statistical Metrics:

Statistical metrics such as R2 (Coefficient of Determination), cc (Pearson Correlation Coefficient), NSE (Nash-Sutcliffe Efficiency), PBIAS (Percent Bias), RMSE (Root Mean Square Error), and MAE (Mean Absolute Error) have been used in this study to evaluate the performance of CIMP6 models compared to observed dataset.

- R^2 (Coefficient of Determination): R^2 measures the proportion of the variance in the dependent variable that is predictable from the independent variable(s). It ranges from 0 to 1, with higher values indicating a better fit of the model to the data. Below is the equation of R^2.

$$R^2 = 1 - \frac{\sum_{i=1}^{n}(y_i - \hat{y}_i)^2}{\sum_{i=1}^{n}(y_i - \bar{y})^2}$$

- cc (Pearson Correlation Coefficient): The Pearson correlation coefficient assesses the linear relationship between two variables. It ranges from -1 to 1, with values closer to 1 indicating a strong positive correlation, values closer to -1 indicating a strong negative correlation, and 0 indicating no correlation.

$$cc = \frac{\sum_{i=1}^{n}(x_i - \bar{x})(y_i - \bar{y})}{\sqrt{\sum_{i=1}^{n}(x_i - \bar{x})^2 \sum_{i=1}^{n}(y_i - \bar{y})^2}}$$

- NSE (Nash-Sutcliffe Efficiency): NSE is a measure of model performance that compares the simulated values with observed values, taking into account the mean of the observed data. It ranges from negative infinity to 1, with values greater than 0 indicating acceptable model performance.

$$NSE = 1 - \frac{\sum_{i=1}^{n}(y_i - \hat{y}_i)^2}{\sum_{i=1}^{n}(y_i - \bar{y})^2}$$

- PBIAS (Percent Bias): PBIAS quantifies the average tendency of the simulated values to be larger or smaller than the observed values, expressed as a percentage. A value of 0 indicates perfect agreement between simulated and observed values, while generally values between -25 to 25 % considered as acceptable values.

$$PBIAS = \frac{\sum_{i=1}^{n}(y_i - \hat{y}_i)}{\sum_{i=1}^{n} y_i} \times 100\%$$

- RMSE (Root Mean Square Error): RMSE measures the average magnitude of the errors between predicted and observed values. It provides a measure of the model's accuracy, with lower values indicating better agreement between predicted and observed values.

$$RMSE = \sqrt{\frac{\sum_{i=1}^{n}(y_i - \hat{y}_i)^2}{n}}$$

- MAE (Mean Absolute Error): MAE calculates the average absolute difference between predicted and observed values. It provides a measure of the model's accuracy and is less sensitive to outliers compared to RMSE.

$$MAE = \frac{\sum_{i=1}^{n}|y_i - \hat{y}_i|}{n}$$

Where:

yi or xi represents the observed values, $\bar{y}$ represents the simulated values, $\hat{y}$ or $\hat{x}$ represents the mean of the observed values, and n is the number of data points.

Furthermore, these statistical metrics are commonly used to assess the performance of models, validate experimental results, or compare different datasets.

- Distribution Curve Analysis:

An analysis of distribution curves was undertaken to delineate the rainfall characteristics represented by different distribution types observed across a range of datasets, including historical GCMs simulations, SSPs projections, and observed data. The objective of this analysis was to discern the distribution pattern that most accurately reflects the data. Through the superimposition of distribution curves onto the dataset distributions, we evaluated the goodness of fit and identified the most appropriate distribution type for each dataset, among the most common used rainfall distributions (i.e. Normal, Log Normal, Gamma, Log Gamma, and exponential), under investigation. This approach facilitated the determination of the optimal representation of dataset distribution, thereby enhancing the precision of data interpretation and analysis.

- Trend Analysis:

In this study, an annual trend analysis of General Circulation Models (GCMs) historical and projected data was conducted to examine the similarity between GCMs historical trends and observed data (1990-2014), as well as to identify trends in projected data for the time period (2020-2060). Annual data was chosen over daily and monthly formats to enhance visualization clarity.

- Spatial Anomaly Analysis:

Spatial anomaly analysis was employed to assess the spatio-temporal variability of rainfall across different datasets spanning from 1990 to 2060 over the Eastern Nile Basin. This analysis involved calculating the difference between the 5-year average rainfall from the long-term average for the historical period (1990-2014) and the 7-year average for the projection period (2020-2060).

Furthermore, Python scripts were developed to conduct the analysis and generate plots for all of the aforementioned analyses. These scripts leverage various libraries such as pandas for data manipulation, matplotlib for plotting, and possibly other specialized libraries depending on the nature of the analyses, ensuring efficient processing and visualization of the results. The use of Python facilitates automation, reproducibility, and scalability in the analysis pipeline, enabling researchers to derive insights from the data effectively.

4.0 Results and Discussion:

In this section, we will present and discuss all the results obtained from the applied methodologies based on each Eastern Nile Sub basin. Through rigorous analysis and application of appropriate methodologies, we have scrutinized the data pertaining to each sub basin to derive meaningful insights and conclusion.

4.1. Statistical Assessment of CMIP6 Simulations:

4.1.1 Baro Akobo Sobat Basin (BAS)

The data presented in Figure 3 illustrates the mean monthly observations (CHIRPS) depicted in black alongside other GCM models. Despite variations where some models underestimate or overestimate the observed data m where the study's reference period spans from 1990 to 2014. A consistent seasonal pattern is discernible across all models except for MRI-ESM2, which fails to capture the seasonality adequately. Nevertheless, the models exhibit a discernible ability to identify wet and dry periods in the sub basin, which showcases monthly rainfall averages of the CMIP6 models alongside observed data.

Furthermore, detailed statistical analyses elucidating how the 8 CMIP6 models simulate the annual cycles of rainfall within BAS are presented in Figures 4 and 5, respectively.

Additionally, Figure 4 illustrates a comparison between observed data and CMIP6 models using scatter plots. It is evident that some models overestimate, some underestimate, and some fit the observed data well. This correlation is reflected in the R^2 and pbias values, which signify accuracy. A tight clustering around the diagonal line indicates a high degree of alignment between model predictions and observed values, emphasizing reliability. Moreover, a comparative analysis allows us to identify the best-performing model based on scatter plot fit, as calculated in

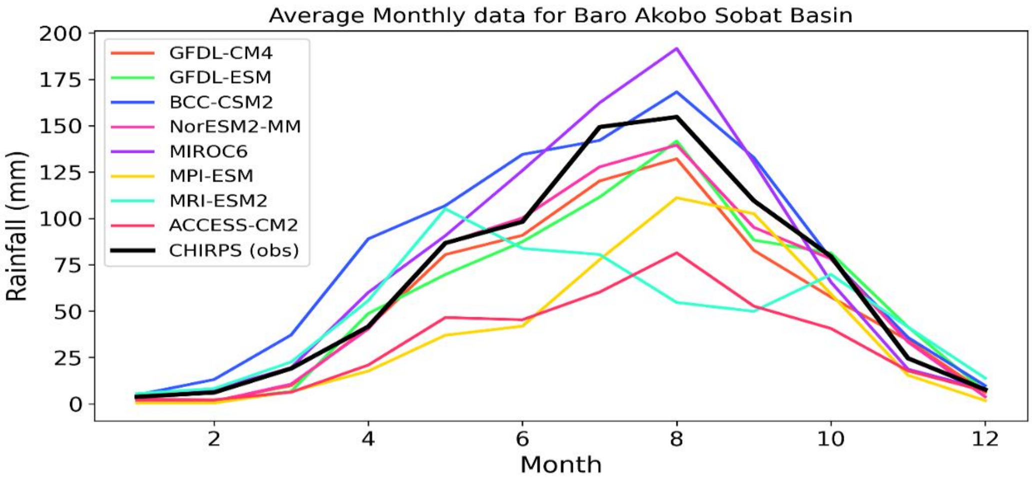

Figure 3: Average monthly data for Baro Akobo Sobat (Observed vs GCMs)

Table 3, which displays the ranking of the best-performing models in the BAS basin based on the highest R^2 scores, lowest acceptable pbias (ranging from -25% to 25%), and lowest RMSE scores. Additionally, metrics including NSE, CC, MAE, and RMSE were also calculated. Remarkably, visually from Figures 3 and 4, and statistically from Table 3, MIROC6 demonstrates superior performance over the BAS basin, followed by NorESM2-MM and MPI-ESM. Conversely, MRI-ESM2 demonstrates the poorest performance among the models evaluated.

The box plots presented in Figures 5 and 6 provide valuable insights into the distribution and central tendency of model outputs relative to observed data. Each box plot delineates the distribution of model results, including the median, quartiles, and outliers, across historical and projection scenarios. However, it was observed that the symmetry, spread, and variability of CHIRPS data changed based on the time scale (daily, monthly, annually), irrespective of the values. Conversely, other GCM models exhibited variations in symmetry, spread, variability, and outliers depending on the time scale (e.g., monthly, annually).

Given that all previous analyses were conducted on a monthly basis to reflect the seasonality of GCMs and ensure analytical consistency, box plots will be analysed on a monthly basis. However, the annual-based box plots will remain to assess the significance of differences in box plot analysis among different time scales (i.e., monthly and annually), necessitating further investigation and research.

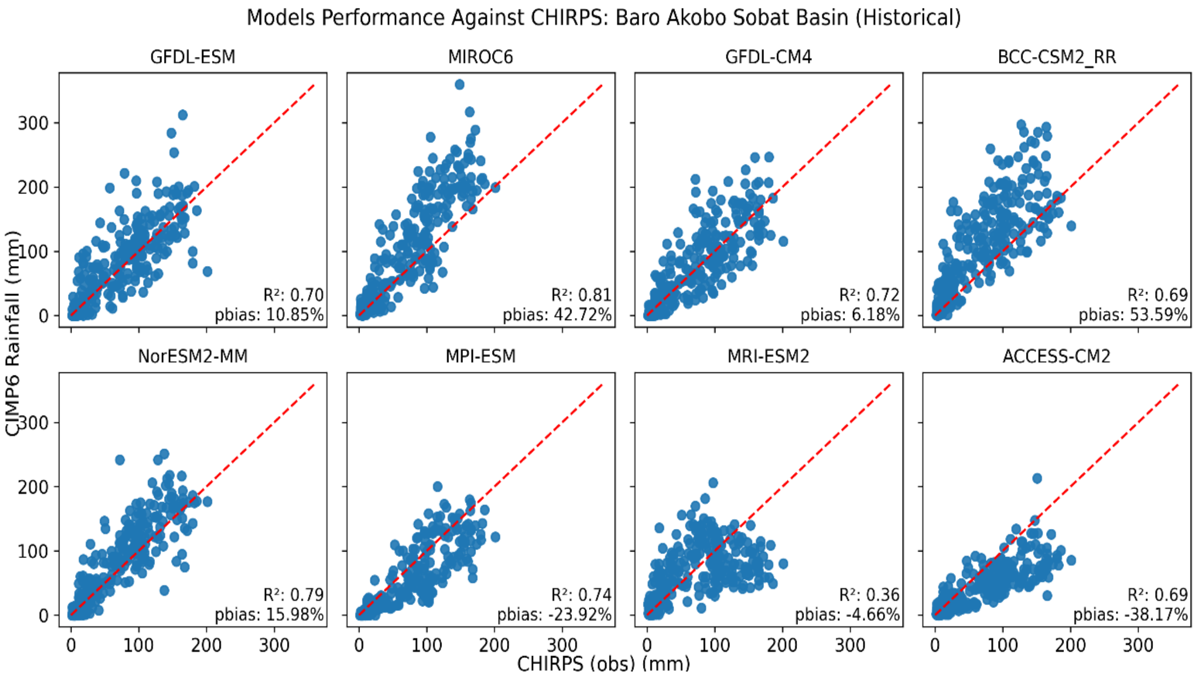

Figure 4: Models performance against CHIRPS using scatter plots - BAS

Figure 6 reveals monthly outliers for ACCESS-CM2 and GFDL-ESM. Moreover, GFDL-CM4 closely fits CHIRPS data in terms of median value, symmetry, spread, and variability of the data, followed by GFDL-ESM and NorESM2-MM, with slight differences in spread, variability, and slightly higher median (NorESM2 shows slightly higher spread in data compared to CHIRPS), and then MRI-ESM2 with less spread in data. Furthermore, across all scenarios, the best-fit models in the box plots show that GFDL-CM4 indicates no change for SSP245 and an increasing trend in terms of median and data spread for SSP585, while GFDL-ESM and NorESM2 indicate no change across all scenarios.

Table 3: Models ranking based on the statistical metrics - BAS

		Statistical Metrics					
Ranking	Model	R2	CC	NSE	PBIAS	RMSE	MAE
1	MIROC6	0.79	0.89	0.66	15.98	31.69	21.08
2	NorESM2-MM	0.74	0.86	0.65	-23.92	31.79	22.93
3	MPI-ESM	0.72	0.85	0.63	6.18	32.74	22.70
4	GFDL-CM4	0.70	0.84	0.57	10.85	35.55	23.40
5	GFDL-ESM	0.69	0.83	0.46	-38.17	39.82	28.25
6	ACCESS-CM2	0.36	0.60	0.31	-4.66	44.80	32.89
7	BCC-CSM2-RR	0.81	0.90	0.15	42.72	49.74	33.82
8	MRI-ESM2	0.69	0.83	-0.06	53.59	55.44	39.18

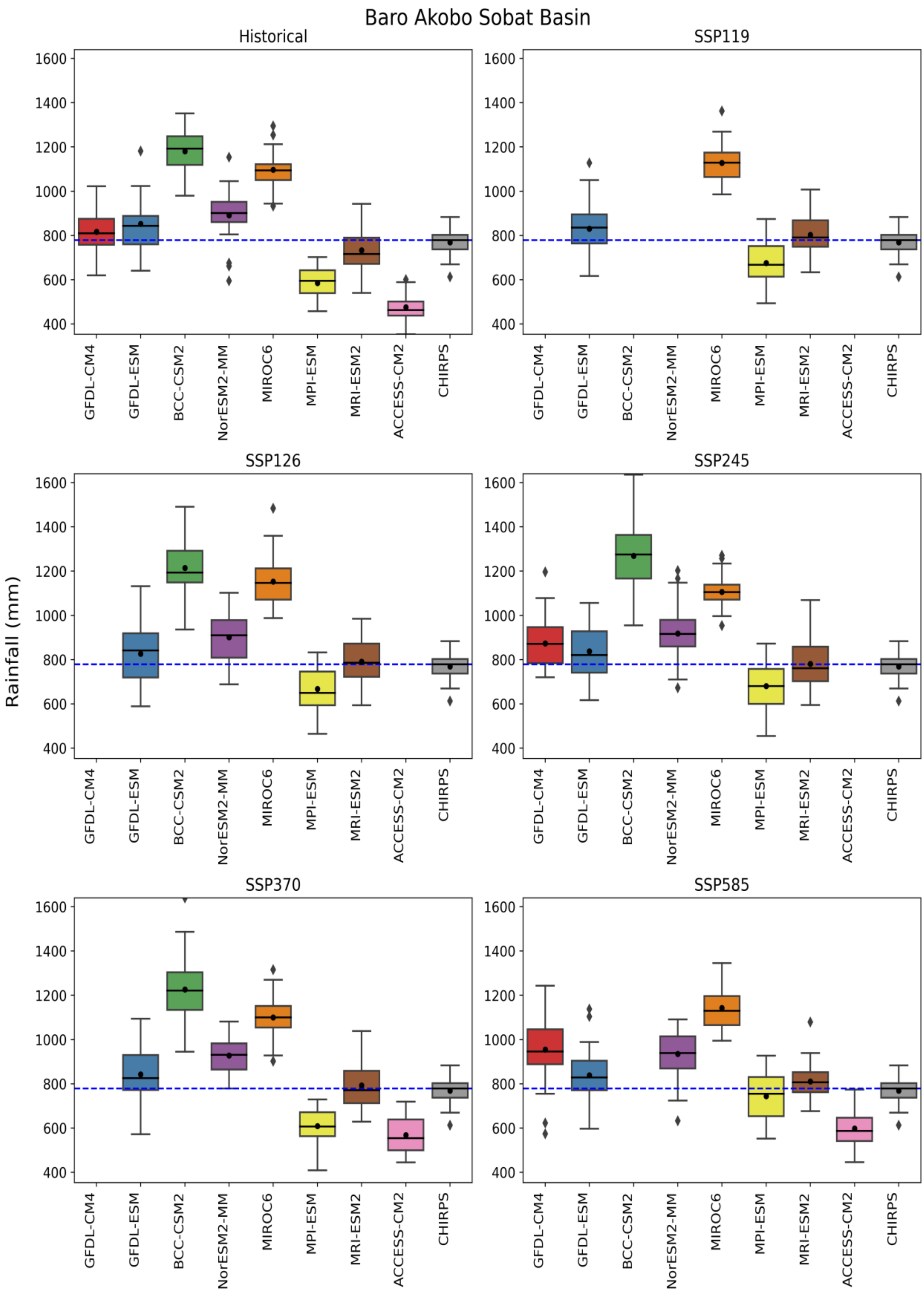

Figure 5: Box Plot Analysis for BAS Basin – Historical and Projection Scenarios Compared to CHIRPS – Annual Rainfall (mm)

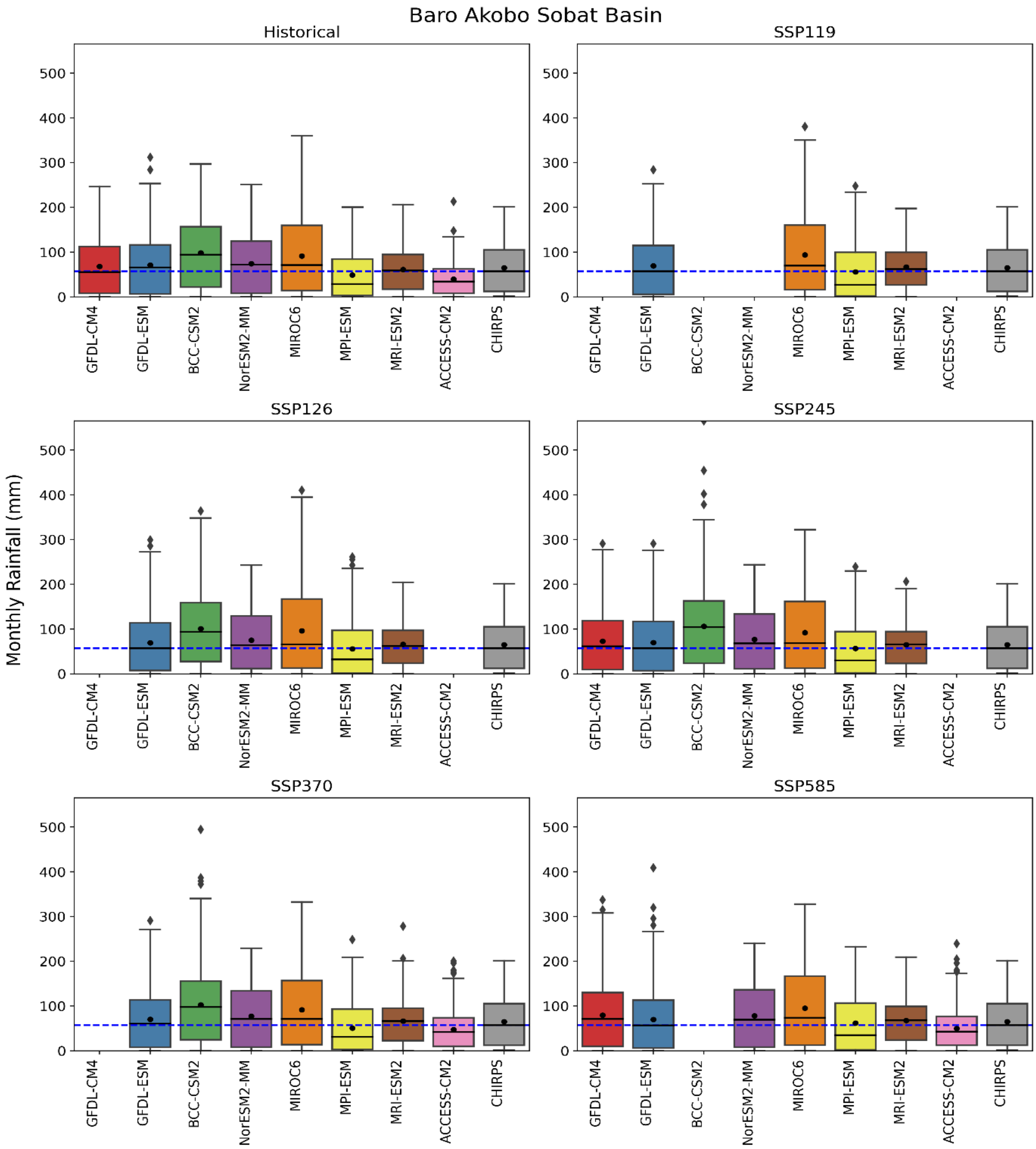

Figure 6: Box Plot Analysis for BAS Basin – Historical and Projection Scenarios Compared to CHIRPS – Monthly Rainfall (mm)

Figure 6 exhibits the best fit distribution curves derived from the five most widely used distributions in rainfall analysis. It elucidates the diverse rainfall characteristics represented by different distribution types across a spectrum of datasets, encompassing historical GCM simulations, SSPs projections, and observed data. However, the model scenarios reveal higher variability in terms of shifts in mean values, either increasing or decreasing, alongside alterations in the frequency of occurrences, particularly concerning the mean. As shown in Table 3, the top three performing models are MIROC6, NorESM2-MM, and MPI-ESM. However, MIROC6 and NorESM2-MM exhibit no significant shifts in the mean across all projections, whereas MPI-ESM demonstrates increasing changes in the mean with lower frequency in most scenarios. Moreover, the frequency of occurrences notably increases for the SSP245 and SSP370 scenarios for NorESM2-MM, while it decreases in most other scenarios.

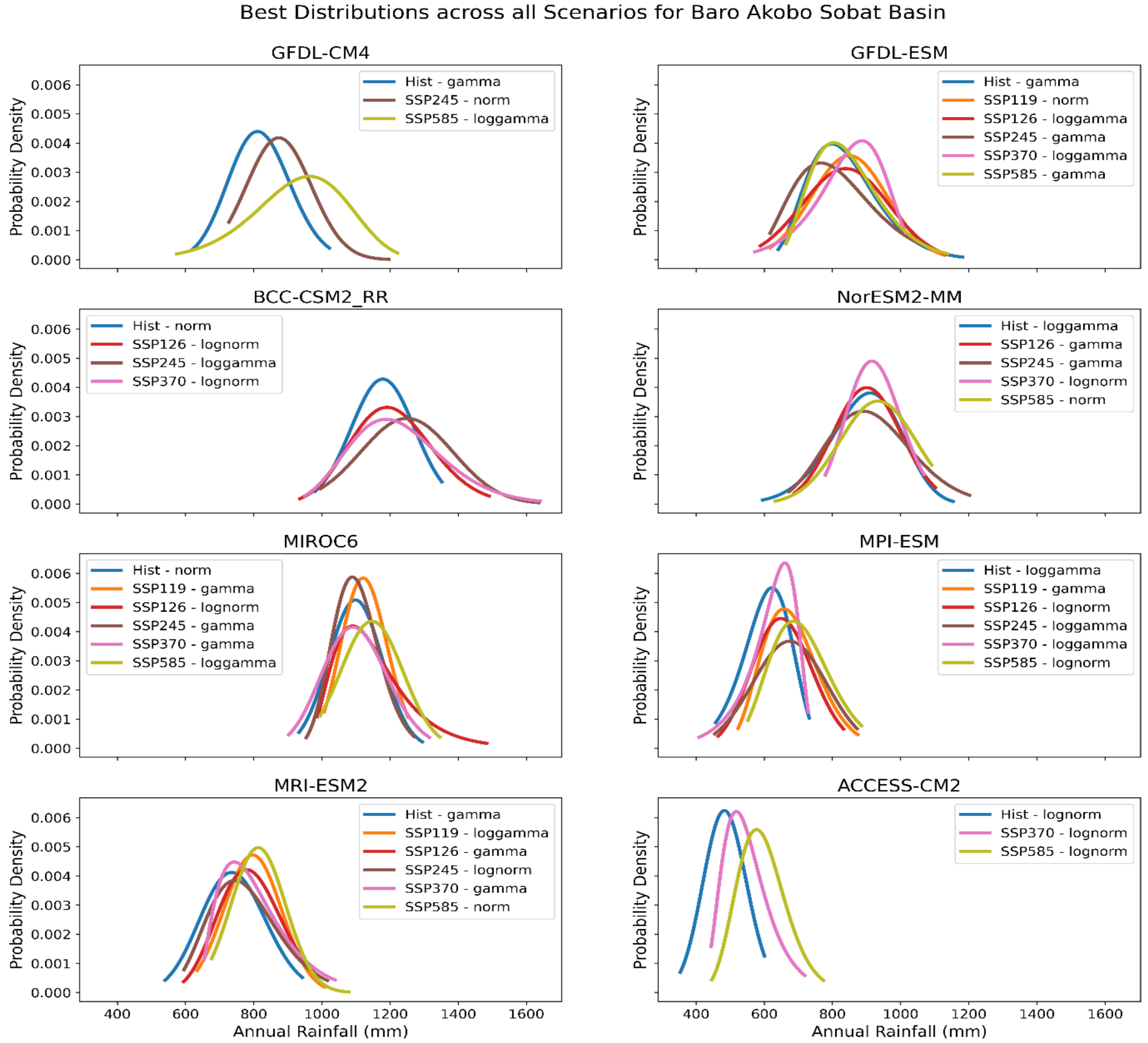

Figure 7: Best Distributions for all scenarios across the BAS compared to the observed

Trend analysis depicted in Figures 7-12 reveals heightened variability and uncertainty in both historical and projected trends. Notably, 50% of historical scenarios from GCMs show no discernible increase or decrease in trends, with 25% indicating a decreasing trend and the remaining 25% showing increasing trends in the BAS region. However, CHIRPS, the observed data, consistently presents an increasing trend historically. Even among the top three performing models over BAS, uncertainty persists. For instance, MIROC6 historically indicates increasing trends similar to CHIRPS, while NorESM2-MM and MPI-ESM show no historical change in trends.

In terms of projections, the top three models—MIROC6, MPI-ESM, and NorESM2-MM—suggest slight decreases in trends for SSP245, with NorESM2-MM indicating a slight increase. However, for SSP585, MIROC6 and NorESM2-MM suggest to some extent that there is no significant change in trends, while MPI-ESM indicates a significant increase in trends.

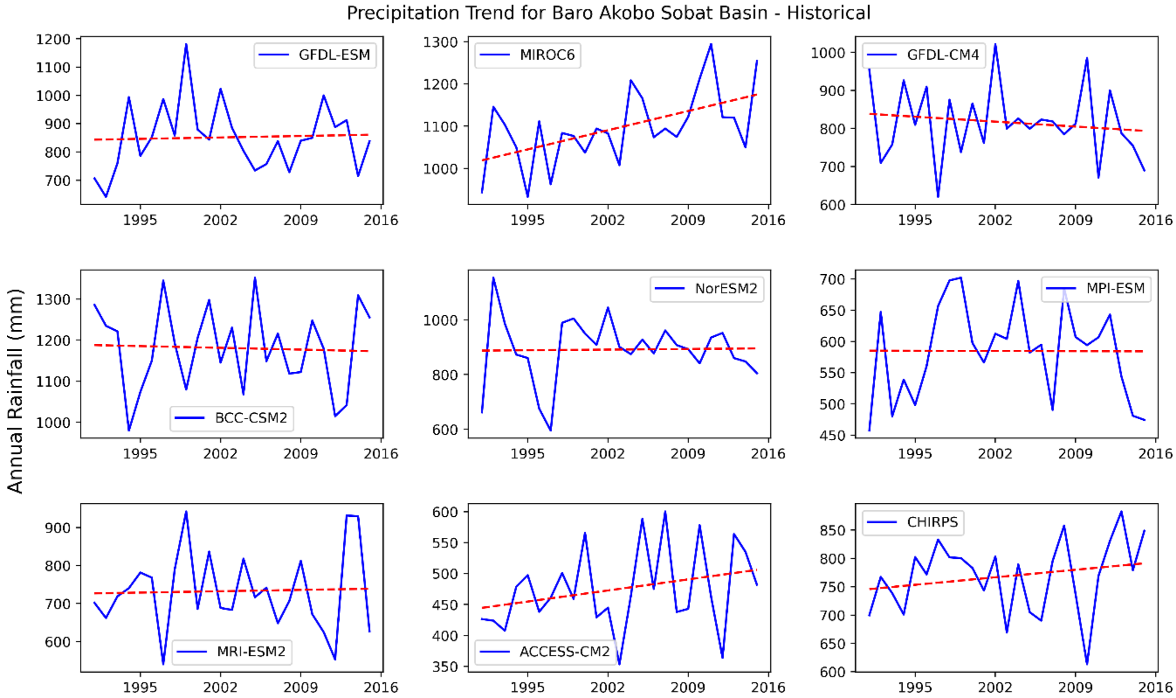

Figure 8: Historical Rainfall trends for BAS

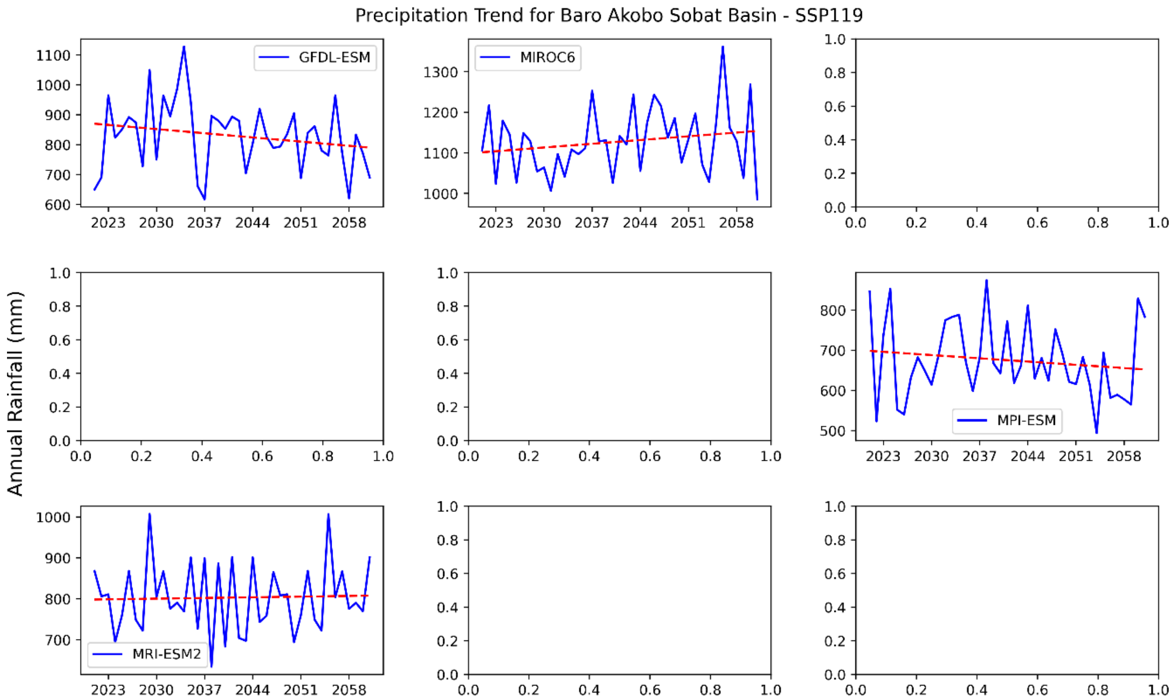

Figure 9: SSP119 Rainfall Projections trend for BAS

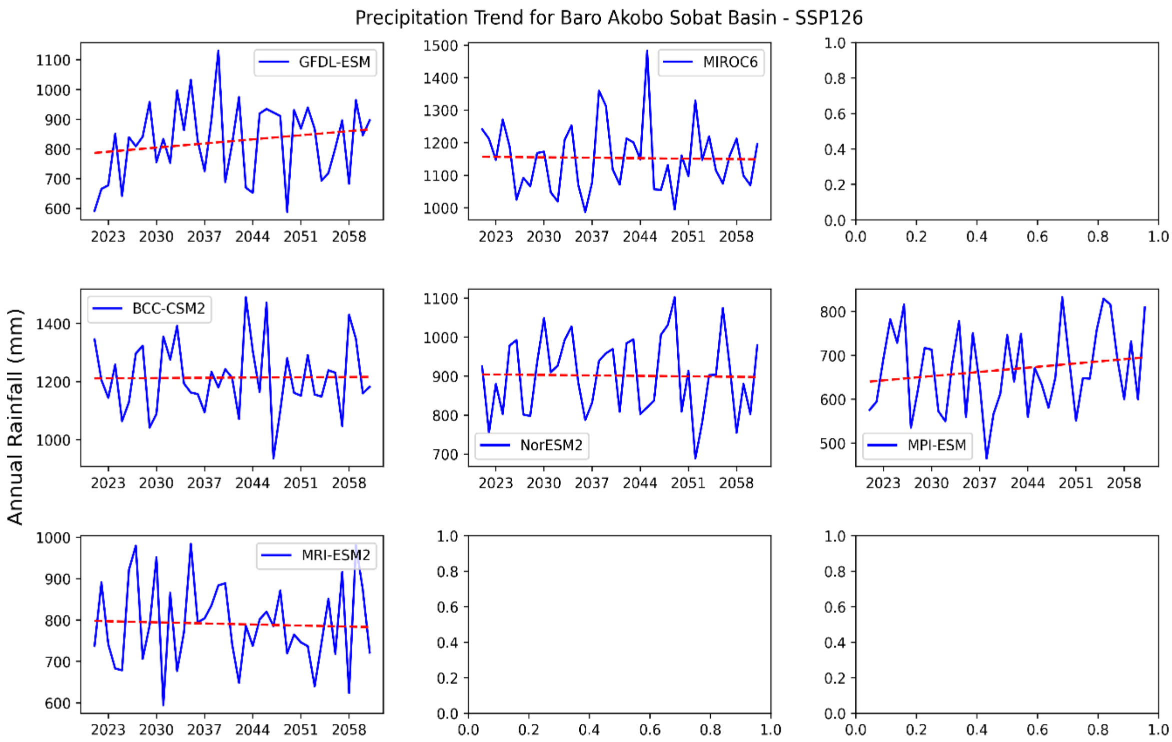

Figure 10: SSP126 Rainfall Projections trend for BAS

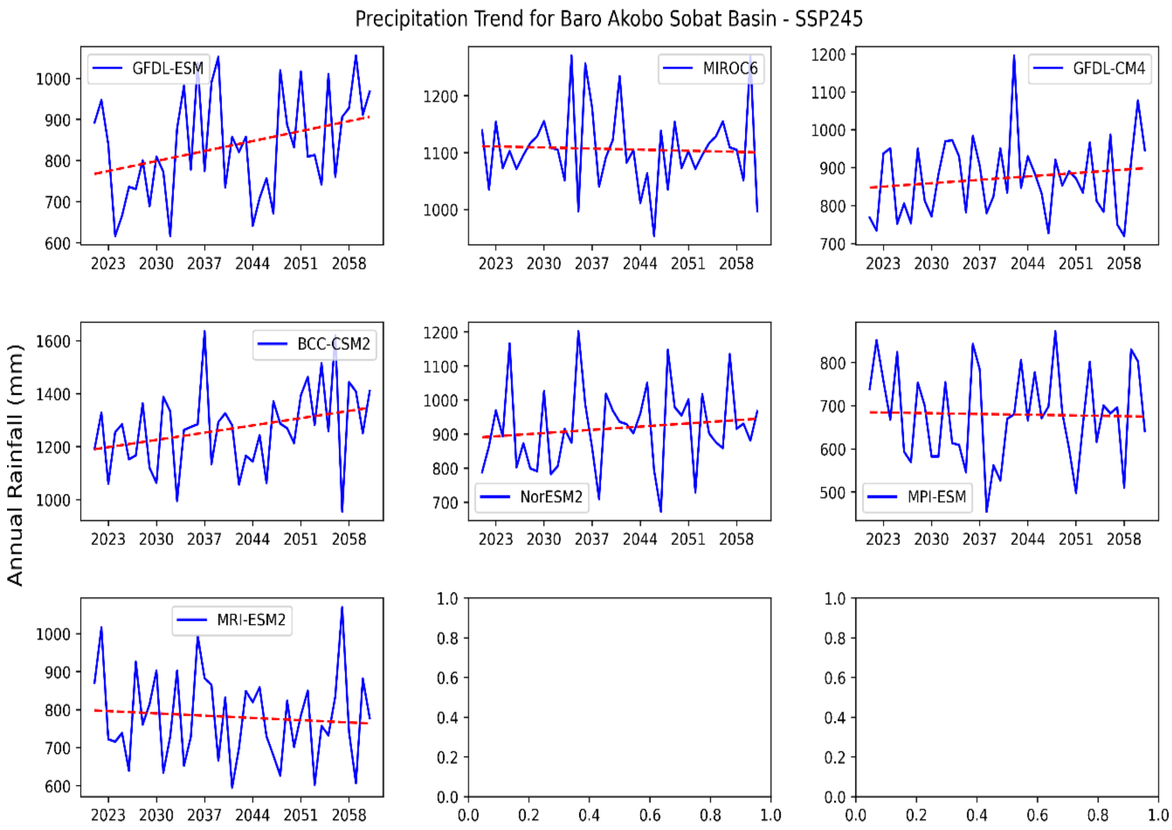

Figure 11: SSP245 Rainfall Projections trend for BAS

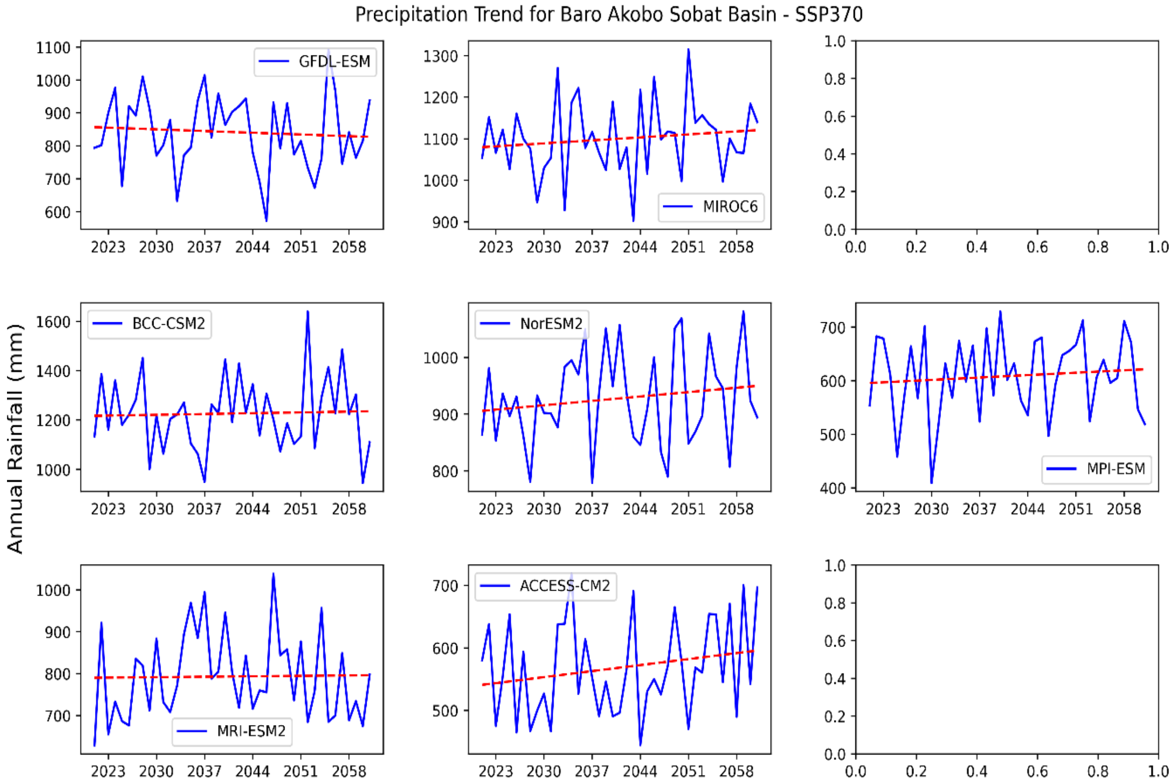

Figure 12: SSP370 Rainfall Projections trend for BAS

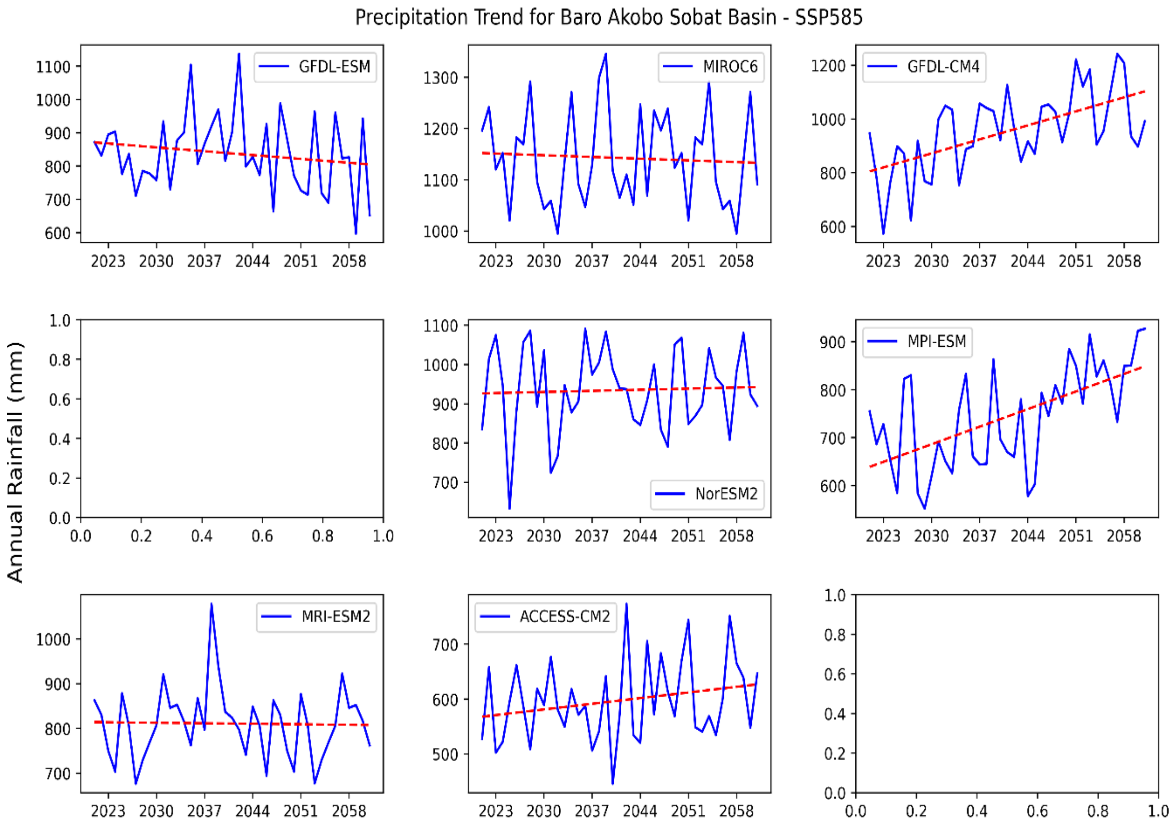

Figure 13: SSP585 Rainfall Projections trend for BAS

4.1.2. Blue Nile Basin (BN)

The analysis of Figure 14 reveals a noticeable seasonal pattern consistently observed across all models, although sometimes exhibiting overestimation or underestimation in comparison to CHIRPS data. Notably, NorEMS2-MM, followed by BCC-CSM2, GFDL-CM4, and GFDL-ESM, demonstrated commendable capability in accurately capturing the seasonality of the Blue Nile over the months, even though with slight underestimation. Contrariwise, MIROC6 also exhibited proficiency in detecting the seasonal pattern; however, it displayed a tendency towards higher levels of overestimation.

Furthermore, Figure 15 provides a comprehensive comparison between observed data and CMIP6 models through scatter plots. The analysis reveals a spectrum of model performances, with some models displaying overestimation, some underestimation, and others closely fitting the observed data as indicated also by Figure 14. However, and according to Figure 15 and Moreover, across all scenarios, the best-fit models in the box plots show that GFDL-CM4 indicates no change for SSP245 and an increasing trend in terms of median and data spread for SSP585. GFDL-ESM shows a decrease in data spread, becoming narrower for SSP245 and no significant change for SSP585, while BCC-CSM2 indicates some changes in data spreading and variability for SSP245, with a slight increase for SSP370.

Table 4 GFDL-CM4, followed by GFDL-ESM and BCC-CSM2, showcased superior statistical fitting to the observed data within the Blue Nile Basin, indicating robust performance across the basin. Contrariwise, MIROC6 demonstrated the lowest performance among the models analysed within the Blue Nile Basin, suggesting potential areas for improvement in its modelling approach.

Figure 17 shows monthly outliers for ACCESS-CM2, MPI-ESM, and GFDL-ESM. Additionally, GFDL-CM4, followed by GFDL-ESM and NorESM2-MM, fits the observed data well in terms of median value, symmetry, spread, and variability. However, MPI-ESM and ACCESS-CM2, followed by GFDL-ESM, share the same median as the observed data but exhibit lower data spread compared to CHIRPS. Conversely, as depicted in Figure 14, MIROC6 overestimates the data significantly in terms of the median and data spread.

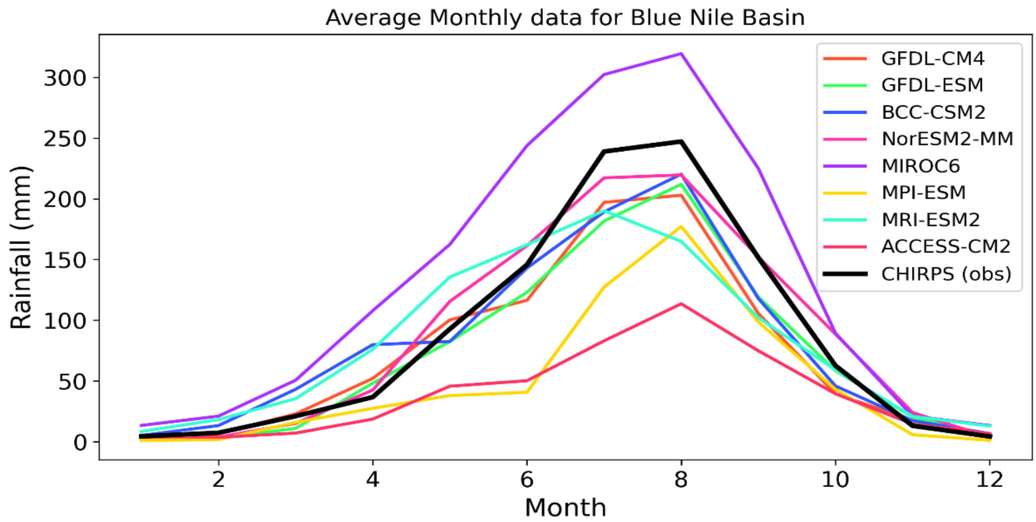

Figure 14: Average monthly data for Blue Nile (Observed vs GCMs)

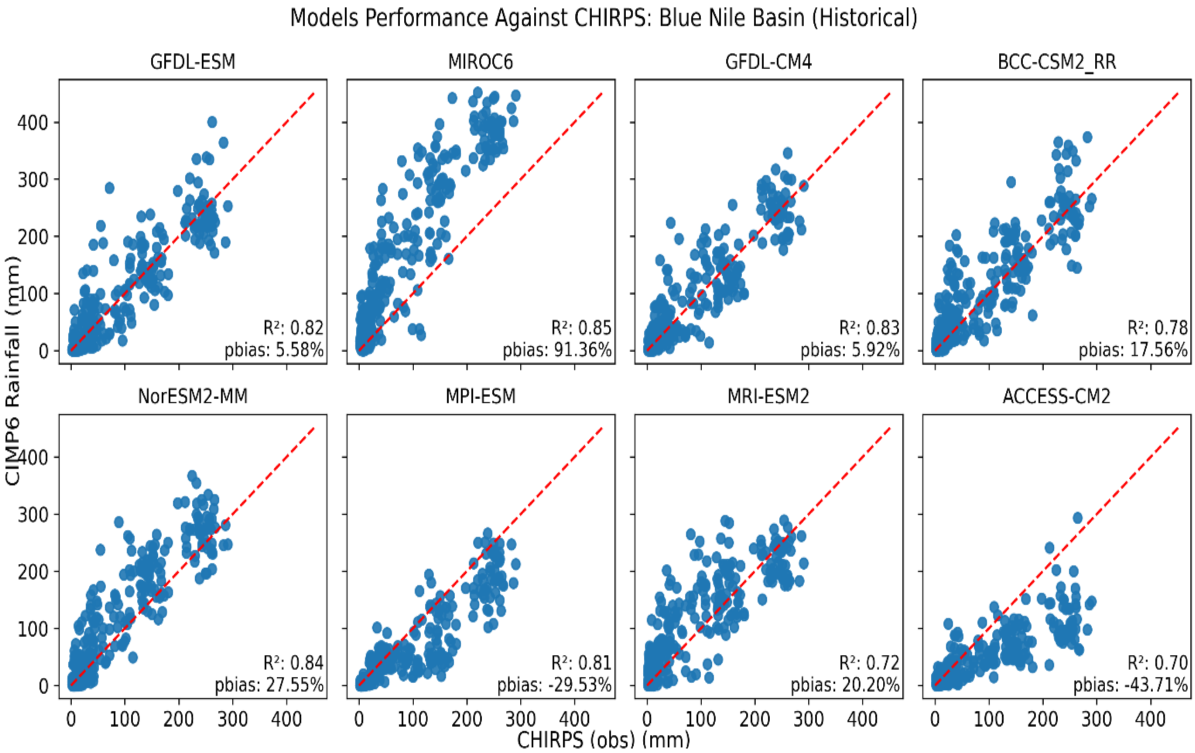

Figure 15: Models performance against CHIRPS using scatter plots - BN

Moreover, across all scenarios, the best-fit models in the box plots show that GFDL-CM4 indicates no change for SSP245 and an increasing trend in terms of median and data spread for SSP585. GFDL-ESM shows a decrease in data spread, becoming narrower for SSP245 and no significant change for SSP585, while BCC-CSM2 indicates some changes in data spreading and variability for SSP245, with a slight increase for SSP370.

Table 4: Models ranking based on the statistical metrics - BN

		Statistical Metrics					
Ranking	Model	R2	CC	NSE	PBIAS	RMSE	MAE
1	GFDL-CM4	0.83	0.91	0.81	5.92	37.83	25.84
2	GFDL-ESM	0.82	0.91	0.80	5.58	39.51	25.32
3	BCC-CSM2-RR	0.78	0.89	0.72	17.56	46.29	31.97
4	MPI-ESM	0.81	0.90	0.72	-29.53	46.47	30.44
5	NorESM2-MM	0.84	0.92	0.69	27.55	48.57	33.03
6	MRI-ESM2	0.72	0.85	0.67	20.20	50.39	36.73
7	ACCESS-CM2	0.70	0.83	0.44	-43.71	65.78	43.65
8	MIROC6	0.85	0.92	-0.44	91.36	105.25	80.28

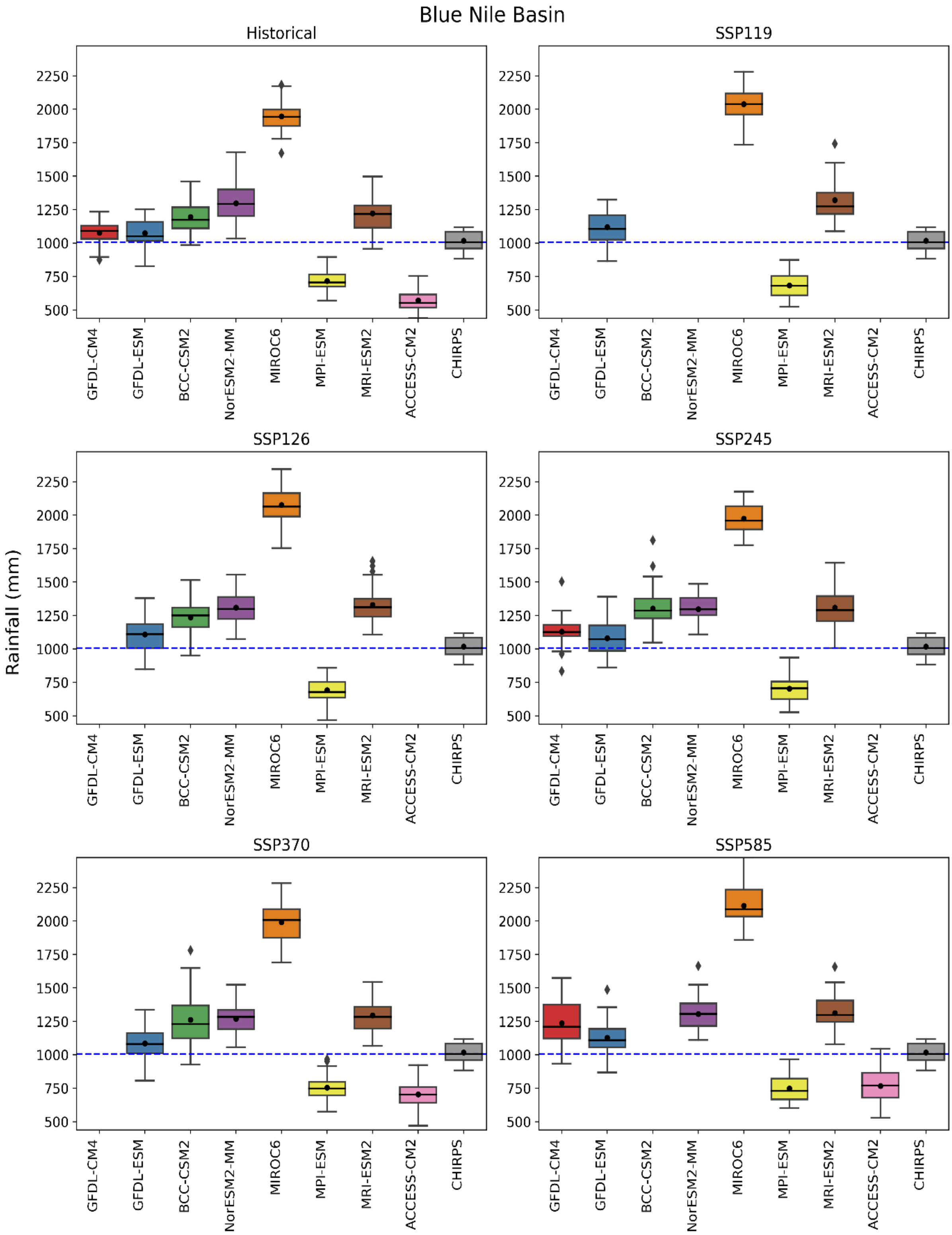

Figure 16 Box Plot Analysis for BN Basin – Historical and Projection Scenarios Compared to CHIRPS – Annual Rainfall (mm):

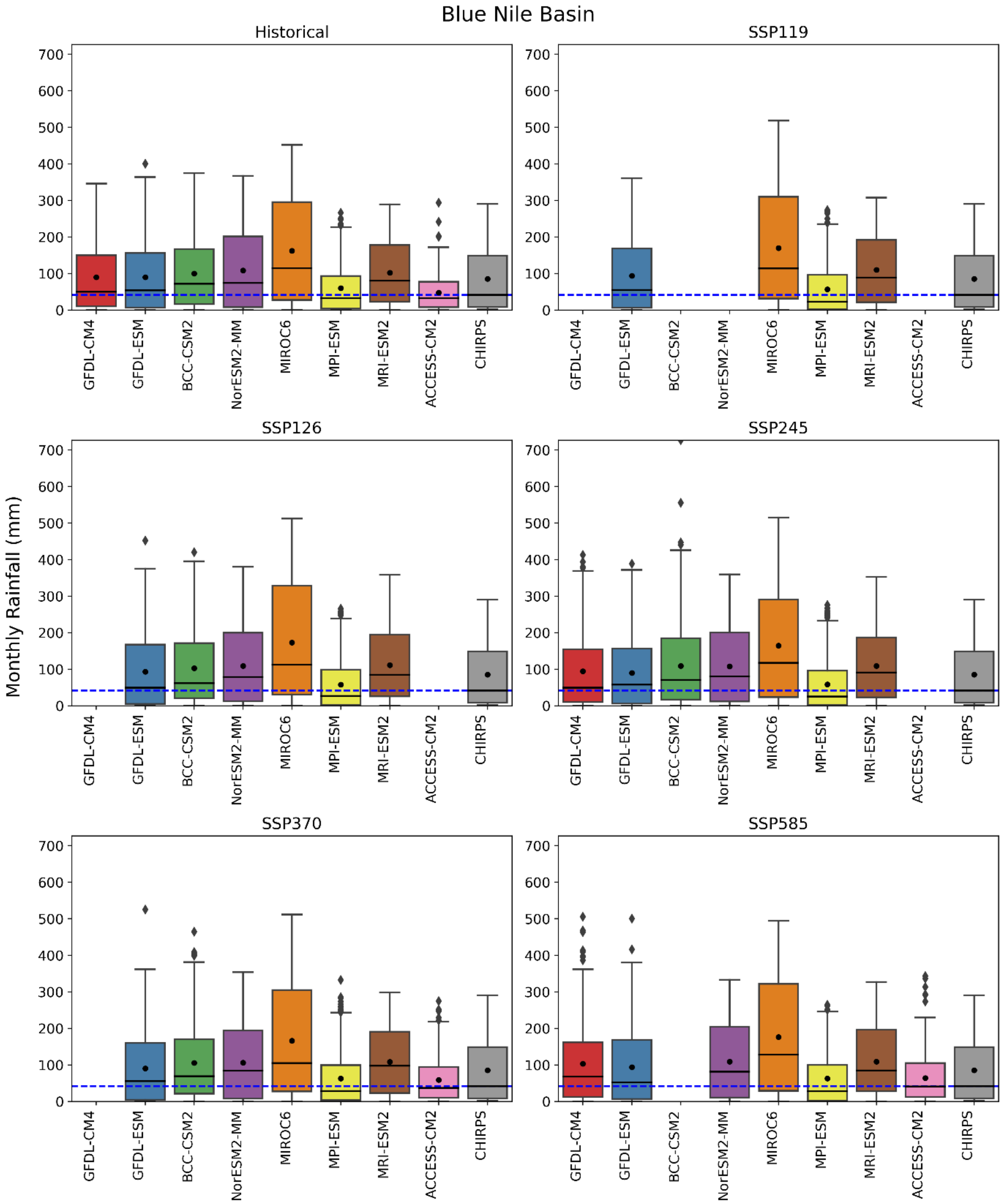

Figure 17: Box Plot Analysis for BN Basin – Historical and Projection Scenarios Compared to CHIRPS – Monthly Rainfall (mm)

From Figure 18, GFDL-CM4 indicates there will be increasing shifts in the mean but with lower frequency. Meanwhile, GFDL-ESM indicates that in all scenarios, there is no significant change in the mean, but all means become less frequent. BCC-CSM2 suggests that in terms of scenarios SSP245 and SSP585, means will be higher with a greater frequency of occurrence, indicating increasing shifts in the mean in the future for the Blue Nile Basin.

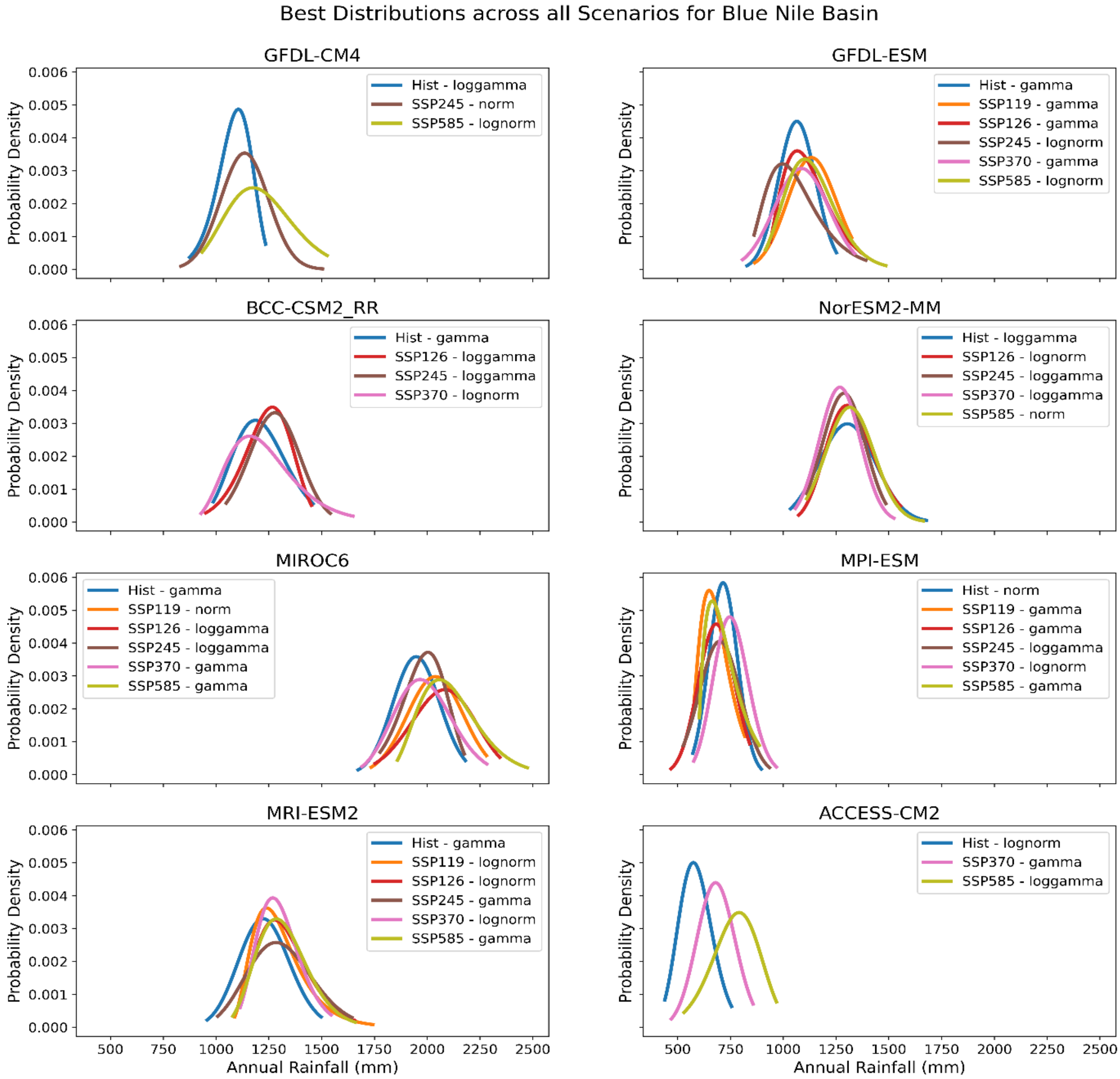

Figure 18: Best Distributions for all scenarios across the BN compared to the observed

Figures 19-24 highlight the historical and future trends, variability, and uncertainty for the Blue Nile Basin. Among historical scenarios from GCMs, 50% show an increasing trend, namely GFDL-ESM, MIROC6, MRI-ESM2, and ACCESS-CM2, which aligns with the trend of the observed data, CHIRPS. Additionally, 37.5% of the models indicate no change in the trends, while only one model indicates a decreasing trend for the BN region. Surprisingly, the top three performing models over BN each indicate a different trend (e.g., no change, increasing, and decreasing for GFDL-CM4, GFDL-ESM, and BCC-CSM2, respectively).

Regarding projection scenarios, the top three models, GFDL-CM4 and GFDL-ESM, indicate no change, increasing, increasing, and slight decreasing trends for SSP245 and SSP585, respectively. Meanwhile, BCC-CSM2 suggests increasing trends for both scenarios SSP245 and SSP370.

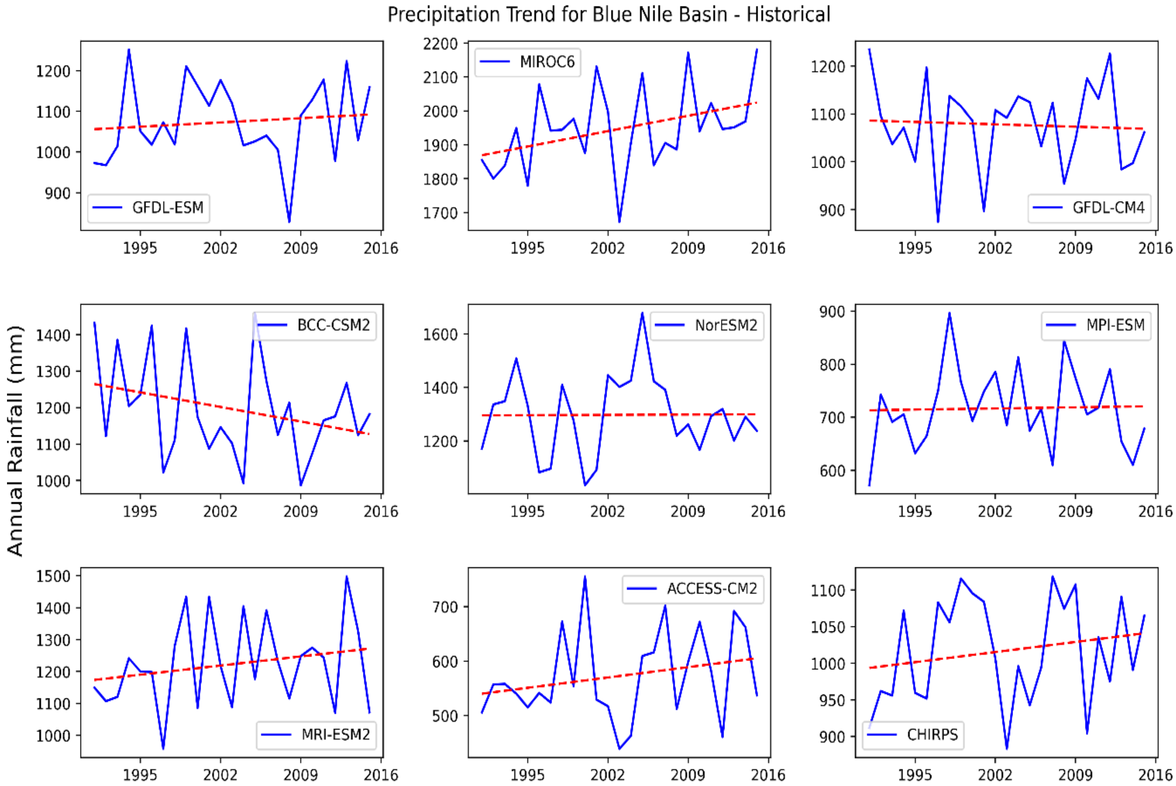

Figure 19: Historical Rainfall trends for BN

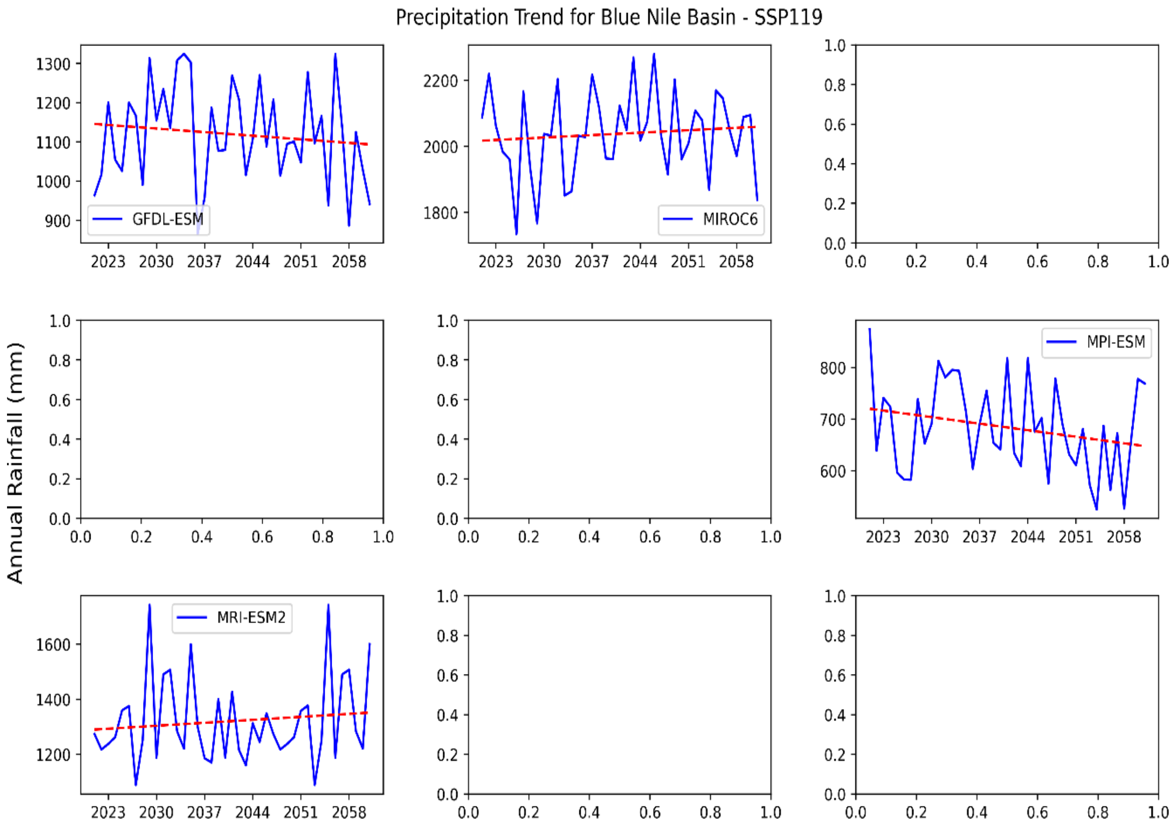

Figure 20: SSP119 Rainfall Projections trend for BN

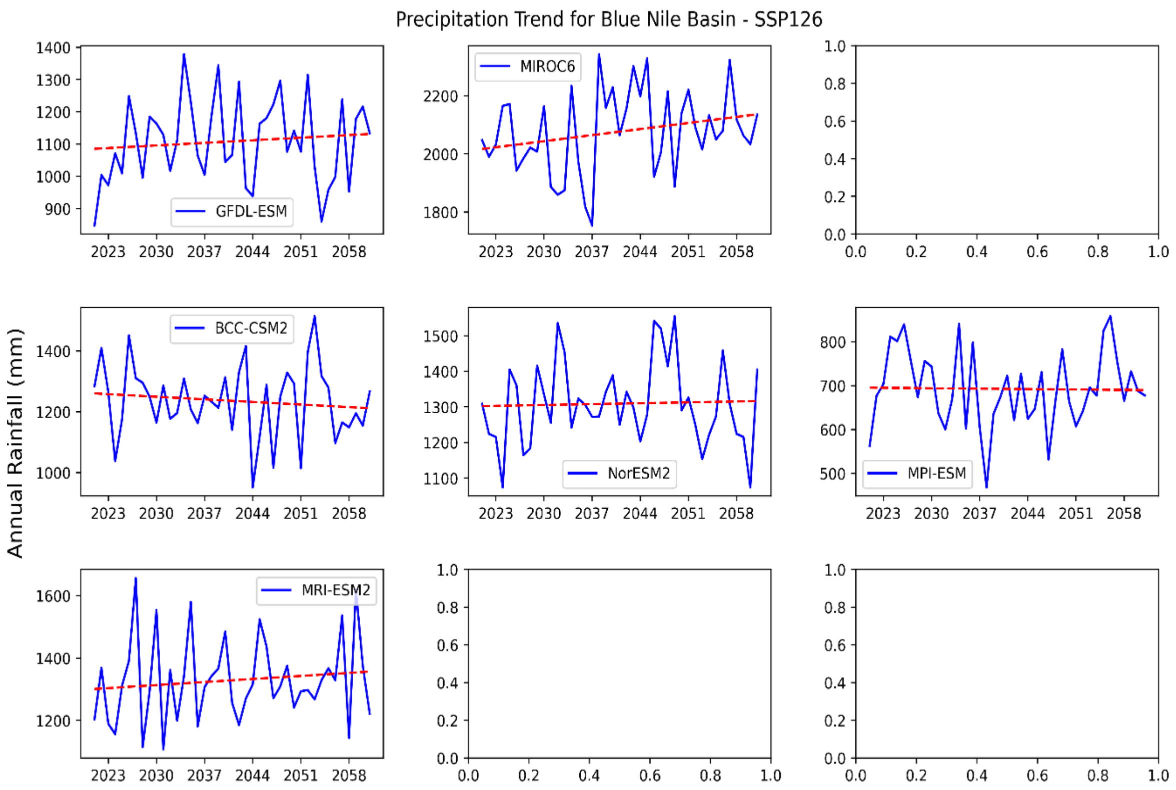

Figure 21: SSP126 Rainfall Projections trend for BN

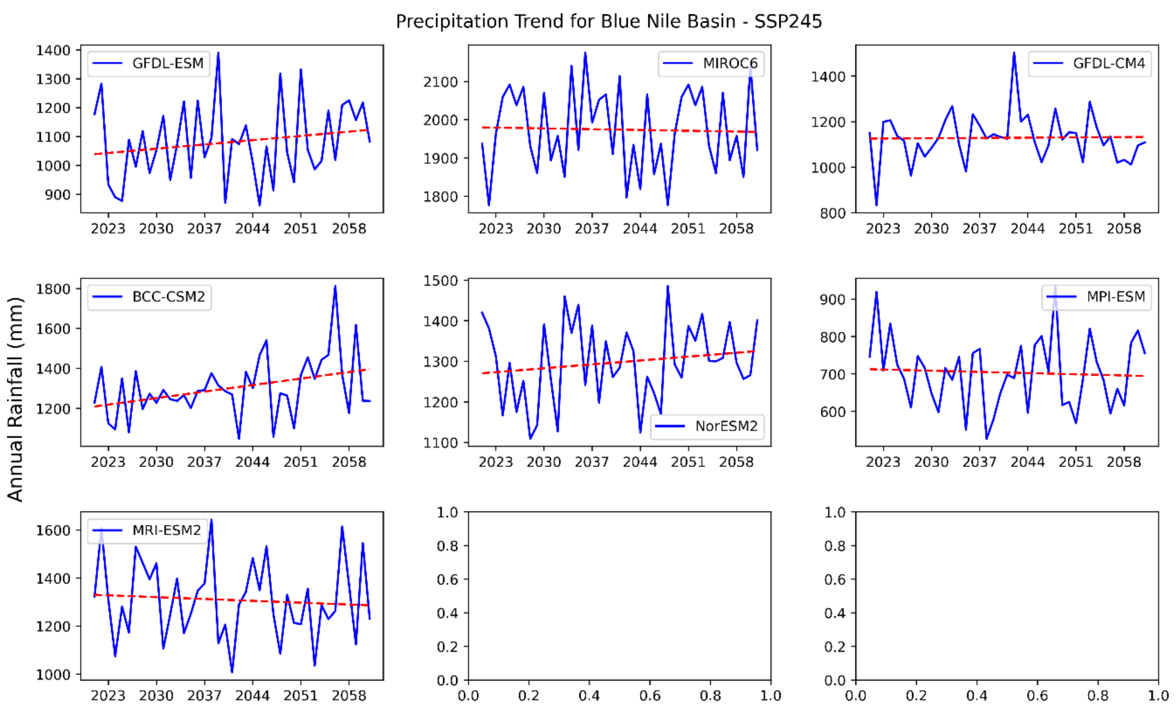

Figure 22: SSP245 Rainfall Projections trend for BN

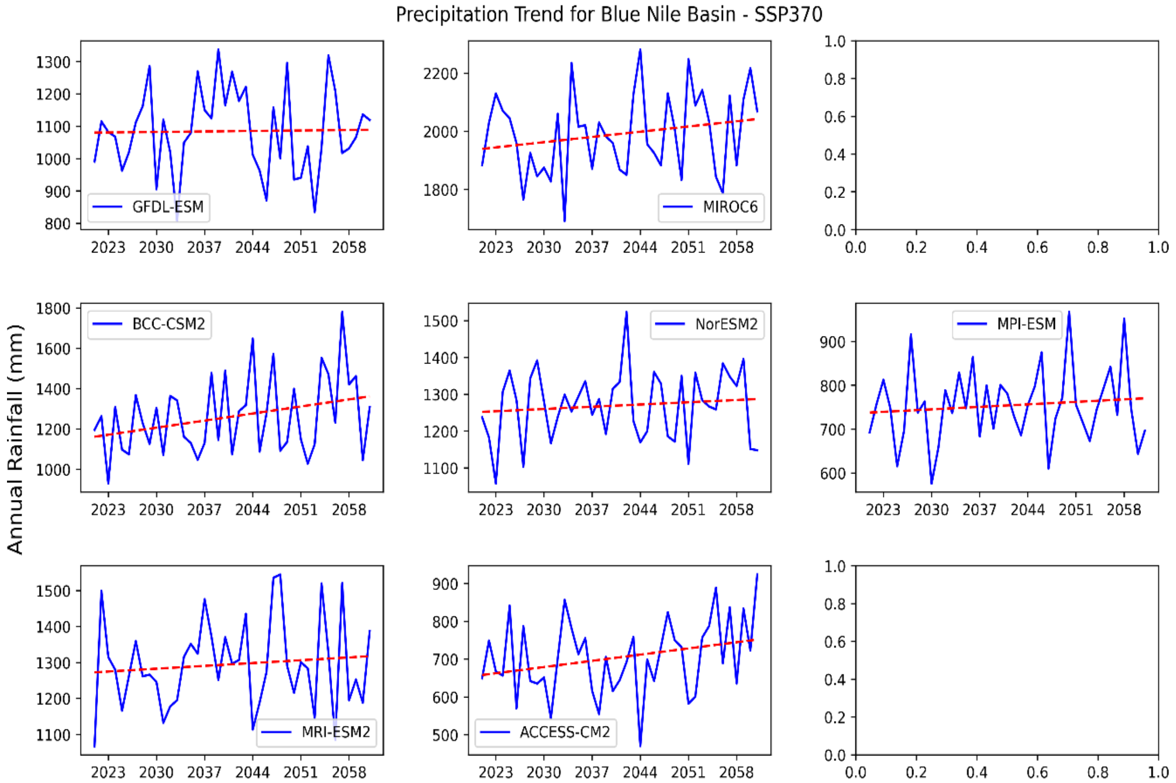

Figure 23: SSP370 Rainfall Projections trend for BN

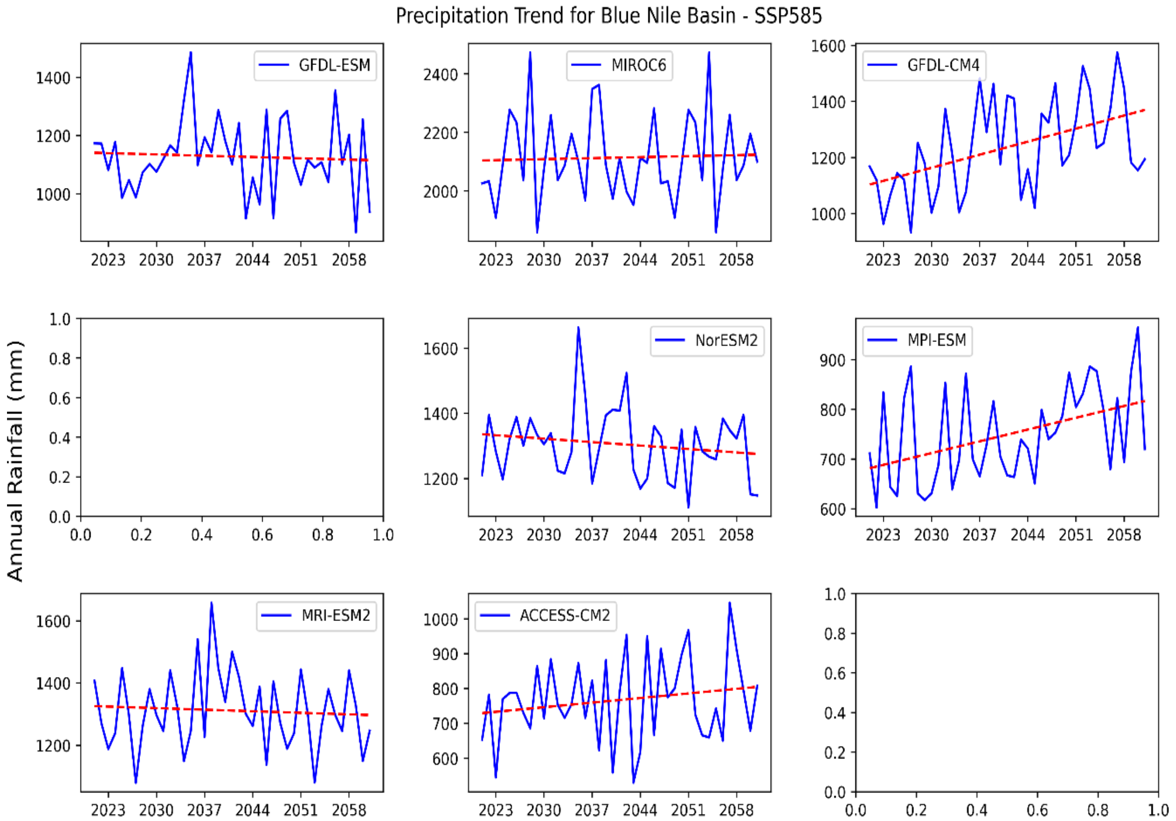

Figure 24: SSP585 Rainfall Projections trend for BN

4.1.3. Tekeze Setit Atbara Basin (TSA)

The primary season for the TSA is the JJAS, with some rainfall occurring from March to May (MAM), as indicated by the observed data in Figure 25. However, the same figure shows that NorESM2-MM consistently captures the seasonality of the TSA basin with slight underestimation overall. This is followed by MIROC6, although it highly overestimates the MAM period, and then GFDL-CM4, despite generally underestimating the mean values, successfully captures the pattern of the TSA's seasonality.

Furthermore, Figure 26 provides a comparison between observed data and CMIP6 models through scatter plots. According to Figure 26 and Table 5, NorESM2-MM, followed by GFDL-CM4 and GFDL-ESM, performed well statistically in the TSA compared to the observed data, while ACCESS-CM2 exhibited poor performance among the other models in the TSA.

Figure 28 presents monthly outliers for all CMIP6 models except MRI-ESM2. Additionally, NorESM2-MM, followed by GFDL-ESM and GFDL-CM4, symmetrically fit the observed data very well in terms of median value, spread, and variability. However, BCC-CSM2, followed by MPI-ESM and ACCESS-CM2, share the same median as the observed data but exhibit lower data spread in the intermediate quartiles compared to CHIRPS. Moreover, across all scenarios, the best-fit models in the box plots show that all outliers will increase in all scenarios, indicating an increase in extremes for the TSA region. However, NorESM2 shows slight increases in SSP245 and SSP585 in terms of the median and intermediate quartiles of the data. GFDL-ESM indicates no significant change for both SSP245 and SSP585. GFDL-CM4 shows a slight decrease in data spread and the median for SSP245 and no significant change for SSP585.

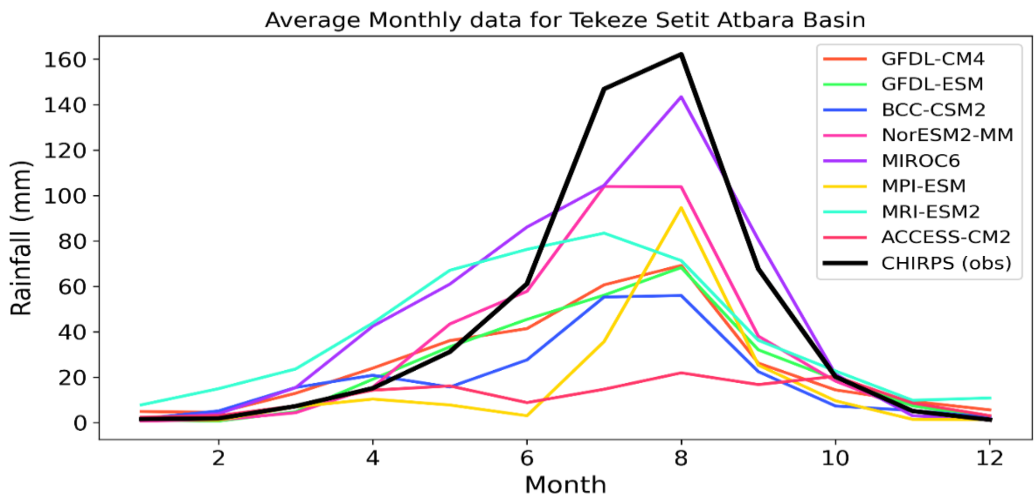

Figure 25: Average monthly data for Tekeze Setit Atbara Basin (Observed vs GCMs)

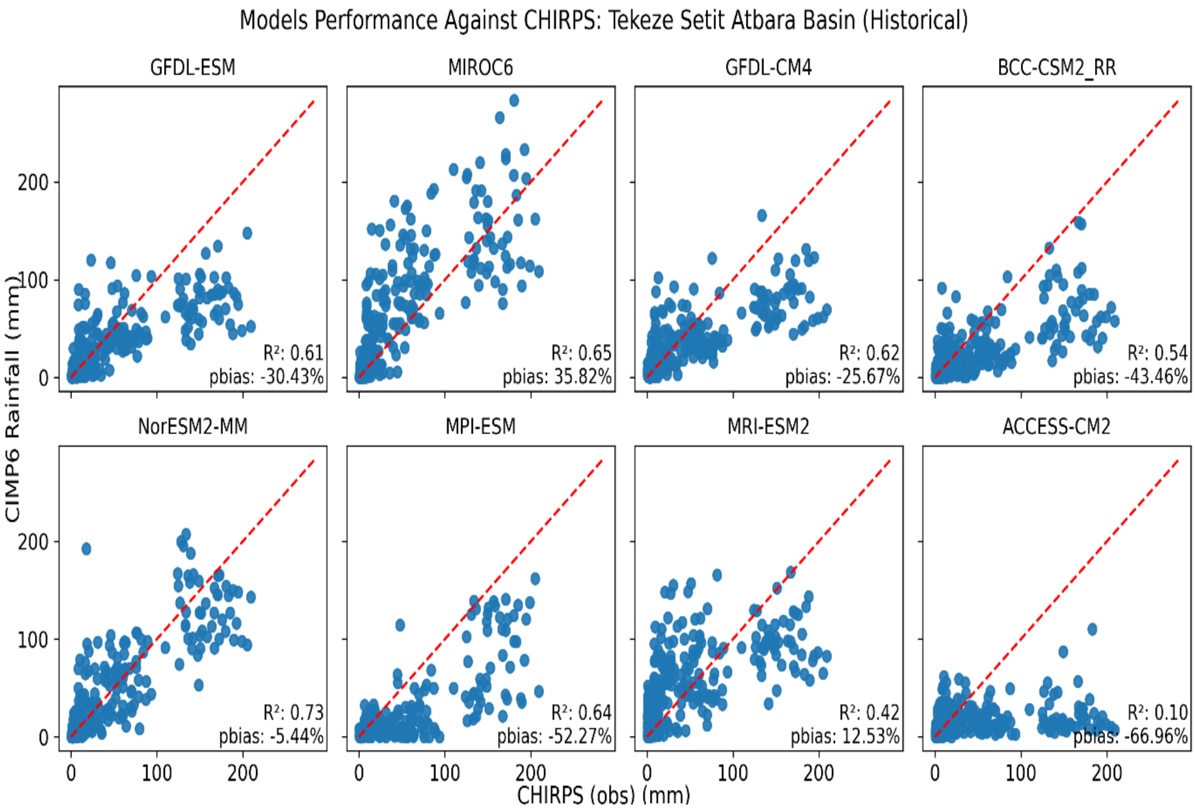

Figure 26:Models performance against CHIRPS using scatter plots - TSA

Table 5: Models ranking based on the statistical metrics - TSA

		Statistical Metrics					
Ranking	Model	R2	CC	NSE	PBIAS	RMSE	MAE
1	NorESM2-MM	0.73	0.85	0.72	-5.44	29.43	17.97
2	GFDL-CM4	0.62	0.79	0.52	-25.67	38.67	24.24
3	GFDL-ESM	0.61	0.78	0.52	-30.43	38.93	23.09
4	MIROC6	0.65	0.81	0.47	35.82	40.61	26.18
5	MPI-ESM	0.64	0.80	0.44	-52.27	41.79	24.96
6	MRI-ESM2	0.42	0.64	0.40	12.53	43.33	31.35
7	BCC-CSM2-RR	0.54	0.73	0.37	-43.46	44.25	26.82
8	ACCESS-CM2	0.10	0.32	-0.17	-66.96	60.40	35.53

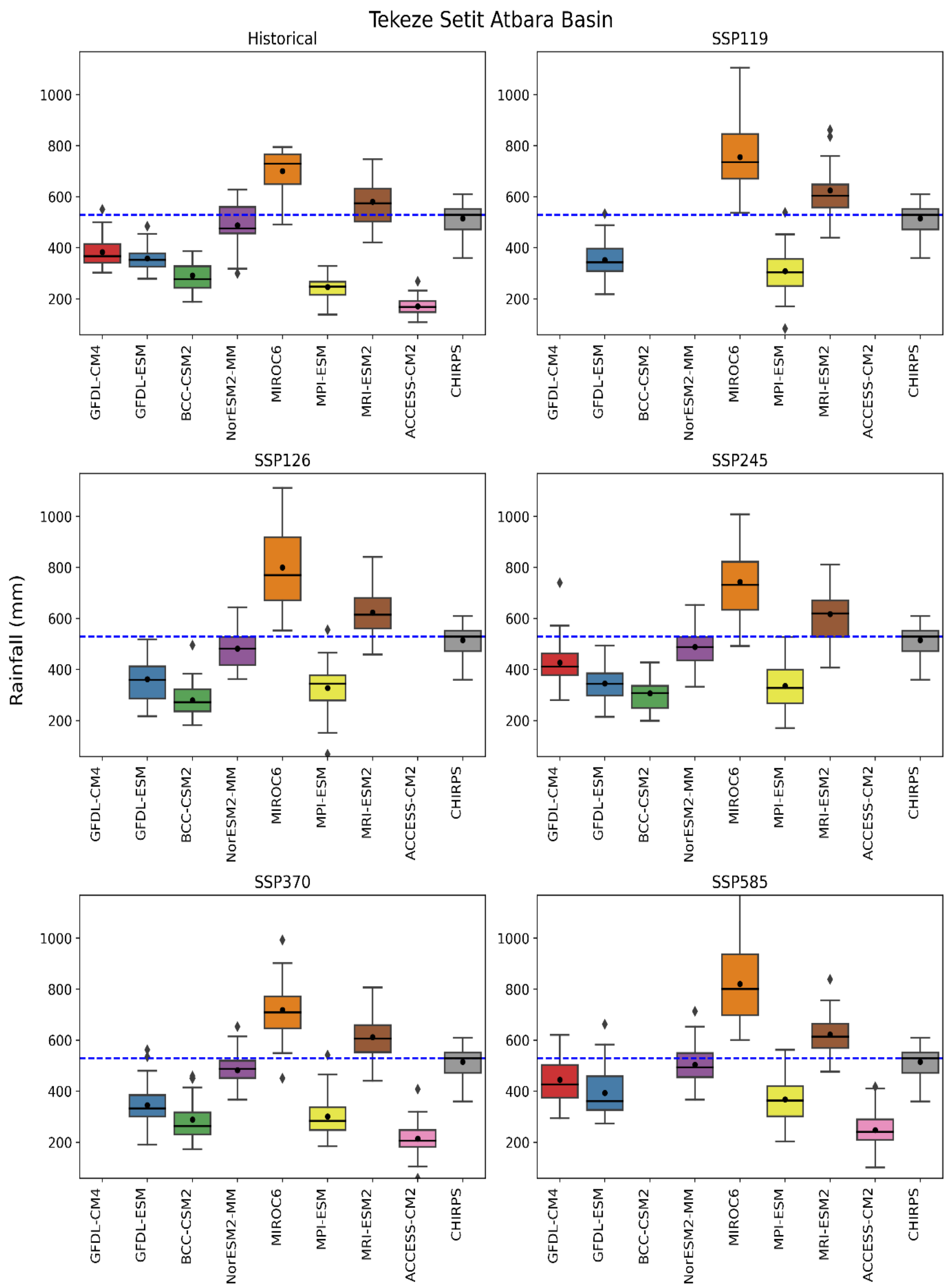

Figure 27:Box Plot Analysis for TSA Basin – Historical and Projection Scenarios Compared to CHIRPS – Annual Rainfall (mm):

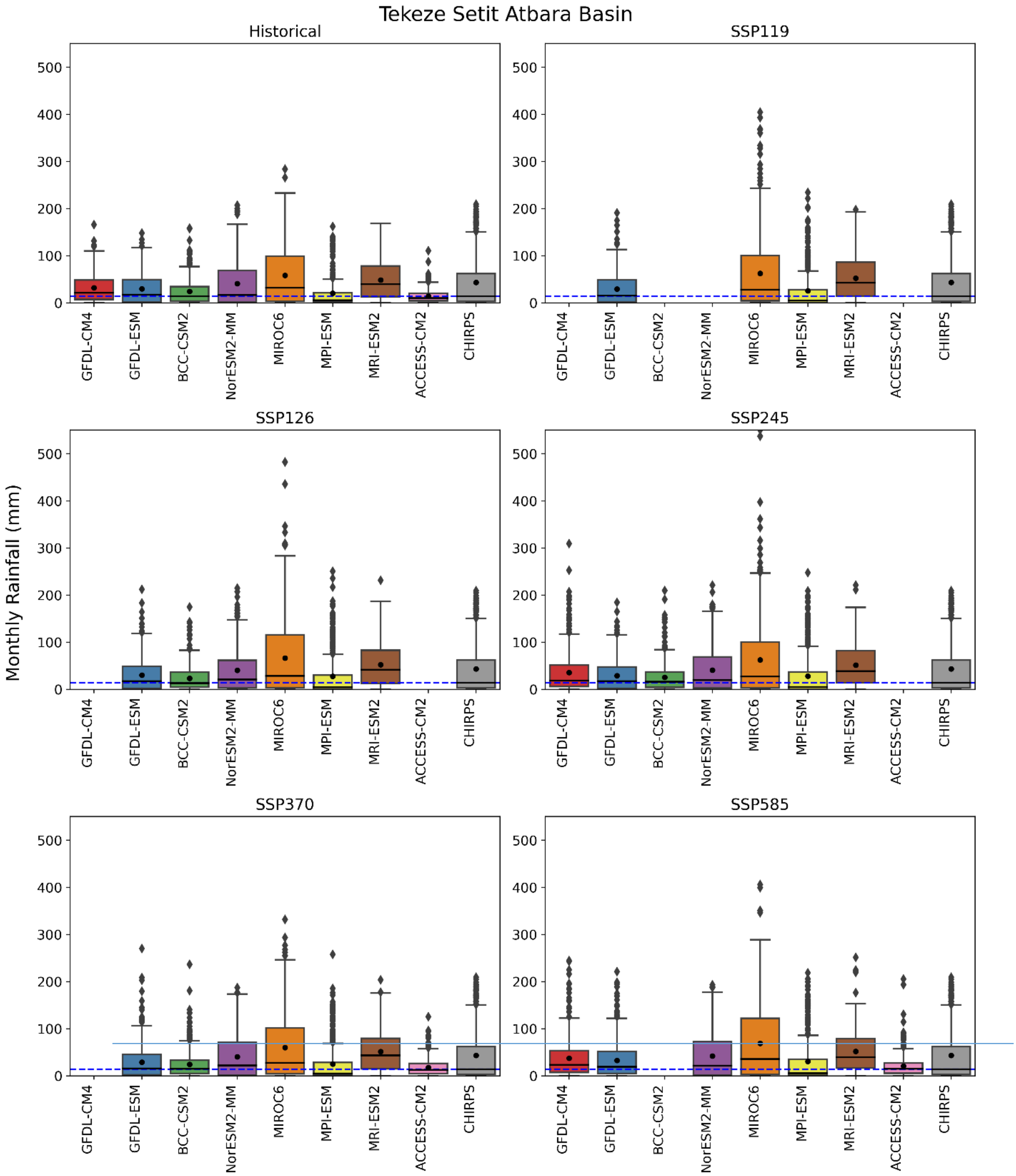

Figure 28: Box Plot Analysis for TSA Basin – Historical and Projection Scenarios Compared to CHIRPS – Monthly Rainfall (mm)

From Figure 29, NorESM2-MM shows a slight decrease in means for SSP245, no change in trend across SSP585, but an increased probability for the mean. Meanwhile, GFDL-ESM indicates that in all scenarios, there is no significant change in the mean, but all means become less frequent. GFDL-CM4 shows an increasing shift in means but with lower probabilities across SSP245 and SSP585.

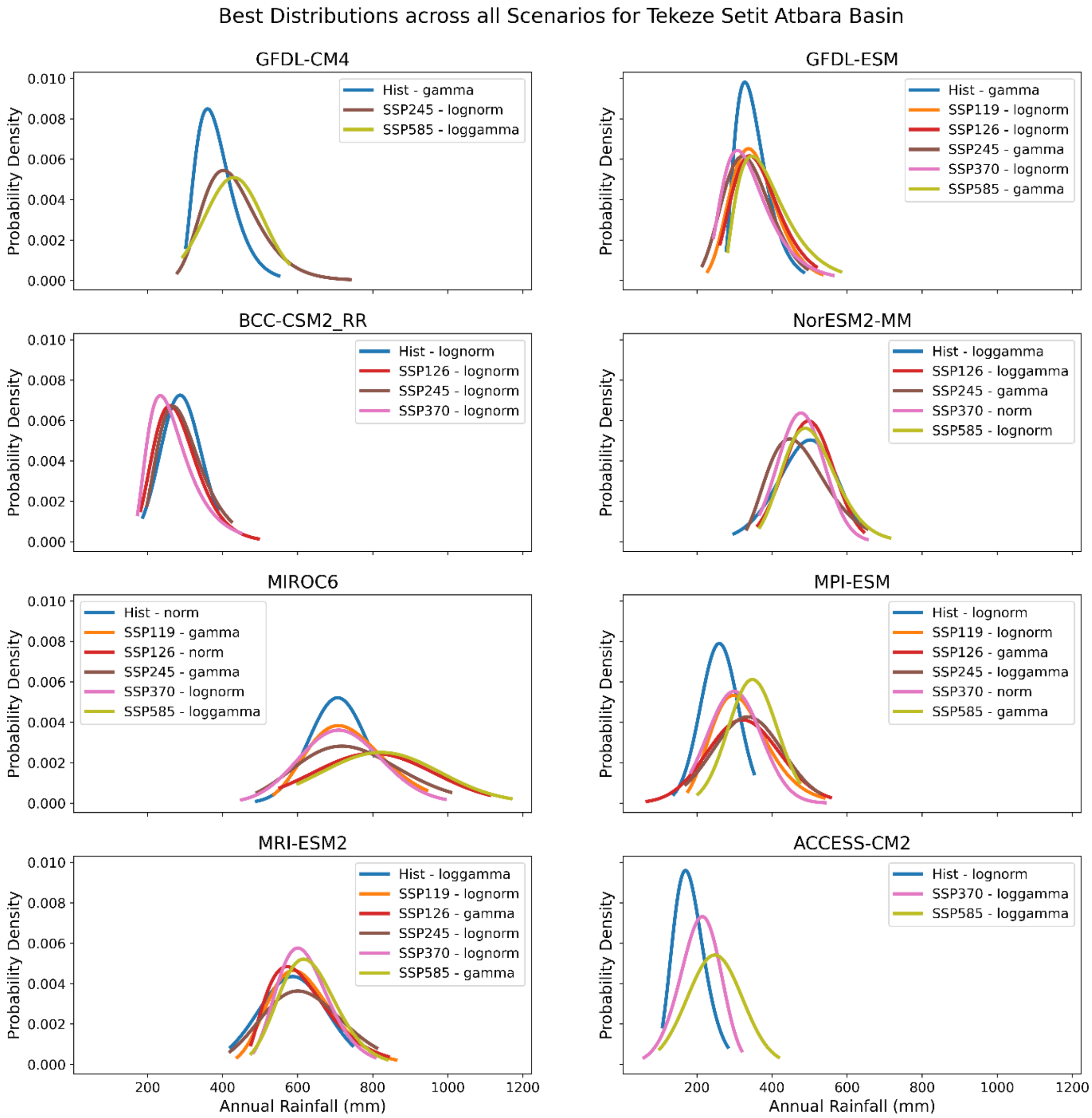

Figure 29: Best Distributions for all scenarios across the TSA compared to the observed

Figures 30-35 highlight the historical and future trends, variability, and uncertainty for the Tekeze Setit Atbara Basin. Among historical scenarios from GCMs, 50% show a decreasing trend. Additionally, 37.5% of the models indicate an increasing trend, which aligns with the trend of the observed data, CHIRPS, while only one model indicates no change in the trends. The top three performing models over TSA each indicate a different trend: a decreasing trend for GFDL-CM4 and GFDL-ESM, and an increasing trend for NorESM2-MM.

For the SSP245 scenario, NorESM2-MM and GFDL-ESM show an increasing trend, while GFDL-CM4 shows no change in trend. For SSP585, there is a decreasing trend for NorESM2-MM and increasing trends for GFDL-ESM and GFDL-CM4, respectively.

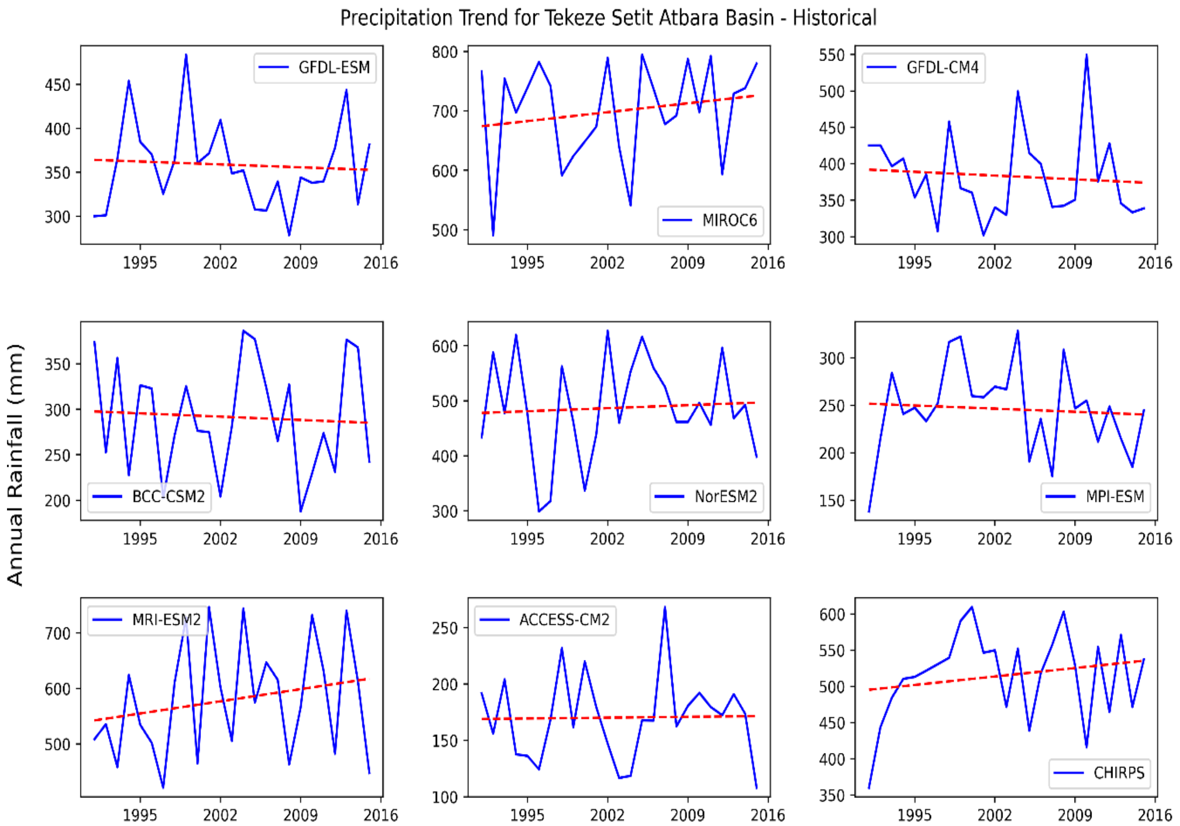

Figure 30: Historical Rainfall trends for TSA

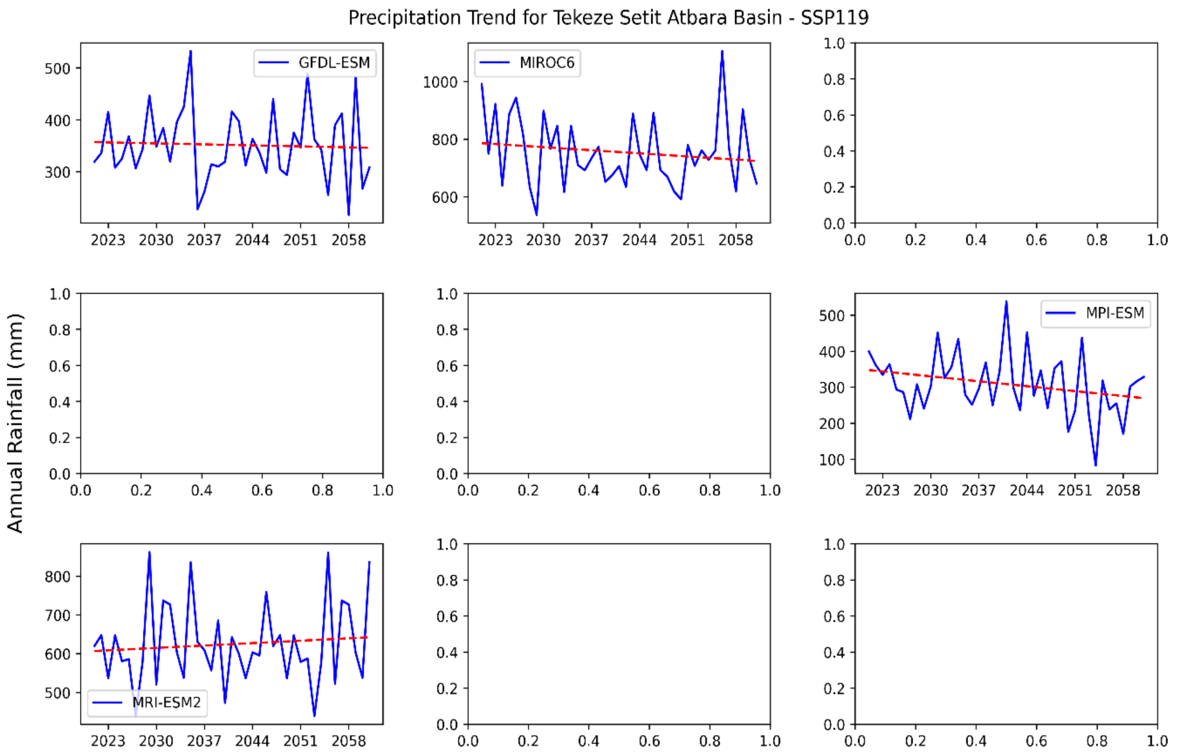

Figure 31: SSP119 Rainfall Projections trend for TSA

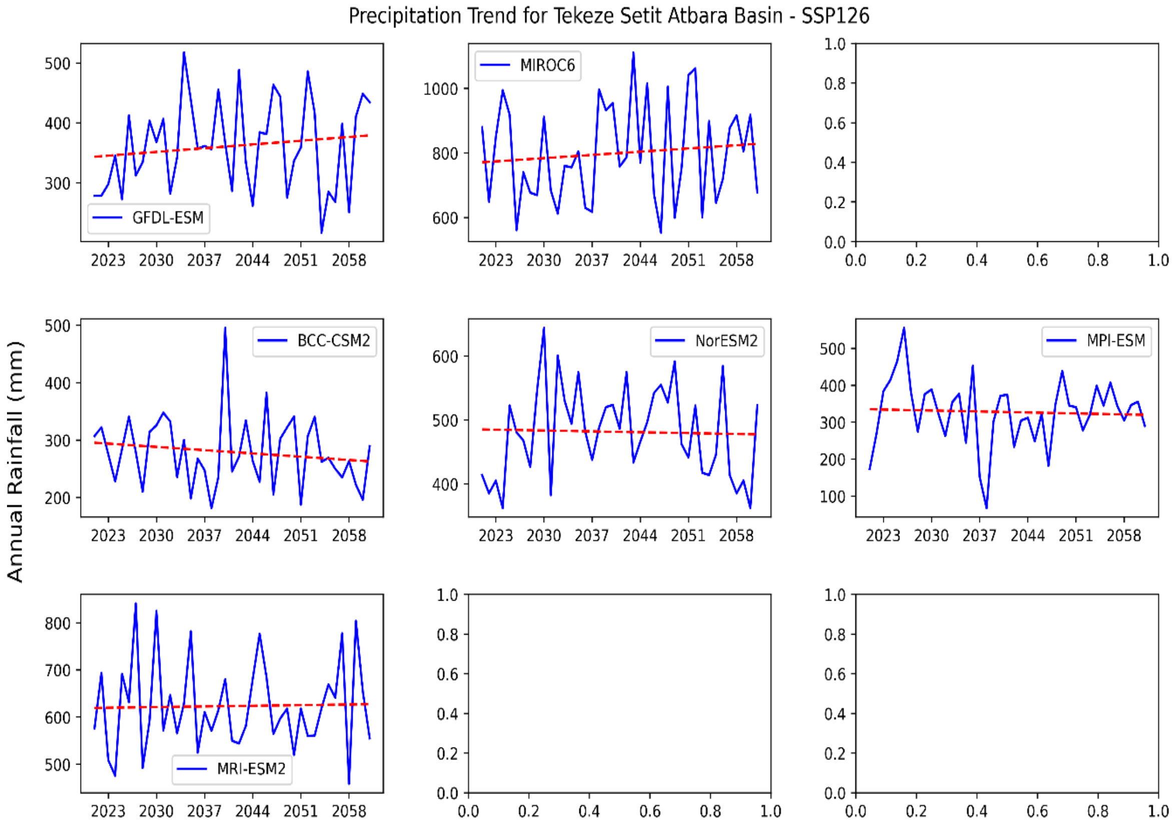

Figure 32: SSP126 Rainfall Projections trend for TSA

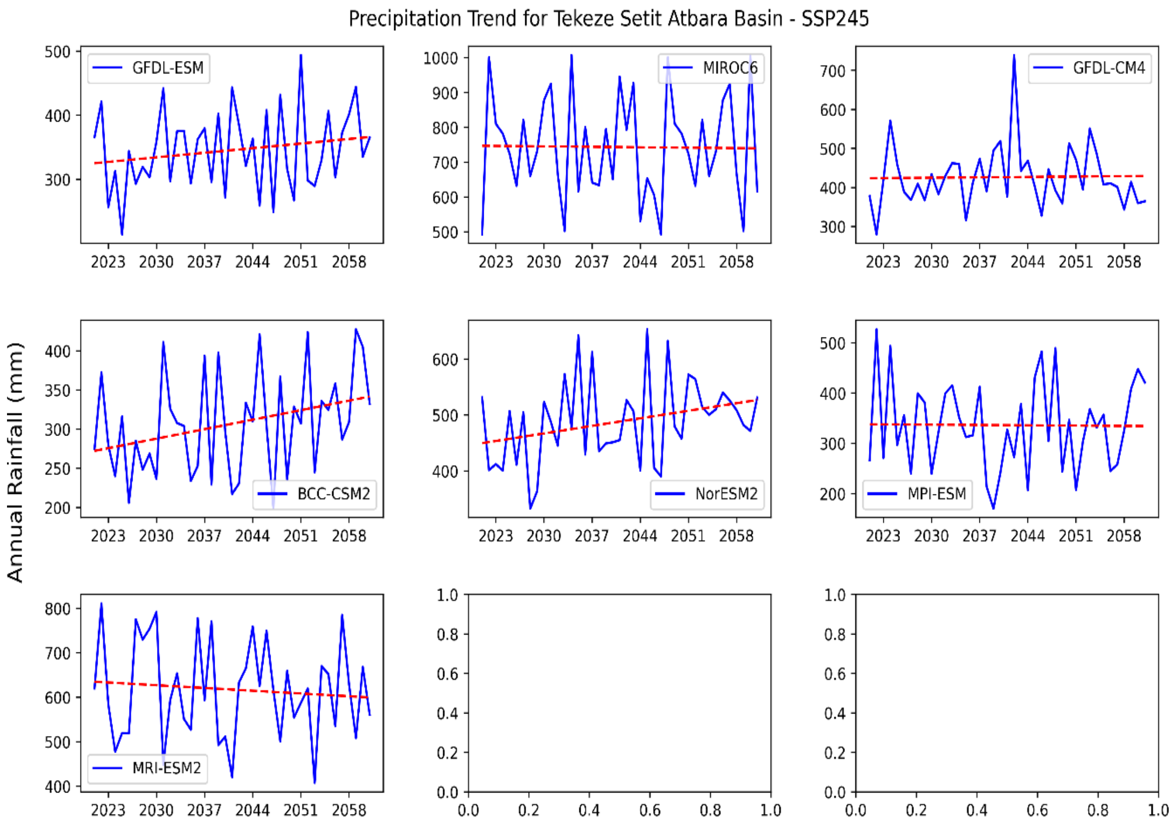

Figure 33: SSP245 Rainfall Projections trend for TSA

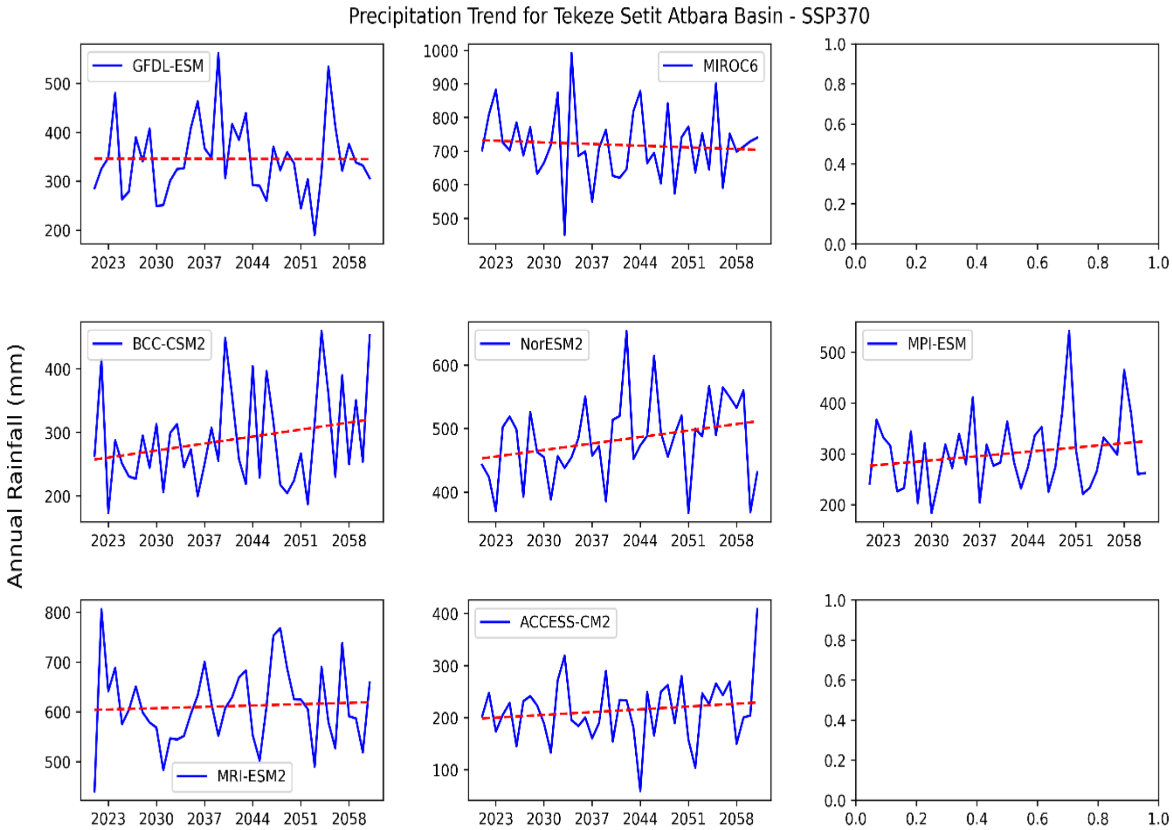

Figure 34: SSP370 Rainfall Projections trend for TSA

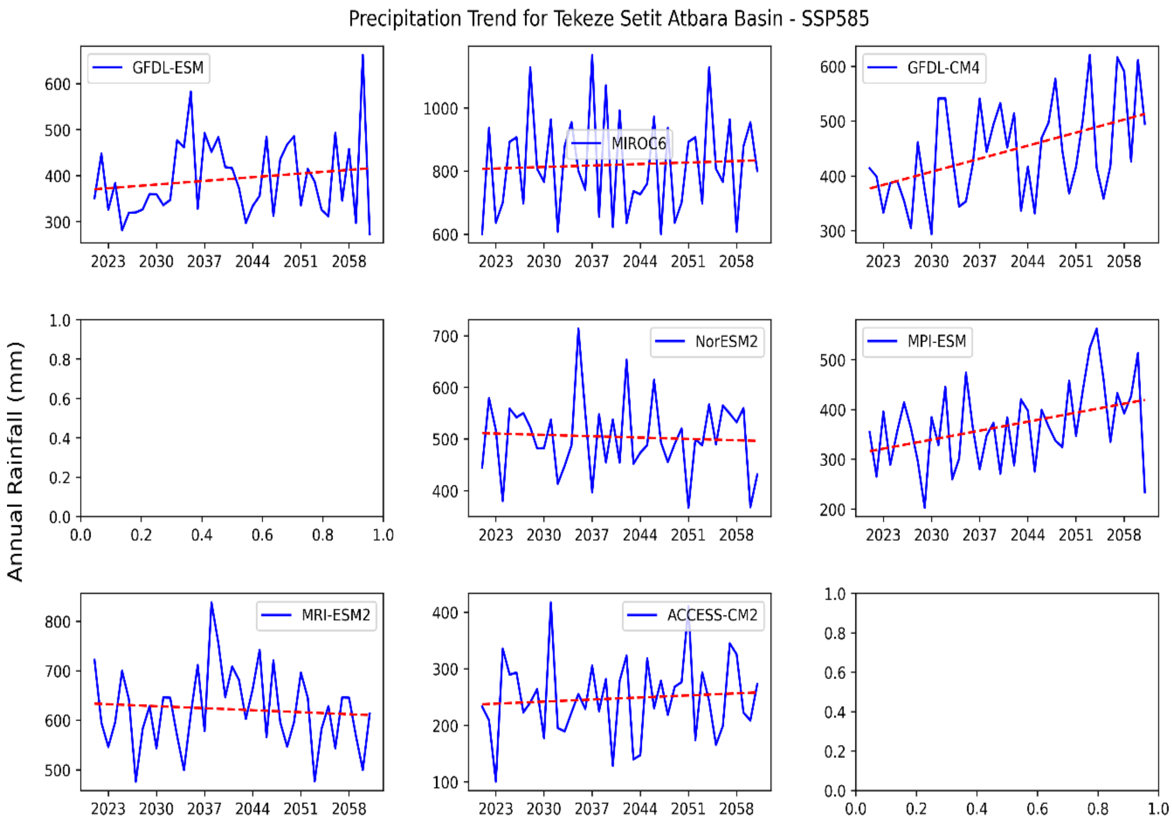

Figure 35: SSP585 Rainfall Projections trend for TSA

4.1.4. Upper Main Nile Basin (UMN)

As shown in Figure 36, The main season for the Upper Main Nile (UMN) basin is JJAS. With the exception of MIROC6, all models in the sub basin either fail to capture the peak or incorrectly detect it earlier, or tend to misrepresent the seasonality of observed data, as depicted in Figure 36. While MIROC6 captured the seasonality to some extent, it tends to overestimate the observed data. Furthermore, Figure 37 compares observed data with CMIP6 models through scatter plots, revealing poor performances generally compared to CHIRPS, varying accuracies indicated by R^2 and pbias values. Moreover, both visually and statistically, MPI-ESM demonstrates superior performance among all models, followed by NorESM2-MM, GFDL-ESM, and GFDL-CM4 in the UMN basin. Despite MIROC6 performing well in capturing seasonality, as indicated by its R2 and correlation, it exhibits the highest RMSE and pbias when compared with observed data. Consequently, it ranks lowest among the models listed in Table 6. The box plots among all models in the basin exhibit numerous outliers, resulting in narrow plots confined within a limited chart framework, as depicted in Figure 38, which makes analysis more challenging. To address this, we focused solely on the historical scenario, as shown in Figure 40, enabling a clearer evaluation of the models. In Figure 40, it is evident that BCC-CSM2 typically aligns well with the observed data, followed by GFDL-CM4 and GFDL-ESM in terms of median and interquartiles spread. Unfortunately, assessing these models across projection scenarios proves to be arduous due to the complexities observed in the box plots and mentioned above. However, their future projections will be assessed using distribution fits and trend analysis below.

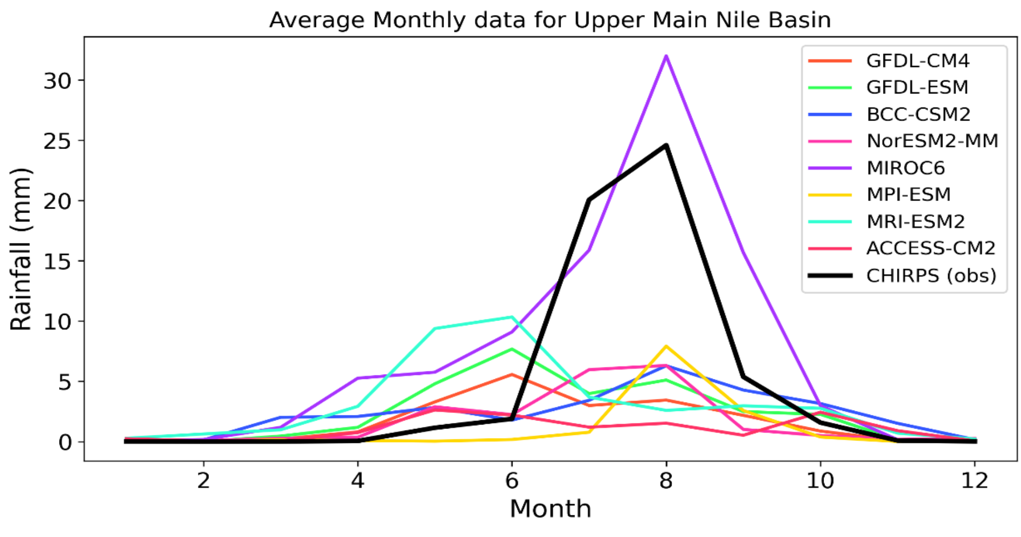

Figure 36:Average monthly data for Upper Main Nile (Observed vs GCMs)

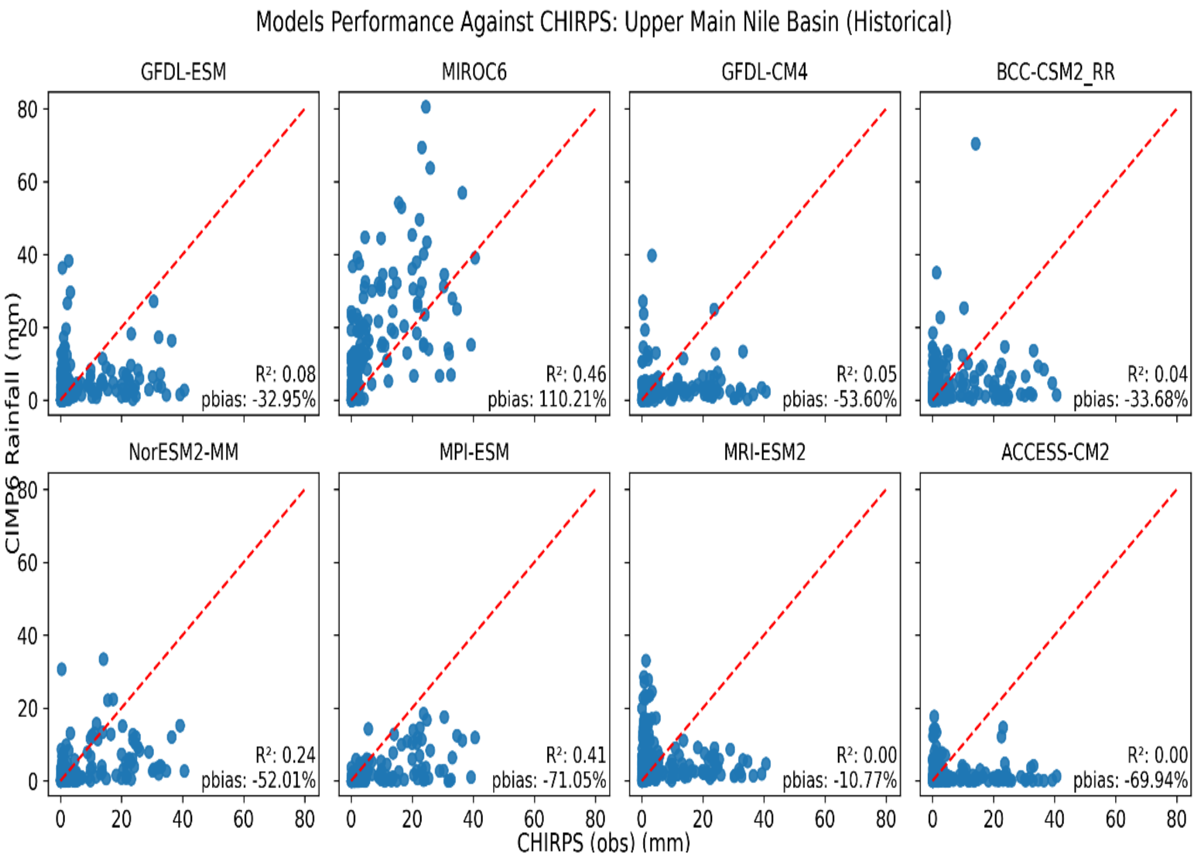

Figure 37:Models performance against CHIRPS using scatter plots - UMN

Table 6: Models ranking based on the statistical metrics - UMN

		Statistical Metrics					
Ranking	Model	R2	CC	NSE	PBIAS	RMSE	MAE
1	MPI-ESM	0.41	0.64	0.21	-71.05	7.52	3.28
2	NorESM2-MM	0.24	0.49	0.17	-52.01	7.74	3.54
3	GFDL-ESM	0.08	0.28	-0.06	-32.95	8.72	4.34
4	GFDL-CM4	0.05	0.23	-0.09	-53.60	8.86	4.10
5	ACCESS-CM2	0.00	0.07	-0.18	-69.94	9.20	4.49
6	BCC-CSM2-RR	0.04	0.20	-0.22	-33.68	9.34	4.70
7	MRI-ESM2	0.00	0.04	-0.39	-10.77	9.99	5.79
8	MIROC6	0.46	0.68	-0.74	110.21	11.17	6.12

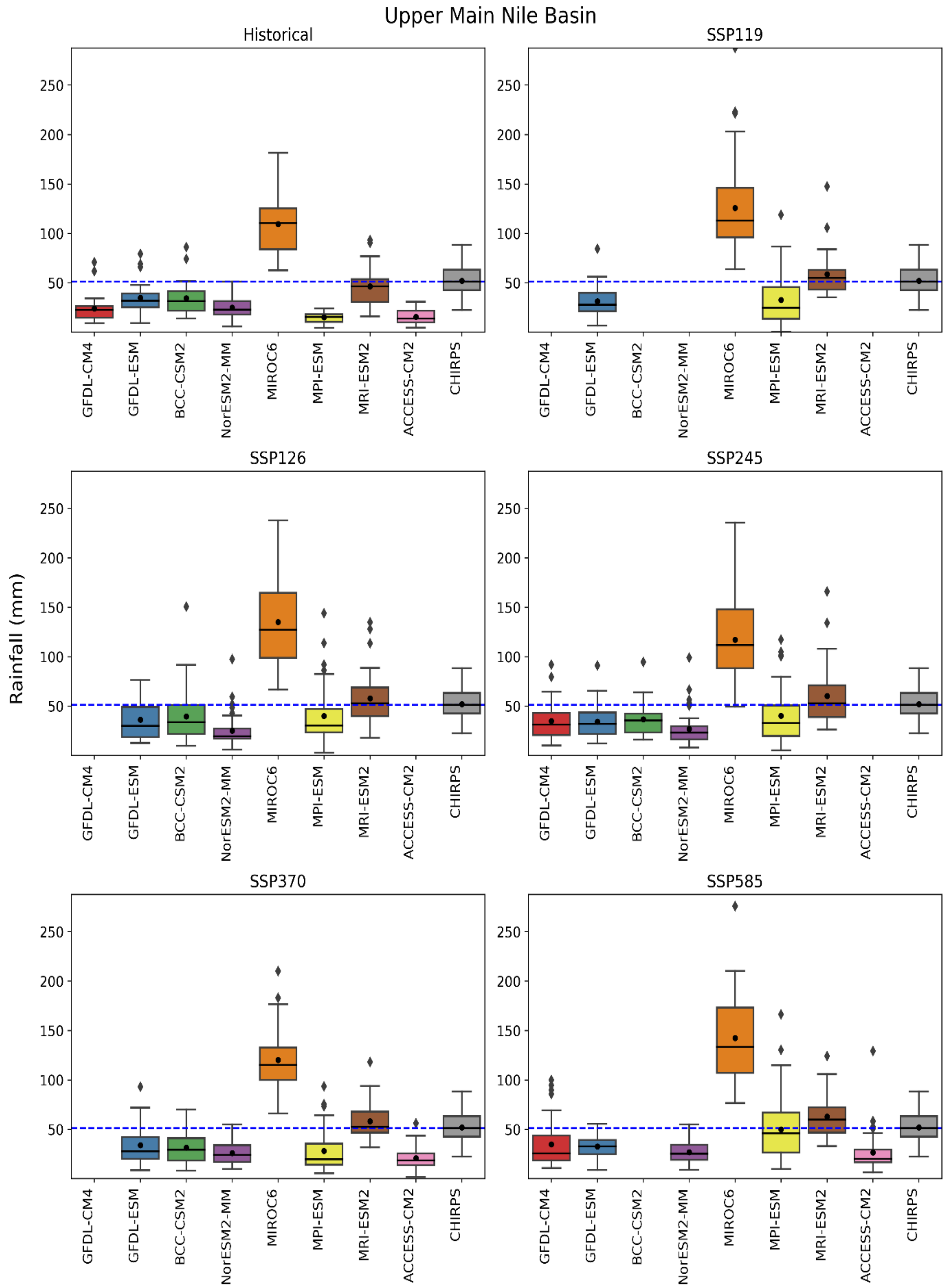

Figure 38: Box Plot Analysis for UMN Basin – Historical and Projection Scenarios Compared to CHIRPS – Annual Rainfall (mm)

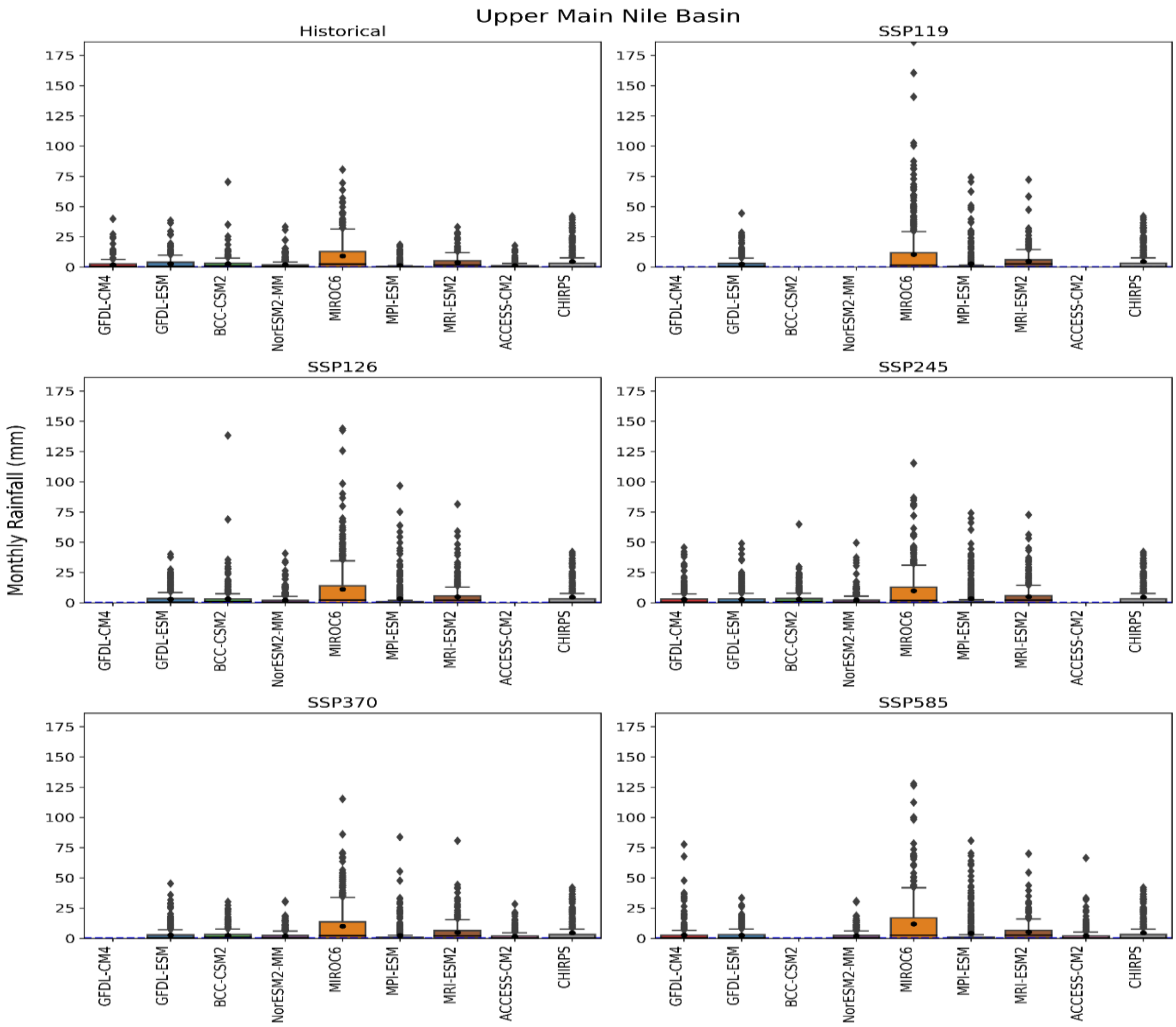

Figure 39: Box Plot Analysis for UMN Basin – Historical and Projection Scenarios Compared to CHIRPS – Monthly Rainfall (mm)

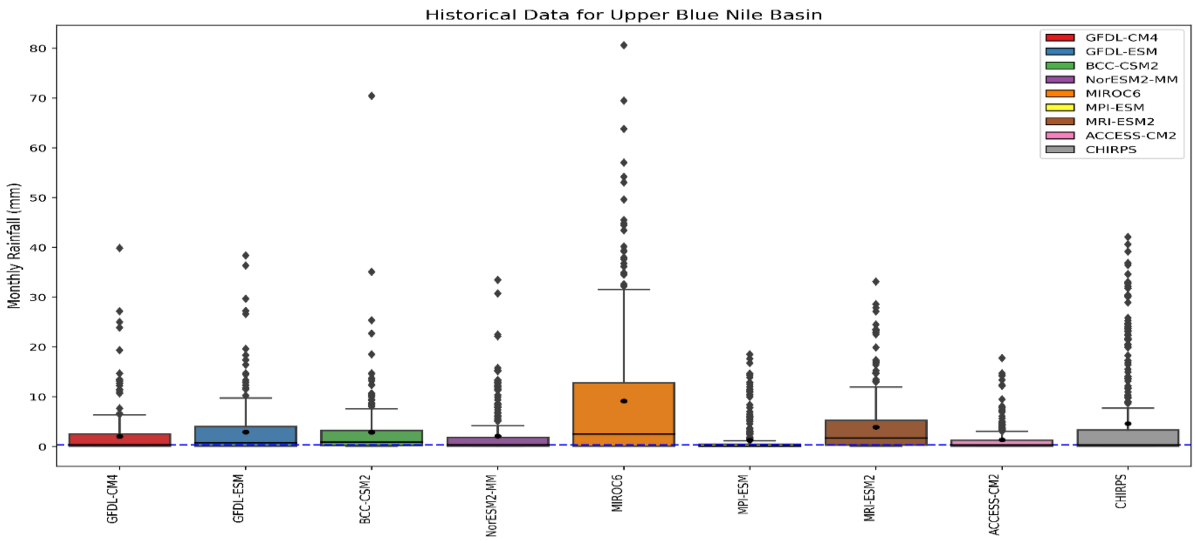

Figure 40: Box Plot Analysis for UMN Basin – Historical scenario Compared to CHIRPS – Monthly Rainfall (mm)

From Figure 41, MPI-ESM shows stability in means for SSP245, with a slight increase in mean shift for SSP585, both occurrences being less frequent. NorESM2-MM indicates no change in means for SSP245 but shows an increase in means for SSP585. On the other hand, BCC-CSM2 maintains similar means for SSP245, occurring more frequently, while exhibiting decreasing means for SSP370. GFDL-CM4 displays no significant trend change for SSP245 but shows an increasing mean shift with lower probability for SSP585. GFDL-ESM demonstrates decreasing means for SSP245 and increasing means for SSP585, with both occurrences having higher probability.

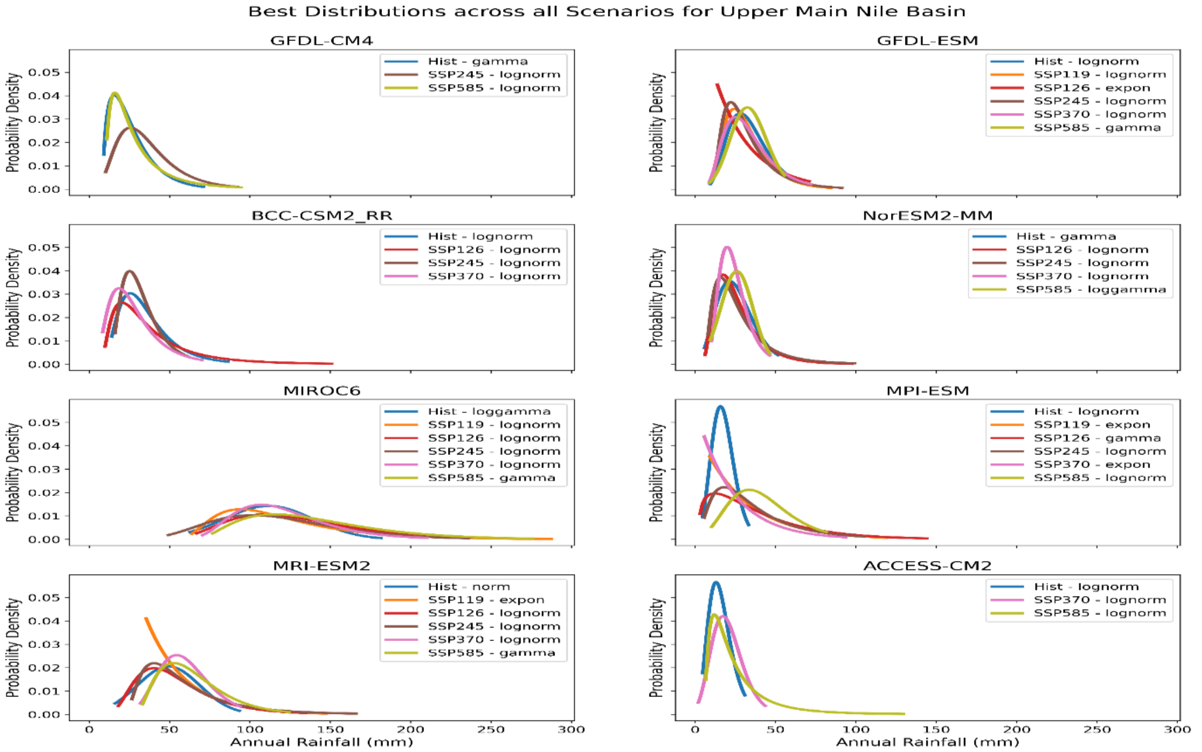

Figure 41: Best Distributions for all scenarios across the UMN compared to the observed

Figures 42-47 provide insights into the historical and future trends, variability, and uncertainty within the Upper Main Nile Basin. Among the historical scenarios from General Circulation Models (GCMs), 37.5% indicate an increasing trend, which corresponds to the observed data trend represented by CHIRPS, while only two models suggest no change in trends. Moreover, 37.5% of the models show a decreasing trend. Remarkably, among the top-performing models over UMN (NorESM2-MM, MPI-ESM, GFDL-ESM, and BCC-CSM2), four out of five models agree on a decreasing trend historically, while GFDL-CM4 suggests a stable trend. This is noteworthy as CHIRPS data indicates an opposing trend, namely an increase.

For the SSP245 scenario, all top-performing models indicate increasing trends. Similarly, in the SSP585 scenario, all top performing models suggest increasing trends, except for GFDL-ESM, which shows a decreasing trend.

Figure 42: Historical Rainfall trends for UMN

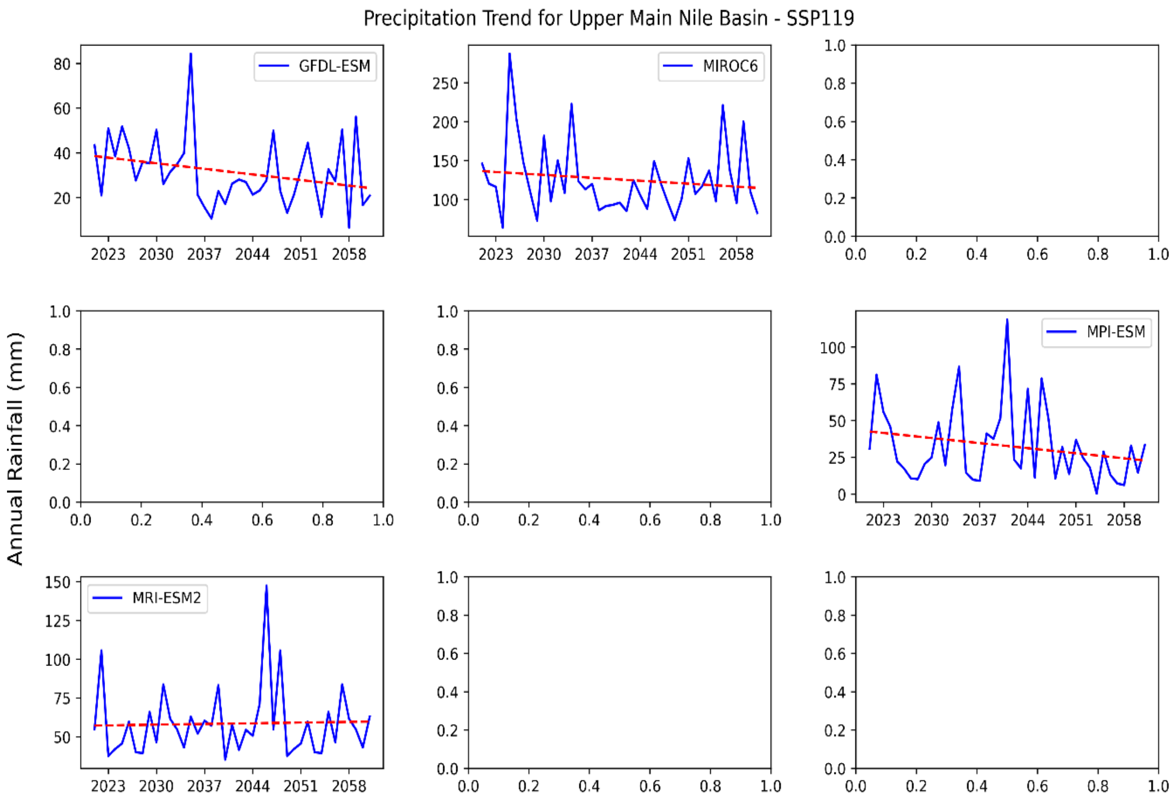

Figure 43: SSP119 Rainfall Projections trend for UMN

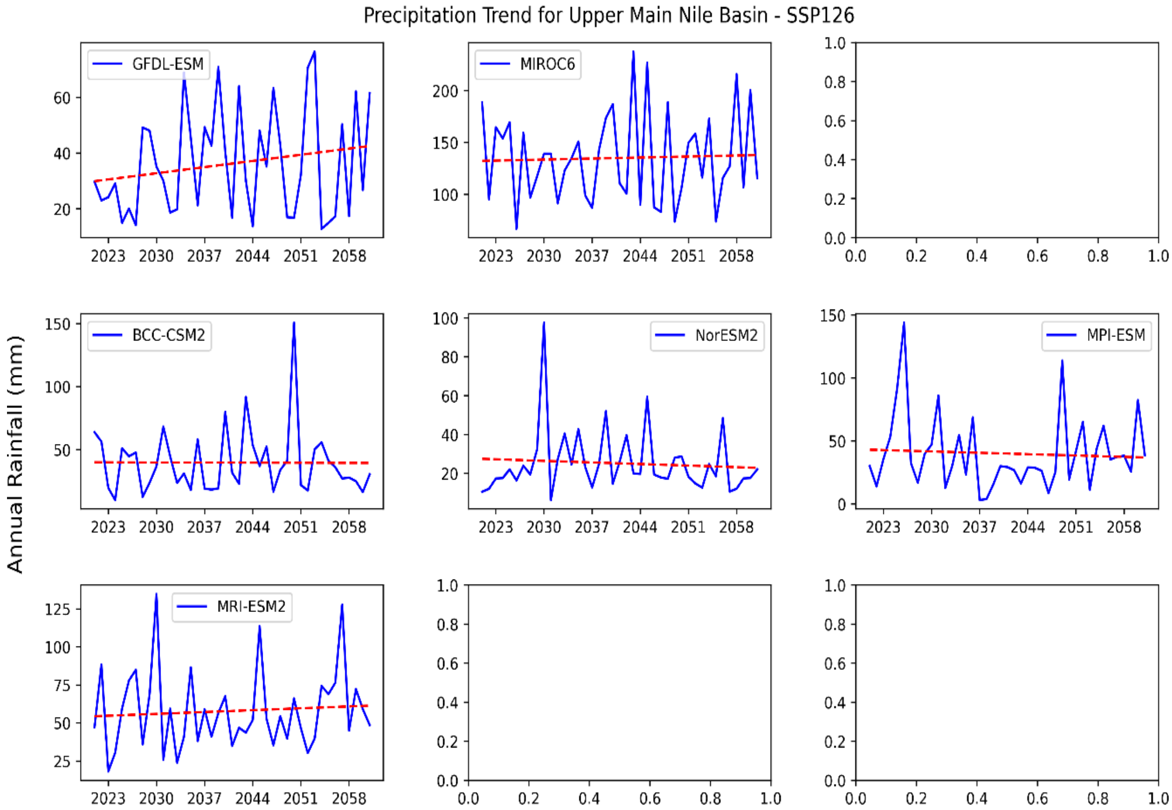

Figure 44: SSP126 Rainfall Projections trend for UMN

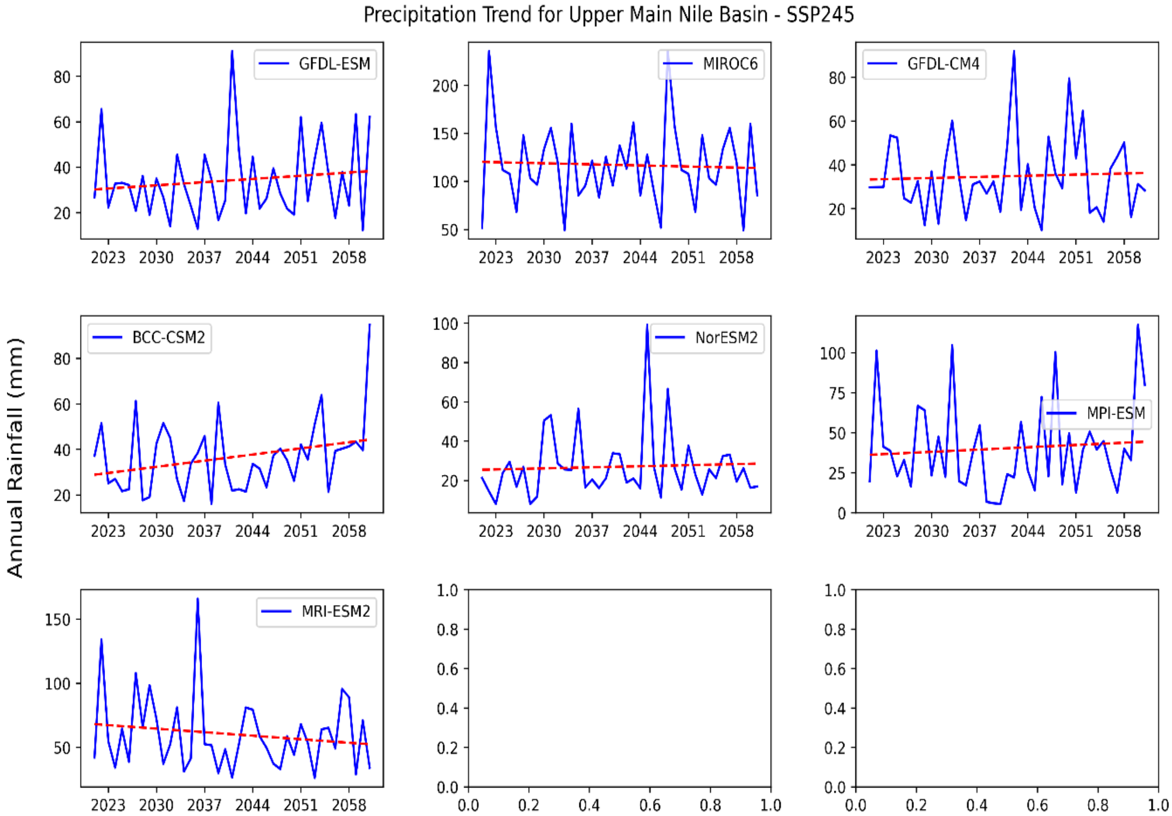

Figure 45: SSP245 Rainfall Projections trend for UMN

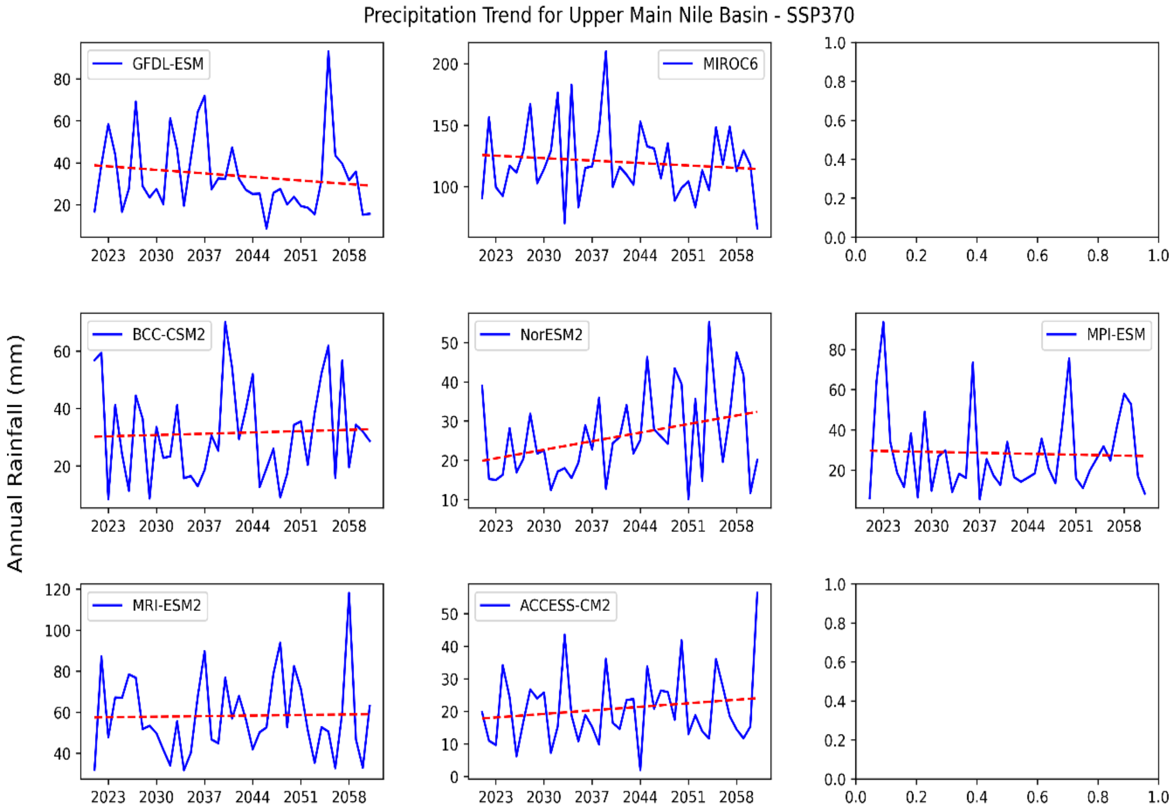

Figure 46: SSP370 Rainfall Projections trend for UMN

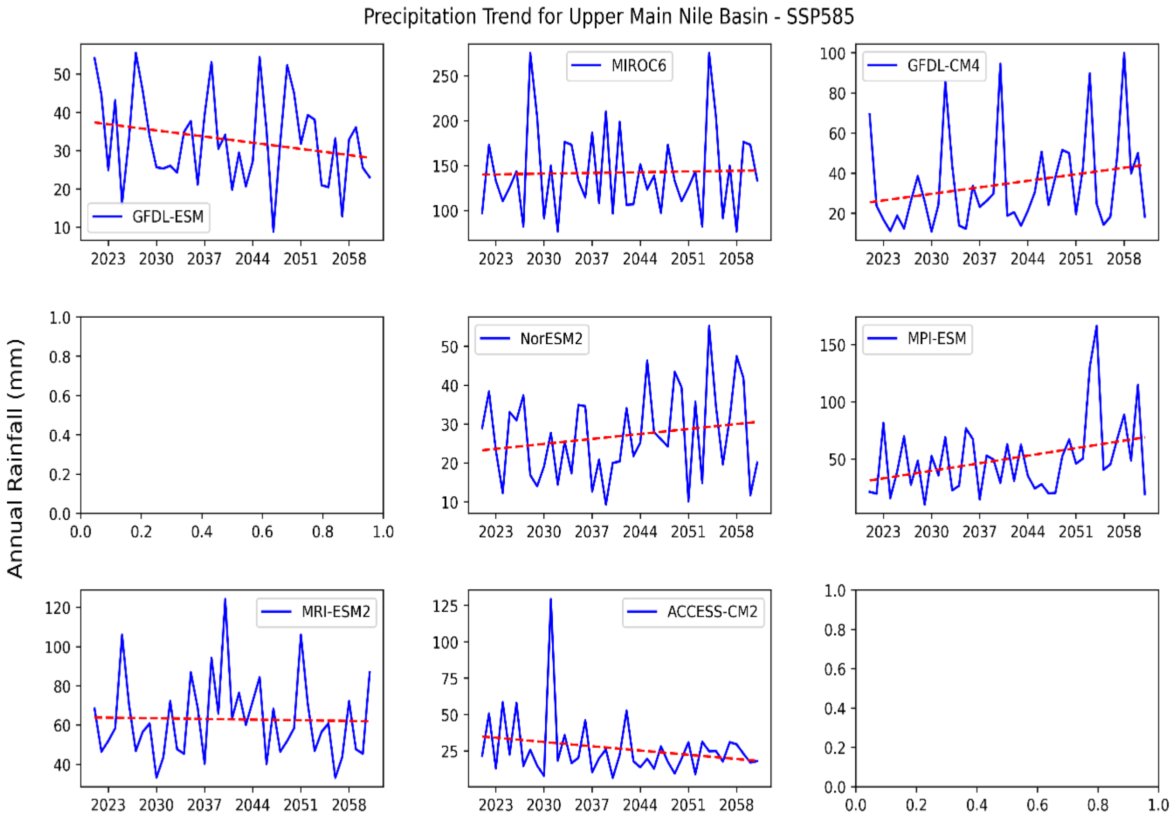

Figure 47: SSP585 Rainfall Projections trend for UMN

4.1.5. Lower Main Nile Basin (LMN)

As depicted in Figure 48, the primary season for the Lower Main Nile (LMN) basin is characterized by winter rainfalls occurring from October to January (ONDJ). Regrettably, with the exception of MPI-ESM, all models in the sub-basin fail to accurately capture the observed data pattern for LMN.

Figure 49 provides a comparison between observed data and CMIP6 models via scatter plots, revealing generally weak performances compared to CHIRPS. Despite weaker correlation scores and higher pbias values, lower RMSEs rank ACCESS-CM2 as the top-performing model over LMN, followed by GFDL-ESM and MPI-ESM, as indicated in Table 7. Conversely, MRI-ESM2 exhibits the poorest performance in this region.

The box plots among all models in the basin showcase numerous outliers, as illustrated in Figure 51, thus rendering analysis more challenging. Nonetheless, Figure 51 highlights that GFDL-ESM, followed by NorESM2-MM and ACCESS-CM2, closely align with the observed data. Unfortunately, assessing these models across projection scenarios proves arduous due to complexities observed in the box plots and aforementioned challenges. However, future projections of these models will undergo assessment using distribution fits and trend analysis to gain deeper insights about their projections.

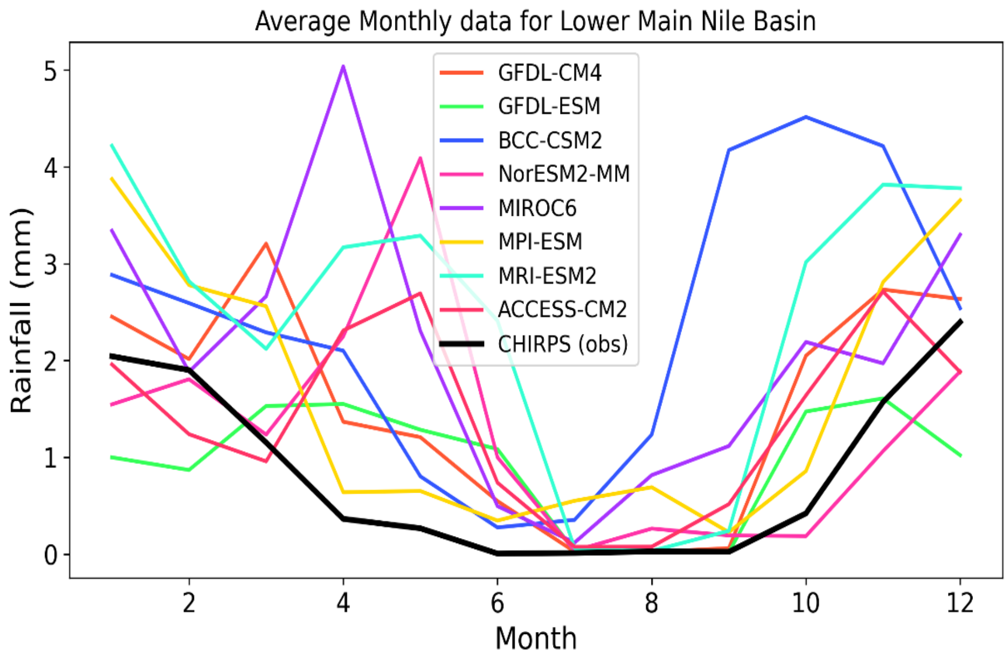

Figure 48: Average monthly data for Lower Main Nile Basin (Observed vs GCMs)

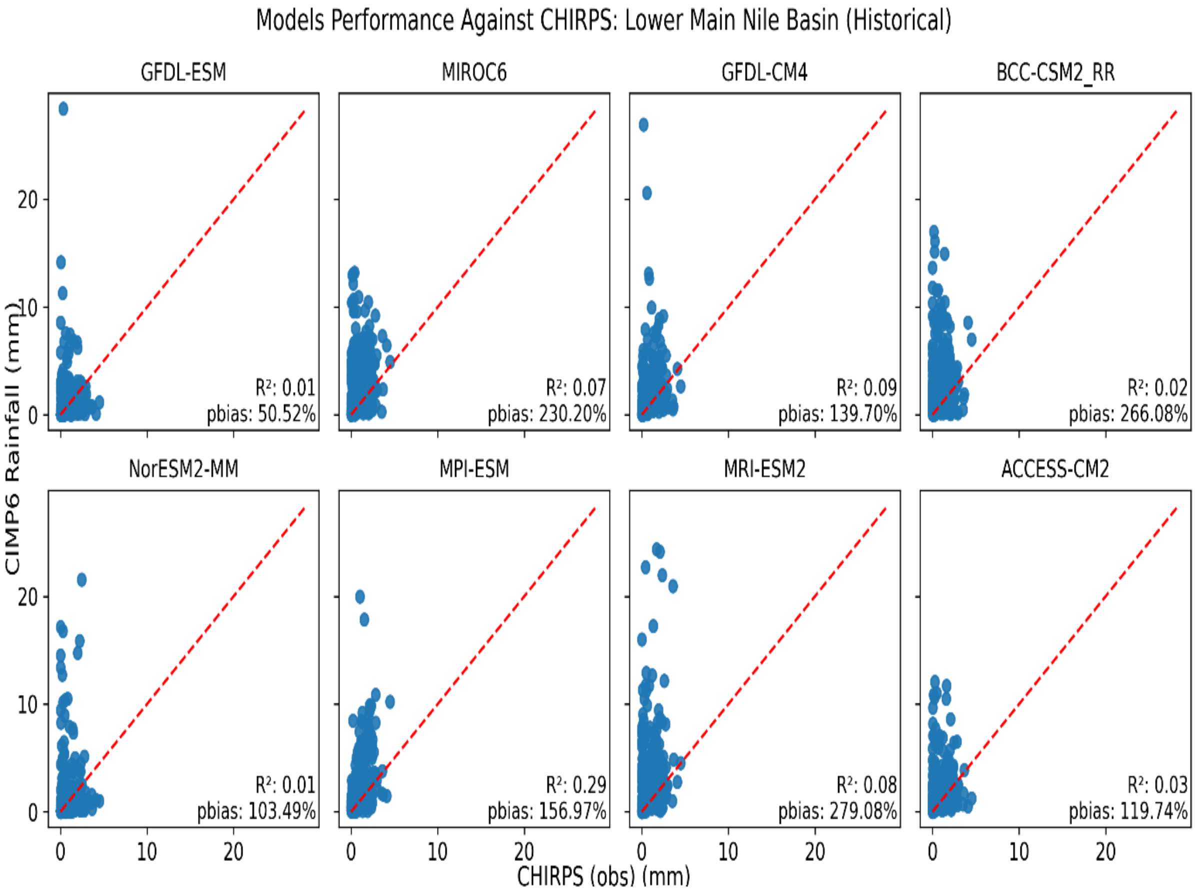

Figure 49: Models performance against CHIRPS using scatter plots - LMN

Table 7: Models ranking based on the statistical metrics - LMN

		Statistical Metrics					
Ranking	Model	R2	CC	NSE	PBIAS	RMSE	MAE
1	ACCESS-CM2	0.03	0.18	-5.97	119.74	2.45	1.36
2	GFDL-ESM	0.01	0.07	-6.36	50.52	2.51	1.12
3	MPI-ESM	0.29	0.54	-7.12	156.97	2.64	1.48
4	GFDL-CM4	0.09	0.30	-8.88	139.70	2.91	1.39
5	NorESM2-MM	0.01	0.10	-10.90	103.49	3.20	1.50
6	MIROC6	0.07	0.26	-11.32	230.20	3.25	2.05
7	BCC-CSM2-RR	0.02	0.13	-15.55	266.08	3.77	2.41
8	MRI-ESM2	0.08	0.29	-21.48	279.08	4.39	2.44

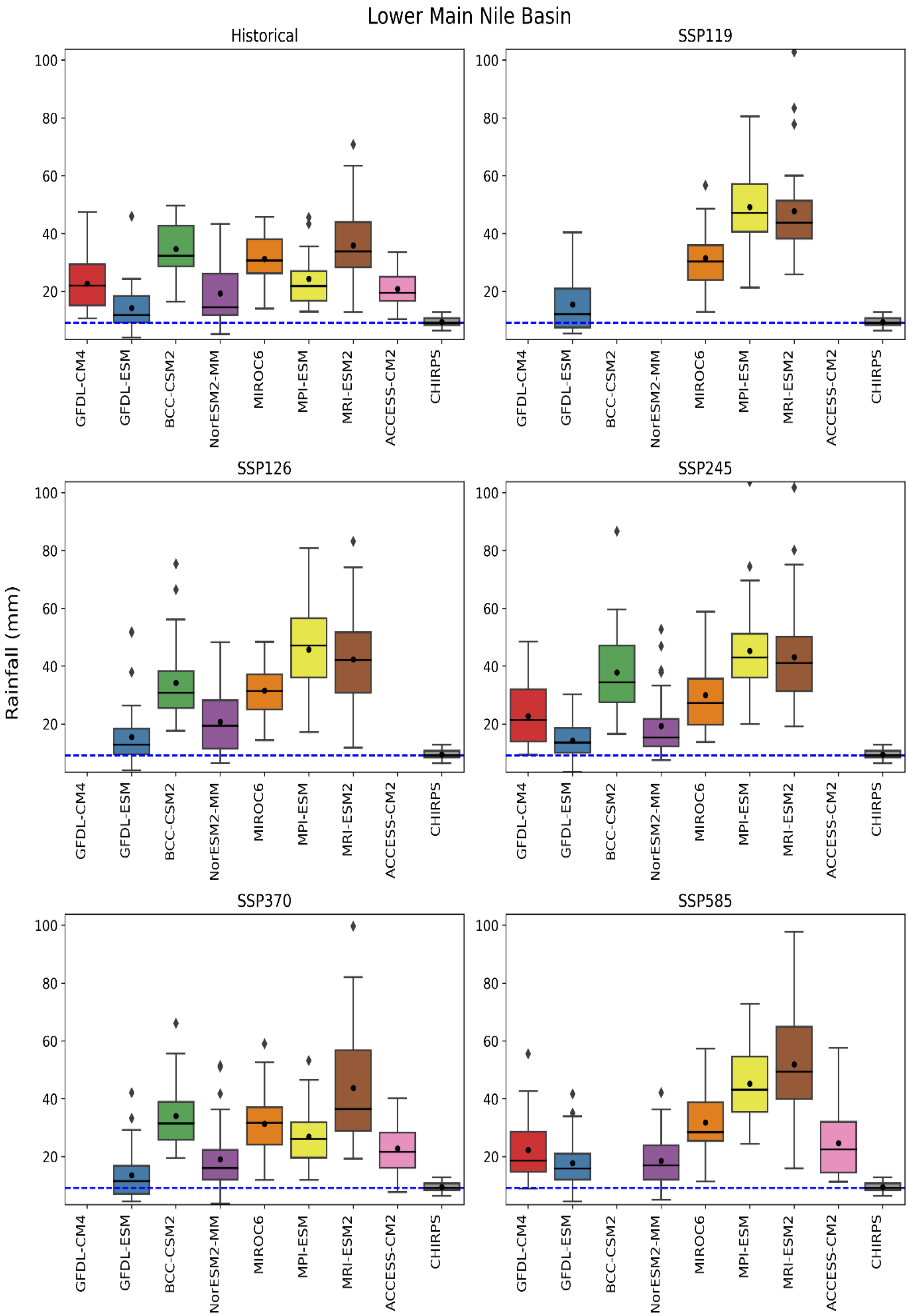

Figure 50: Box Plot Analysis for LMN Basin – Historical and Projection Scenarios Compared to CHIRPS – Annual Rainfall (mm)

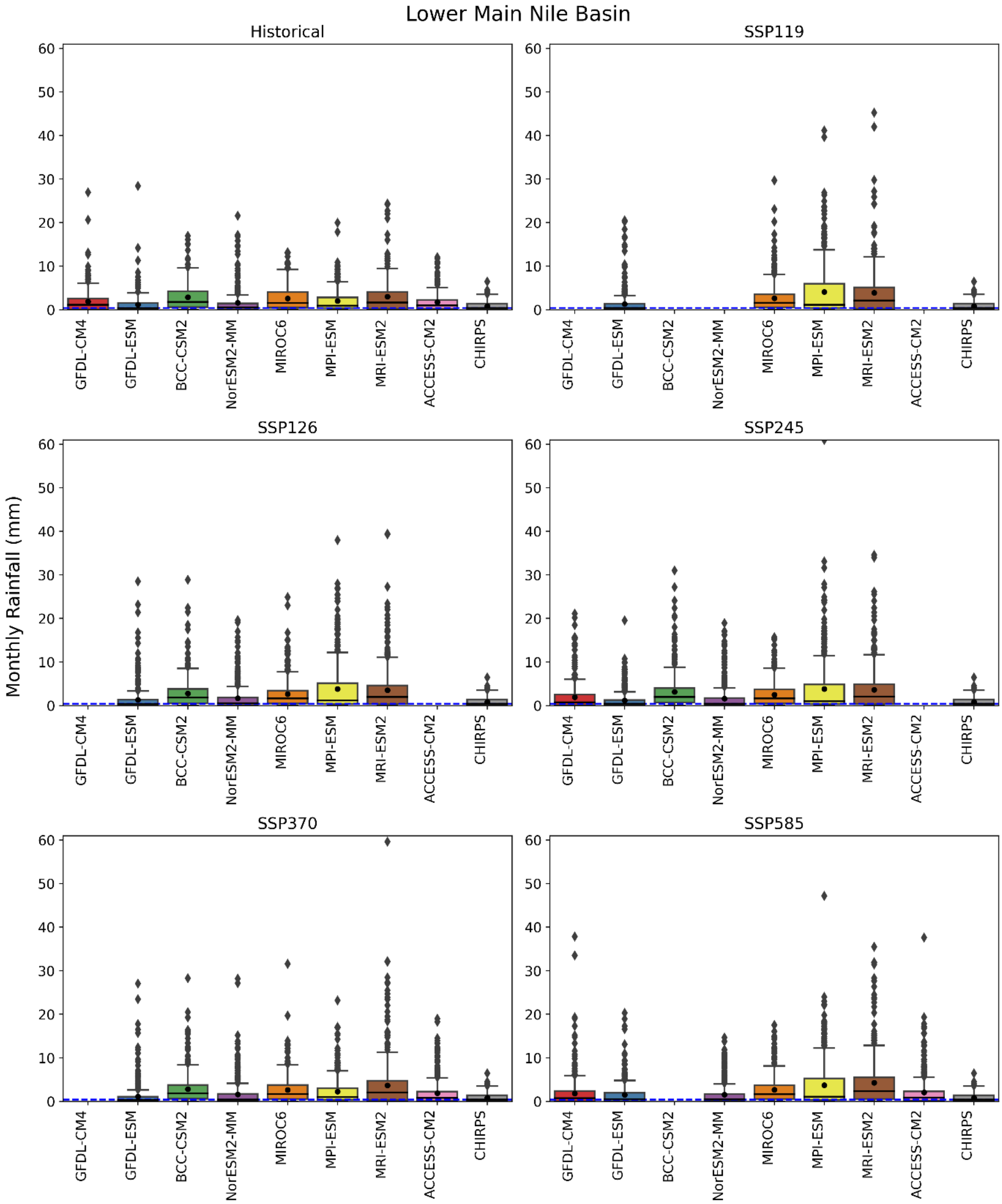

Figure 51: Box Plot Analysis for LMN Basin – Historical and Projection Scenarios Compared to CHIRPS – Monthly Rainfall (mm)

As shown in Figure 52, MPI-ESM illustrates a significant increase in means and a wider spread of data around the mean for both scenarios SSP245 and SSP585, albeit with lower frequency occurrences. Conversely, ACCESS-CM2 indicates no change in means for SSP370, albeit less frequently observed, while displaying an exponential trend with decreasing means occurring more frequently for SSP585.

GFDL-ESM exhibits increasing shifts in means with higher frequency for SSP245, while the probability decreases for SSP585.

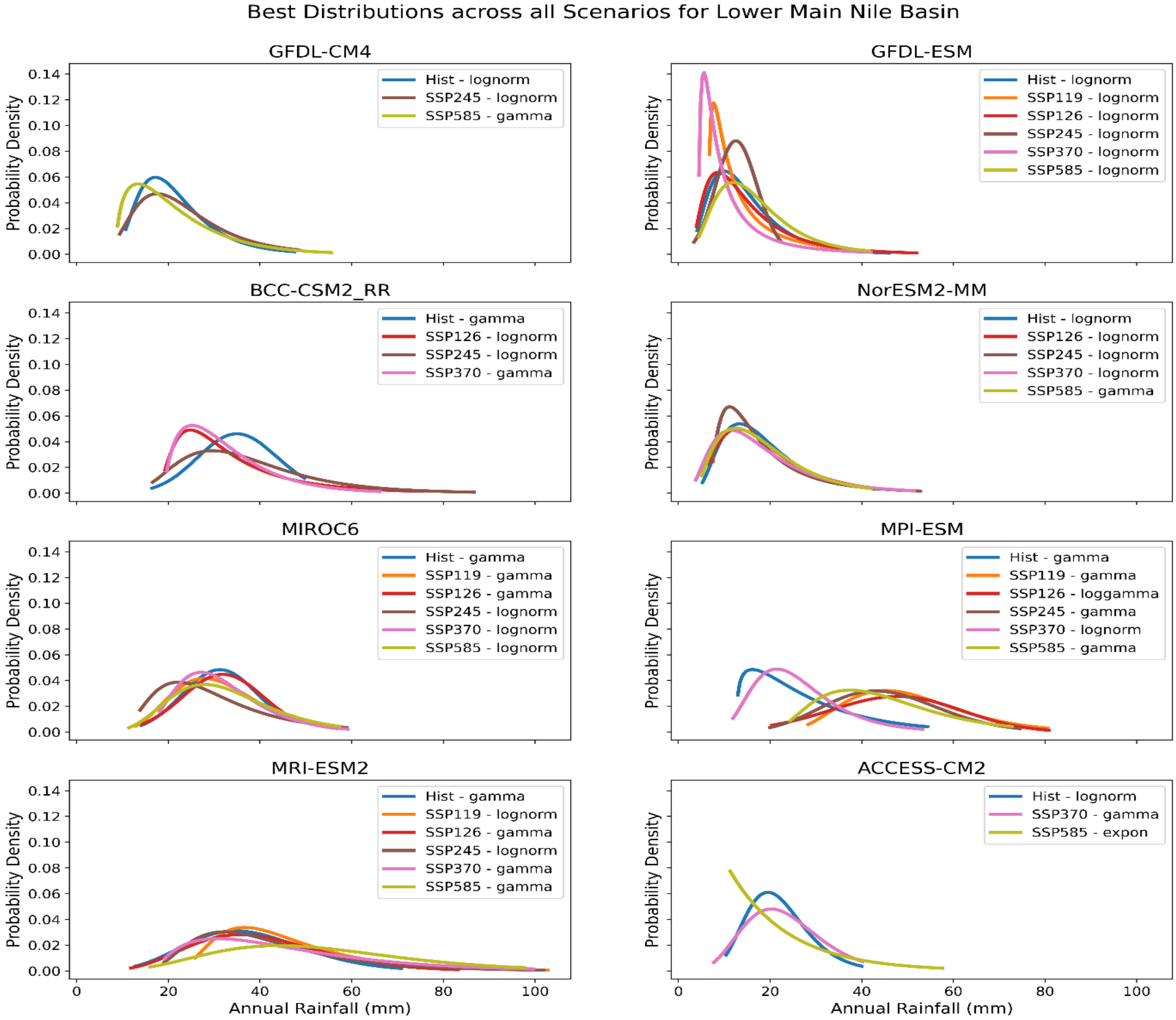

Figure 52: Best Distributions for all scenarios across the LMN compared to the observed

Figures 42-47 offer valuable insights into the historical and future trends, variability, and uncertainties within the Upper Main Nile Basin. Among the historical scenarios analysed from different GCMs, 37.5% indicate an increasing trend, while only two models suggest no change in trends. Moreover, 37.5% of the models exhibit a decreasing trend, consistent with the trend observed in CHIRPS data. Notably, the uncertainty analysis reveals varying trends among the top-performing models historically. For instance, ACCESS-CM2 indicates a decreasing trend, GFDL-ESM suggests an increasing trend, while MPI-ESM indicates no change in the trend. Remarkably, among the top-performing models over LMN, GFDL-ESM suggests a decreasing trend, whereas MPI-ESM indicates a slight increase for the SSP245 scenario. Looking ahead to the SSP585 scenario, both MPI-ESM and ACCESS-CM2 predict decreasing trends in the future, while GFDL-ESM forecasts a slight increase. These findings underscore the complexity and variability of future climate trends projected by different models, highlighting the need for comprehensive assessment and interpretation in climate research.

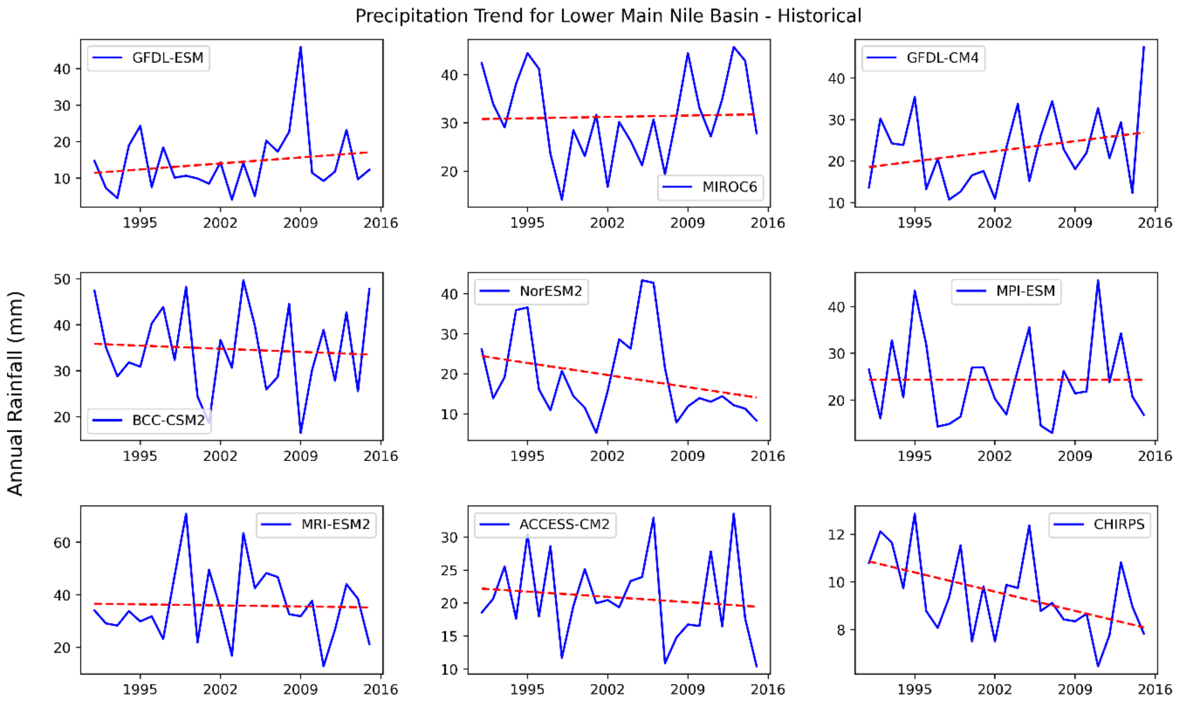

Figure 53: Historical Rainfall trends for LMN

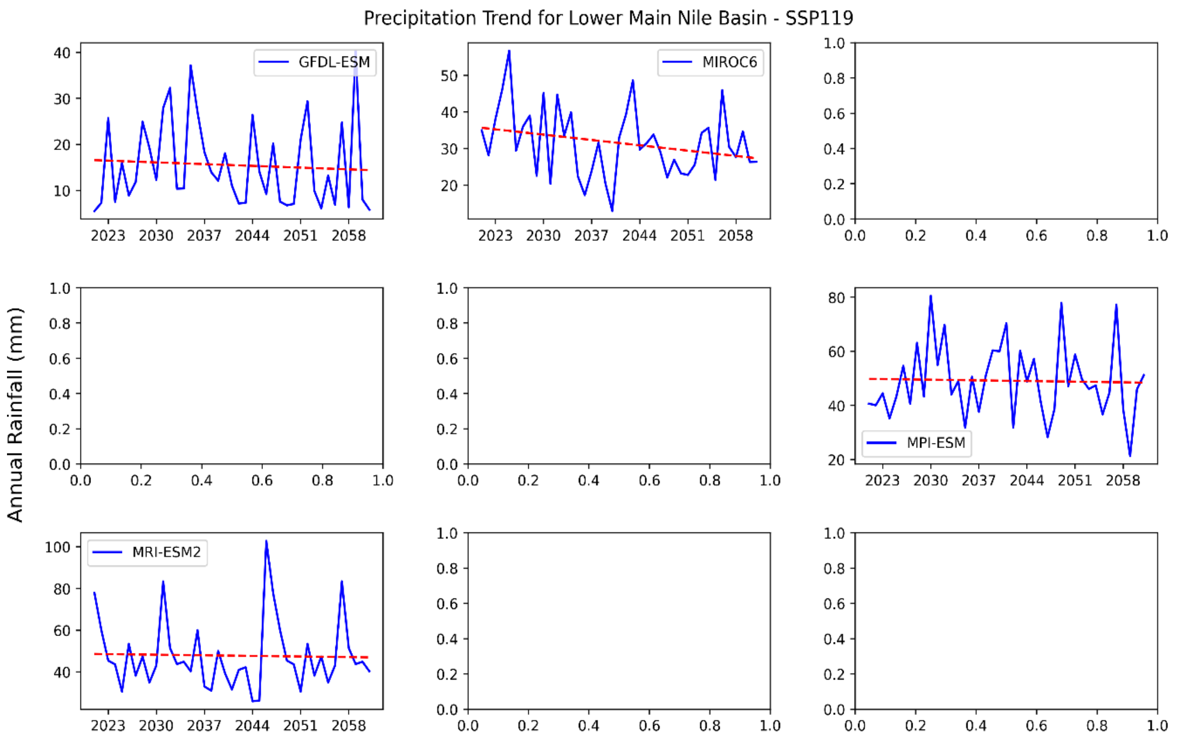

Figure 54: SSP119 Rainfall Projections trend for LMN

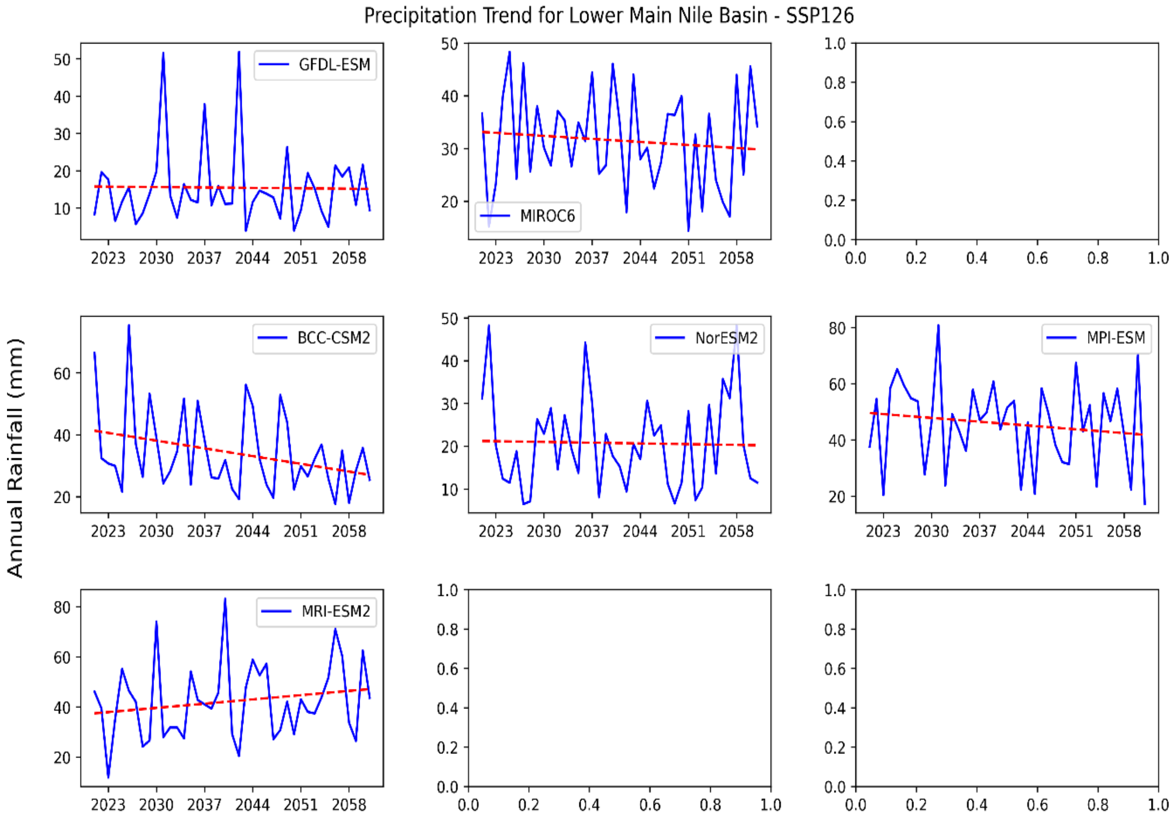

Figure 55: SSP126 Rainfall Projections trend for LMN

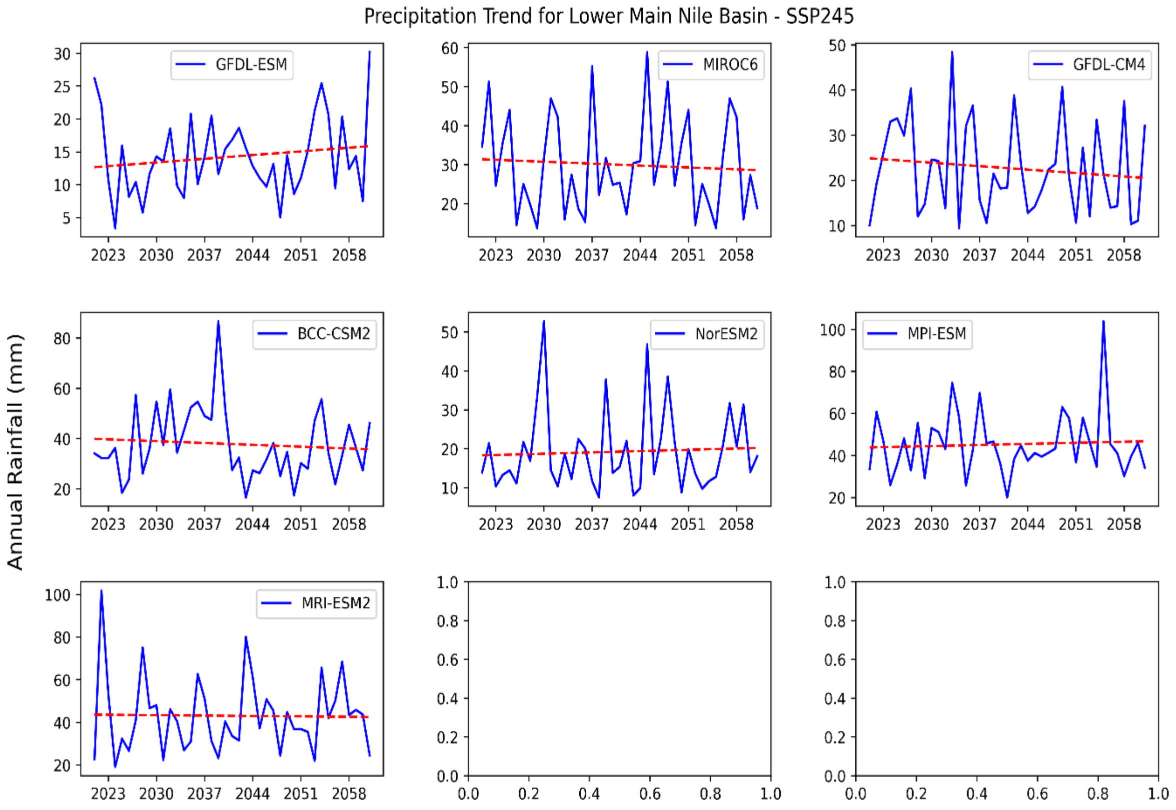

Figure 56: SSP245 Rainfall Projections trend for LMN

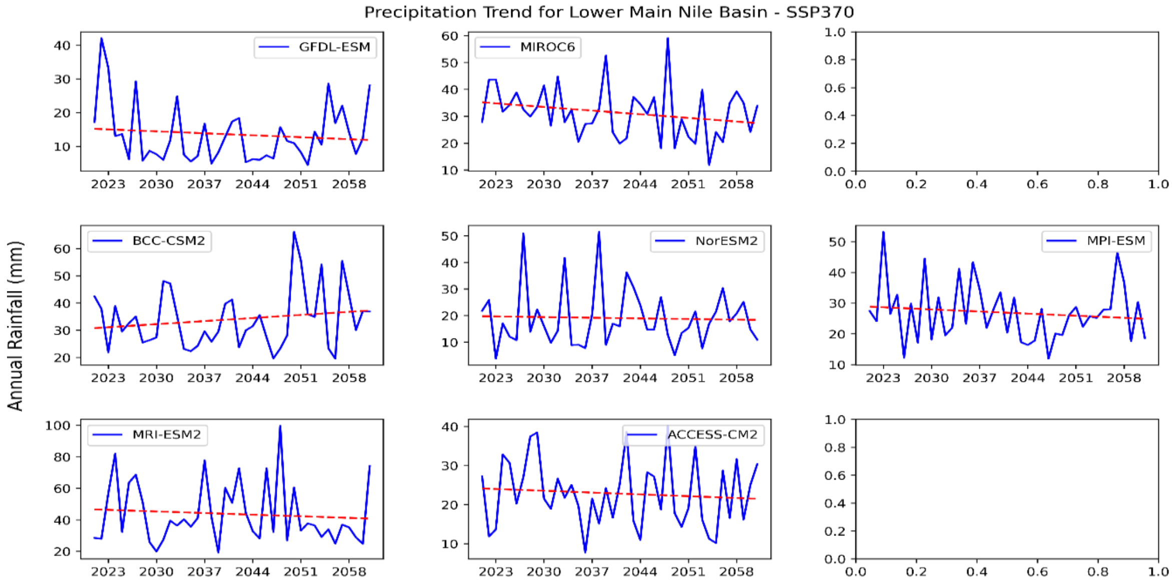

Figure 57: SSP370 Rainfall Projections trend for LMN

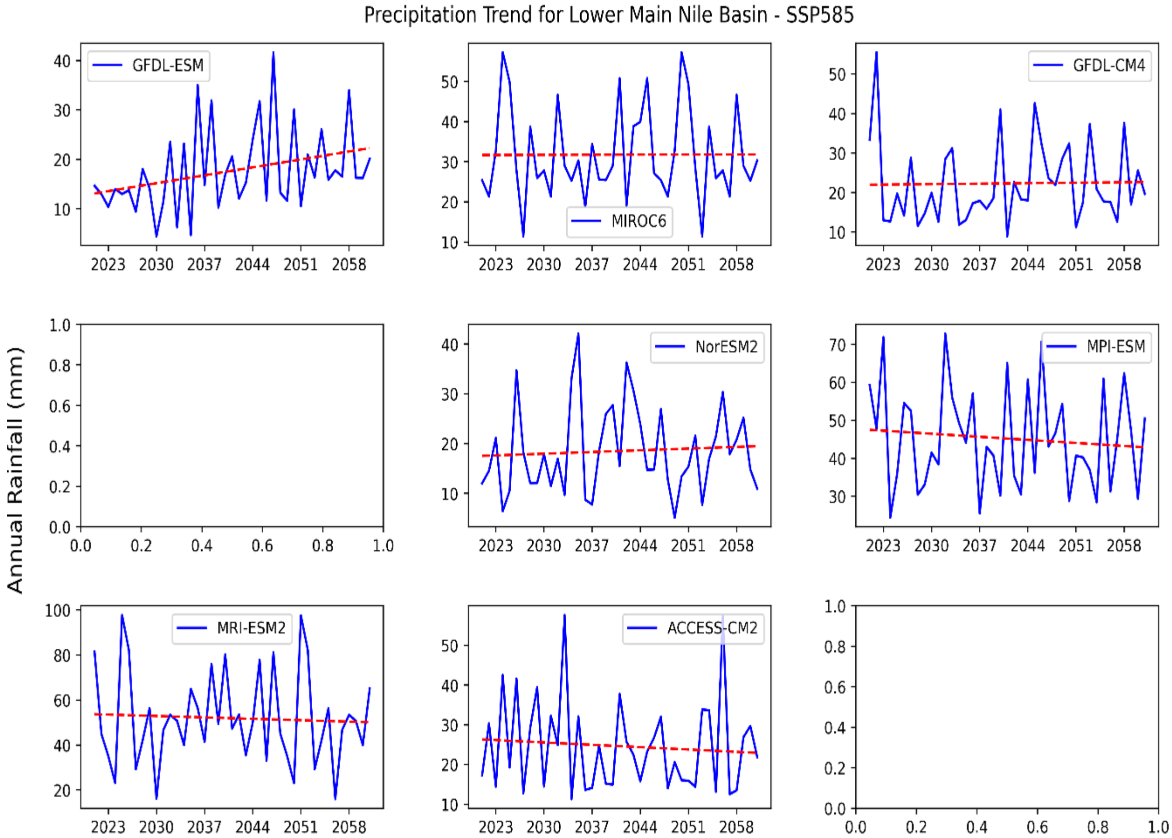

Figure 58: SSP585 Rainfall Projections trend for LMN

4.2. Spatial Anomaly Analysis:

Spatial anomaly mapping and analysis have been employed in this study to examine the spatio-temporal rainfall dynamics within the Eastern Nile Basin across all GCMs utilized, spanning the years 1990 to 2060. This comprehensive analysis encompasses both historical and projected scenarios. However, it is essential to acknowledge the inherent uncertainties and biases associated with projected rainfall data derived from GCMs. In this study, the spatial anomaly analysis entailed a particular examination of historical rainfall data, where the mean rainfall was computed for each five-year interval. Similarly, for projection scenarios, the mean rainfall was assessed over every seven-year periods. Subsequently, the spatial anomaly was calculated by subtracting the five or seven-year averages from thier long-term averages, thus offering additional insights into spatio-temporal patterns and rainfall variability over the ENB.

Upon analysing Figures 59-64, it becomes apparent that there is a notable level of uncertainty present across all models, alongside significant spatio-temporal variability within the ENB. However, certain models portray normal conditions, while others depict wet or dry conditions for the same period and scenario. This divergence underscores the complexity inherent in predicting future rainfall patterns and highlights the need for further investigation and refinement in modeling techniques to better understand and anticipate regional climate dynamics.

However, under the SSP245 scenario, BCC-CSM2 indicated generally normal to wet spells across the basin, except for limited areas in BAS showing dry spells until 2043. Subsequently, a seven-year period of generally normal conditions prevailed across the basin with some dry signs in different areas, followed by an extreme seven-year dry spell, especially over the BN and BAS. GFDL-CM4 introduced seven years of wet conditions for the upstream basins followed by a normal period with some extreme dry signs in the most upstream areas of BAS and BN. This period was followed by a dry period, especially in TSA, with the basin recovering in the subsequent years, experiencing variations between normal and wet conditions up to 2060. GFDL-ESM initiated with a wet spell for the first seven years, followed by dry conditions for the next 15 years with some wet spells, returning to normal in the subsequent 15 years. MPI-ESM introduced dry conditions for the initial seven years, transitioning to wet to normal conditions in intermediate periods, and then returning to normal with some extreme dry signs. Nor-ESM2-MM generally introduced wet conditions in the first period, contrasting MPI-ESM, while sharing similar conditions in the other periods up to 2060.

Furthermore, under the SSP585 scenario, GFDL-CM4 introduced continuous moderate wet spells over the upstream basin of the ENB from 2020 to 2035, followed by normal to moderate dry spells in the upstream basins of ENB from 2036 to 2060. GFDL-ESM introduced a wet spell in the first seven years, followed by moderate seven dry years with minor wet signs over the BAS basin, normal conditions in TSA, BN, UMN, LMN, with dry spells in the following seven years over BAS. The basin then recovered over the following 15 years to normal conditions with some wet spells in the BAS basin. MPI-ESM introduced normal to wet conditions over the basin up to 2043, transitioning to normal to dry conditions for the rest of the years up to 2060. Nor-ESM2-MM generally introduced highly spatial rainfall variability over the basins of ENB among all periods, varying from normal to dry to wet conditions between the basins across the periods.

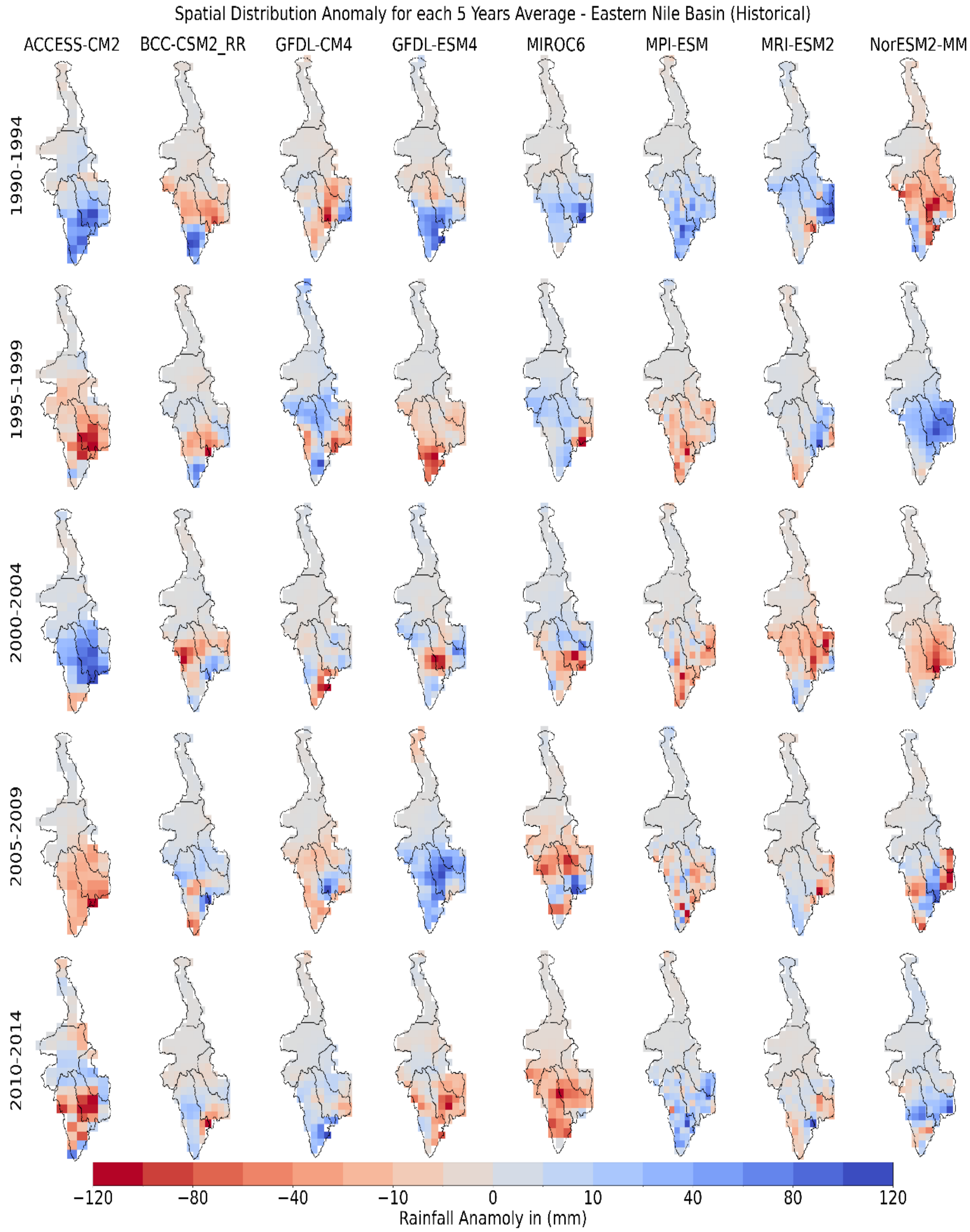

Figure 59: Spatial Distribution Anomaly for each 5 Years Average - Eastern Nile Basin (Historical)

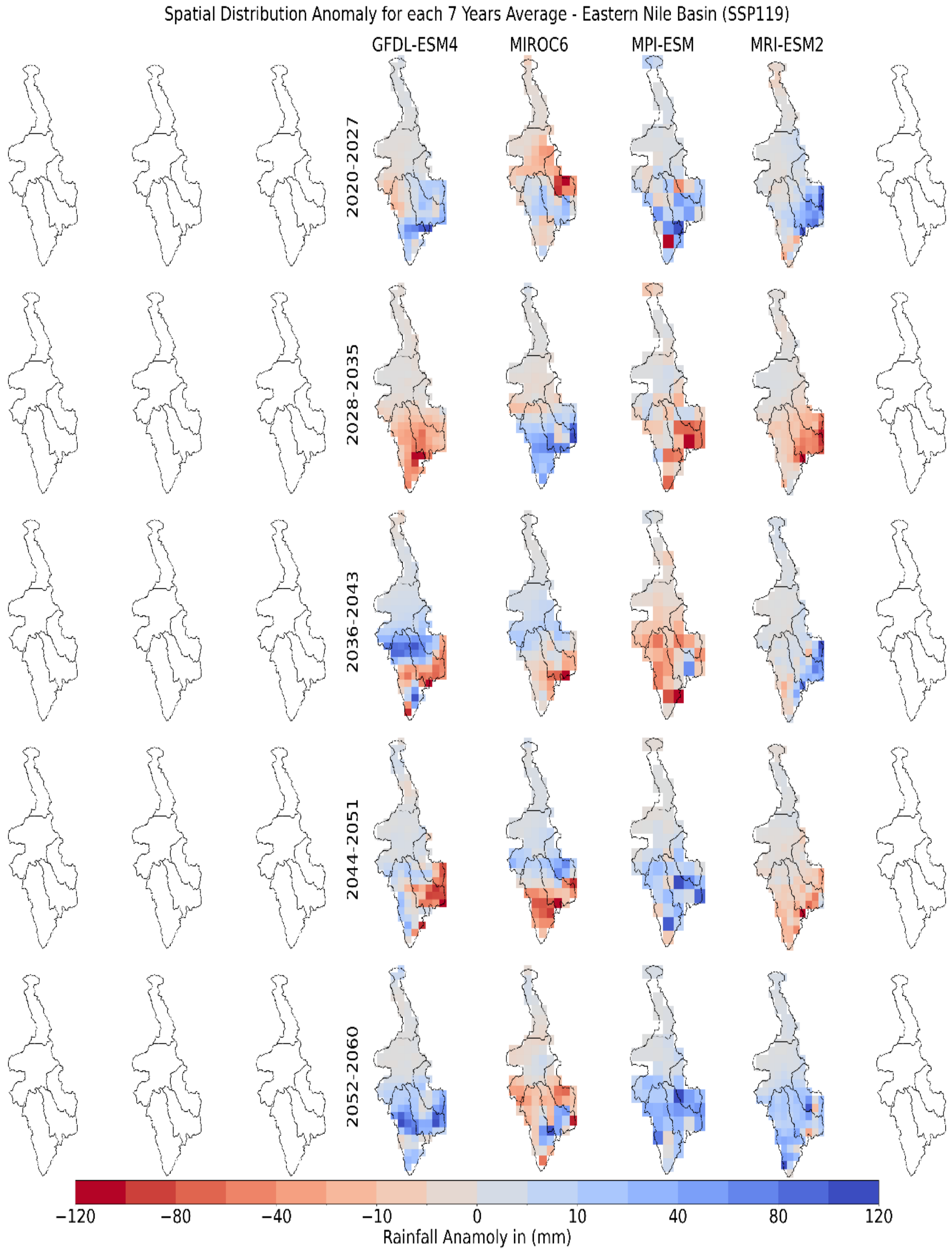

Figure 60: Spatial Distribution Anomaly for each 7 Years Average - Eastern Nile Basin (SSP119)

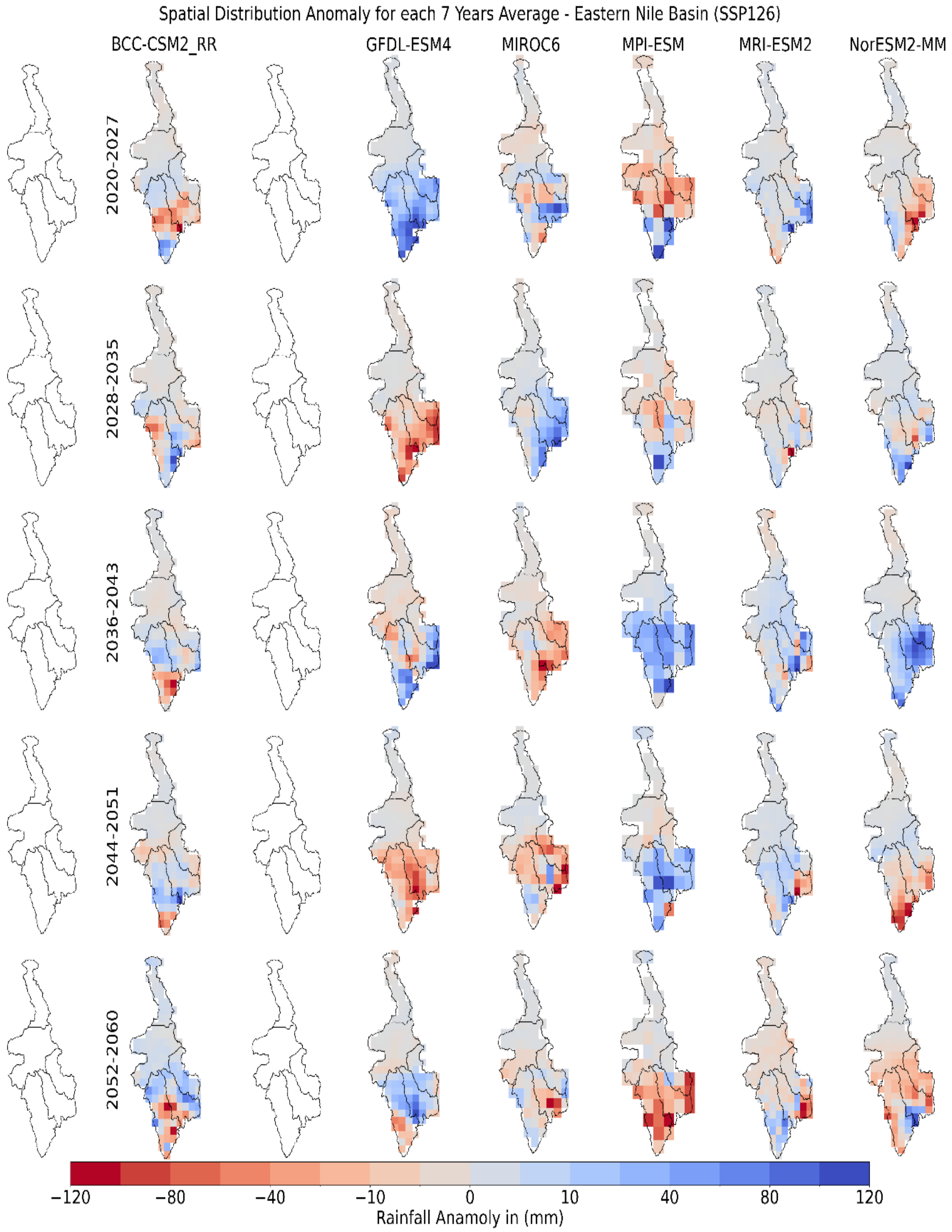

Figure 61: Spatial Distribution Anomaly for each 7 Years Average - Eastern Nile Basin (SSP126)

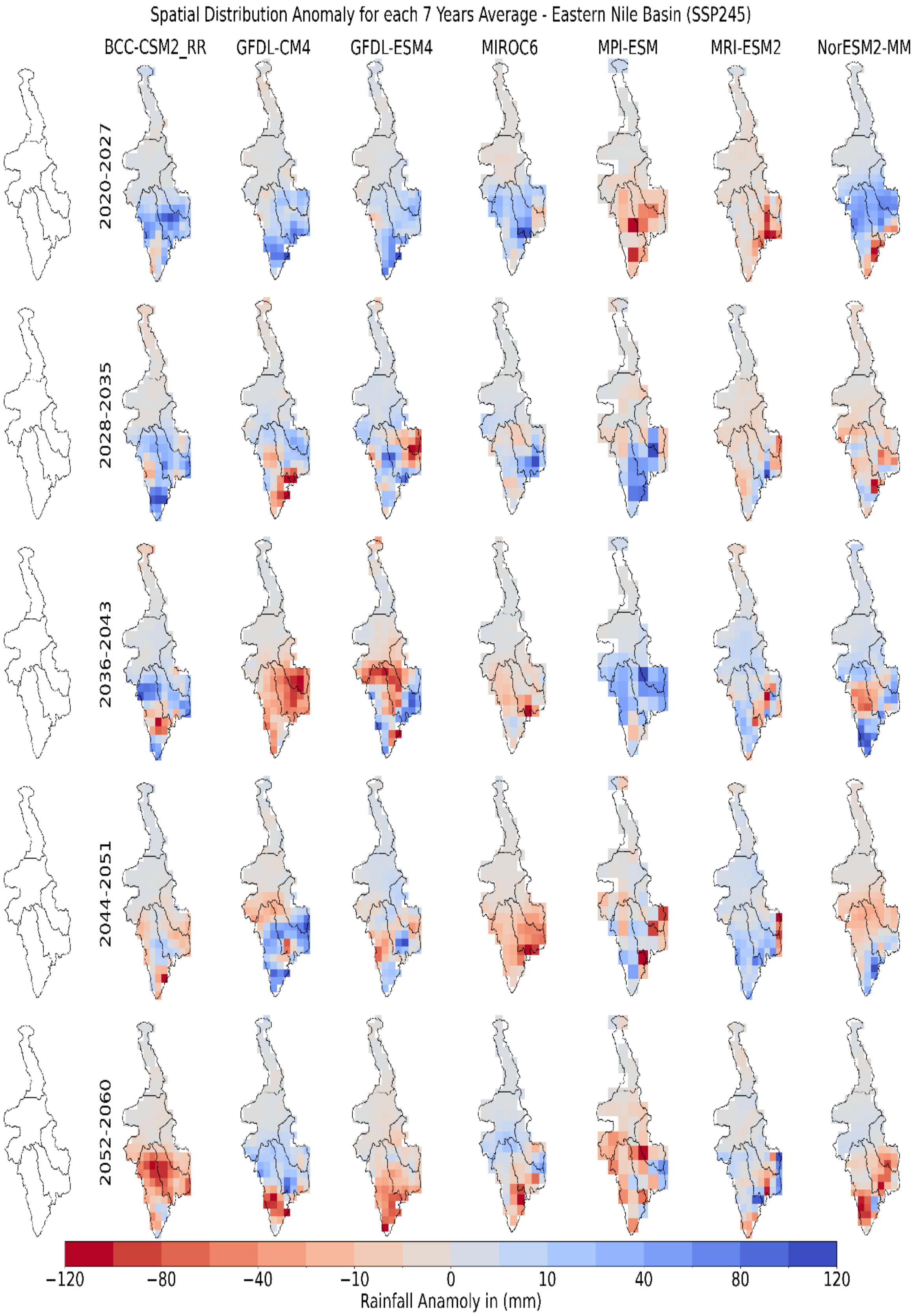

Figure 62: Spatial Distribution Anomaly for each 7 Years Average - Eastern Nile Basin (SSP245)

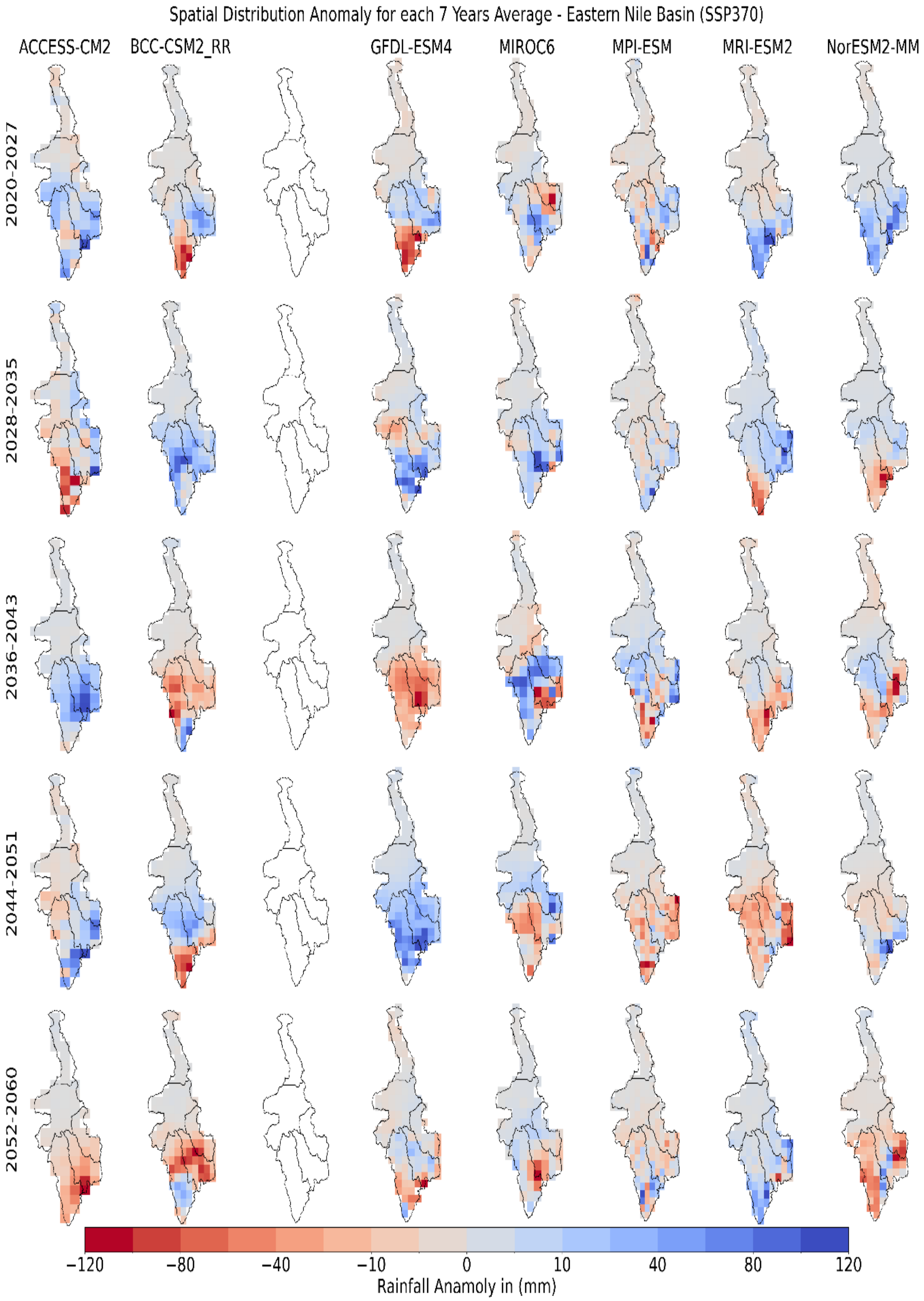

Figure 63: Spatial Distribution Anomaly for each 7 Years Average - Eastern Nile Basin (SSP370)

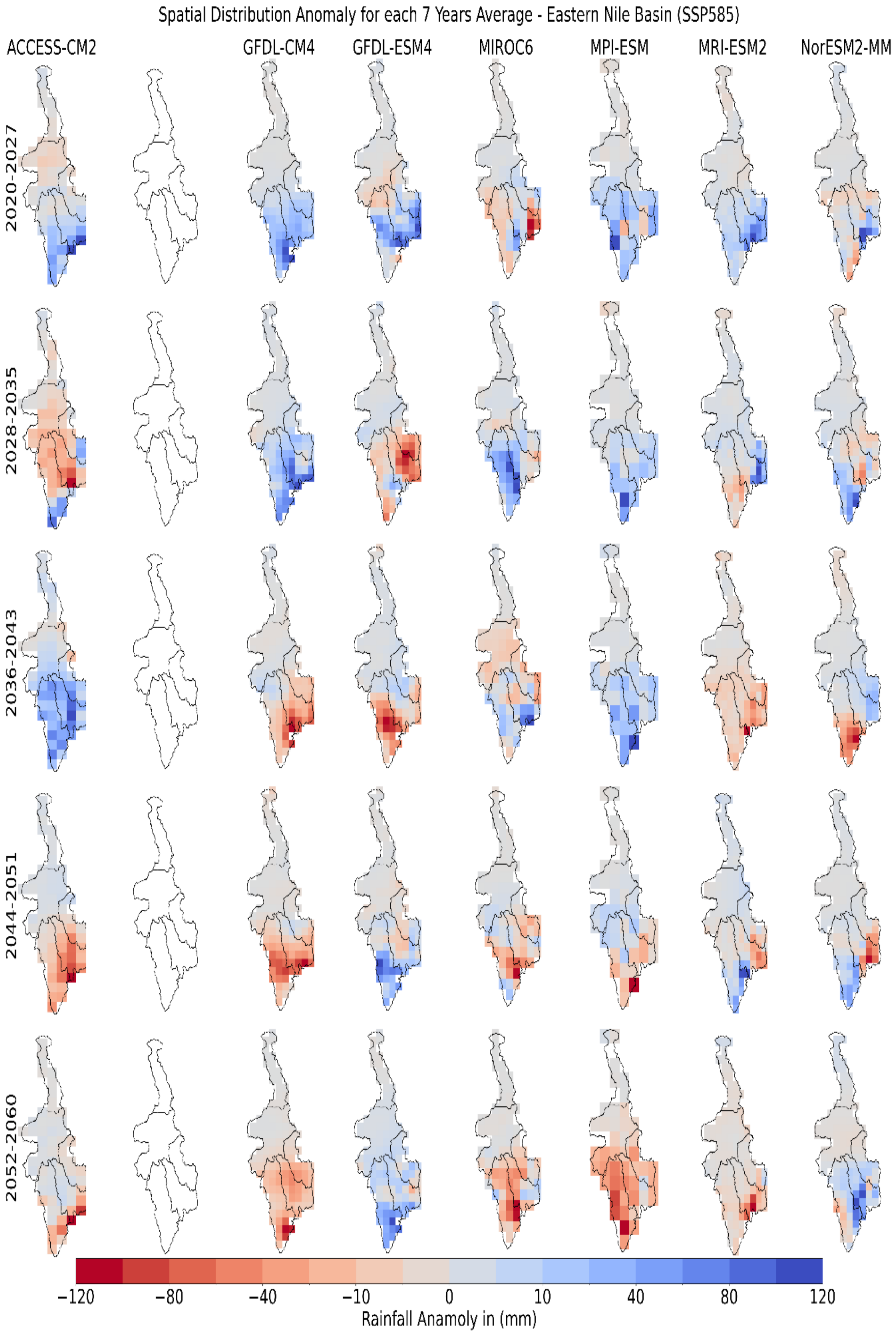

Figure 64: Spatial Distribution Anomaly for each 7 Years Average - Eastern Nile Basin (SSP585)

5.0 Conclusions and Recommendations

5.1. Conclusions

In this study, eight CIMP6 climate models were comprehensively evaluated across the sub-basins of the Eastern Nile Basin, using observed data from CHIRPS due to a scarcity of ground data in the region, given that CHIRPS dataset demonstrates strong agreement with ground observations across various climatic zones worldwide, including outstanding performance in the ENB region. The selection process for the models was meticulous, with four chosen for their global prevalence and broad applicability, namely MIROC6, ACCESS-CM2, MPI-ESM, and MRI-ESM2. The remaining four models, namely GFDL-CM4, GFDL-ESM, NorESM2-MM, and BCC-CSM2, were selected based on an exhaustive literature survey that demonstrated their superior performance across the region.

The evaluation aimed to identify the top-performing CIMP6 models across the ENB sub-basins. Various statistical and spatial analysis techniques were employed to extract essential insights into rainfall trends and projections. Efforts were made to establish meaningful correlations between current observations and anticipated future projections derived from the evaluation of rainfall trends.

However, the seasonal patterns of rainfall for each sub-basin were consistently observed across most of the models, especially in BAS, BN, and TSA, where most models accurately captured the patterns. Nonetheless, some models exhibited overestimation or underestimation compared to the observed data. However, this underscores the significance of the models' ability to capture seasonality, reflecting the sound climatic and physical assumptions embedded within their simulations. The observed deviations, though, can be addressed through bias correction techniques, thereby enhancing the models' accuracy and reliability in representing real-world climatic conditions.

However, the performance of various CMIP6 models varied significantly across the Baro Akobo Sobat Basin (BAS), Blue Nile Basin (BN), Tekeze Setit Atbara Basin (TSA), Upper Main Nile Basin (UMN), and Lower Main Nile Basin (LMN). In BAS, MIROC6 exhibited the best performance, closely followed by NorESM2-MM and MPI-ESM, as evidenced by good statistical metrics such as the lowest RMSE, lowest pbias, and highest R2. Conversely, in the BN, GDFL-CM4 led the pack, followed by GFDL-ESM and BCC-CSM2. Over the TSA region, NOR-ESM2-MM demonstrated superior performance, followed by GFDL-CM4 and GFDL-ESM. Moving to the UMN basin, MPI-ESM emerged as the top-performing model, trailed by NOR-ESM2-MM and GFDL-ESM. Meanwhile, ACCESS-CM2, GFDL-ESM, and MPI-ESM were the top performers over the LMN basin. It's worth noting that the correlation between the models and observed data was notably poor over the UMN and LMN basins, with relatively higher pbias and RMSEs observed.

In terms of data characteristics and distribution across quarterly intervals, GFDL-CM4, GFDL-ESM, and Nor-ESM2-MM demonstrated alignment with the median of observed data, as well as sharing similar spread and distribution over quartiles in the BAS basin. Likewise, for the BN basin, GFDL-CM4, GFDL-ESM, and Nor-ESM2-MM closely mirrored the observed data in terms of quartile distribution. BCC-CSM2, MPI-ESM, and ACCESS-CM2 exhibited a close fit to observed data in the TSA basin, showing congruence in median and quartile distribution. However, both UMN and LMN basins revealed numerous outliers in monthly assessments. Despite this, BCC-CSM2, followed by GFDL-CM4 and GFDL-ESM, performed well in the UMN basin, while ACCESS-CM2, followed by GFDL-ESM and MPI-ESM, demonstrated superior performance in the LMN basin.

Furthermore, all statistical assessments were conducted on a monthly basis to ensure the preservation of data seasonality in the analysis. Nevertheless, it was observed that the general correlations, symmetry, distribution, and variability of models data varied across different timescales (i.e. daily, monthly, annually), indicating the need for further investigation and research into these fluctuations. These findings underscore the complexity of model-data interactions and emphasize the importance of refining analytical approaches to better understand and interpret climate model outputs across various temporal scales.

Ultimately, it is evident that the models selected based on their superior performance in the extensive literature survey across the region, namely GFDL-CM4, GFDL-ESM, NorESM2-MM, and BCC-CSM2, along with MPI-ESM, consistently appeared frequently among the top-performing models for each ENB sub basins based on statistical metrics and data symmetry and distribution compared to observed data. Consequently, this study lends further support to existing literature regarding their performance and recommends researchers to consider utilizing them for different applications in the Eastern Nile Basin region, particularly in the TSA, BAS, and BN basins, which collectively represent the majority of the Eastern Nile Basin's contribution. These models exhibit promising potential for accurately capturing regional climate dynamics and can serve as valuable tools for informed decision-making and water resource management in the Eastern Nile Basin and beyond.

However, future projections up 2060 were also assessed among all models across all scenarios. Drawing from the top-performing models across the Eastern Nile Basin (ENB) basins, including GFDL-CM4, GFDL-ESM, BCC-CSM2, Nor-ESM2, and MPI-ESM, a notable trend emerges regarding future rainfall projections. For the likely SSP scenario SSP245, 80% of the models project an increasing rainfall trend up to 2060, with only one model suggesting no change in trends. Conversely, for the more pessimistic SSP scenario, SSP585, 50% of the models suggest a significant increasing trend, 25% indicate a slight decreasing trend, and another 25% foresee no change in trends by 2060 for the BAS basin.

In the BN basin, 60% of the top-performing models anticipate significant increasing trends for SSP245, while 40% indicate no change in trends. This pattern is mirrored in the TSA basin for the SSP245. For SSP585 over the BN basin, 50% of the models indicate significant increasing trends, while an equal proportion suggests slight decreasing trends. Similarly, in the TSA basin for SSP585, 75% of the models anticipate significant increasing trends, while 25% indicate slight decreasing trends.

Moving to the UMN basin, all models foresee increasing trends for SSP245, while 75% of the models project increasing trends for SSP585. Interestingly, only one model indicates decreasing trends for the UMN basin over SSP585. In the LMN basin, for SSP245, 60% of the models suggest increasing trends, while 40% suggest decreasing trends. However, for SSP585 over the LMN basin, 75% of the models suggest increasing trends, with only one model indicating slight decreasing trends. However, and conclusively, the performance of the top 5 models over the ENB was assessed, and their projected trends were scrutinized to assess the probability of increasing, decreasing, or unchanged trends across the basins for both SSP245 and SSP585 scenarios, as presented in Table 8. Moreover, the average of these top 5 models was employed to visualize the projected scenarios across all ENB sub-basins, as depicted in Figures 65-69. The ultimate finding suggests that all ENB sub-basins are anticipated to undergo an increasing trend in rainfall up to 2060.

Moreover, in this study, Spatial anomaly mapping and analysis offered valuable insights into the spatio-temporal dynamics and variability of rainfall within the Eastern Nile Basin, shedding light on significant variability and uncertainty across all models and scenarios. However, under the SSP245 scenario, BCC-CSM2 indicated generally normal to wet spells across the basin, except for limited areas in BAS showing dry spells until 2043. Subsequently, a seven-year period of generally normal conditions prevailed across the basin with some dry signs in different areas, followed by an extreme seven-year dry spell, especially over the BN and BAS. GFDL-CM4 introduced seven years of wet conditions for the upstream basins followed by a normal period with some extreme dry signs in the most upstream areas of BAS and BN. This period was followed by a dry period, especially in TSA, with the basin recovering in the subsequent years, experiencing variations between normal and wet conditions up to 2060. GFDL-ESM initiated with a wet spell for the first seven years, followed by dry conditions for the next 15 years with some wet spells, returning to normal in the subsequent 15 years. MPI-ESM introduced dry conditions for the initial seven years, transitioning to wet to normal conditions in intermediate periods, and then returning to normal with some extreme dry signs. Nor-ESM2-MM generally introduced wet conditions in the first period, contrasting MPI-ESM, while sharing similar conditions in the other periods up to 2060.

Furthermore, under the SSP585 scenario, GFDL-CM4 introduced continuous moderate wet spells over the upstream basin of the ENB from 2020 to 2035, followed by normal to moderate dry spells in the upstream basins of ENB from 2036 to 2060. GFDL-ESM introduced a wet spell in the first seven years, followed by moderate seven dry years with minor wet signs over the BAS basin, normal conditions in TSA, BN, UMN, LMN, with dry spells in the following seven years over BAS. The basin then recovered over the following 15 years to normal conditions with some wet spells in the BAS basin. MPI-ESM introduced normal to wet conditions over the basin up to 2043, transitioning to normal to dry conditions for the rest of the years up to 2060. Nor-ESM2-MM generally introduced highly spatial rainfall variability over the basins of ENB among all periods, varying from normal to dry to wet conditions between the basins across the periods.

Table 8: Future projections for all the ENB sub-basins across the scenarios SSP245 and SSP585

	Scenario: SSP245					Scenario: SSP585				
Trend	BAS	BN	TSA	UMN	LMN	BAS	BN	TSA	UMN	LMN
Increasing	80%	60%	60%	100%	60%	50%	50%	75%	75%	75%
Decreasing					40%	25%	50%	25%	25%	25%
No-Change	20%	40%	40%			25%				
Conclusion	Increasing	Increasing	Increasing	Increasing	Increasing	Increasing	Not Clear	Increasing	Increasing	Increasing

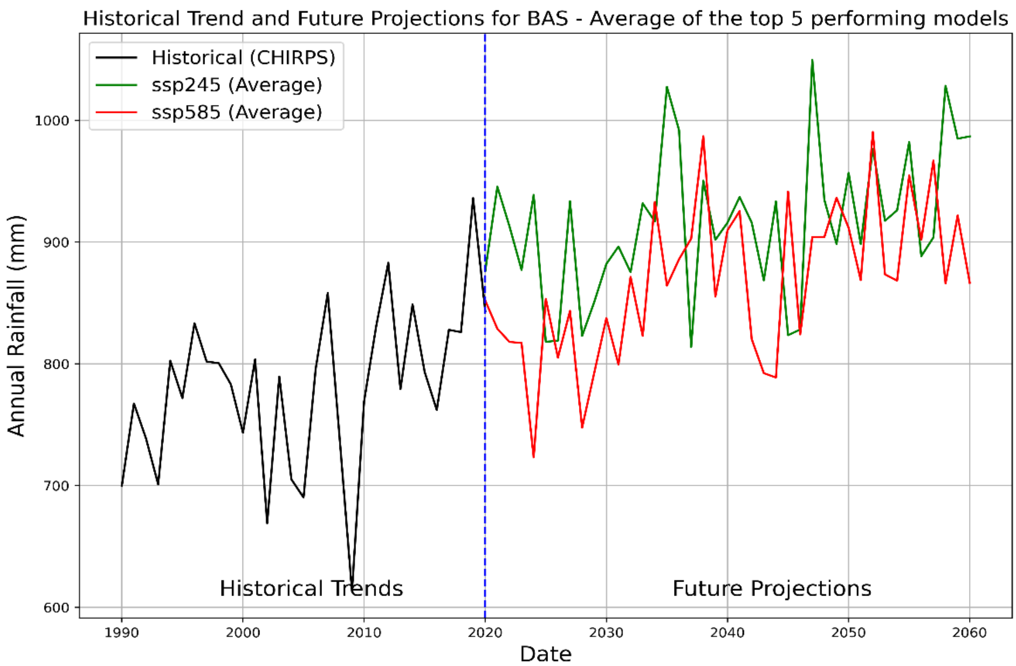

Figure 65: Historical Trend and Future Projections for the Baro Akobo Sobat Basin - Average of the top 5 performing models for SSPs

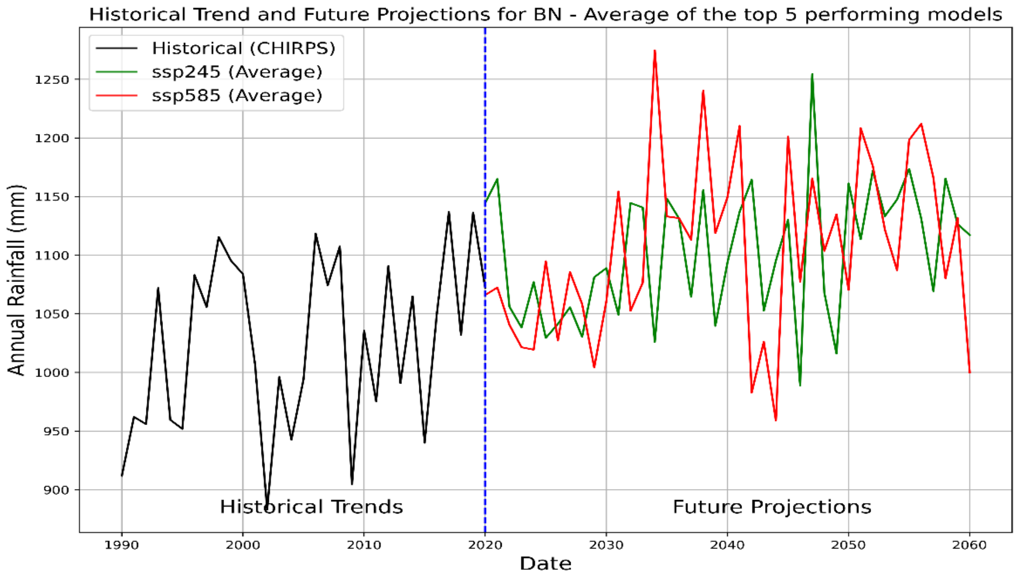

Figure 66: Historical Trend and Future Projections for the Blue Nile Basin - Average of the top 5 performing models for SSPs

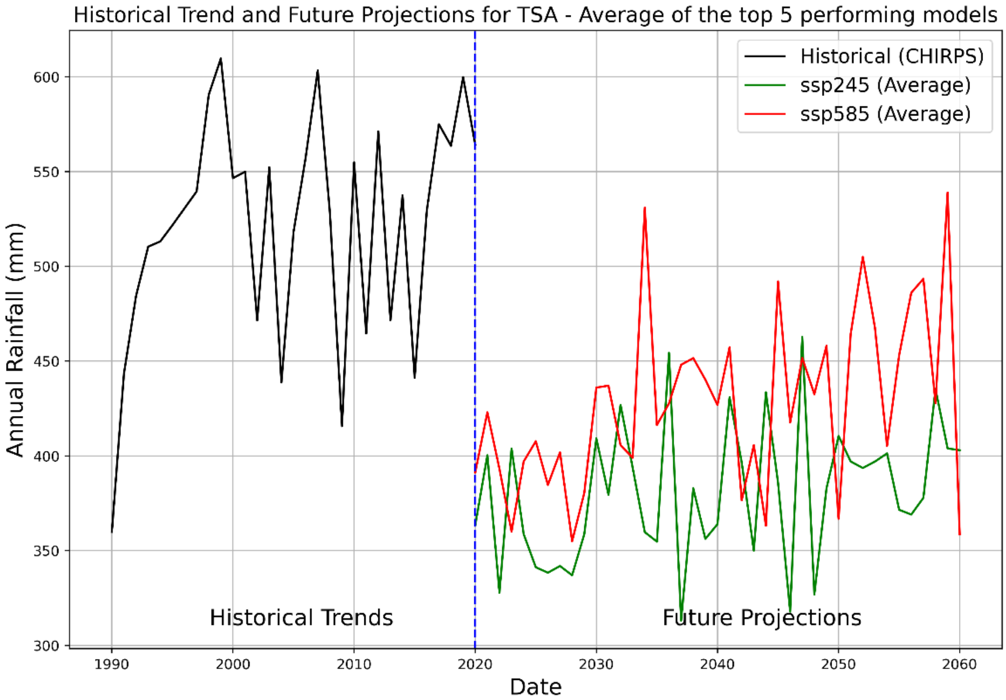

Figure 67: Historical Trend and Future Projections for the Tekeze Setit Atbara Basin - Average of the top 5 performing models for SSPs

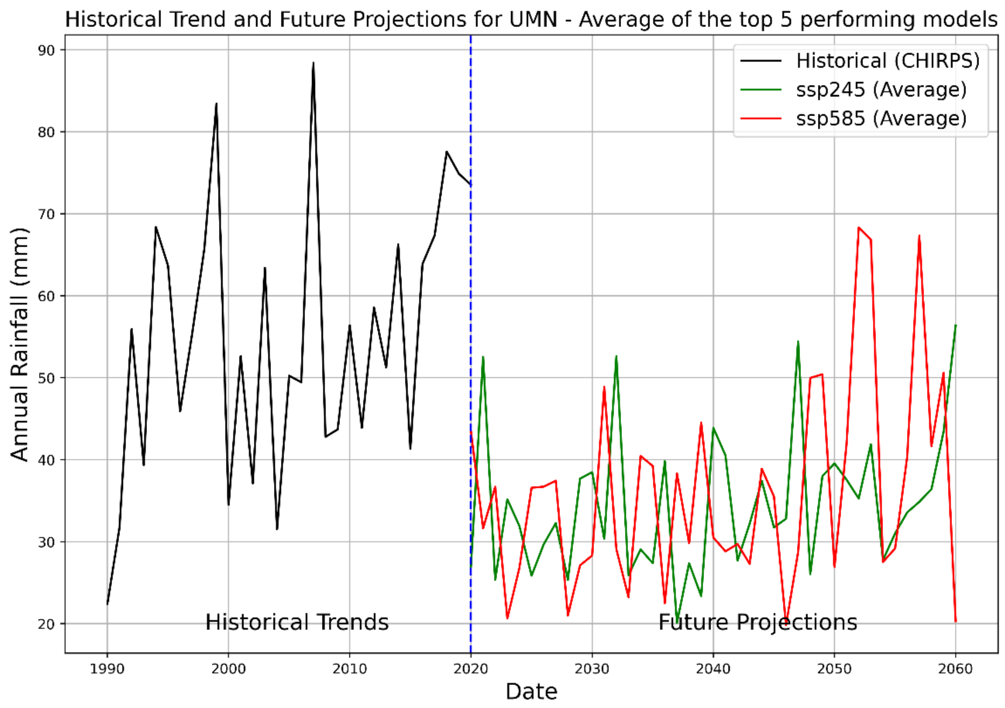

Figure 68: Historical Trend and Future Projections for the Upper Main Nile Basin - Average of the top 5 performing models for SSPs

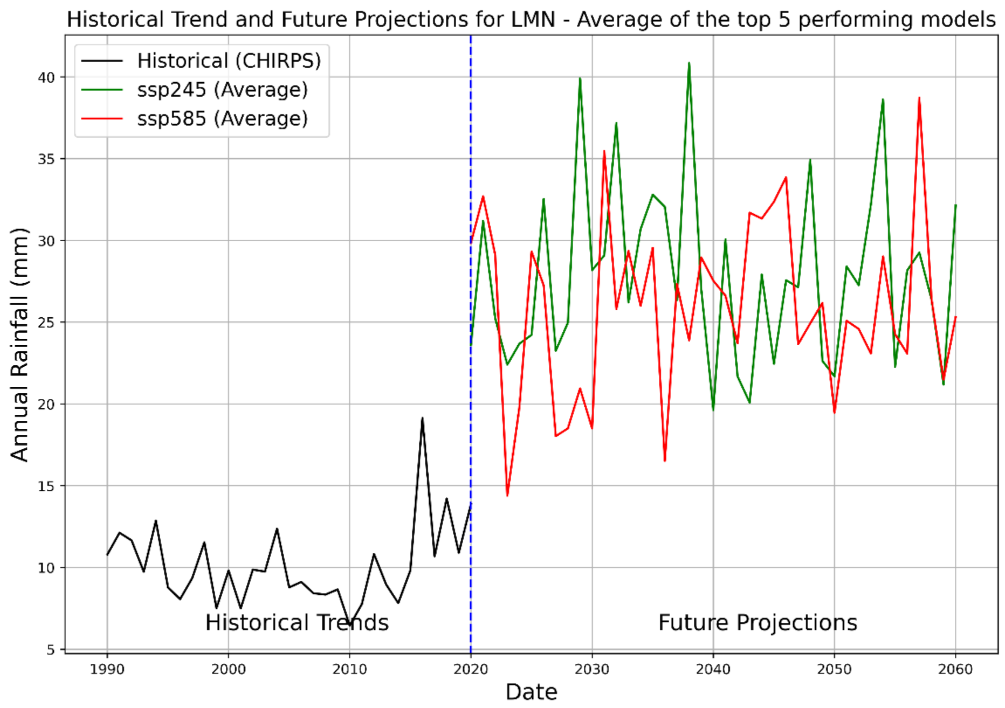

Figure 69: Historical Trend and Future Projections for the Lower Main Nile Basin - Average of the top 5 performing models for SSPs

5.2. Recommendations:

Climate models play a crucial role in understanding regional climate dynamics and informing policy decisions, particularly in regions like ENB where vulnerability to climate change impacts is high. However, current CMIP6 models exhibit coarse resolution, limiting their ability to accurately capture spatial variability at the regional level (e.g. Africa), including ENB. However, to address this limitation, there is a critical need for further refinement and downscaling of CMIP6 models under initiatives like the Coordinated Regional Downscaling Experiment (CORDEX). This refinement would enable the detection of spatial variability more effectively, enhancing the accuracy and reliability of climate projections for SSA and the Extended Nubian Basin (ENB) region.

Moreover, while some CMIP6 models capture seasonality well, they may exhibit over or under estimations, indicating the necessity for dynamical bias correction tailored to specific regions and characteristics. Such corrections, based on produced best-fit distributions, can significantly improve the reliability of CMIP6 models for climate projections in the ENB.

Collaboration between researchers and climate modellers is essential for the development of more robust and reliable climate models. Ensemble modelling approaches could offer a means to quantify uncertainties inherent in climate projections, providing comprehensive insights into future climate scenarios. Additionally, effective communication of uncertainties associated with climate modelling to policymakers and stakeholders is crucial for informed decision-making.

Ultimately, integrated assessment studies that consider the socio-economic implications of climate change are imperative for developing adaptive strategies and policies to mitigate risks and vulnerabilities within the ENB. Furthermore, enhancing ground station networks is recommended to support the quality of satellite data and facilitate accurate model evaluation and bias correction processes. By adopting these recommendations, stakeholders can better understand and respond to evolving climate dynamics, ultimately enhancing resilience and sustainability in the region.

6.0 References:

Adcroft, Alistair, Whit Anderson, V Balaji, Chris Blanton, Mitchell Bushuk, Carolina O Dufour, John P Dunne, Stephen M Griffies, Robert Hallberg, and Matthew J %J Journal of Advances in Modeling Earth Systems Harrison. 2019. 'The GFDL global ocean and sea ice model OM4. 0: Model description and simulation features', 11: 3167-211.

Addisu, Solomon, Yihenew G Selassie, Getachew Fissha, and Birhanu %J Environmental Systems Research Gedif. 2015. 'Time series trend analysis of temperature and rainfall in lake Tana Sub-basin, Ethiopia', 4: 1-12.

Ahmadalipour, Ali, Arun Rana, Hamid Moradkhani, Ashish %J Theoretical Sharma, and applied climatology. 2017. 'Multi-criteria evaluation of CMIP5 GCMs for climate change impact analysis', 128: 71-87.

Alaminie, Addis A, Seifu A Tilahun, Solomon A Legesse, Fasikaw A Zimale, Gashaw Bimrew Tarkegn, and Mark R %J Water Jury. 2021. 'Evaluation of past and future climate trends under CMIP6 scenarios for the UBNB (Abay), Ethiopia', 13: 2110.

Almazroui, Mansour, Fahad Saeed, Sajjad Saeed, M Nazrul Islam, Muhammad Ismail, Nana Ama Browne Klutse, Muhammad Haroon %J Earth Systems Siddiqui, and Environment. 2020. 'Projected change in temperature and precipitation over Africa from CMIP6', 4: 455-75.

Awulachew, Seleshi B, Solomon S Demissie, Fitsum Hagos, Teklu Erkossa, and Don Peden. 2013. 'Water management intervention analysis in the Nile Basin.' in, *The Nile River Basin* (Routledge).

Ayehu, Getachew Tesfaye, Tsegaye Tadesse, Berhan Gessesse, and Tufa %J Atmospheric Measurement Techniques Dinku. 2018. 'Validation of new satellite rainfall products over the Upper Blue Nile Basin, Ethiopia', 11: 1921-36.

Ayugi, Brian, Victor Dike, Hamida Ngoma, Hassen Babaousmail, Richard Mumo, and Victor Ongoma. 2021. 'Future Changes in Precipitation Extremes over East Africa Based on CMIP6 Models', *Water*, 13.

Babaousmail, Hassen, Rongtao Hou, Brian Ayugi, Moses Ojara, Hamida Ngoma, Rizwan Karim, Adharsh Rajasekar, and Victor %J Atmosphere Ongoma. 2021. 'Evaluation of the performance of CMIP6 models in reproducing rainfall patterns over North Africa', 12: 475.

Basheer, Mohammed, and Nadir Ahmed %J Atmospheric Research Elagib. 2019. 'Performance of satellite-based and GPCC 7.0 rainfall products in an extremely data-scarce country in the Nile Basin', 215: 128-40.

Belete, Marye, Jinsong Deng, Ke Wang, Mengmeng Zhou, Enyan Zhu, Eshetu Shifaw, and Yared %J Science of the Total Environment Bayissa. 2020. 'Evaluation of satellite rainfall products for modeling water yield over the source region of Blue Nile Basin', 708: 134834.

Berhanu, Daniel, Tena Alamirew, Meron Teferi Taye, Degefie Tibebe, Solomon Gebrehiwot, Gete %J Journal of Water Zeleke, and Climate Change. 2023. 'Evaluation of CMIP6 models in reproducing observed rainfall over Ethiopia', 14: 2583-605.

Butts, Michael B, Carlo Buontempo, Jens K Lørup, Karina Williams, Camilla Mathison, Oluf Z Jessen, Niels D Riegels, Paul Glennie, Carol McSweeney, and Mark %J Proceedings of the International Association of Hydrological Sciences Wilson. 2016. 'A regional approach to climate adaptation in the Nile Basin', 374: 3-7.

Conway, D, and M %J Climatic change Hulme. 1993. 'Recent fluctuations in precipitation and runoff over the Nile sub-basins and their impact on main Nile discharge', 25: 127-51.

Conway, Declan %J Geographical Journal. 2000. 'The climate and hydrology of the Upper Blue Nile River', 166: 49-62.

Conway, Declan, Edward Allison, Richard Felstead, Marisa %J Philosophical Transactions of the Royal Society A: Mathematical Goulden, Physical, and Engineering Sciences. 2005. 'Rainfall variability in East Africa: implications for natural resources management and livelihoods', 363: 49-54.

Digna, Reem F, Mario E Castro-Gama, Pieter Van der Zaag, Yasir A Mohamed, Gerald Corzo, and Stefan %J Water Uhlenbrook. 2018. 'Optimal operation of the Eastern Nile System using Genetic Algorithm, and benefits distribution of water resources development', 10: 921.

Dinku, Tufa, Chris Funk, Pete Peterson, Ross Maidment, Tsegaye Tadesse, Hussein Gadain, and Pietro %J Quarterly Journal of the Royal Meteorological Society Ceccato. 2018. 'Validation of the CHIRPS satellite rainfall estimates over eastern Africa', 144: 292-312.

Elshamy, Mohamed E, Ivar Ambjørn Seierstad, Asgeir %J Hydrology Sorteberg, and Earth System Sciences. 2009. 'Impacts of climate change on Blue Nile flows using bias-corrected GCM scenarios', 13: 551-65.

Feyissa, Tolera Abdissa, Tamene Adugna Demissie, Fokke Saathoff, and Alemayehu %J Sustainability Gebissa. 2023. 'Evaluation of General Circulation Models CMIP6 Performance and Future Climate Change over the Omo River Basin, Ethiopia', 15: 6507.

Funk, Chris, Pete Peterson, Martin Landsfeld, Diego Pedreros, James Verdin, Shraddhanand Shukla, Gregory Husak, James Rowland, Laura Harrison, and Andrew %J Scientific data Hoell. 2015. 'The climate hazards infrared precipitation with stations—a new environmental record for monitoring extremes', 2: 1-21.

Gebisa, Bekele Terefe, Wakjira Takala Dibaba, Alemayehu %J Journal of Water Kabeta, and Climate Change. 2023. 'Evaluation of historical CMIP6 model simulations and future climate change projections in the Baro River Basin', 14: 2680-705.

Gebremicael, Tesfay G, Matthew J Deitch, Haley N Gancel, Amanda C Croteau, Gebremedhin G Haile, Awetahegne N Beyene, and Love %J Atmospheric Research Kumar. 2022. 'Satellite-based rainfall estimates evaluation using a parsimonious hydrological model in the complex climate and topography of the Nile River Catchments', 266: 105939.

Gidden, Matthew J, Keywan Riahi, Steven J Smith, Shinichiro Fujimori, Gunnar Luderer, Elmar Kriegler, Detlef P Van Vuuren, Maarten Van Den Berg, Leyang Feng, and David %J Geoscientific model development Klein. 2019. 'Global emissions pathways under different socioeconomic scenarios for use in CMIP6: a dataset of harmonized emissions trajectories through the end of the century', 12: 1443-75.

Hausfather, Zeke. 2018. 'Explainer: How ‘Shared Socioeconomic Pathways’ explore future climate change', *https://www.carbonbrief.org/explainer-how-shared-socioeconomic-pathways-explore-future-climate-change/*.

———. 2019. 'CMIP6: the next generation of climate models explained', *https://www.carbonbrief.org/cmip6-the-next-generation-of-climate-models-explained/*.

Held, IM, H Guo, A Adcroft, JP Dunne, LW Horowitz, J Krasting, E Shevliakova, M Winton, M Zhao, and M %J Journal of Advances in Modeling Earth Systems Bushuk. 2019. 'Structure and performance of GFDL's CM4. 0 climate model', 11: 3691-727.

Heumann, Christian, and Michael Schomaker Shalabh. 2016. *Introduction to statistics and data analysis* (Springer).

IPCC. 2014. 'Impacts, adaptation and vulnerability', *Part A: global sectoral aspects. Contribution of working group II to the fifth assessment report of the intergovernmental Panel on Climate Change*, 1132.

Jury, Mark R, and Chris %J International Journal of Climatology Funk. 2013. 'Climatic trends over Ethiopia: regional signals and drivers', 33: 1924-35.

Kawai, Hideaki, Seiji Yukimoto, Tsuyoshi Koshiro, Naga Oshima, Taichu Tanaka, Hiromasa Yoshimura, and Ryoji %J Geoscientific Model Development

Nagasawa. 2019. 'Significant improvement of cloud representation in the global climate model MRI-ESM2', 12: 2875-97.
Klutse, Nana Ama Browne, Kwesi Akumenyi Quagraine, Francis Nkrumah, Kwesi Twentwewa Quagraine, Rebecca Berkoh-Oforiwaa, Joshua Fafanyo Dzrobi, Mouhamadou Bamba %J Earth Systems Sylla, and Environment. 2021. 'The climatic analysis of summer monsoon extreme precipitation events over West Africa in CMIP6 simulations', 5: 25-41.
Mbigi, Dickson, Augustine Omondi Onyango, Zacharia Florence Mtewele, Paul Kiprotich, and Ziniu %J International Journal of Climatology Xiao. 2022. 'Coupled Model Intercomparison Project Phase 6 simulations of the spatial structure of rainfall variability over East Africa: Evaluation and projection', 42: 9865-85.
McGill, Robert, John W Tukey, and Wayne A %J The american statistician Larsen. 1978. 'Variations of box plots', 32: 12-16.
Merem, EC, YA Twumasi, J Wesley, D Olagbegi, M Crisler, C Romorno, M Alsarari, P Isokpehi, A Hines, and GS %J World Environment Ochai. 2020. 'Issues in Transboundary Water Use in the River Nile Basin Area of Africa', 10: 27-44.
Mohamed, Nader Noureldeen %J The Nile River. 2017. 'Productivity of rainfed agriculture of the upper Nile river': 467-501.
Mostafa, Hany, Hazem Saleh, Mahmoud El Sheikh, and Khaled %J J Am Sci Kheireldin. 2016. 'Assessing the impacts of climate changes on the eastern Nile flow at Aswan', 12: 1-9.
Nashwan, Mohamed Salem, Shamsuddin Shahid, and Xiaojun Wang. 2019. 'Assessment of satellite-based precipitation measurement products over the hot desert climate of Egypt', *J Remote Sensing*, 11: 555.
NBI. 2016. 'Nile Basin Water Resources Atlas', *Nile Basin Initiative*.
Ngoma, Hamida, Wang Wen, Brian Ayugi, Hassen Babaousmail, Rizwan Karim, and Victor %J International Journal of Climatology Ongoma. 2021. 'Evaluation of precipitation simulations in CMIP6 models over Uganda', 41: 4743-68.
NOAA. 2021. 'Climate Forcing', *https://www.climate.gov/maps-data/climate-data-primer/predicting-climate/climate-forcing*.
O'Neill, Brian C, Claudia Tebaldi, Detlef P Van Vuuren, Veronika Eyring, Pierre Friedlingstein, George Hurtt, Reto Knutti, Elmar Kriegler, Jean-Francois Lamarque, and Jason %J Geoscientific Model Development Lowe. 2016. 'The scenario model intercomparison project (ScenarioMIP) for CMIP6', 9: 3461-82.
Omay, Paulino Omoj, Nzioka J Muthama, Christopher Oludhe, Josiah M Kinama, Guleid Artan, and Zachary Atheru. 2023. 'Evaluation of CMIP6 Historical Simulations over IGAD region of Eastern Africa'.
Ortega, Geusep, Paola A Arias, Juan Camilo Villegas, Pablo A Marquet, and Paulo %J International Journal of Climatology Nobre. 2021. 'Present-day and future climate over central and South America according to CMIP5/CMIP6 models', 41: 6713-35.
Otieno, Vincent O., and R. O. Anyah. 2013. 'CMIP5 simulated climate conditions of the Greater Horn of Africa (GHA). Part II: projected climate', *Climate Dynamics*, 41: 2099-113.
Rettie, Fasil M, Sebastian Gayler, Tobias KD Weber, Kindie Tesfaye, and Thilo %J Scientific Data Streck. 2023. 'High-resolution CMIP6 climate projections for Ethiopia using the gridded statistical downscaling method', 10: 442.

Samy, Abeer, Mona G. Ibrahim, Wael Elham Mahmod, Manabu Fujii, Amr Eltawil, and Waled %J Water Daoud. 2019. 'Statistical assessment of rainfall characteristics in Upper Blue Nile Basin over the period from 1953 to 2014', 11: 468.

Seland, Øyvind, Mats Bentsen, Dirk Olivié, Thomas Toniazzo, Ada Gjermundsen, Lise Seland Graff, Jens Boldingh Debernard, Alok Kumar Gupta, Yan-Chun He, and Alf %J Geoscientific Model Development Kirkevåg. 2020. 'Overview of the Norwegian Earth System Model (NorESM2) and key climate response of CMIP6 DECK, historical, and scenario simulations', 13: 6165-200.

Srivastava, Abhishekh, Richard Grotjahn, Paul A %J Weather Ullrich, and Climate Extremes. 2020. 'Evaluation of historical CMIP6 model simulations of extreme precipitation over contiguous US regions', 29: 100268.

Strzepek, Kenneth M, David N Yates, and Dia El Din %J Climate Research El Quosy. 1996. 'Vulnerability assessment of water resources in Egypt to climatic change in the Nile Basin', 6: 89-95.

Su, Fengge, Xiaolan Duan, Deliang Chen, Zhenchun Hao, and Lan %J Journal of climate Cuo. 2013. 'Evaluation of the global climate models in the CMIP5 over the Tibetan Plateau', 26: 3187-208.

Sutton, Stephen G., and Renae C. Tobin. 2011. 'Constraints on community engagement with Great Barrier Reef climate change reduction and mitigation', *Global Environmental Change*, 21: 894-905.

Tukey, John W. 1977. *Exploratory data analysis* (Reading, MA).

Wang, Yi-Chi, Huang-Hsiung Hsu, Chao-An Chen, Wan-Ling Tseng, Pei-Chun Hsu, Cheng-Wei Lin, Yu-Luen Chen, Li-Chiang Jiang, Yu-Chi Lee, and Hsin-Chien %J Journal of Advances in Modeling Earth Systems Liang. 2021. 'Performance of the Taiwan earth system model in simulating climate variability compared with observations and CMIP6 model simulations', 13: e2020MS002353.

WCRP. 2021a. 'WCRP History'. https://www.wcrp-climate.org/about-wcrp/about-history.

———. 2021b. 'The Working Group on Coupled Modelling (WGCM)'. https://www.wcrp-climate.org/wgcm-overview.

Wu, Tongwen, Yixiong Lu, Yongjie Fang, Xiaoge Xin, Laurent Li, Weiping Li, Weihua Jie, Jie Zhang, Yiming Liu, and Li %J Geoscientific Model Development Zhang. 2019. 'The Beijing Climate Center climate system model (BCC-CSM): The main progress from CMIP5 to CMIP6', 12: 1573-600.

Annexes

Best fit Distribution Plots

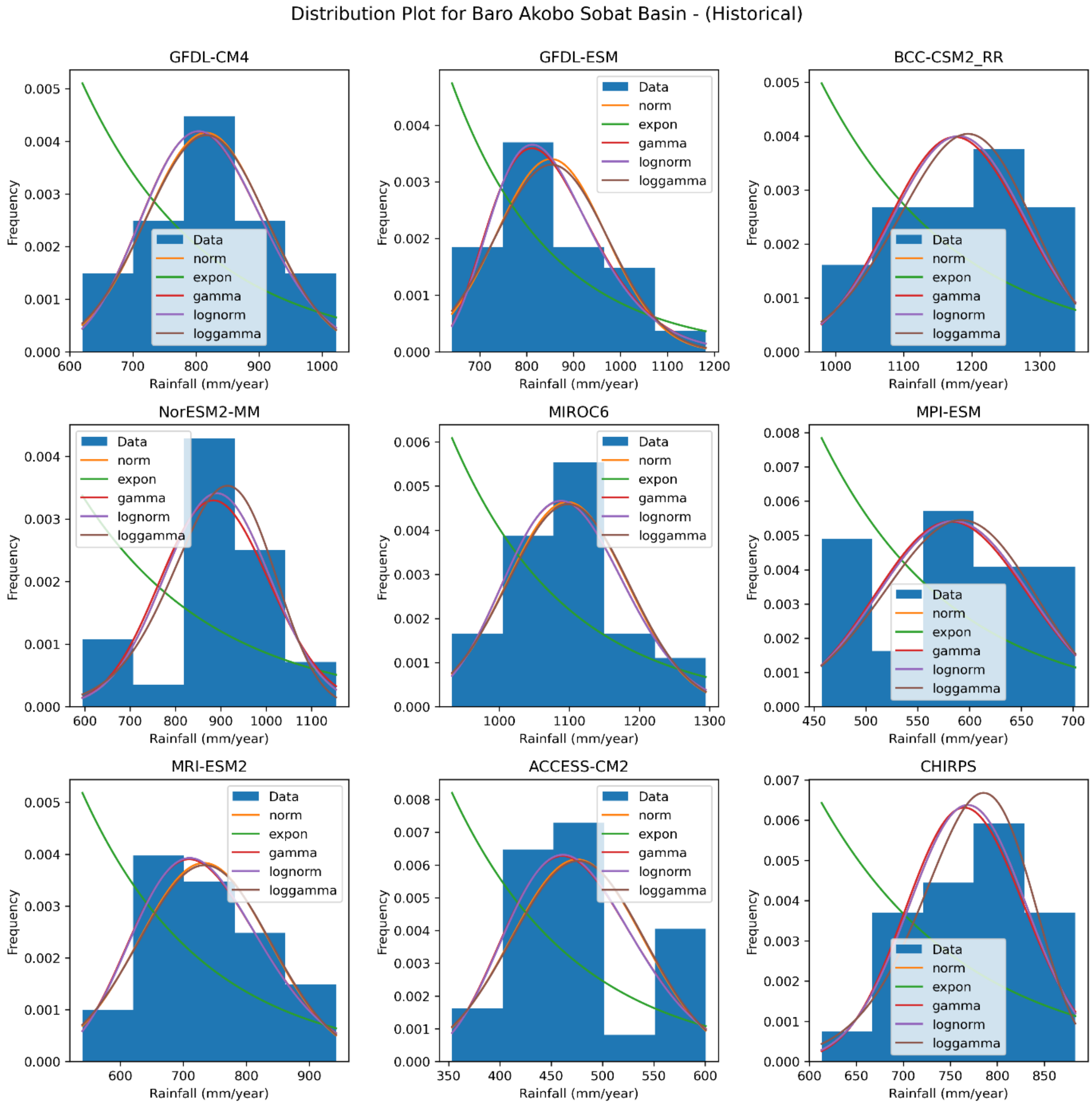

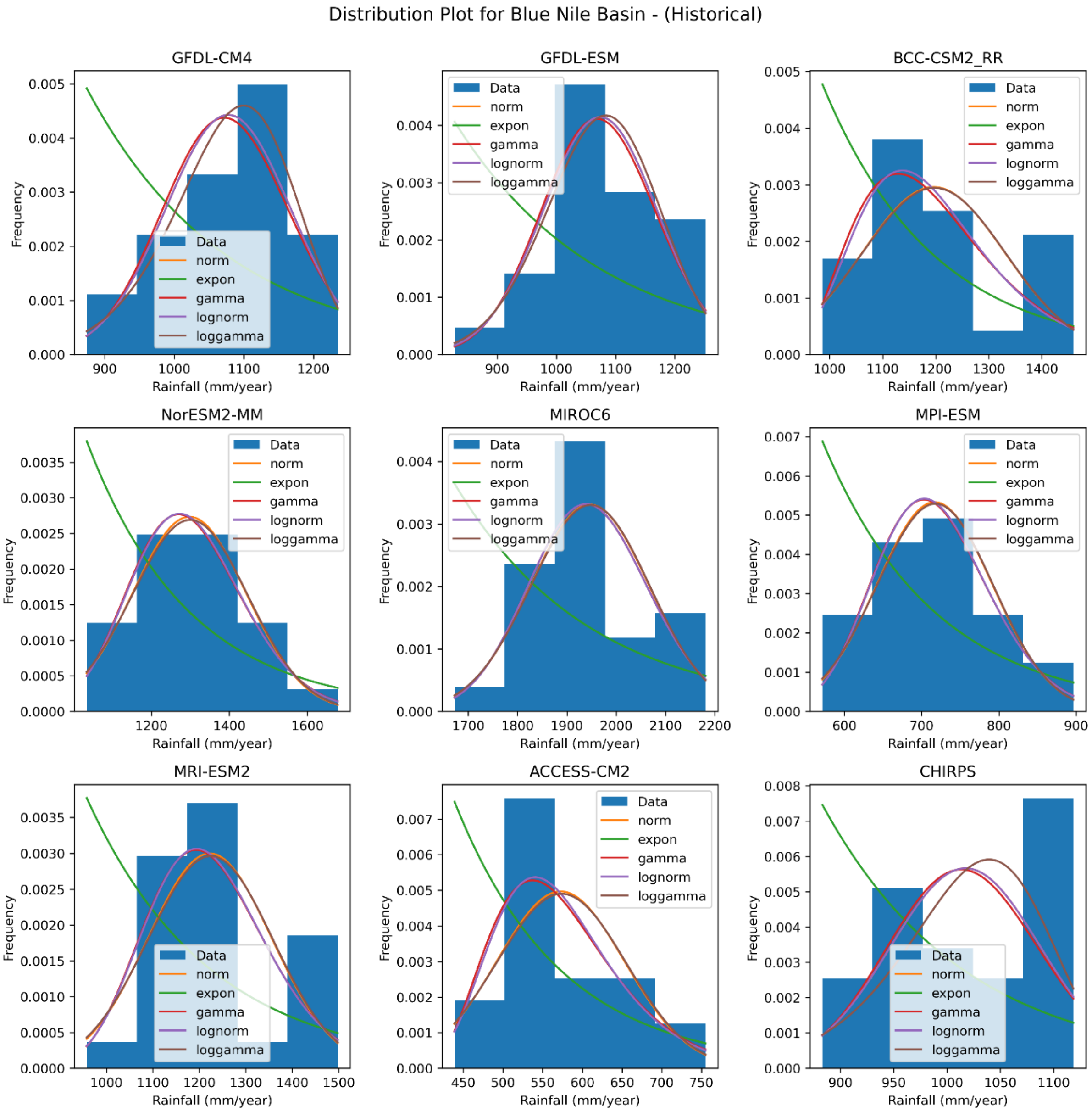
Distribution Plot for Blue Nile Basin - (Historical)
GFDL-CM4
GFDL-ESM
BCC-CSM2_RR
NorESM2-MM
MIROC6
MPI-ESM
MRI-ESM2
ACCESS-CM2
CHIRPS
Data
norm
expon
gamma
lognorm
loggamma
Frequency
Rainfall (mm/year)

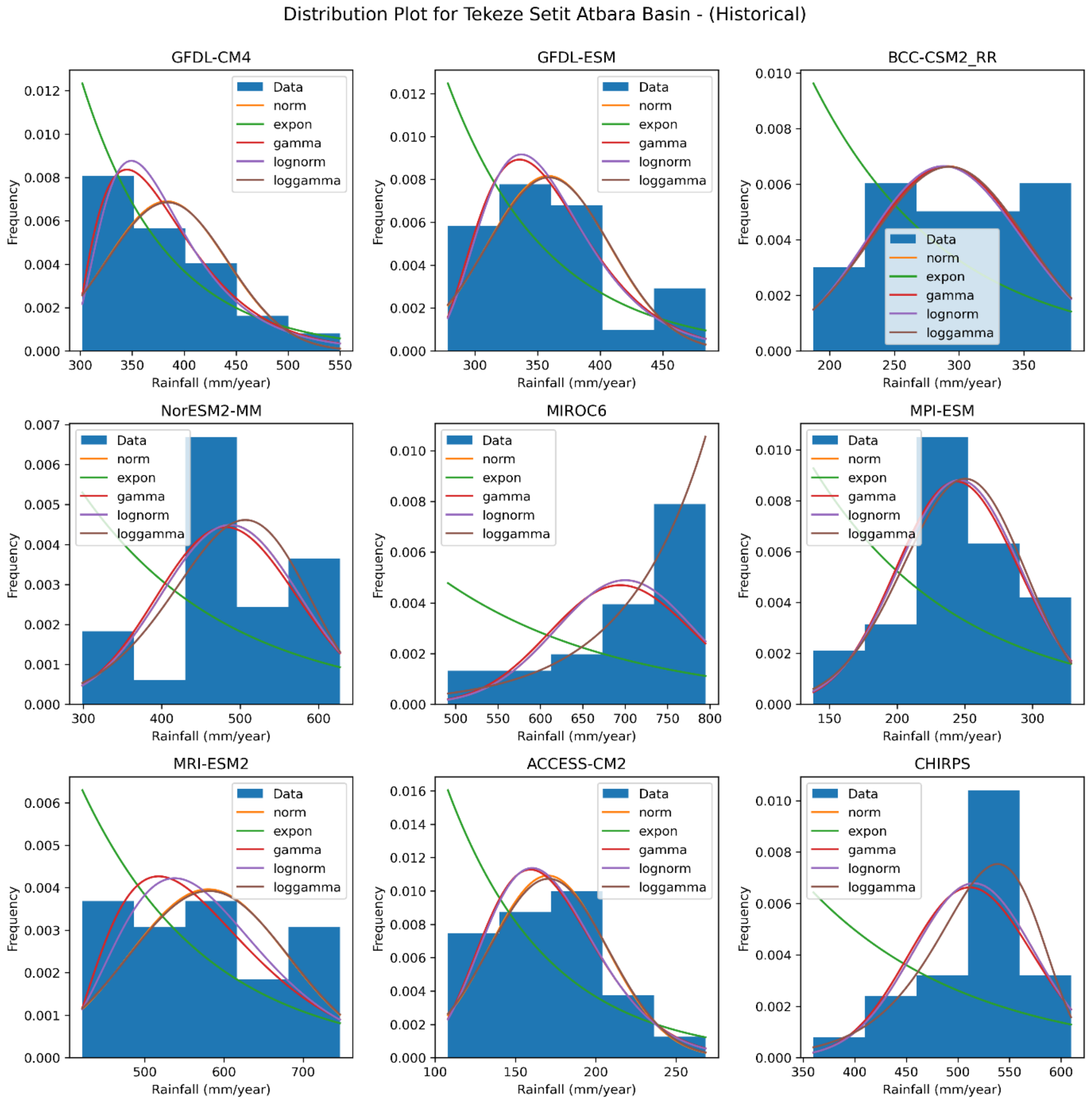
Distribution Plot for Tekeze Setit Atbara Basin - (Historical)
GFDL-CM4
GFDL-ESM
BCC-CSM2_RR
NorESM2-MM
MIROC6
MPI-ESM
MRI-ESM2
ACCESS-CM2
CHIRPS
Data
norm
expon
gamma
lognorm
loggamma
Frequency
Rainfall (mm/year)

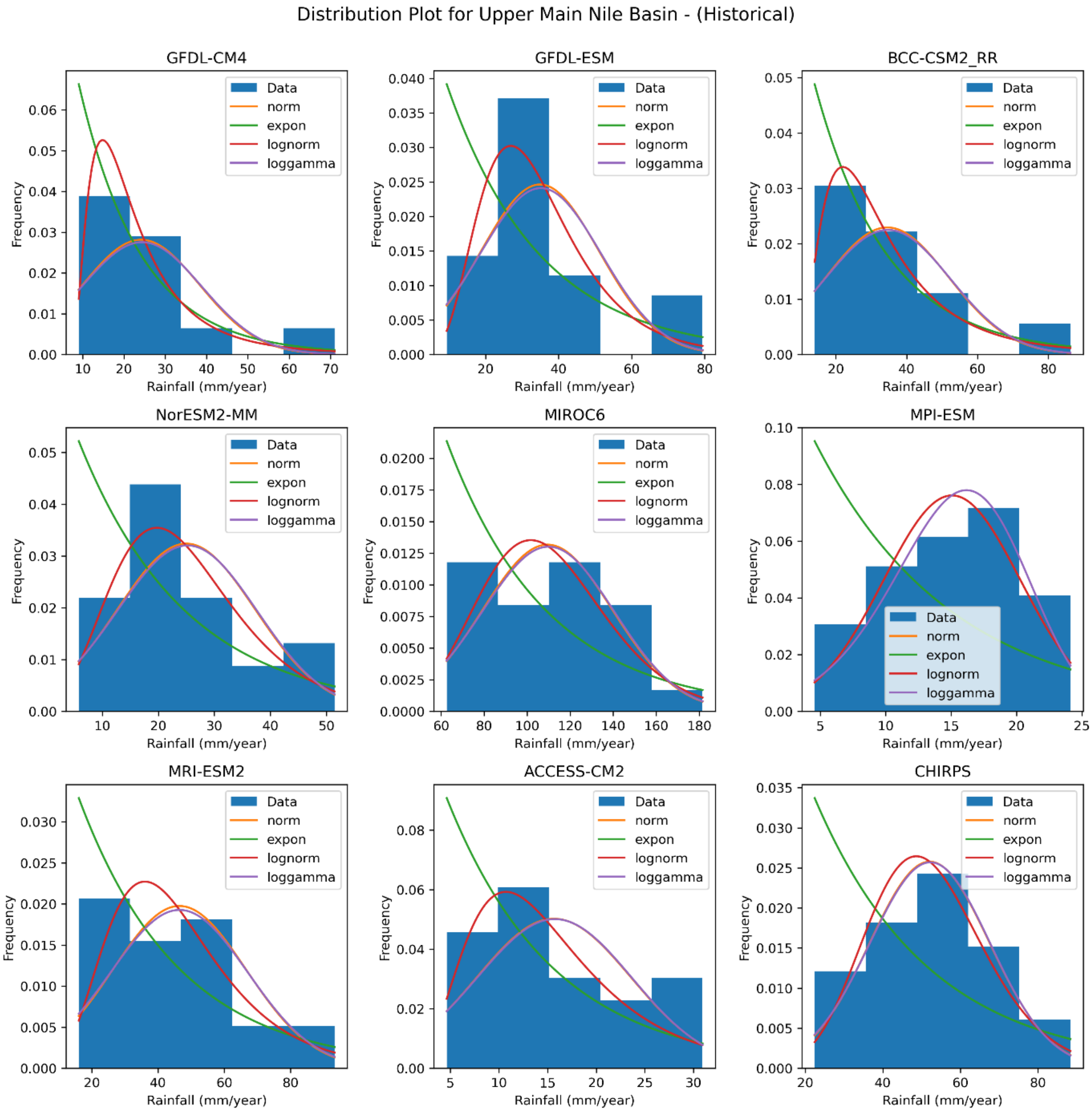
Distribution Plot for Upper Main Nile Basin - (Historical)
GFDL-CM4
GFDL-ESM
BCC-CSM2_RR
NorESM2-MM
MIROC6
MPI-ESM
MRI-ESM2
ACCESS-CM2
CHIRPS
Data
norm
expon
lognorm
loggamma
Frequency
Rainfall (mm/year)

Distribution Plot for Lower Main Nile Basin - (Historical)

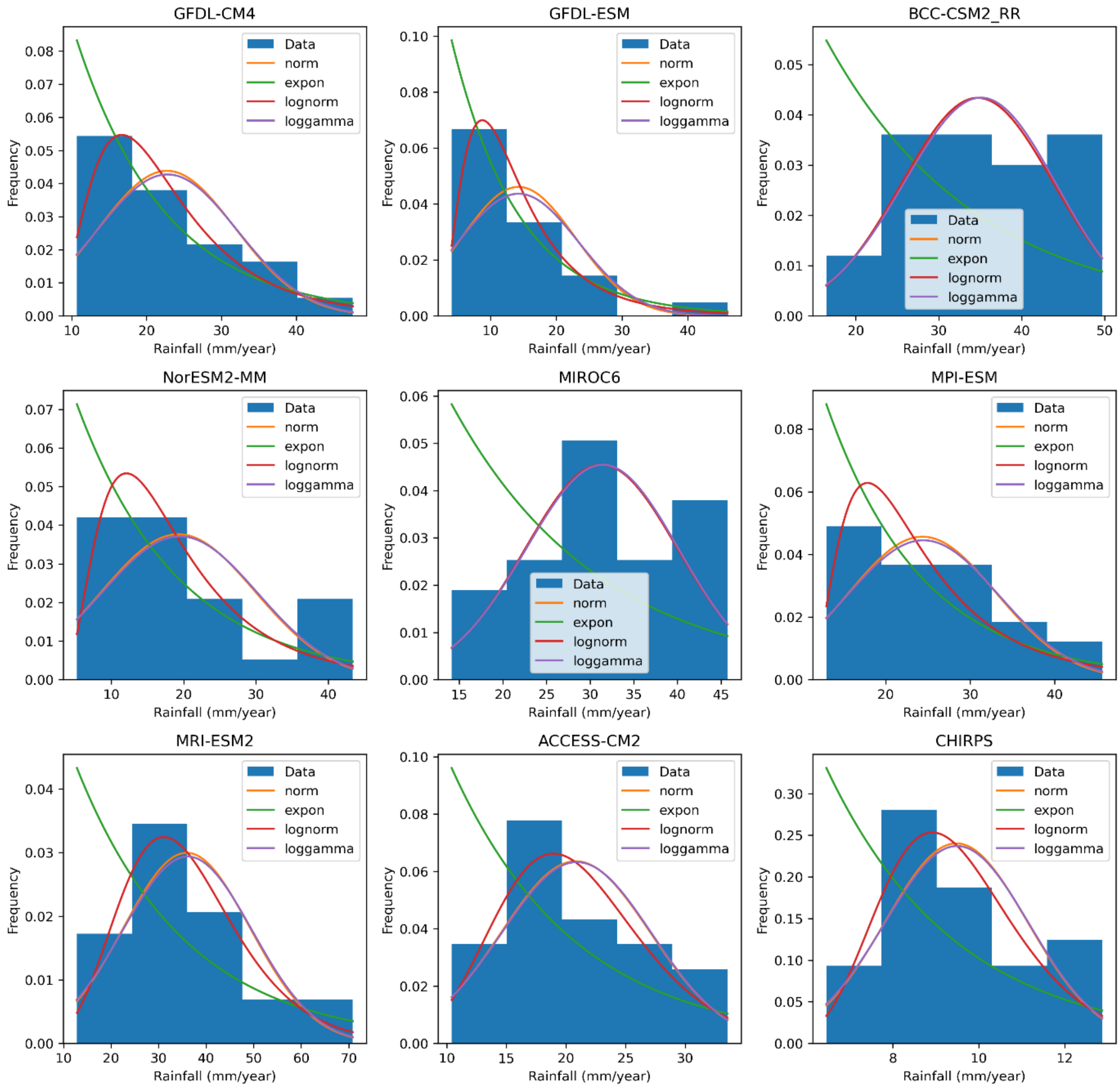

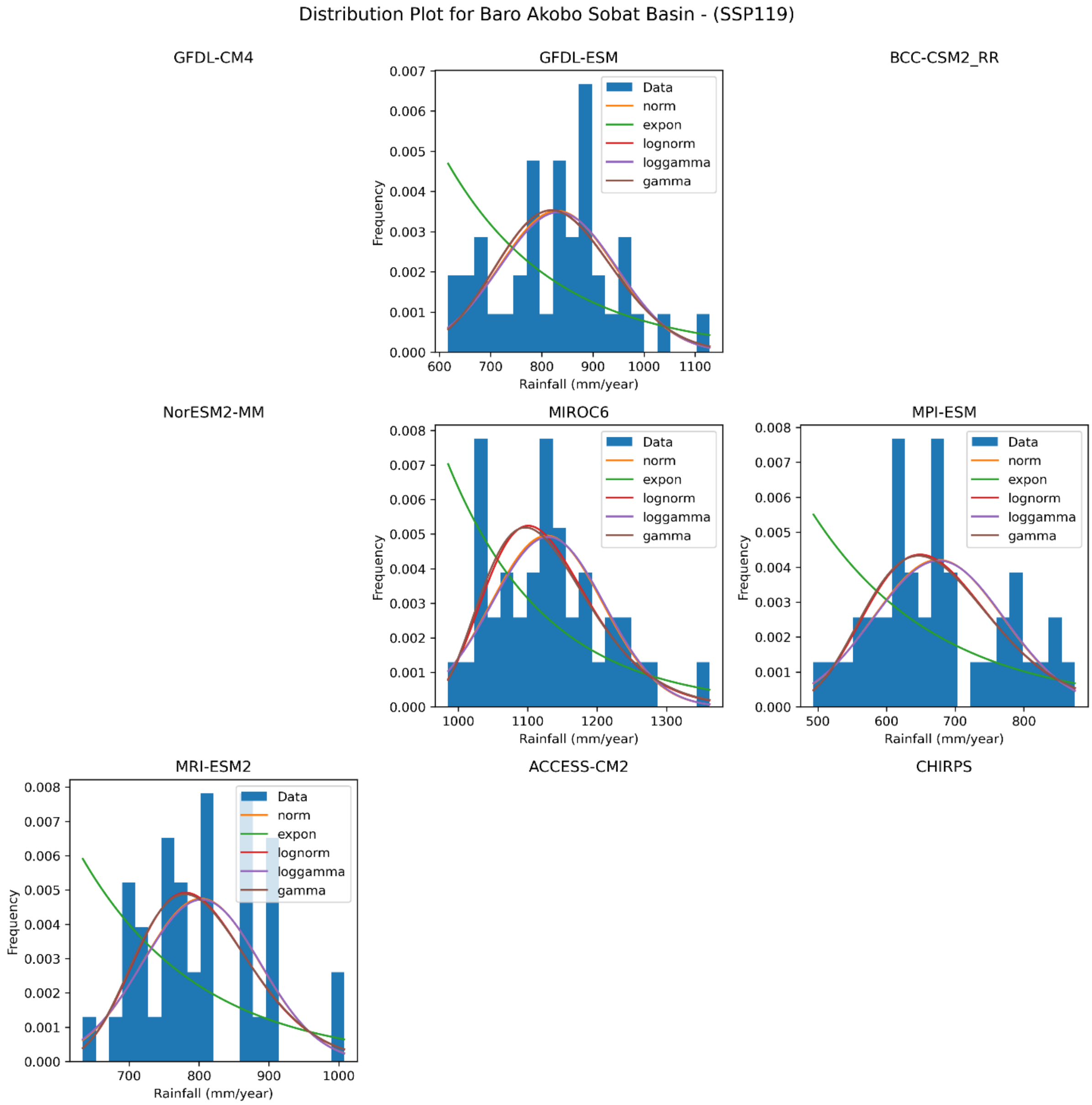
Distribution Plot for Baro Akobo Sobat Basin - (SSP119)
GFDL-CM4
GFDL-ESM
BCC-CSM2_RR
NorESM2-MM
MIROC6
MPI-ESM
MRI-ESM2
ACCESS-CM2
CHIRPS
Data
norm
expon
lognorm
loggamma
gamma
Frequency
Rainfall (mm/year)

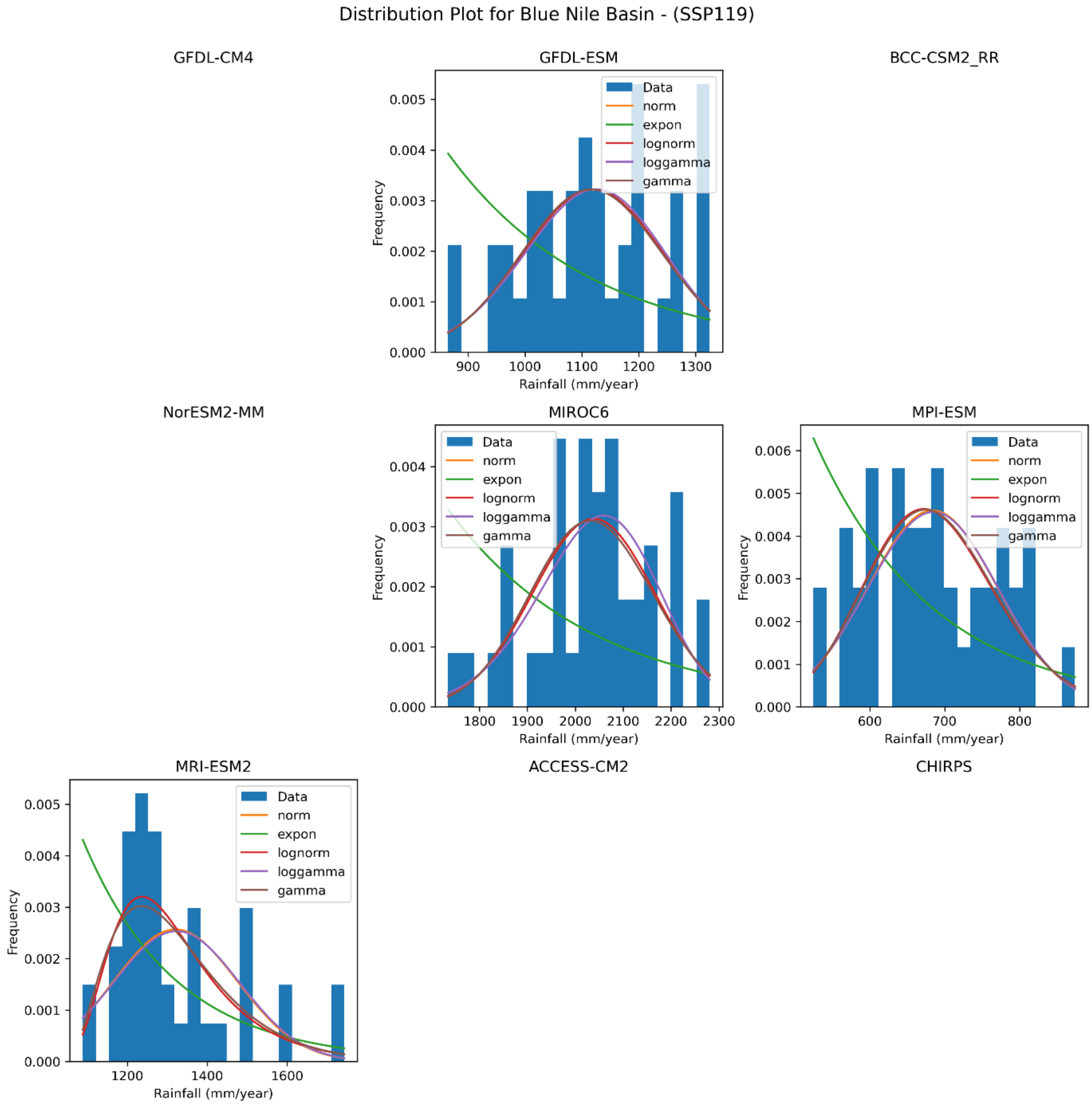
Distribution Plot for Blue Nile Basin - (SSP119)
GFDL-CM4
GFDL-ESM
BCC-CSM2_RR
NorESM2-MM
MIROC6
MPI-ESM
MRI-ESM2
ACCESS-CM2
CHIRPS
Data
norm
expon
lognorm
loggamma
gamma
Frequency
Rainfall (mm/year)

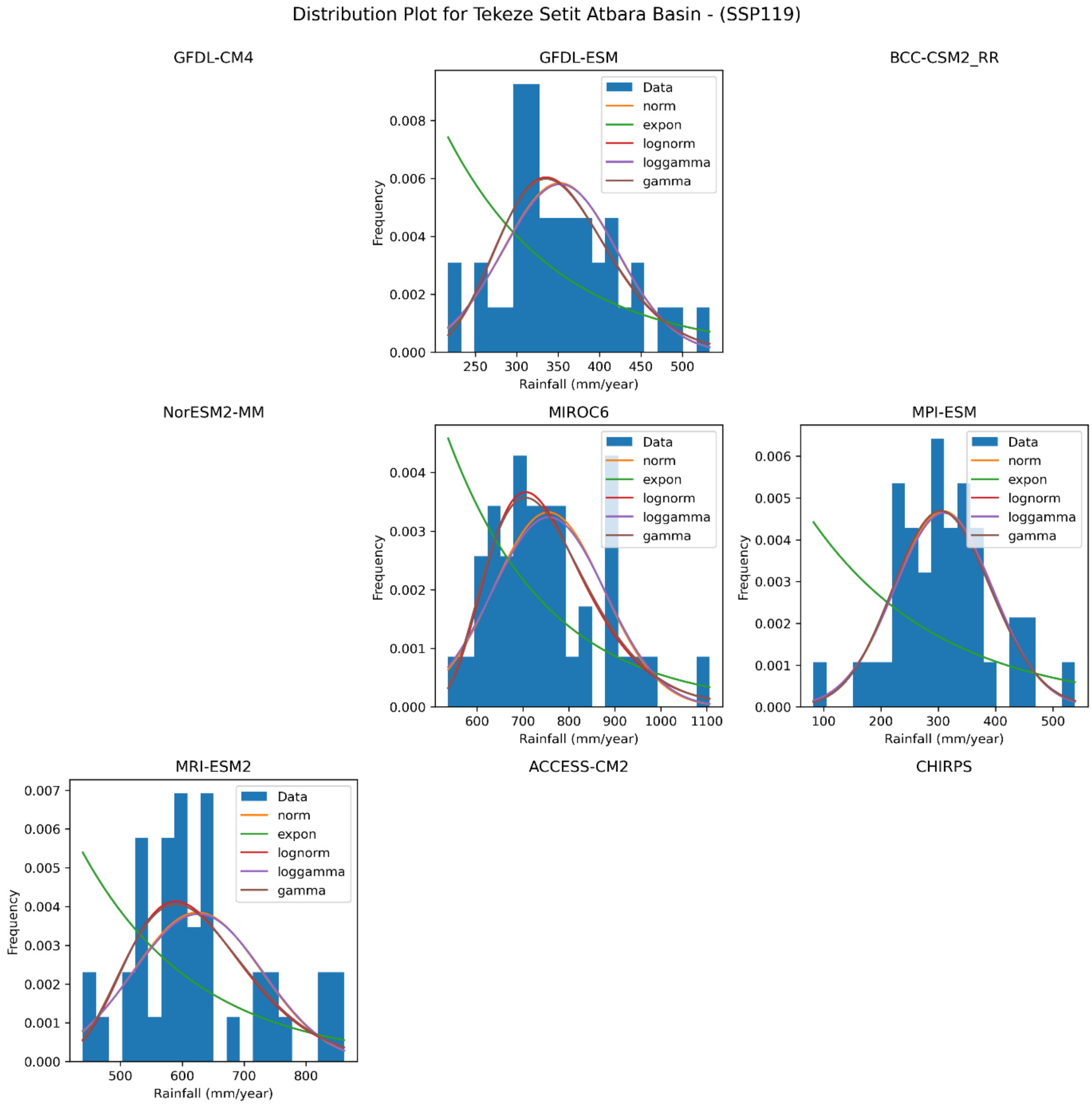
Distribution Plot for Tekeze Setit Atbara Basin - (SSP119)
GFDL-CM4
GFDL-ESM
BCC-CSM2_RR
NorESM2-MM
MIROC6
MPI-ESM
MRI-ESM2
ACCESS-CM2
CHIRPS
Data
norm
expon
lognorm
loggamma
gamma
Frequency
Rainfall (mm/year)

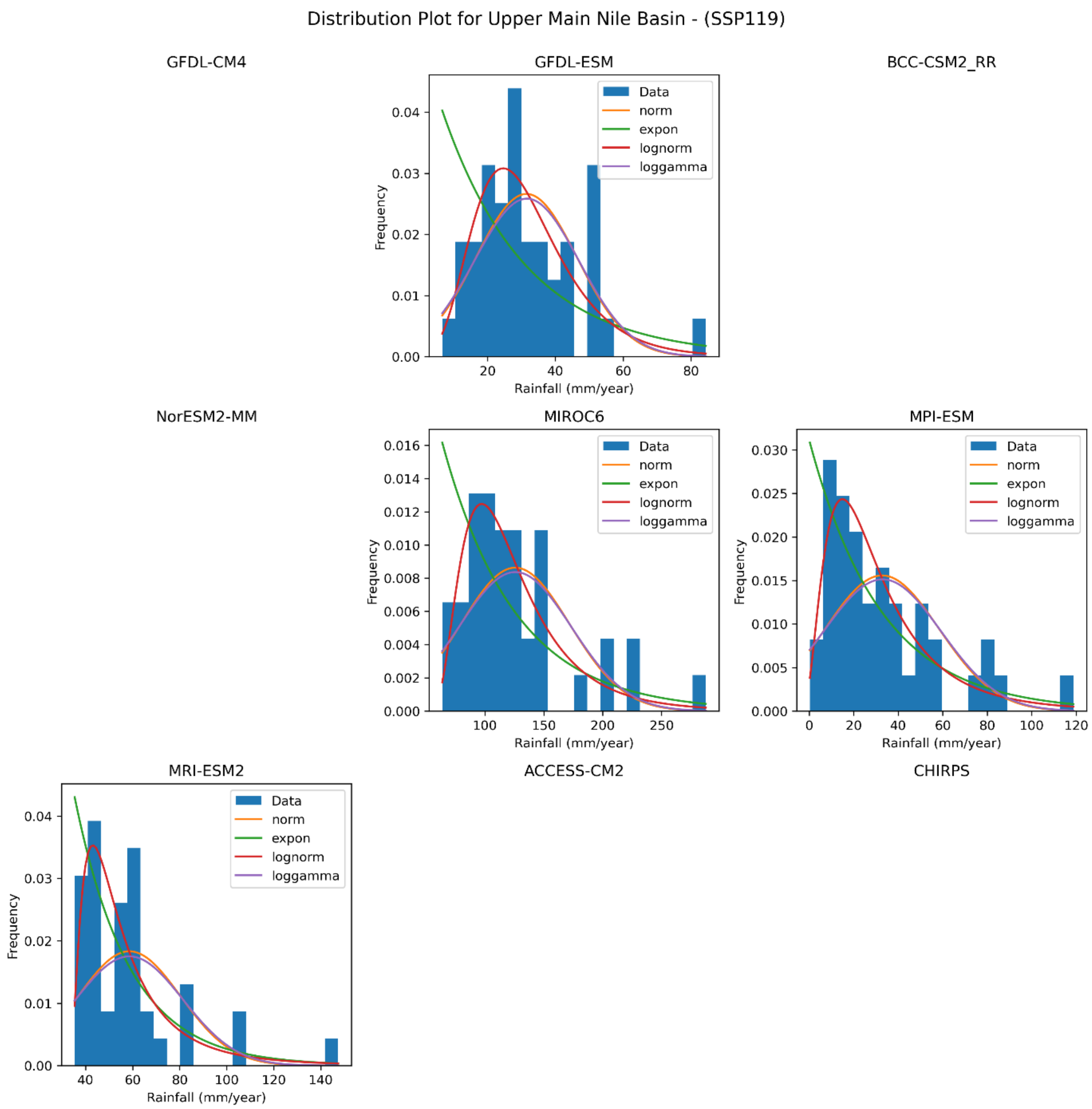
Distribution Plot for Upper Main Nile Basin - (SSP119)
GFDL-CM4
GFDL-ESM
BCC-CSM2_RR
NorESM2-MM
MIROC6
MPI-ESM
MRI-ESM2
ACCESS-CM2
CHIRPS
Data
norm
expon
lognorm
loggamma
Frequency
Rainfall (mm/year)

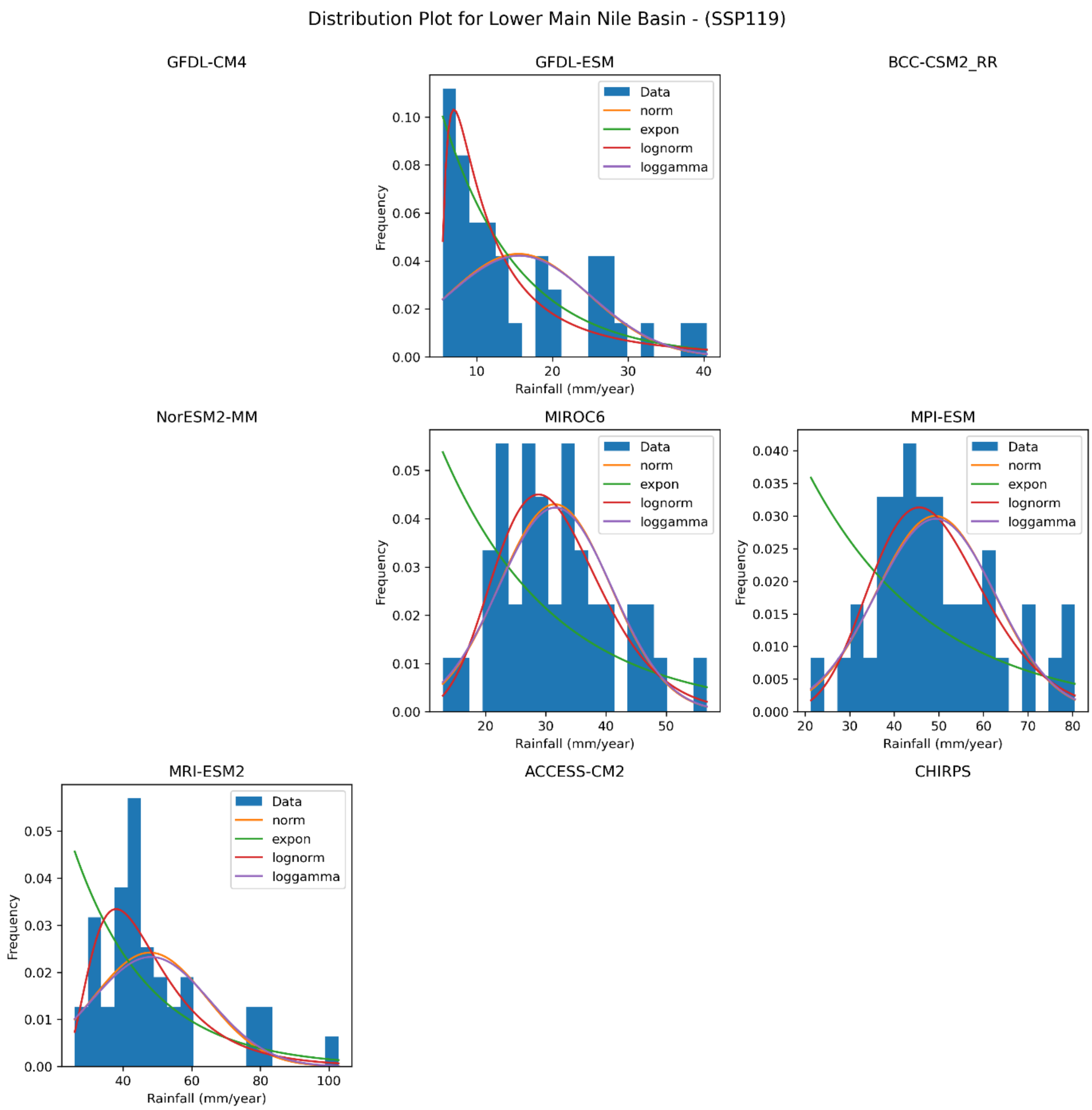
Distribution Plot for Lower Main Nile Basin - (SSP119)
GFDL-CM4
GFDL-ESM
BCC-CSM2_RR
NorESM2-MM
MIROC6
MPI-ESM
MRI-ESM2
ACCESS-CM2
CHIRPS
Data
norm
expon
lognorm
loggamma
Frequency
Rainfall (mm/year)

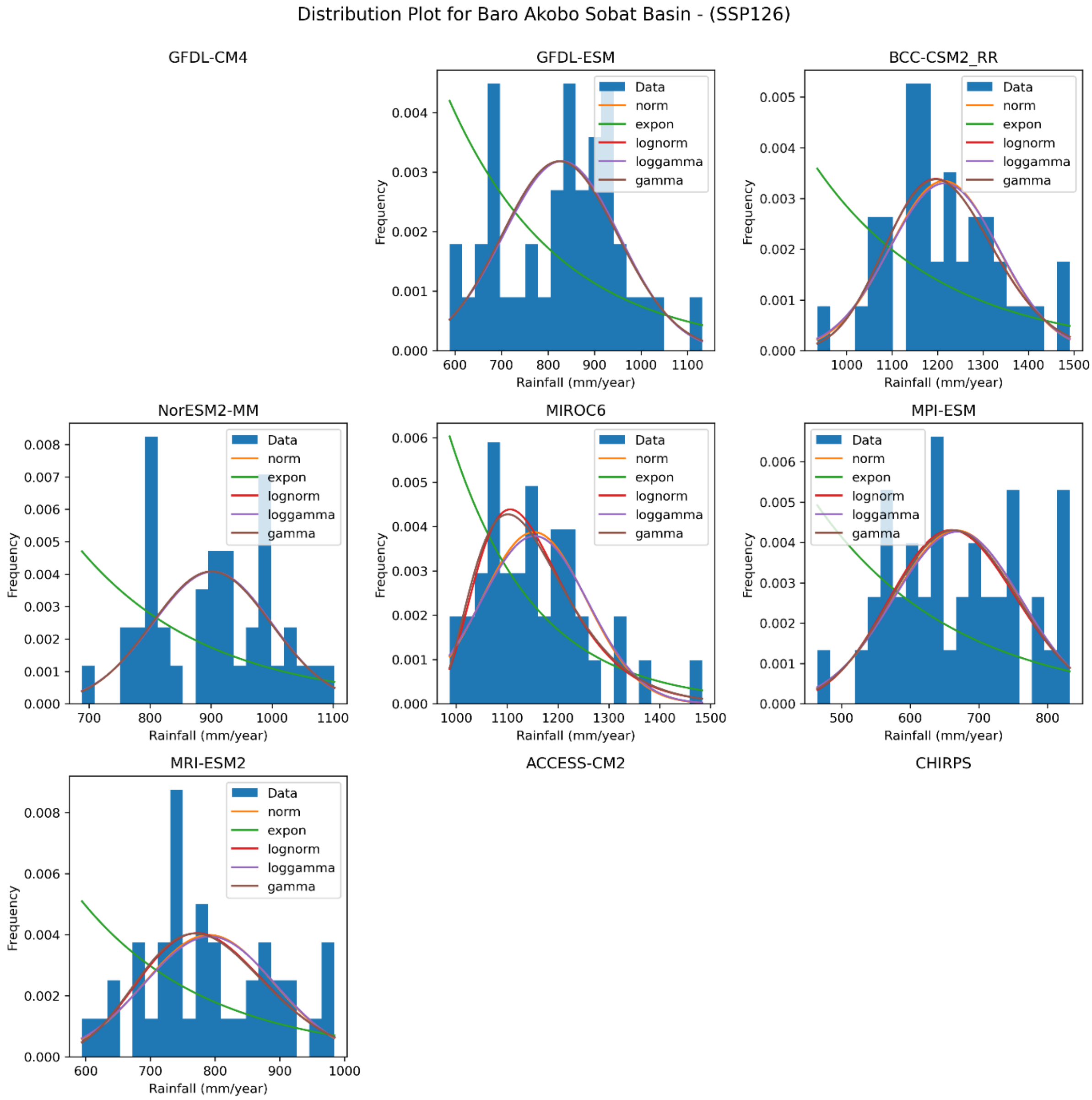
Distribution Plot for Baro Akobo Sobat Basin - (SSP126)
GFDL-CM4
GFDL-ESM
BCC-CSM2_RR
NorESM2-MM
MIROC6
MPI-ESM
MRI-ESM2
ACCESS-CM2
CHIRPS
Data
norm
expon
lognorm
loggamma
gamma
Frequency
Rainfall (mm/year)

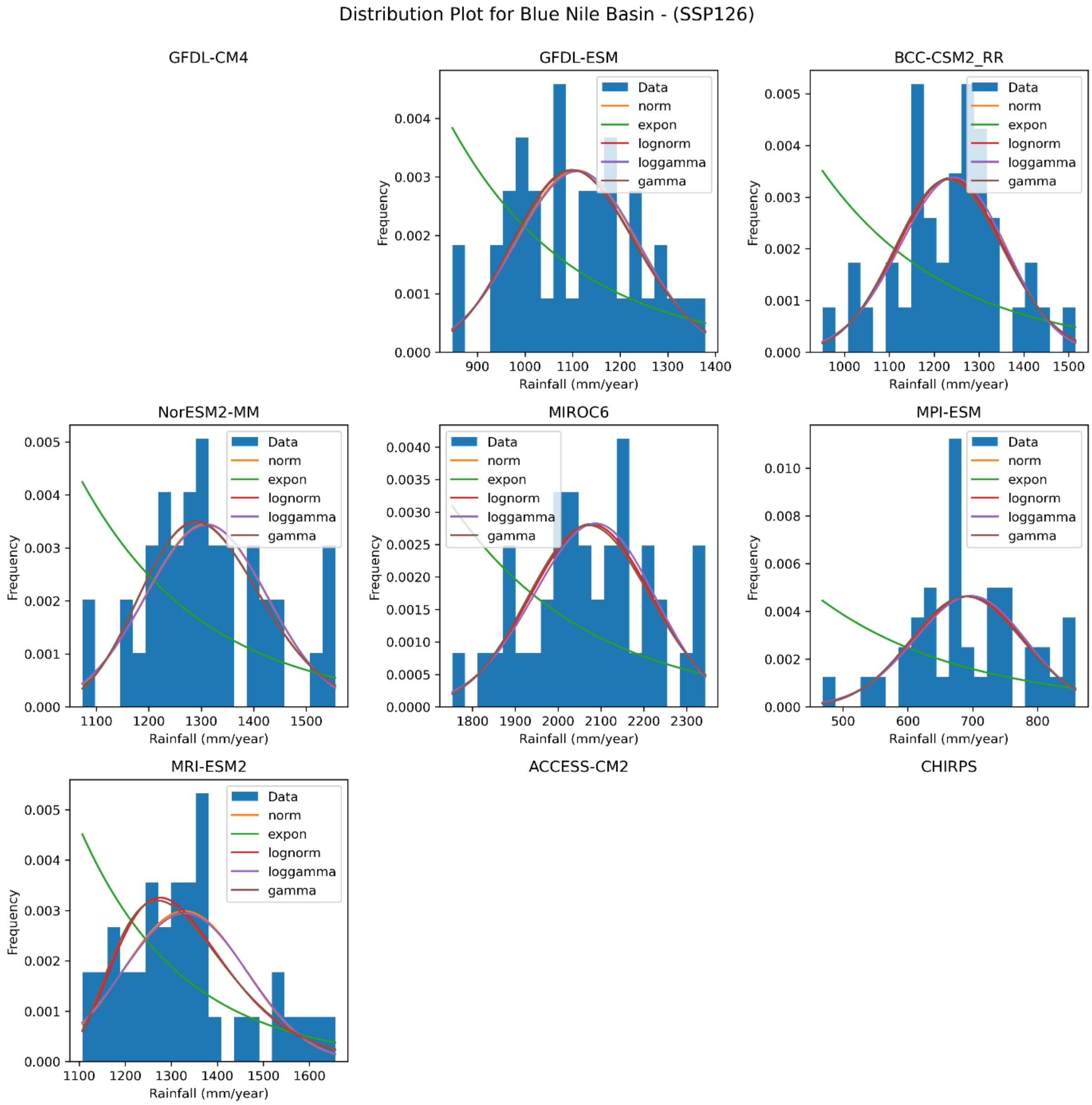
Distribution Plot for Blue Nile Basin - (SSP126)
GFDL-CM4
GFDL-ESM
BCC-CSM2_RR
NorESM2-MM
MIROC6
MPI-ESM
MRI-ESM2
ACCESS-CM2
CHIRPS
Data
norm
expon
lognorm
loggamma
gamma
Frequency
Rainfall (mm/year)

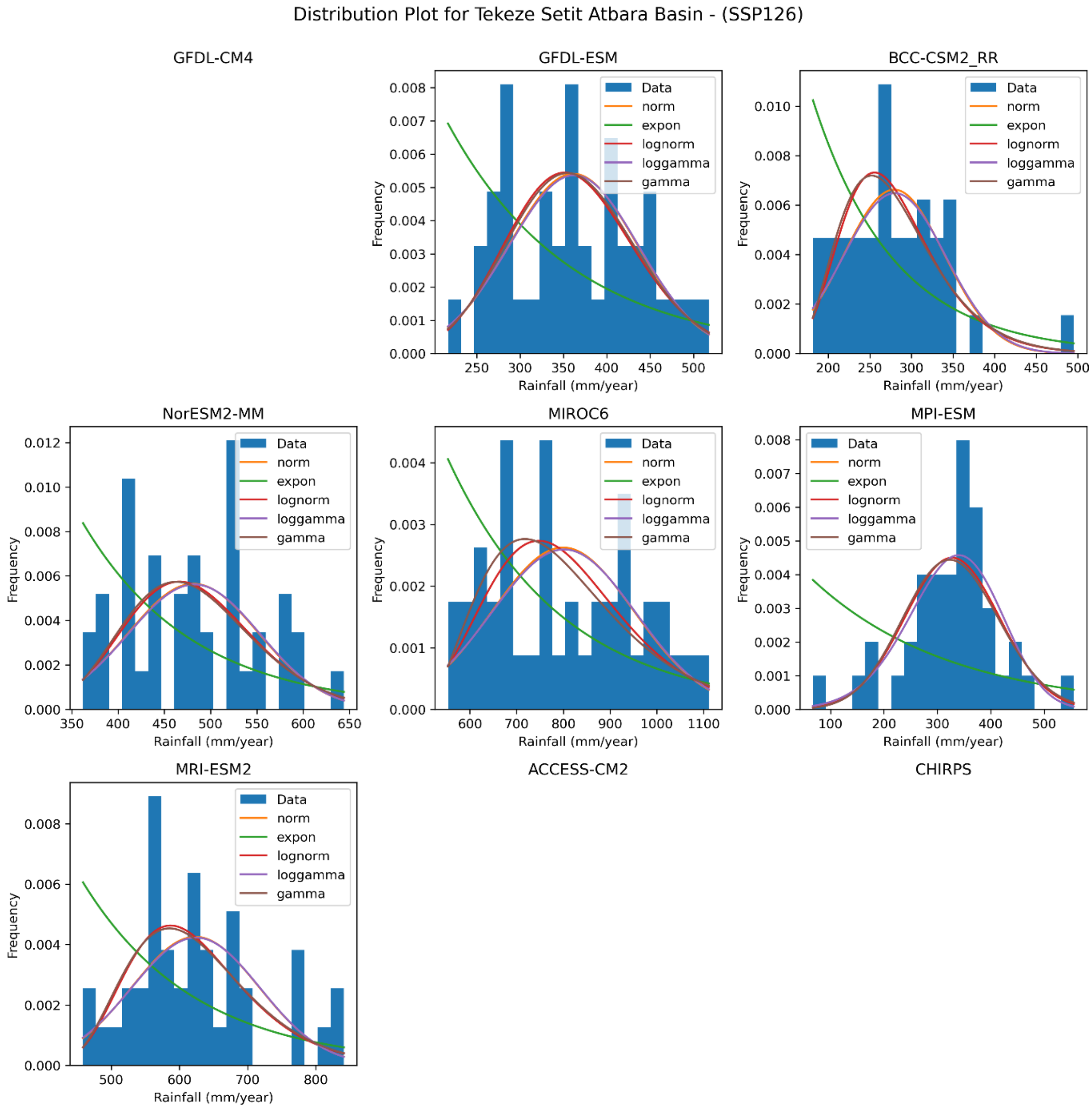
Distribution Plot for Tekeze Setit Atbara Basin - (SSP126)
GFDL-CM4
GFDL-ESM
BCC-CSM2_RR
NorESM2-MM
MIROC6
MPI-ESM
MRI-ESM2
ACCESS-CM2
CHIRPS
Data
norm
expon
lognorm
loggamma
gamma
Frequency
Rainfall (mm/year)

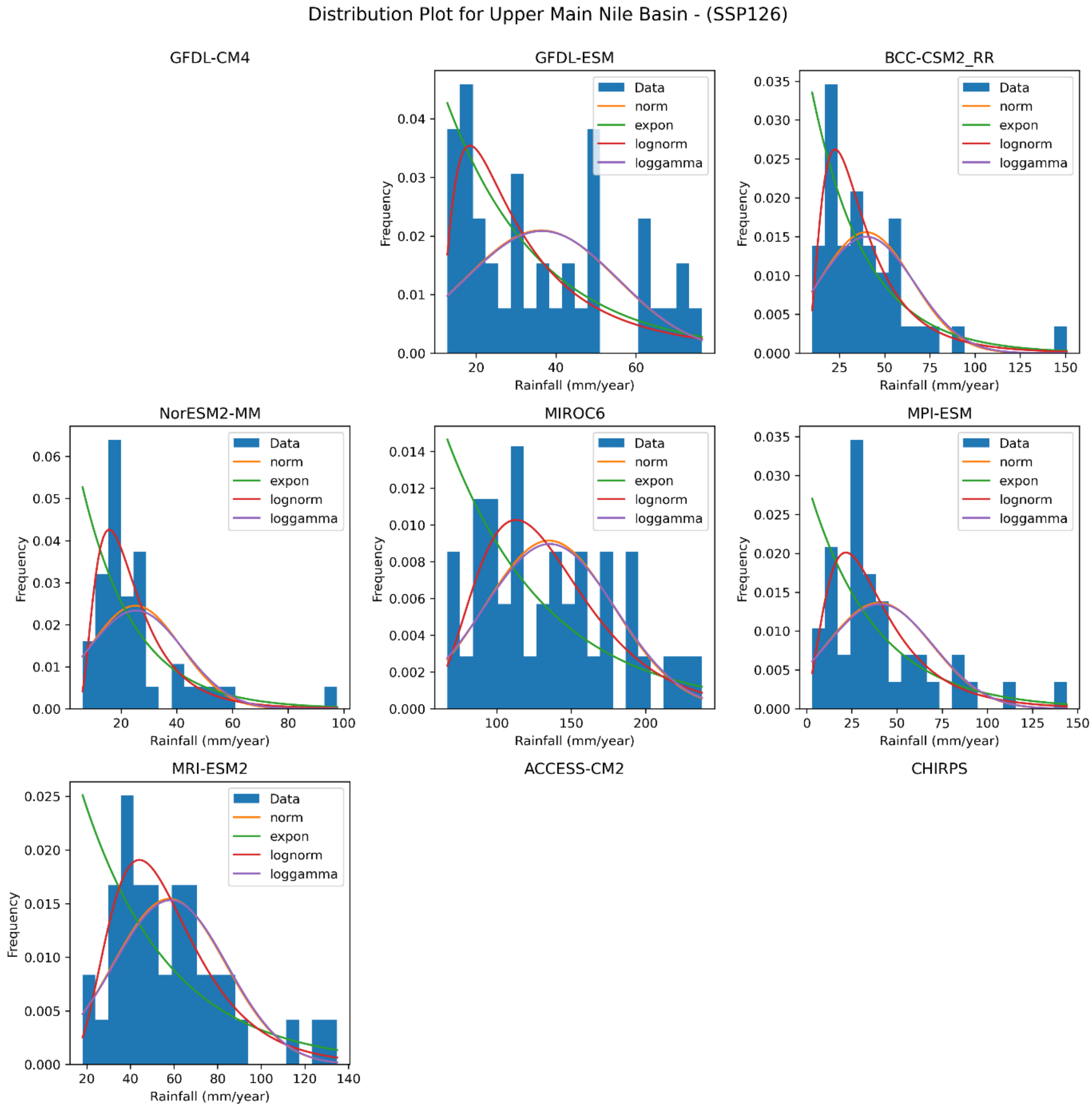

Distribution Plot for Upper Main Nile Basin - (SSP126)
GFDL-CM4
GFDL-ESM
BCC-CSM2_RR
NorESM2-MM
MIROC6
MPI-ESM
MRI-ESM2
ACCESS-CM2
CHIRPS
Data
norm
expon
lognorm
loggamma
Frequency
Rainfall (mm/year)

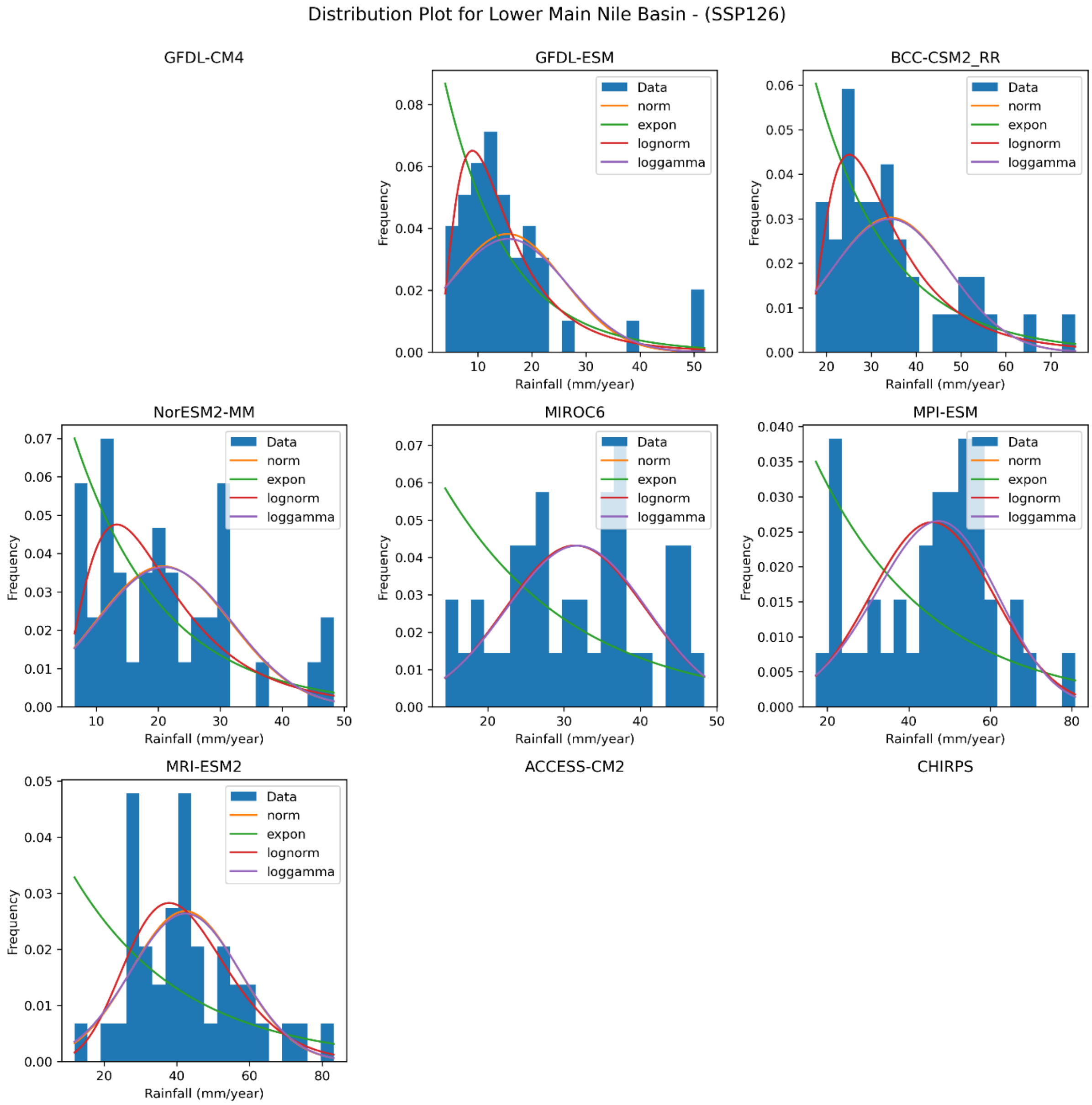
Distribution Plot for Lower Main Nile Basin - (SSP126)
GFDL-CM4
GFDL-ESM
BCC-CSM2_RR
NorESM2-MM
MIROC6
MPI-ESM
MRI-ESM2
ACCESS-CM2
CHIRPS
Data
norm
expon
lognorm
loggamma
Frequency
Rainfall (mm/year)

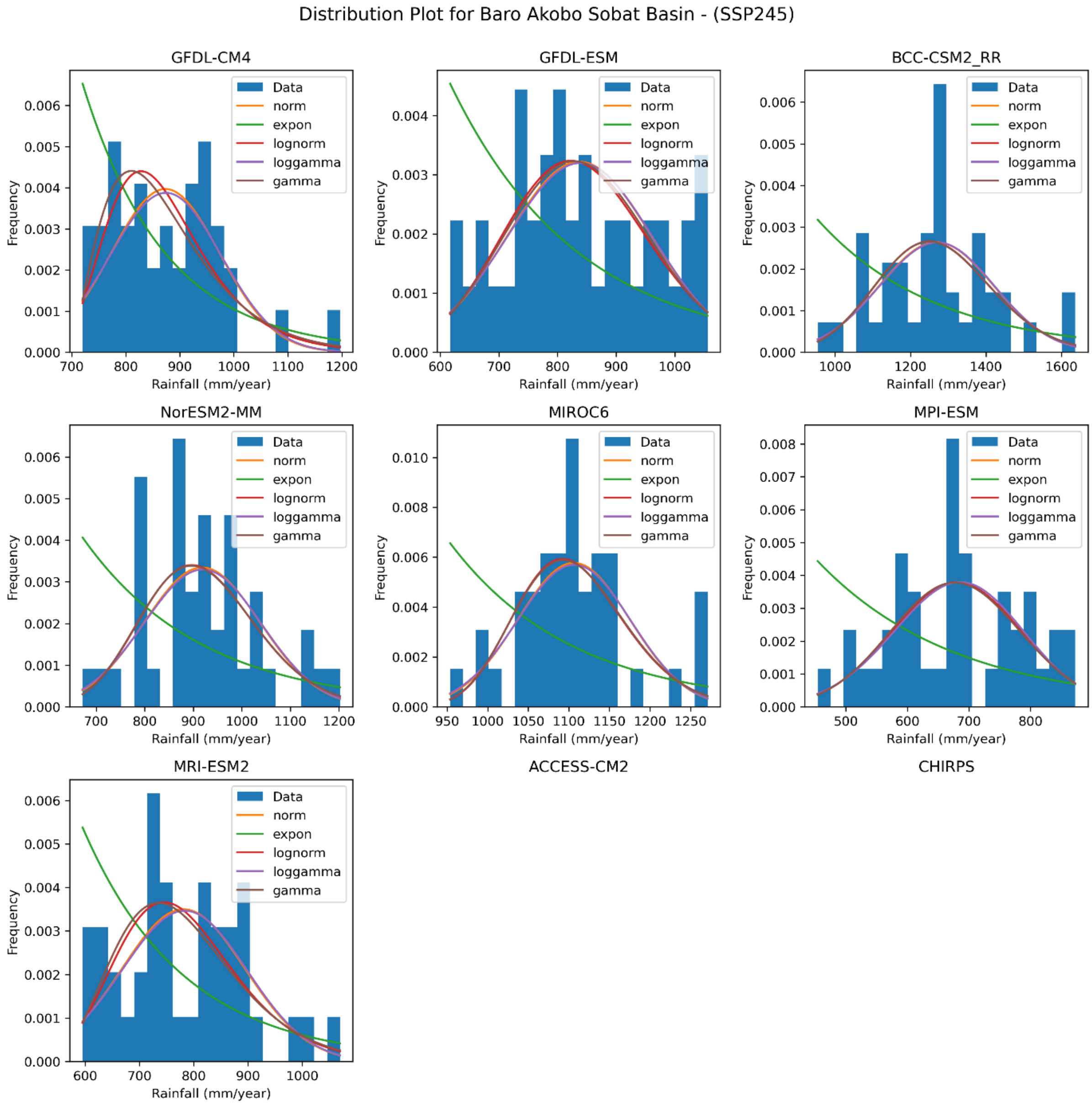
Distribution Plot for Baro Akobo Sobat Basin - (SSP245)
GFDL-CM4
GFDL-ESM
BCC-CSM2_RR
NorESM2-MM
MIROC6
MPI-ESM
MRI-ESM2
ACCESS-CM2
CHIRPS
Data
norm
expon
lognorm
loggamma
gamma
Frequency
Rainfall (mm/year)

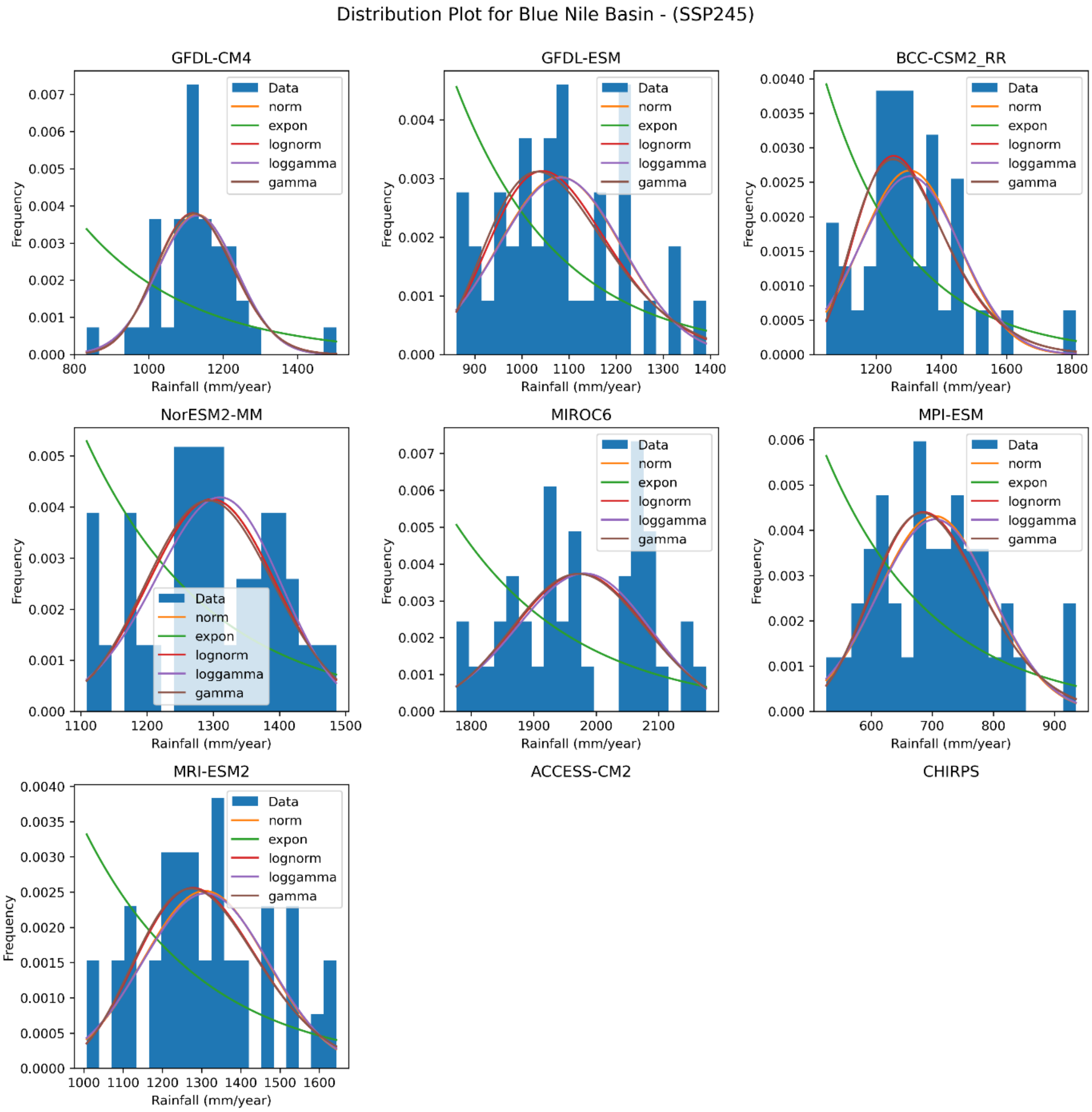
Distribution Plot for Blue Nile Basin - (SSP245)
GFDL-CM4
GFDL-ESM
BCC-CSM2_RR
NorESM2-MM
MIROC6
MPI-ESM
MRI-ESM2
ACCESS-CM2
CHIRPS
Data
norm
expon
lognorm
loggamma
gamma
Frequency
Rainfall (mm/year)

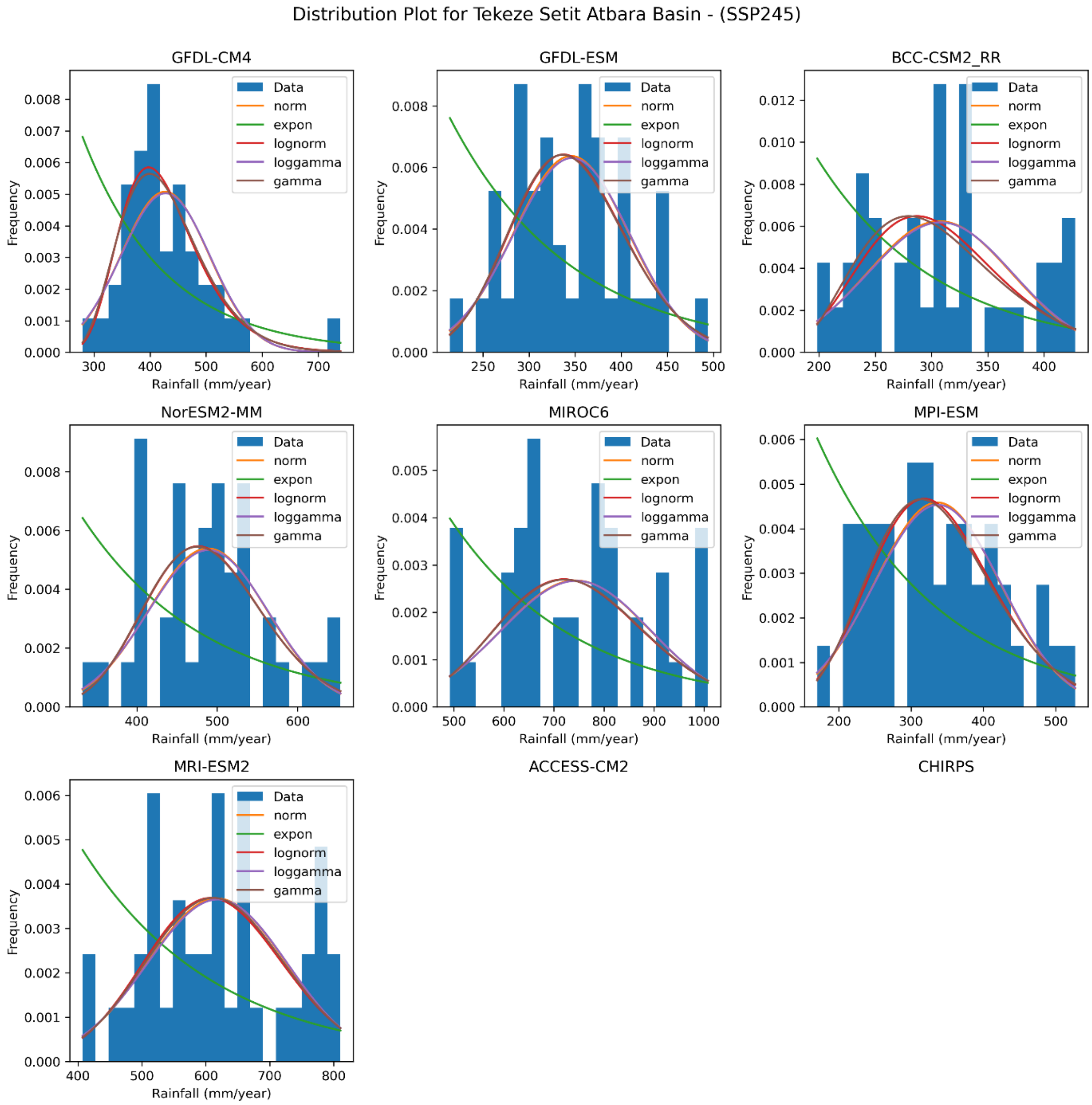
Distribution Plot for Tekeze Setit Atbara Basin - (SSP245)
GFDL-CM4
GFDL-ESM
BCC-CSM2_RR
NorESM2-MM
MIROC6
MPI-ESM
MRI-ESM2
ACCESS-CM2
CHIRPS
Data
norm
expon
lognorm
loggamma
gamma
Frequency
Rainfall (mm/year)

Distribution Plot for Upper Main Nile Basin - (SSP245)

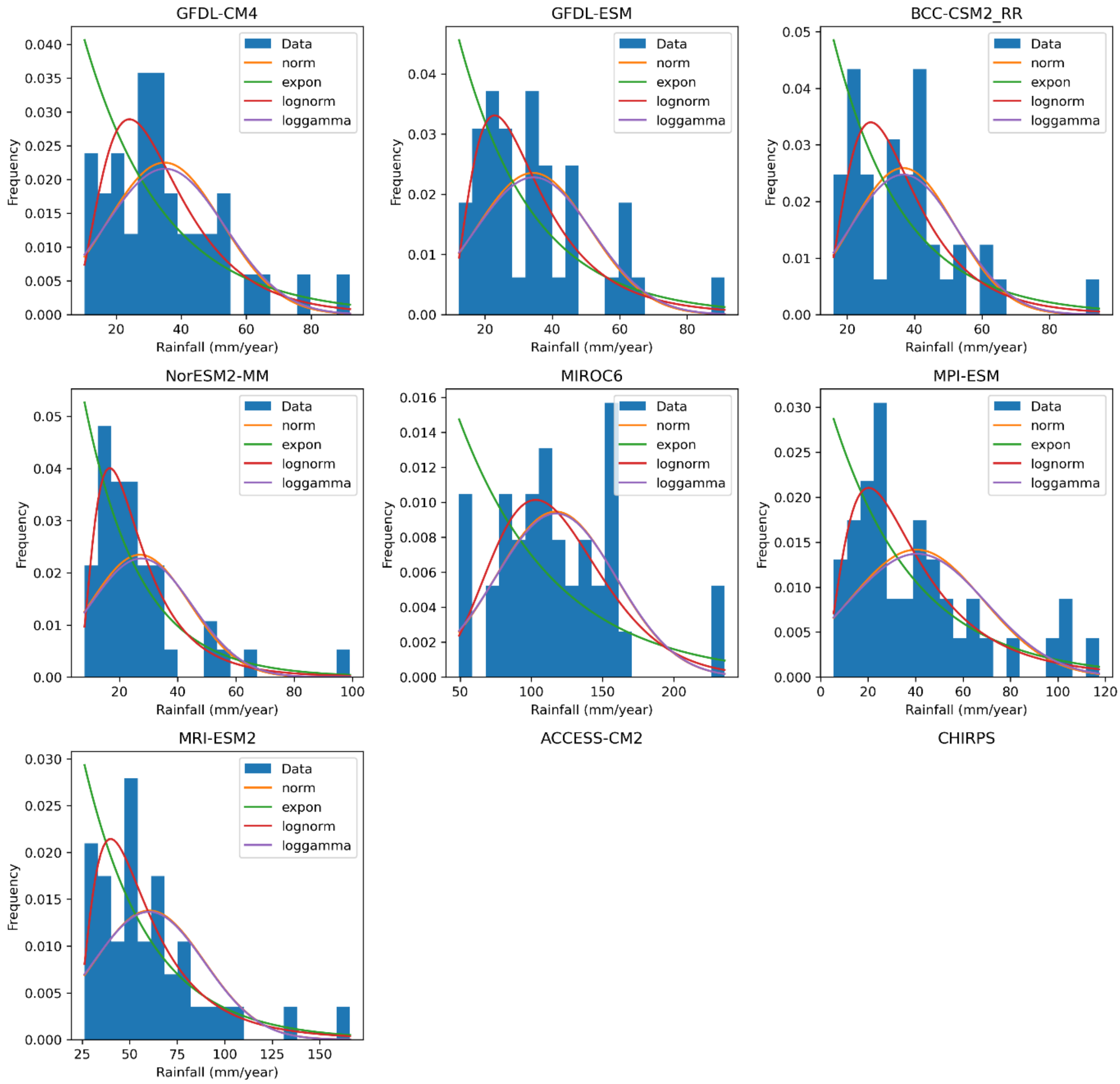

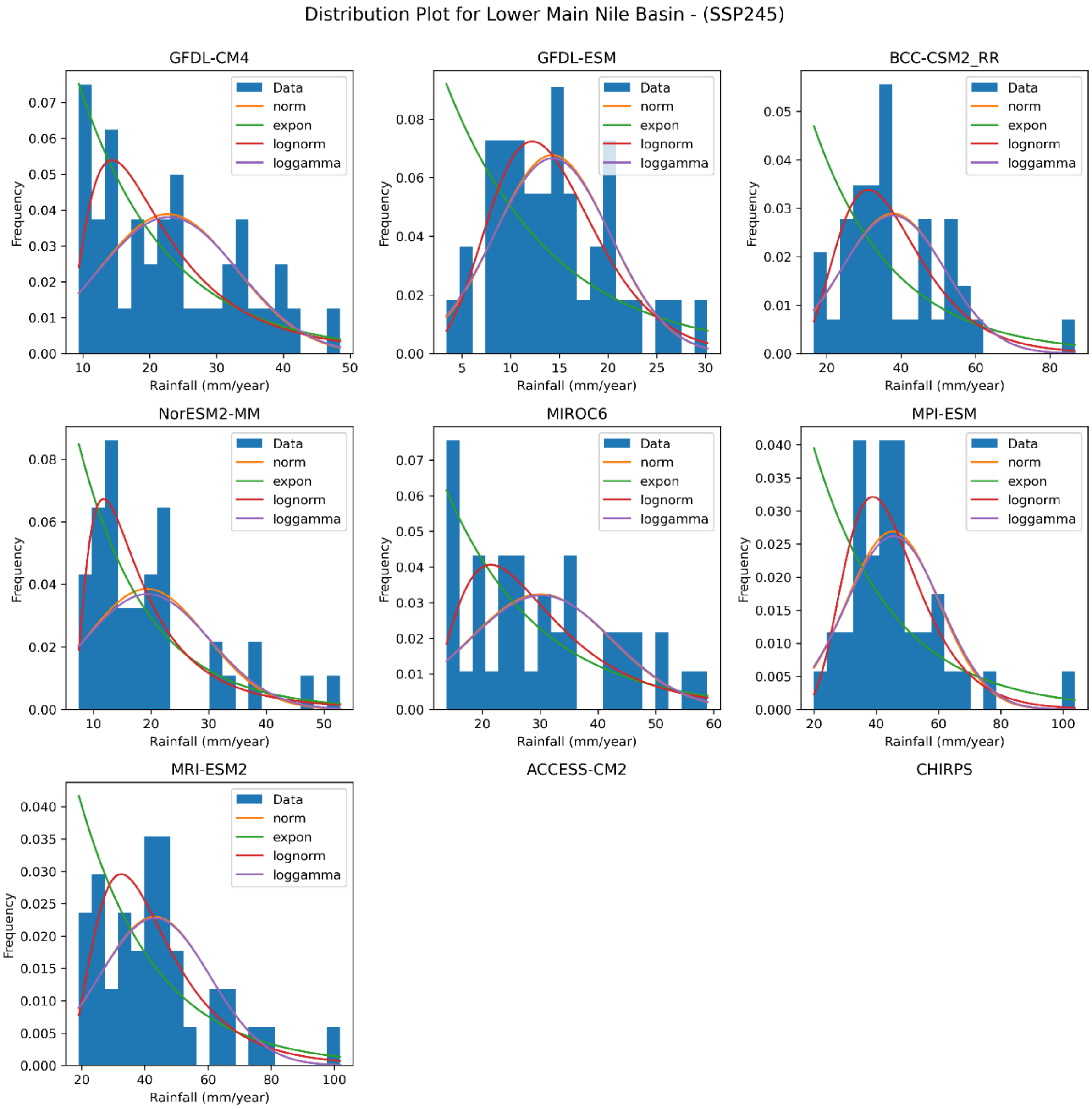
Distribution Plot for Lower Main Nile Basin - (SSP245)
GFDL-CM4
GFDL-ESM
BCC-CSM2_RR
NorESM2-MM
MIROC6
MPI-ESM
MRI-ESM2
ACCESS-CM2
CHIRPS
Data
norm
expon
lognorm
loggamma
Frequency
Rainfall (mm/year)

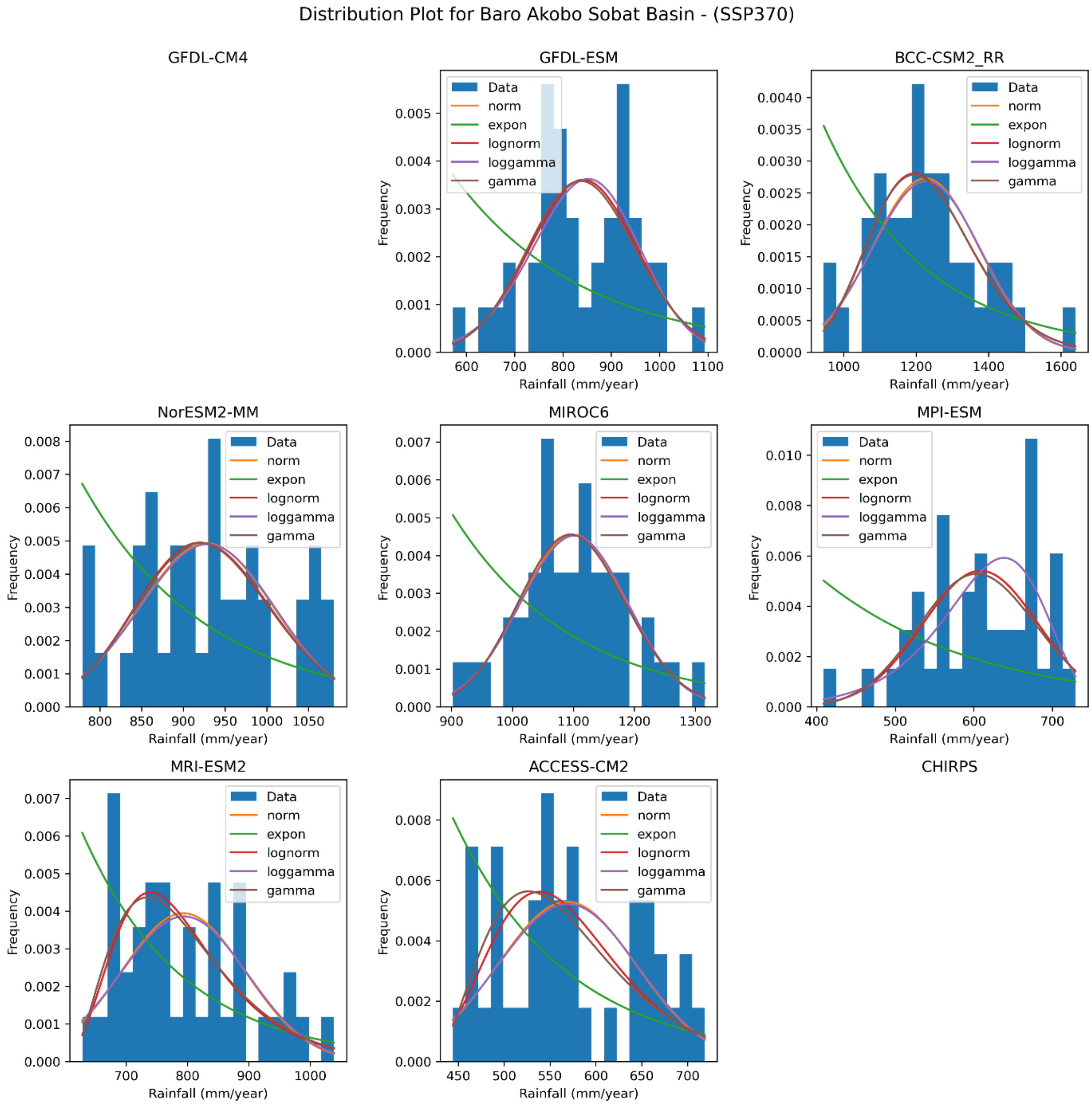
Distribution Plot for Baro Akobo Sobat Basin - (SSP370)
GFDL-CM4
GFDL-ESM
BCC-CSM2_RR
NorESM2-MM
MIROC6
MPI-ESM
MRI-ESM2
ACCESS-CM2
CHIRPS
Data
norm
expon
lognorm
loggamma
gamma
Frequency
Rainfall (mm/year)

Distribution Plot for Blue Nile Basin - (SSP370)

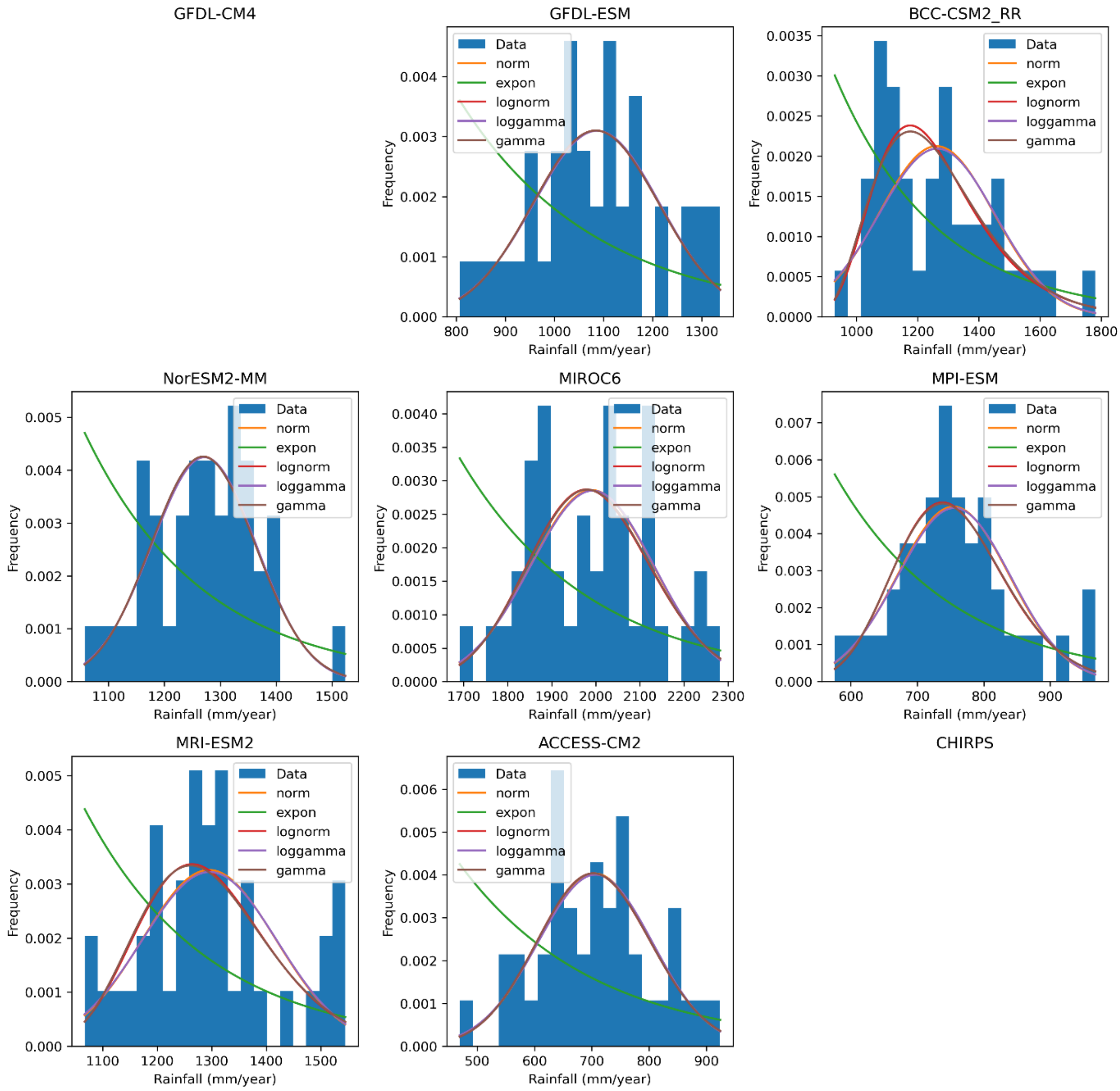

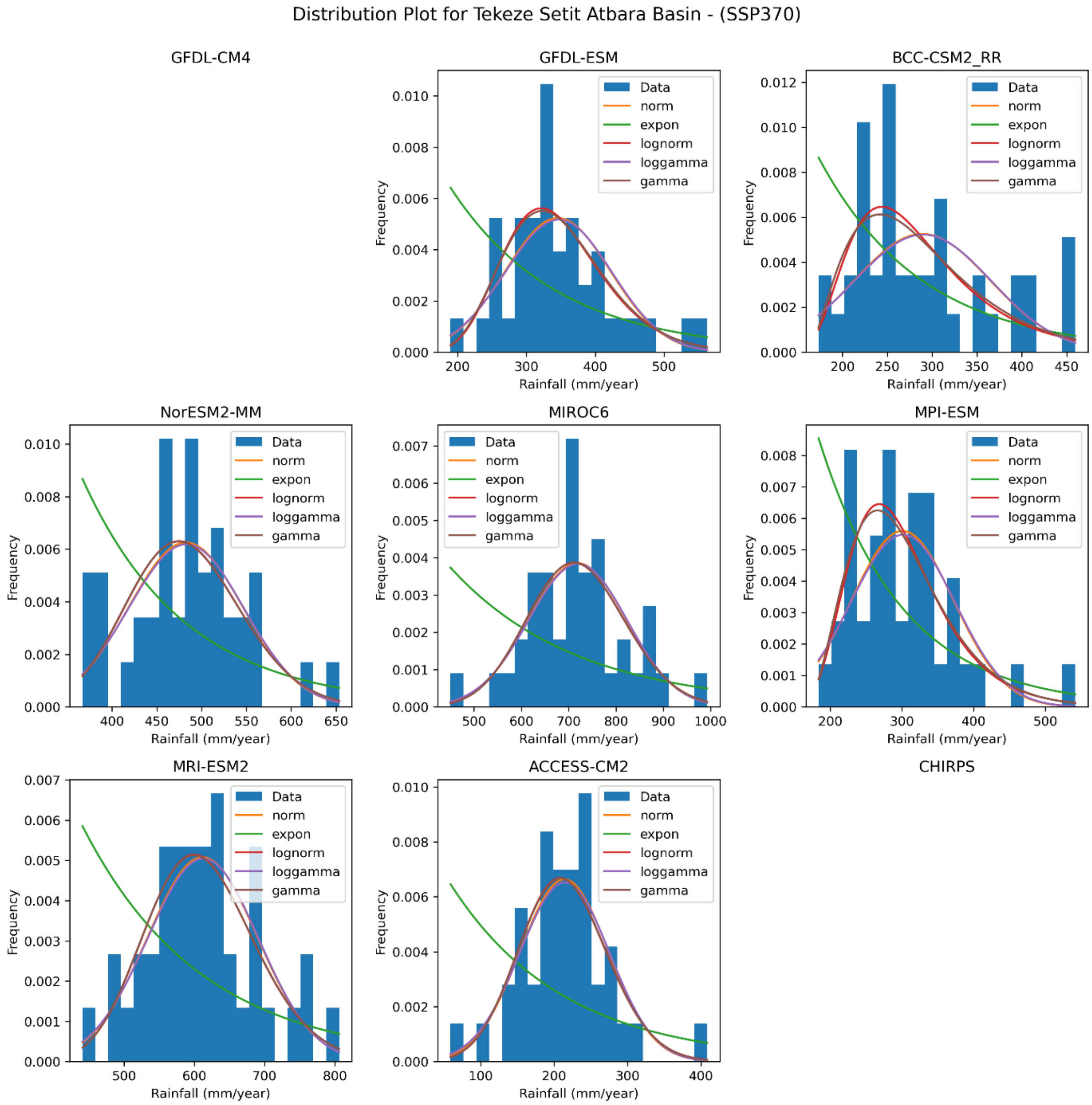
Distribution Plot for Tekeze Setit Atbara Basin - (SSP370)
GFDL-CM4
GFDL-ESM
BCC-CSM2_RR
NorESM2-MM
MIROC6
MPI-ESM
MRI-ESM2
ACCESS-CM2
CHIRPS
Data
norm
expon
lognorm
loggamma
gamma
Frequency
Rainfall (mm/year)

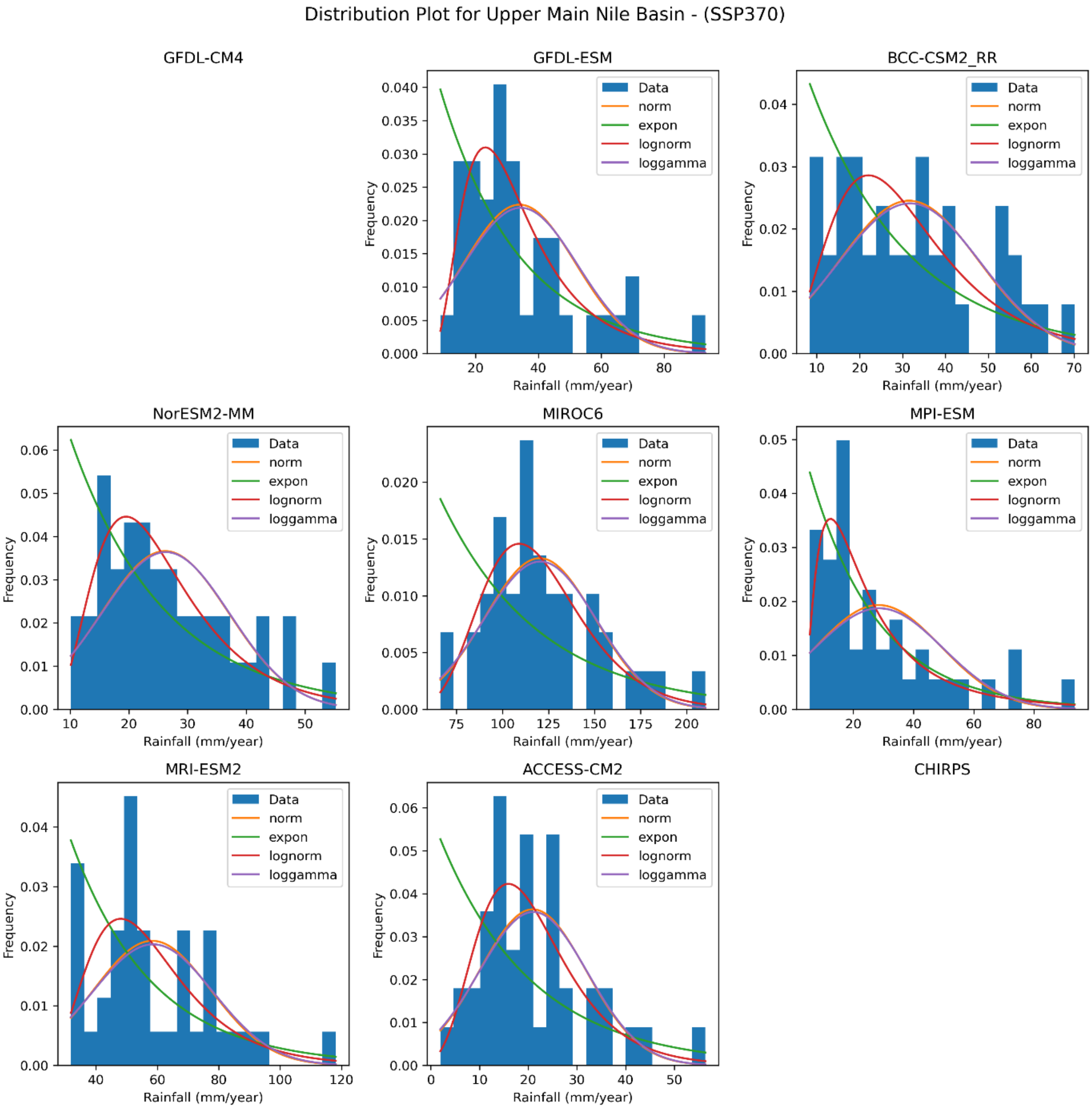
Distribution Plot for Upper Main Nile Basin - (SSP370)
GFDL-CM4
GFDL-ESM
BCC-CSM2_RR
NorESM2-MM
MIROC6
MPI-ESM
MRI-ESM2
ACCESS-CM2
CHIRPS
Data
norm
expon
lognorm
loggamma
Frequency
Rainfall (mm/year)

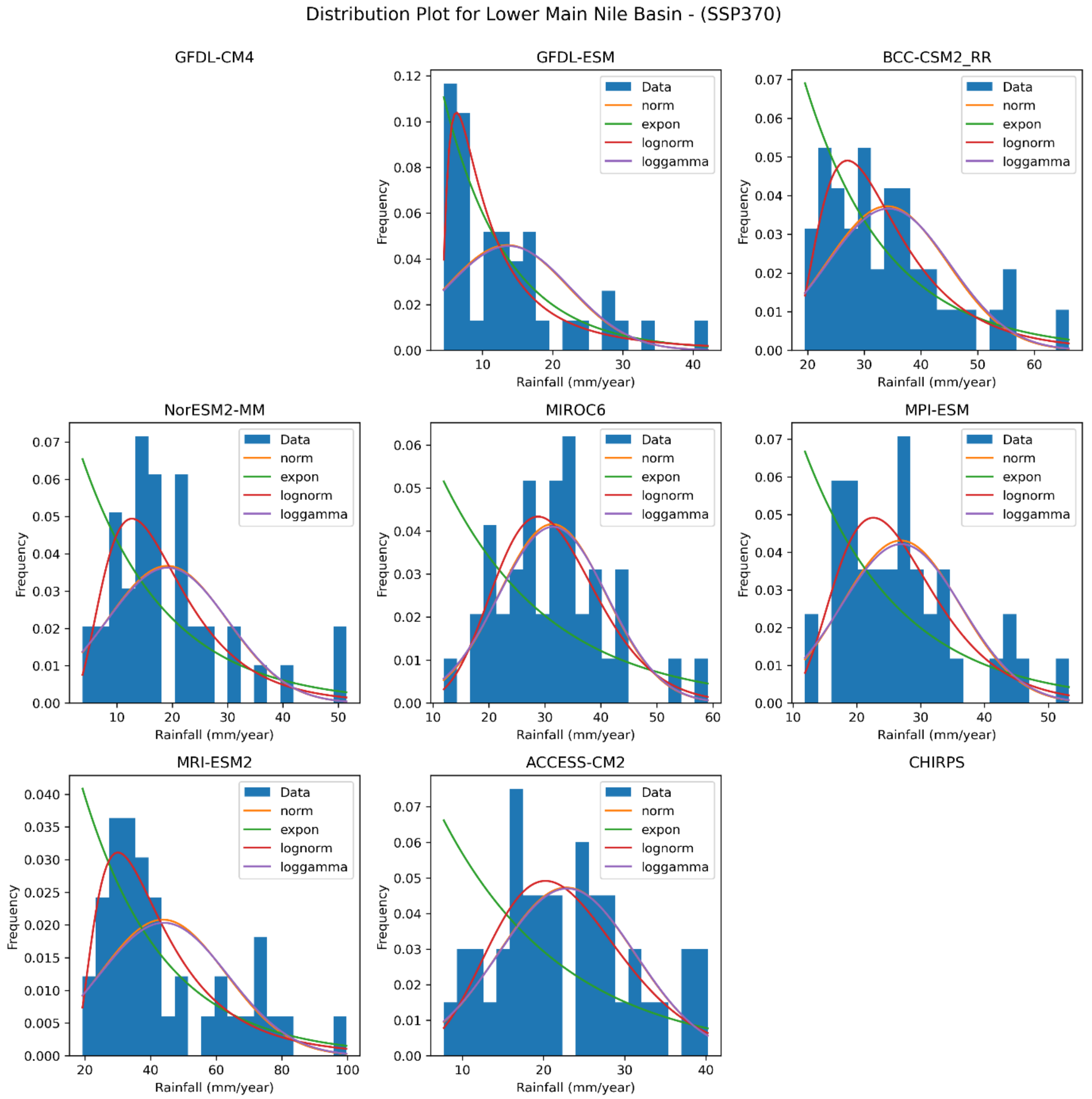
Distribution Plot for Lower Main Nile Basin - (SSP370)
GFDL-CM4
GFDL-ESM
BCC-CSM2_RR
NorESM2-MM
MIROC6
MPI-ESM
MRI-ESM2
ACCESS-CM2
CHIRPS
Data
norm
expon
lognorm
loggamma
Frequency
Rainfall (mm/year)

SSP585

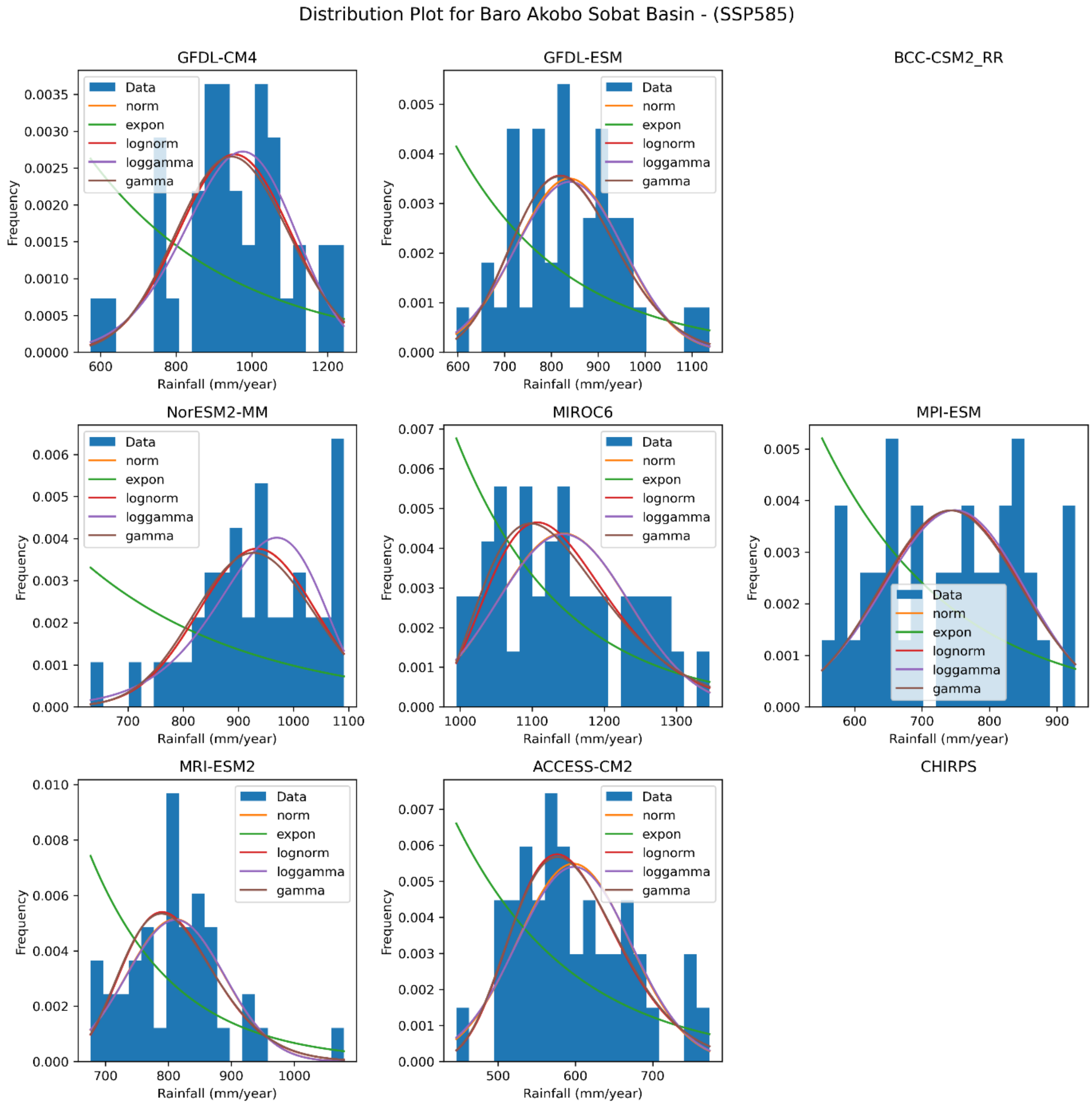
Distribution Plot for Baro Akobo Sobat Basin - (SSP585)
GFDL-CM4
GFDL-ESM
BCC-CSM2_RR
NorESM2-MM
MIROC6
MPI-ESM
MRI-ESM2
ACCESS-CM2
CHIRPS
Data
norm
expon
lognorm
loggamma
gamma
Frequency
Rainfall (mm/year)

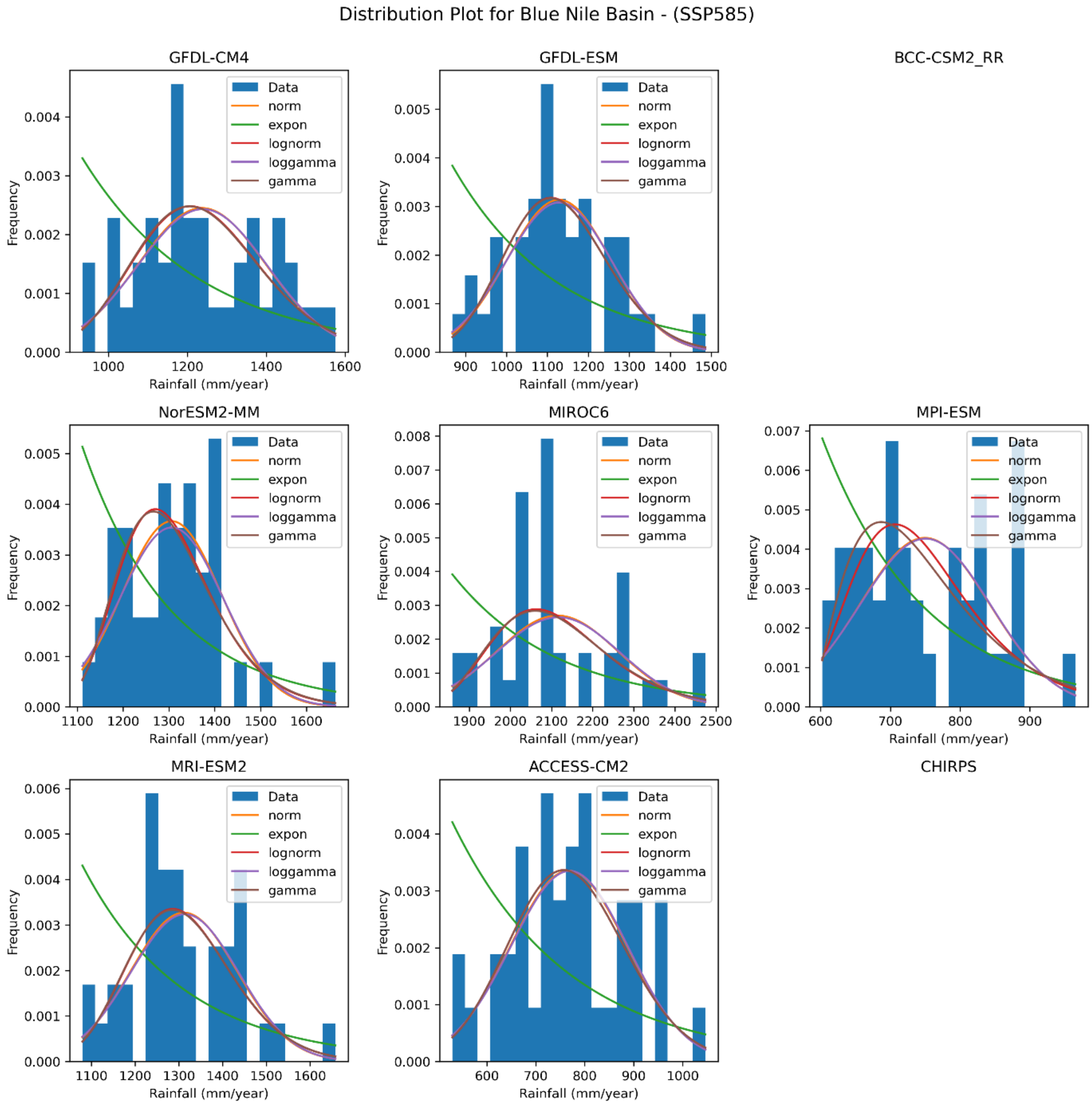
Distribution Plot for Blue Nile Basin - (SSP585)
GFDL-CM4
GFDL-ESM
BCC-CSM2_RR
NorESM2-MM
MIROC6
MPI-ESM
MRI-ESM2
ACCESS-CM2
CHIRPS
Data
norm
expon
lognorm
loggamma
gamma
Frequency
Rainfall (mm/year)

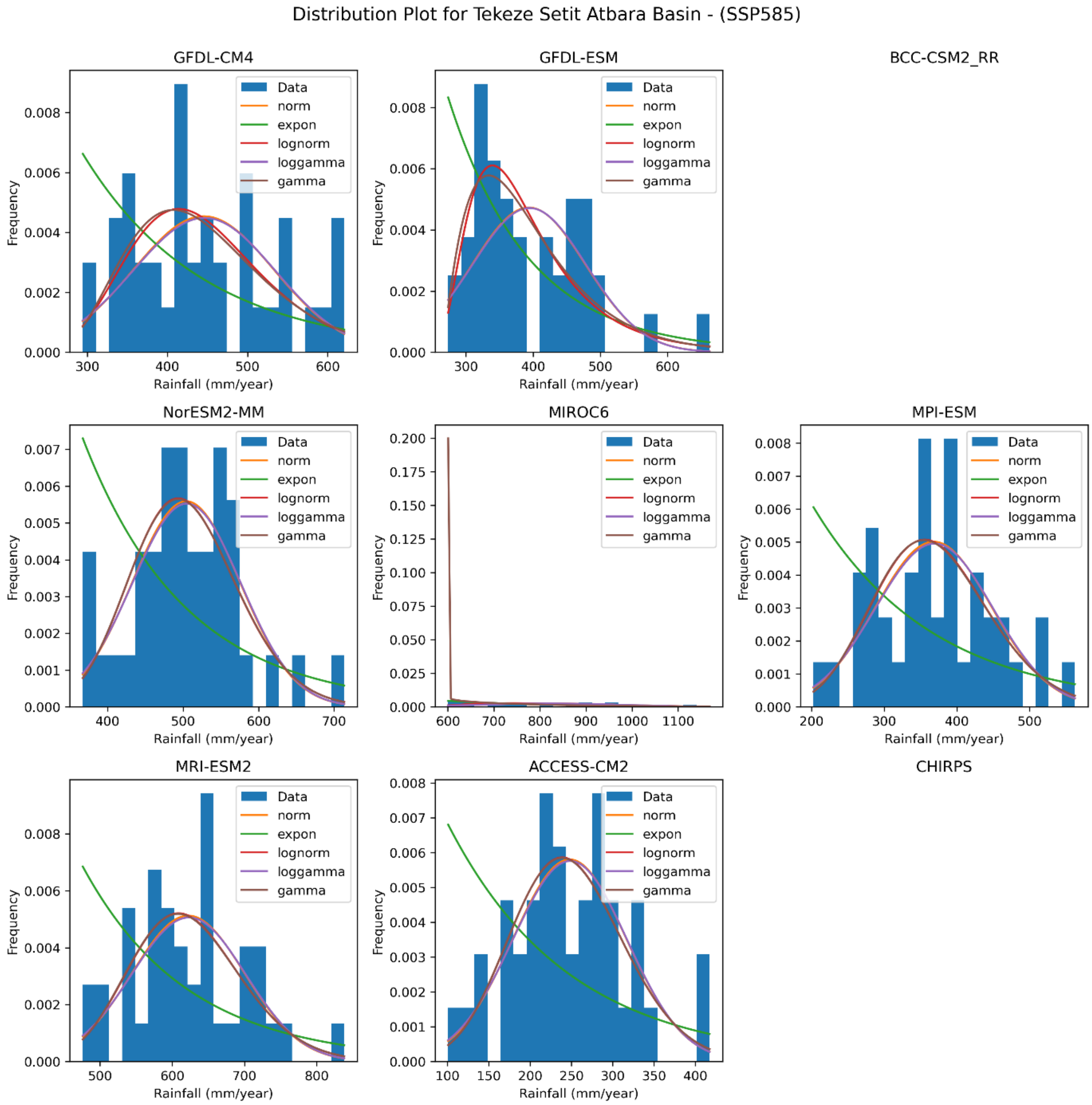
Distribution Plot for Tekeze Setit Atbara Basin - (SSP585)
GFDL-CM4
GFDL-ESM
BCC-CSM2_RR
NorESM2-MM
MIROC6
MPI-ESM
MRI-ESM2
ACCESS-CM2
CHIRPS
Data
norm
expon
lognorm
loggamma
gamma
Frequency
Rainfall (mm/year)

Distribution Plot for Upper Main Nile Basin - (SSP585)

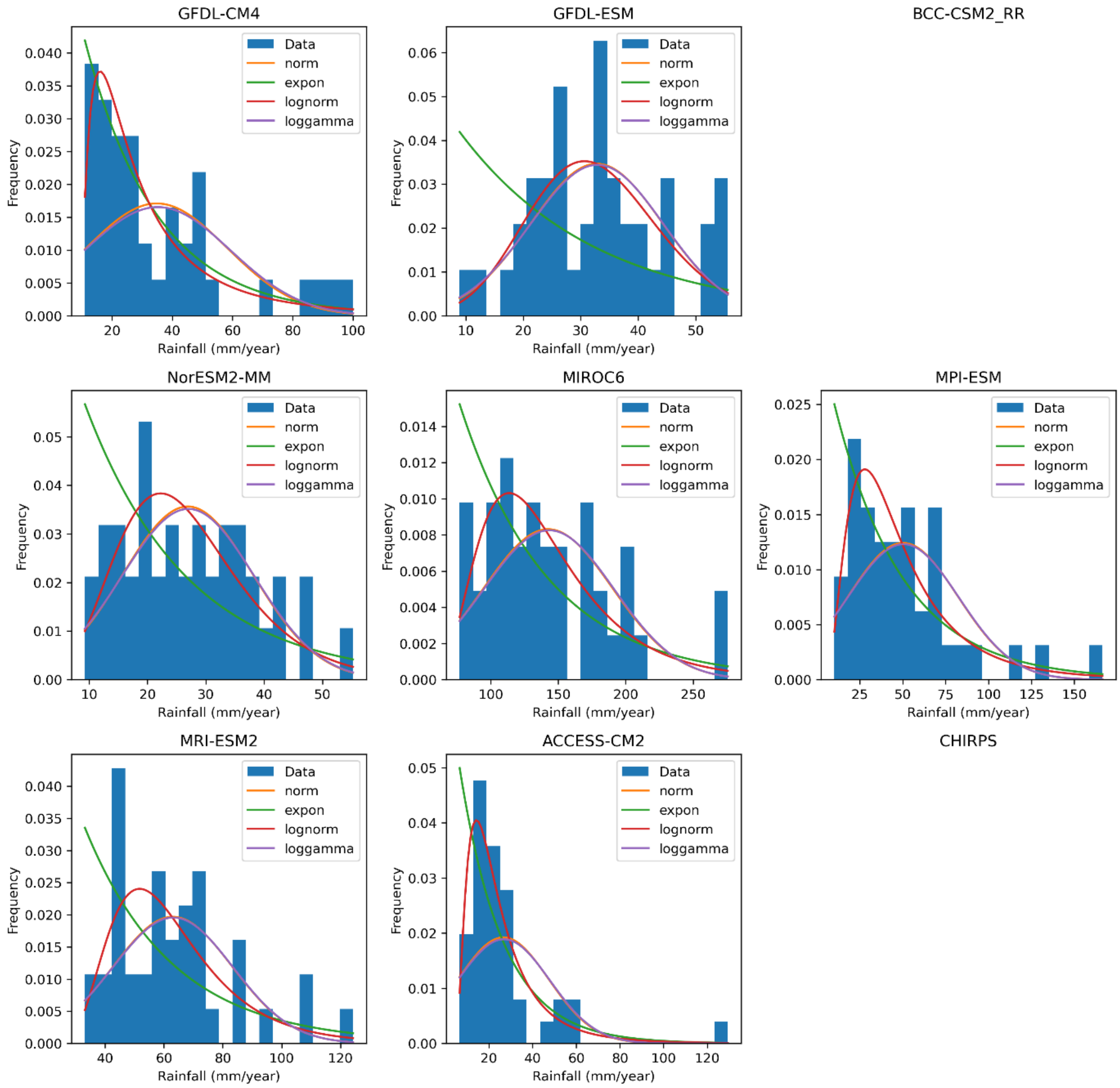

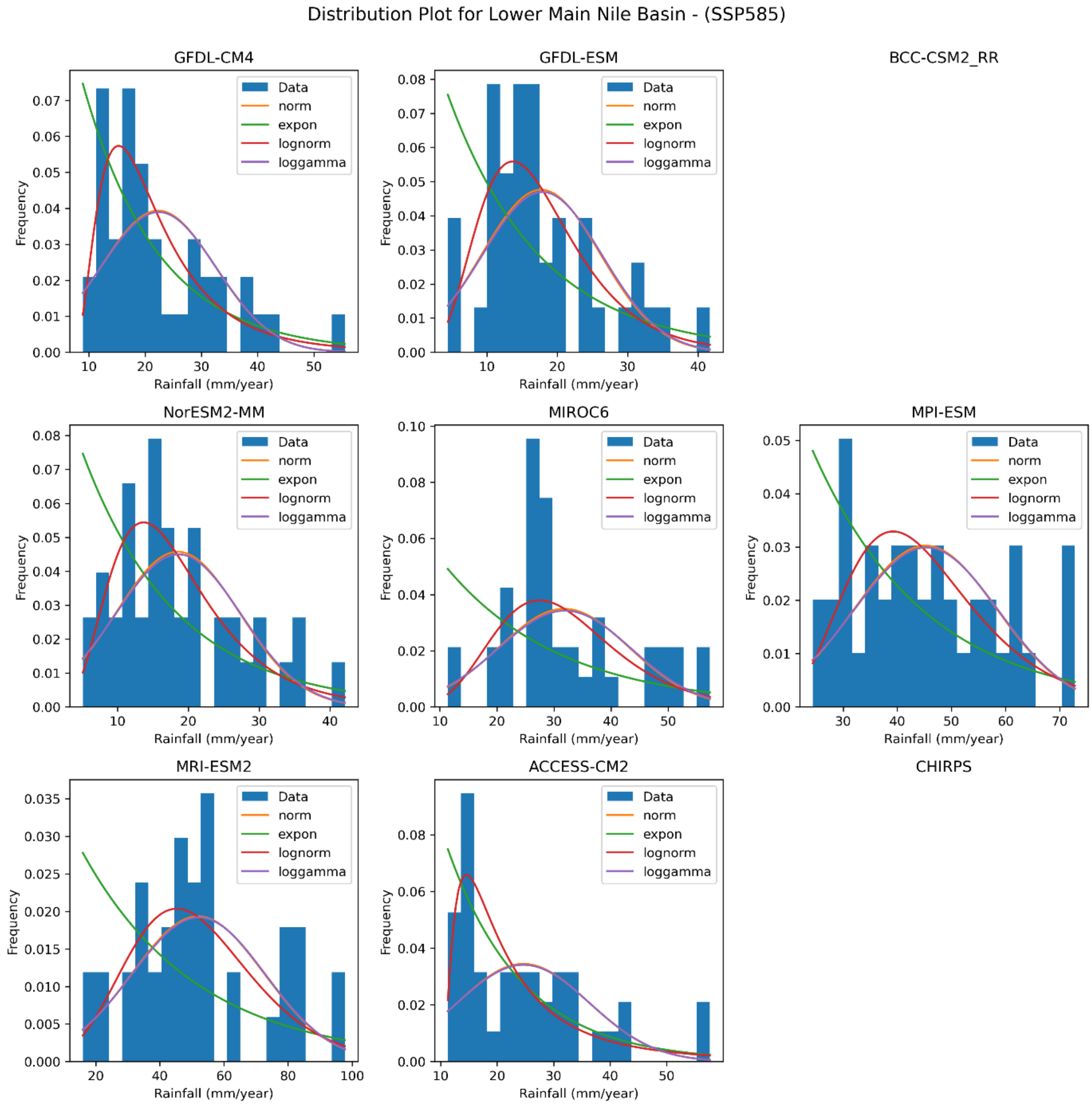

Best Distributions Comparisons for all models across the scenarios

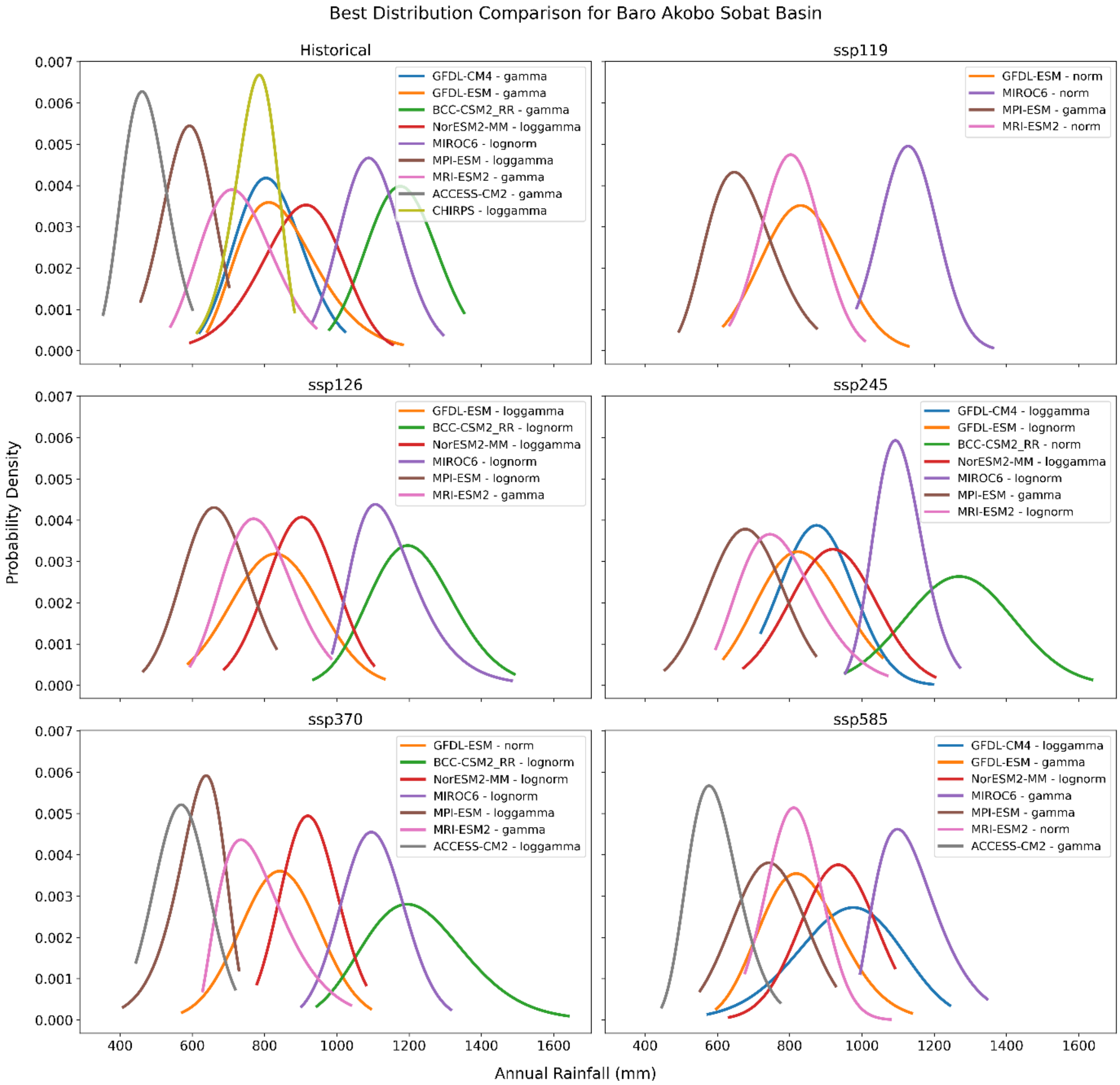

Best Distribution Comparison for Baro Akobo Sobat Basin
Historical
GFDL-CM4 - gamma
GFDL-ESM - gamma
BCC-CSM2_RR - gamma
NorESM2-MM - loggamma
MIROC6 - lognorm
MPI-ESM - loggamma
MRI-ESM2 - gamma
ACCESS-CM2 - gamma
CHIRPS - loggamma
ssp119
GFDL-ESM - norm
MIROC6 - norm
MPI-ESM - gamma
MRI-ESM2 - norm
ssp126
GFDL-ESM - loggamma
BCC-CSM2_RR - lognorm
NorESM2-MM - loggamma
MIROC6 - lognorm
MPI-ESM - lognorm
MRI-ESM2 - gamma
ssp245
GFDL-CM4 - loggamma
GFDL-ESM - lognorm
BCC-CSM2_RR - norm
NorESM2-MM - loggamma
MIROC6 - lognorm
MPI-ESM - gamma
MRI-ESM2 - lognorm
ssp370
GFDL-ESM - norm
BCC-CSM2_RR - lognorm
NorESM2-MM - lognorm
MIROC6 - lognorm
MPI-ESM - loggamma
MRI-ESM2 - gamma
ACCESS-CM2 - loggamma
ssp585
GFDL-CM4 - loggamma
GFDL-ESM - gamma
NorESM2-MM - lognorm
MIROC6 - gamma
MPI-ESM - gamma
MRI-ESM2 - norm
ACCESS-CM2 - gamma
Probability Density
Annual Rainfall (mm)
0.000
0.001
0.002
0.003
0.004
0.005
0.006
0.007
400
600
800
1000
1200
1400
1600

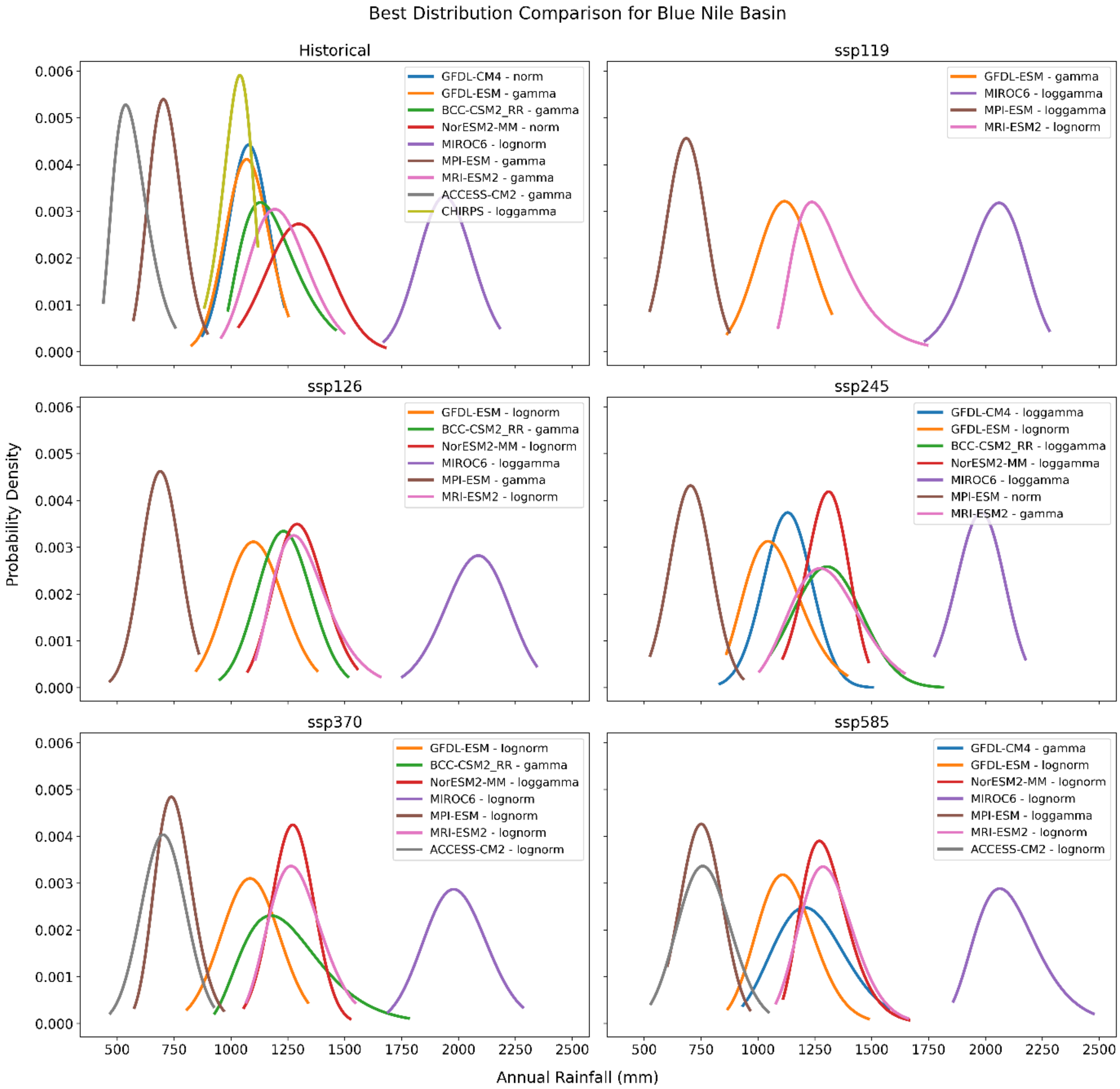
Best Distribution Comparison for Blue Nile Basin
Historical
GFDL-CM4 - norm
GFDL-ESM - gamma
BCC-CSM2_RR - gamma
NorESM2-MM - norm
MIROC6 - lognorm
MPI-ESM - gamma
MRI-ESM2 - gamma
ACCESS-CM2 - gamma
CHIRPS - loggamma
ssp119
GFDL-ESM - gamma
MIROC6 - loggamma
MPI-ESM - loggamma
MRI-ESM2 - lognorm
ssp126
GFDL-ESM - lognorm
BCC-CSM2_RR - gamma
NorESM2-MM - lognorm
MIROC6 - loggamma
MPI-ESM - gamma
MRI-ESM2 - lognorm
ssp245
GFDL-CM4 - loggamma
GFDL-ESM - lognorm
BCC-CSM2_RR - loggamma
NorESM2-MM - loggamma
MIROC6 - loggamma
MPI-ESM - norm
MRI-ESM2 - gamma
ssp370
GFDL-ESM - lognorm
BCC-CSM2_RR - gamma
NorESM2-MM - loggamma
MIROC6 - lognorm
MPI-ESM - lognorm
MRI-ESM2 - lognorm
ACCESS-CM2 - lognorm
ssp585
GFDL-CM4 - gamma
GFDL-ESM - lognorm
NorESM2-MM - lognorm
MIROC6 - lognorm
MPI-ESM - loggamma
MRI-ESM2 - lognorm
ACCESS-CM2 - lognorm
Probability Density
Annual Rainfall (mm)
0.000
0.001
0.002
0.003
0.004
0.005
0.006
500
750
1000
1250
1500
1750
2000
2250
2500

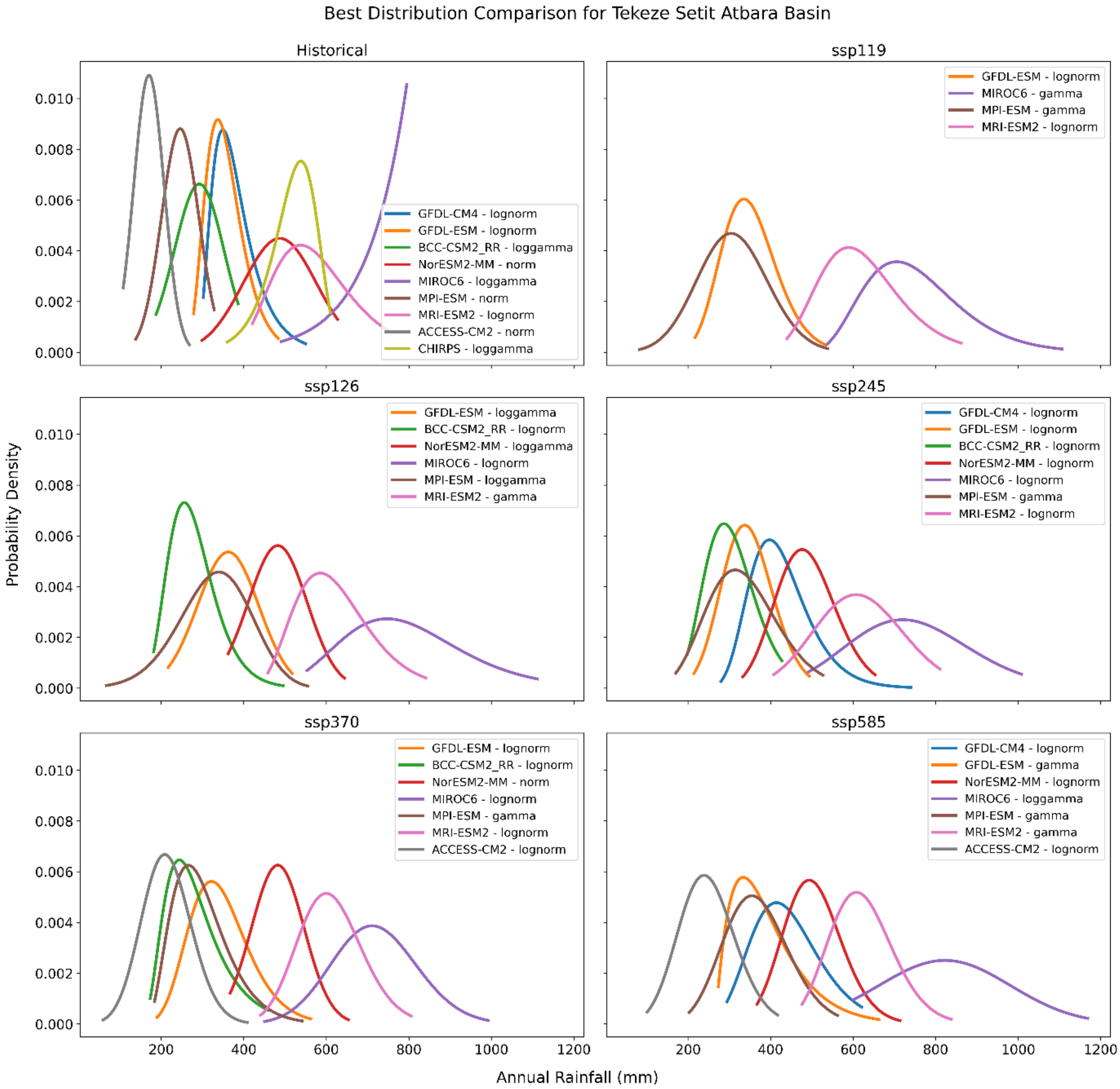

Best Distribution Comparison for Tekeze Setit Atbara Basin
Historical
GFDL-CM4 - lognorm
GFDL-ESM - lognorm
BCC-CSM2_RR - loggamma
NorESM2-MM - norm
MIROC6 - loggamma
MPI-ESM - norm
MRI-ESM2 - lognorm
ACCESS-CM2 - norm
CHIRPS - loggamma
ssp119
GFDL-ESM - lognorm
MIROC6 - gamma
MPI-ESM - gamma
MRI-ESM2 - lognorm
ssp126
GFDL-ESM - loggamma
BCC-CSM2_RR - lognorm
NorESM2-MM - loggamma
MIROC6 - lognorm
MPI-ESM - loggamma
MRI-ESM2 - gamma
ssp245
GFDL-CM4 - lognorm
GFDL-ESM - lognorm
BCC-CSM2_RR - lognorm
NorESM2-MM - lognorm
MIROC6 - lognorm
MPI-ESM - gamma
MRI-ESM2 - lognorm
ssp370
GFDL-ESM - lognorm
BCC-CSM2_RR - lognorm
NorESM2-MM - norm
MIROC6 - lognorm
MPI-ESM - gamma
MRI-ESM2 - lognorm
ACCESS-CM2 - lognorm
ssp585
GFDL-CM4 - lognorm
GFDL-ESM - gamma
NorESM2-MM - lognorm
MIROC6 - loggamma
MPI-ESM - gamma
MRI-ESM2 - gamma
ACCESS-CM2 - lognorm
Probability Density
0.000
0.002
0.004
0.006
0.008
0.010
200
400
600
800
1000
1200
Annual Rainfall (mm)

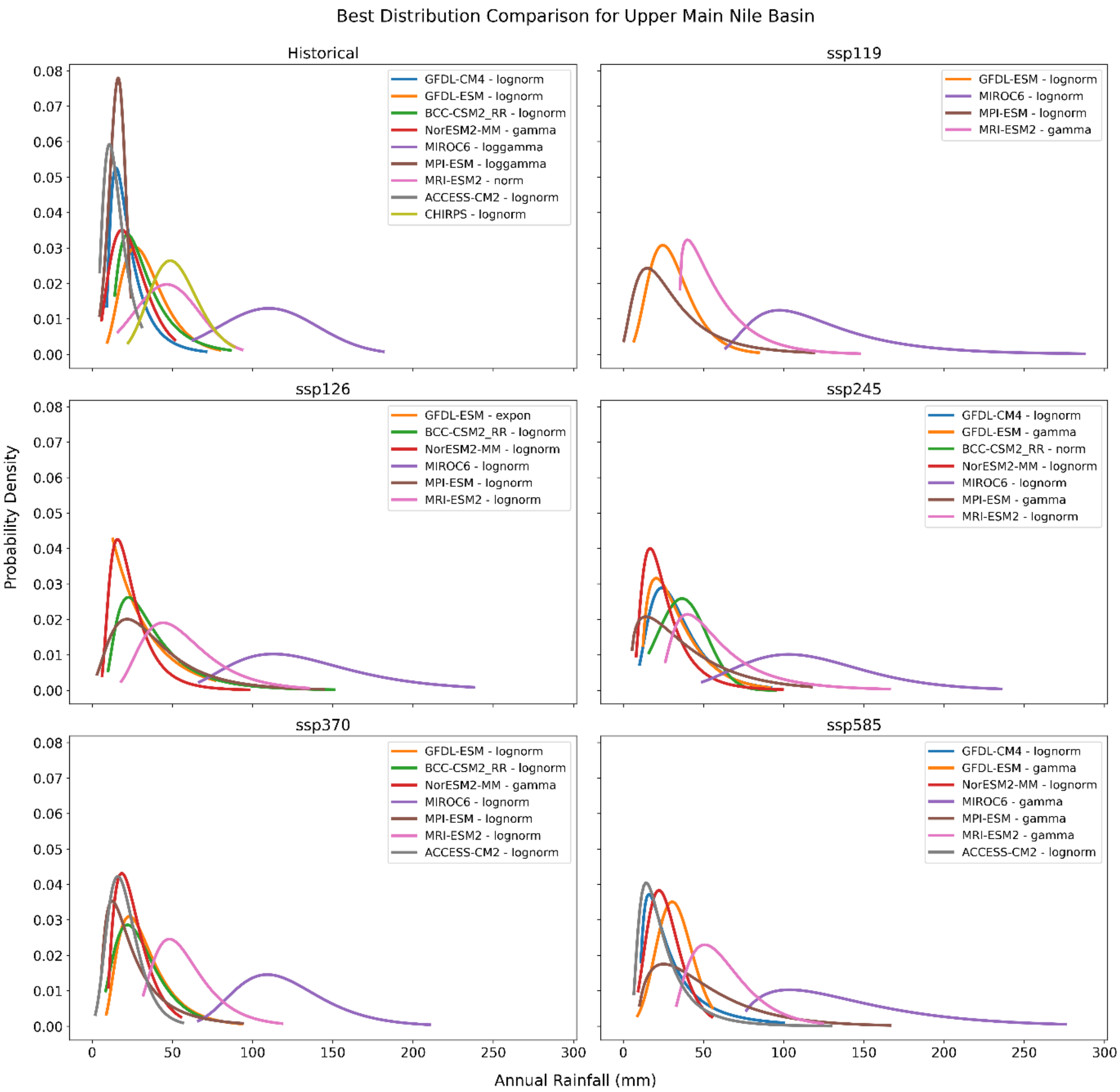

Best Distribution Comparison for Upper Main Nile Basin
Historical
GFDL-CM4 - lognorm
GFDL-ESM - lognorm
BCC-CSM2_RR - lognorm
NorESM2-MM - gamma
MIROC6 - loggamma
MPI-ESM - loggamma
MRI-ESM2 - norm
ACCESS-CM2 - lognorm
CHIRPS - lognorm
ssp119
GFDL-ESM - lognorm
MIROC6 - lognorm
MPI-ESM - lognorm
MRI-ESM2 - gamma
ssp126
GFDL-ESM - expon
BCC-CSM2_RR - lognorm
NorESM2-MM - lognorm
MIROC6 - lognorm
MPI-ESM - lognorm
MRI-ESM2 - lognorm
ssp245
GFDL-CM4 - lognorm
GFDL-ESM - gamma
BCC-CSM2_RR - norm
NorESM2-MM - lognorm
MIROC6 - lognorm
MPI-ESM - gamma
MRI-ESM2 - lognorm
ssp370
GFDL-ESM - lognorm
BCC-CSM2_RR - lognorm
NorESM2-MM - gamma
MIROC6 - lognorm
MPI-ESM - lognorm
MRI-ESM2 - lognorm
ACCESS-CM2 - lognorm
ssp585
GFDL-CM4 - lognorm
GFDL-ESM - gamma
NorESM2-MM - lognorm
MIROC6 - gamma
MPI-ESM - gamma
MRI-ESM2 - gamma
ACCESS-CM2 - lognorm
Probability Density
Annual Rainfall (mm)

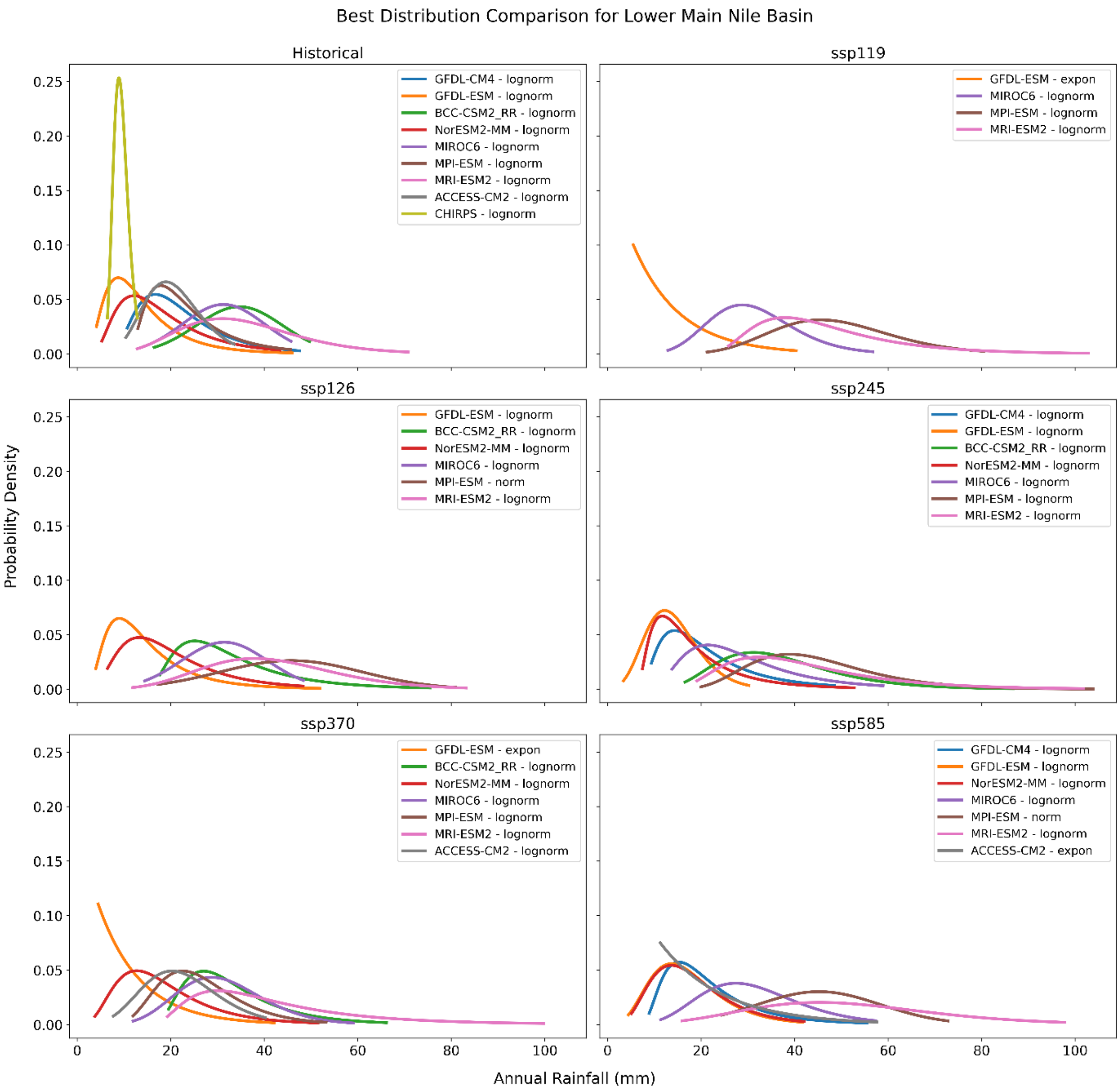
Best Distribution Comparison for Lower Main Nile Basin
Historical
ssp119
ssp126
ssp245
ssp370
ssp585
GFDL-CM4 - lognorm
GFDL-ESM - lognorm
BCC-CSM2_RR - lognorm
NorESM2-MM - lognorm
MIROC6 - lognorm
MPI-ESM - lognorm
MRI-ESM2 - lognorm
ACCESS-CM2 - lognorm
CHIRPS - lognorm
GFDL-ESM - expon
MPI-ESM - norm
ACCESS-CM2 - expon
Probability Density
Annual Rainfall (mm)
0.00
0.05
0.10
0.15
0.20
0.25
0
20
40
60
80
100